Measurement of the double differential neutron cross section of UO2 and determination of the thermal scattering law as a function of temperature

Shuqi Xu

NNT/NL : 2021AIXM0303/031ED352

THÈSE DE DOCTORAT

Soutenue à Aix-Marseille Université
le 17 septembre 2021 par

Shuqi XU

Measurement of the double differential neutron cross section of UO_2 and determination of the thermal scattering law as a function of temperature

Discipline
Physique et Sciences de la Matière

Spécialité
Énergie, Rayonnement et Plasma

École doctorale
ED 352 Physique et Sciences de la Matière

Laboratoire/Partenaires de recherche
CEA/Cadarache/DES/IRESNE/DER/SPRC/
Laboratoire d'Études de Physique

CEA/Cadarache/DES/IRESNE/DEC

Institut Laue-Langevin, Grenoble

Composition du jury

Marie-Claire BELLISSENT-FUNEL CEA-CNRS Saclay	Rapporteur
Luiz LEAL IRSN	Rapporteur
Emily LIU Rensselaer Polytechnic Institute	Examinatrice
Jose BUSTO Aix-Marseille Université	Président du jury
Gilles NOGUERE CEA/Cadarache	Directeur de thèse
Lionel DESGRANGES CEA/Cadarache	Invité

Affidavit

I, undersigned, Shuqi Xu, hereby declare that the work presented in this manuscript is my own work, carried out under the scientific direction of Gilles Noguere, in accordance with the principles of honesty, integrity and responsibility inherent to the research mission. The research work and the writing of this manuscript have been carried out in compliance with both the french national charter for Research Integrity and the Aix-Marseille University charter on the fight against plagiarism.

This work has not been submitted previously either in this country or in another country in the same or in a similar version to any other examination body.

Aix-en-Provence, the 14th of Juin 2021

Aix*Marseille université

PROCES-VERBAL DE SOUTENANCE DE THÈSE DU 17/09/2021 A 14h00
ANNEE UNIVERSITAIRE 2020/2021

RAPPORT DE SOUTENANCE

Doctorant(e) : M. SHUQI XU
Né(e) le : 08/07/1992
Diplôme : Doctorat en Physique et Sciences de la Matière

Membres du Jury :

Nom	Qualité	Etablissement	Rôle	Présence par visioconférence (à cocher)	Président* (à cocher)
Mme MARIE-CLAIRE BELLISSENT- FUNEL	DIRECTEUR DE RECHERCHE	CEA/Saclay	Rapporteur	☐	☐
M. LUIZ LEAL	DIRECTEUR DE RECHERCHE	IRSN	Rapporteur	☐	☐
M. JOSE BUSTO	PROFESSEUR DES UNIVERSITES	UNIVERSITE D'AIX-MARSEILLE	Membre	☐	☒
Mme EMILY LIU	PROFESSEUR DES UNIVERSITES	Etats Unis	Membre	☐	☐
M. GILLES NOGUERE	CHARGE DE RECHERCHE	Commissariat à l'energie atomique	Directeur	☐	☐

* cf Arrêté ministériel du 25 mai 2016 (article 18) : "Les membres du jury désignent parmi eux un président et, le cas échéant, un rapporteur de soutenance. Le président doit être un professeur ou assimilé ou un enseignant de rang équivalent".
Arrêté ministériel du 25 mai 2016 (article 19) : "Le Président signe le rapport de soutenance qui est contresigné par l'ensemble des membres du jury présents à la soutenance".

Rapport de soutenance (p /)

Rapport de soutenance de thèse de M. Shuqi XU

M. Shuqi XU a présenté devant le jury réuni le 17 septembre 2021 au CEA Cadarache, l'ensemble des travaux de sa thèse dont le titre est : " Measurement of the double differential neutron cross section of UO_2 and determination of the thermal scattering law as a function of temperature".

La thèse présentée par M. XU a pour objectif la meilleure compréhension de la neutronique dans les réacteurs nucléaires. D'une manière plus précise, les travaux de M. XU concernent la validation des sections efficaces de diffusion cohérente des neutrons et les lois de diffusion thermique dans l'oxyde d'uranium et dans l'eau légère, en fonction de la température et pour une grande gamme d'énergie des neutrons dans la région de l'eV et en dessous. Pour cela un nouvel outil logiciel, appelé, CINEL, a dû être développé. Cet outil a pu être intégré au code

Aix*Marseille université

PROCES-VERBAL DE SOUTENANCE DE THÈSE DU 17/09/2021 A 14h00
ANNEE UNIVERSITAIRE 2020/2021

RAPPORT DE SOUTENANCE

Doctorant(e) : M. SHUQI XU
Né(e) le : 08/07/1992
Diplôme : Doctorat en Physique et Sciences de la Matière

Rapport de soutenance (p /)

Monte Carlo TRIPOLI-4® afin de comparer les résultats des simulations aux données d'une campagne de mesures effectuées à l'Institut Laue Langevin, utilisant deux différents diffractomètres, D20 et D4. Finalement la thèse se termine par une étude sur la diffusion des neutrons dans la région épithermique pour ^{1}H dans H_2O et ^{16}O dans et UO_2.

Le Jury souligne tout d'abord le travail très important et détaillé présenté par M. Xu qui couvre un vaste domaine allant, de l'étude des données expérimentales aux calculs théoriques dans différents matériaux. Ce travail était bien structuré et présenté de manière pédagogique.

Tout au long de la soutenance, M. Xu, a démontré une très bonne maitrise de son sujet. La réponse aux questions posées était claire et franche.

En conclusion, le jury unanime, a décerné à M. Shuqi XU le grade de Docteur de l'Université d'Aix-Marseille.

Signature du Président :

Signature de l'ensemble des membres du jury :

List of publications and participation in conferences

List of publications[1] produced as part of the thesis project:

1. S. Xu, G. Noguere, L. Desgranges, et al. “Atomic scale Monte-Carlo simulations of neutron diffraction experiments on stoichiometric uranium dioxide up to 1664 K”. in: *Nuclear Instruments and Methods in Physics Research Section A: Accelerators, Spectrometers, Detectors and Associated Equipment* 1002 (2021), p. 165251. ISSN: 0168-9002. DOI: https://doi.org/10.1016/j.nima.2021.165251. URL: https://www.sciencedirect.com/science/article/pii/S0168900221002357

2. G. Noguere, J. P. Scotta, S. Xu, E. Farhi, et al. “Temperature-dependent dynamic structure factors for liquid water inferred from inelastic neutron scattering measurements”. In: *The Journal of Chemical Physics* 155.2 (2021), p. 024502. DOI: 10.1063/5.0055779. eprint: https://doi.org/10.1063/5.0055779. URL: https://doi.org/10.1063/5.0055779

3. G. Noguere, J. P. Scotta, S. Xu, A. Filhol, et al. “Combining density functional theory and Monte Carlo neutron transport calculations to study the phonon density of states of UO_2 up to 1675 K by inelastic neutron scattering”. In: *Phys. Rev. B* 102 (13 Oct. 2020), p. 134312. DOI: 10.1103/PhysRevB.102.134312. URL: https://link.aps.org/doi/10.1103/PhysRevB.102.134312

4. Noguere, Gilles, Xu, Shuqi, Filhol, Alain, et al. “Measurement of the double-differential neutron cross section of UO2 from room temperature to hot full power conditions”. In: *EPJ Web Conf.* 239 (2020), p. 14003. DOI: 10.1051/epjconf/202023914003. URL: https://doi.org/10.1051/epjconf/202023914003

5. S. Xu, G. Noguere, A. Filhol, J. Ollivier, E. Farhi, and Y. Calzavara. “Measurement of the double-differential neutron cross section of UO2 from room temperature to hot full power conditions”. In: *Proceedings of the 11th International Conference on Nuclear Criticality Safety*.

[1] This list includes published articles, articles submitted for publication and articles in preparation as well as books, book chapters and / or all forms of valuation of the results of work specific to the discipline of the thesis project. Reference to publications must follow standard bibliography rules and must comply with AMU’s publications charter.

Participation in conferences[2] and summer schools during the thesis period:

Internal presentations

1. Presentation of poster in doctoral day in April 2019
2. Annual seminar of the laboratory in September 2019
3. Annual seminar of the laboratory in September 2020
4. Annual seminar of the laboratory in Juin 2021

External presentations

1. Participation at ND2019 conference in Beijing in May, as co-author of work presented by my director of thesis on uranium dioxide
2. Presentation at ICNC2019 conference in Paris in September 2019
3. Oral presentation at NAUSICAA Meeting in Grenoble in January 2020
4. Oral presentation at JEFF meetings via Zoom in April 2021
5. Oral presentation at WPEC Subgroup 48 meeting via Zoom in May 2021

International school

Reactor core physics: determinist and Monte Carlo methods. International school in nuclear engineering organized by *Institut National des Sciences et Techniques Nucléaires* (2019).

[2]The term “conference” is generic. It designates both “conference”, “congress”, “workshop”, “colloquia”, “national and / or international meetings”... etc. Indicate whether you made an oral or poster presentation.

Abstract

The Monte-Carlo neutron transport calculations in nuclear fuels depend on the crystalline structure and atom dynamics of materials. In the case of uranium dioxide (UO_2), when neutron energies lie below a few eV, coherent elastic neutron scattering cross section $\sigma_{\text{coh}}^{\text{el}}(E)$ accounts for the crystalline structure of UO_2 and thermal scattering laws (TSLs) or $S(\alpha, \beta)$ take into account the atom vibration behaviors of UO_2. Between a few eV to $400 k_B T$ where k_B is the Boltzmann constant and T represents the temperature of material, the TSLs are not available. Other neutron scattering treatments such as the Sampling the Velocities of the Target nucleus (SVT) algorithm are adopted in the Monte-Carlo calculations.

In the present work, the theoretical formalism enabling to calculate the TSLs for solid crystalline, liquid and gas materials has been studied. Based on these theoretical equations, the data processing tool `CINEL` has been developed. `CINEL` is able to generate the temperature-dependent TSLs in ENDF-6 format with graphic processing unit (GPU) speedup. The generated TSLs can be further processed to be used as neutron scattering library in the Monte-Carlo neutron transport code TRIPOLI-4®.

The performances of the Monte-Carlo calculations are illustrated with the analysis of neutron powder diffraction data on UO_2 measured up to 1664 K with the D4 and D20 diffractometers of the Institut Laue-Langevin (Grenoble, France). The comparison of the experimental and simulated pair distribution functions confirms the unusual decrease of the U-O atomic distances with increasing temperature when an ideal fluorite structure ($Fm\bar{3}m$ space group) with harmonic atomic vibrations is assumed over the full temperature range. The flexibility of the `CINEL` code allowed to explore disorder or anharmonic oxygen vibrations in the $Fm\bar{3}m$ space group, and to investigate other local crystalline symmetries for UO_2 at elevated temperatures.

Several neutron scattering treatments have also been studied, namely AK (Asymptotic Kernel), SVT (Sampling the Velocity of the Target nucleus) at thermodynamic temperature T and effective temperature T_{eff}, FGM (Free Gas Model), SCT (Short Collision Time approximation). Numerical validations of the studied neutron scattering treatments with the TRIPOLI-4® code were performed at room temperature for ^{1}H in ^1H_2O and ^{16}O in UO_2. The principle of the SVT algorithm has been validated with Molecular Dynamics simulations in the case of water molecule. The obtained results indicate that $S(\alpha, \beta)$ tables are correctly used by the TRIPOLI-4® code to simulate the transport of neutrons with energies lying between a few eV and $400 k_B T$. The importance of using the effective temperature and the improvement of the SCT treatment for the up-scattering calculations are confirmed.

Keywords: neutron scattering, uranium dioxide, Monte-Carlo simulation.

Résumé

Les calculs Monte-Carlo de transport des neutrons dans les combustibles nucléaires dépendent de la structure cristalline et de la dynamique atomique des matériaux. Dans le cas de dioxyde d'uranium (UO_2), lorsque les énergies des neutrons sont inférieures à quelques eV, la section efficace de diffusion élastique cohérente des neutrons $\sigma_{\text{coh}}^{\text{el}}(E)$ rend compte de la structure cristalline de UO_2 et les lois de diffusion thermique (TSLs) ou $S(\alpha, \beta)$ prennent en compte la vibration des atomes de UO_2. Entre quelques eV et $400 k_B T$ où k_B est la constante de Boltzmann et T représente la température du matériau, les TSLs ne sont pas disponibles. D'autres traitements de diffusion des neutrons tels que l'algorithme *Sampling the Velocities of the Target nucleus* (SVT) sont adoptés dans les calculs Monte-Carlo.

Dans ce travail, le formalisme théorique permettant de calculer les TSL pour les matériaux solides cristallins, liquides et gazeux a été étudié. Sur la base de ces équations théoriques, l'outil de traitement des données `CINEL` a été développé. `CINEL` est capable de générer les TSLs dépendant de la température au format ENDF-6 avec accélération par processeur graphique (GPU). Les TSLs générés peuvent être traités ultérieurement pour être utilisés comme bibliothèque de diffusion de neutrons dans le code Monte-Carlo TRIPOLI-4®.

Les performances des calculs Monte-Carlo sont illustrées par l'analyse des données de diffraction des neutrons sur UO_2 mesurées jusqu'à 1664 K avec les diffractomètres D4 et D20 de l'Institut Laue-Langevin (Grenoble, France). La comparaison des fonctions de distribution de paires expérimentales et simulées confirme la diminution inhabituelle des distances atomiques U-O avec l'augmentation de la température lorsqu'une structure de type "fluorite idéale" (groupe d'espace $Fm\bar{3}m$) avec des vibrations atomiques harmoniques est utilisée. La flexibilité du code `CINEL` a permis d'explorer le désordre ou les vibrations anharmoniques de l'oxygène dans le groupe d'espace $Fm\bar{3}m$, et d'étudier d'autres symétries cristallines locales pour UO_2 à des températures élevées.

Plusieurs traitements de diffusion des neutrons ont également été étudiés : AK (*Asymptotic Kernel*), SVT (*Sampling the Velocity of the Target nucleus*) à température thermodynamique T et température effective T_{eff}, FGM (*Free Gas Model*), SCT (*Short Collision Time approximation*). Les validations numériques des traitements de diffusion des neutrons étudiés avec le code TRIPOLI-4® ont été effectuées à température ambiante pour ^1H dans ^1H_2O et ^{16}O dans UO_2. Le principe de l'algorithme SVT a été validé avec des simulations de dynamique moléculaire dans le cas de la molécule d'eau. Les résultats obtenus indiquent que les tables $S(\alpha, \beta)$ sont correctement utilisées par le code TRIPOLI-4® pour simuler le transport des neutrons avec des énergies comprises entre quelques eV et $400 k_B T$. L'importance d'utiliser la température ef-

fective et l'amélioration du traitement SCT pour les calculs de l'*up-scattering* sont confirmées.

Mots clés: diffusion de neutron, dioxyde d'uranium, simulation Monte-Carlo.

Acknowledgements

Firstly, I would like to thank my tutor and director of thesis Dr. Gilles Noguere for his direction and suggestions during my three-year PhD. I appreciate his intelligence and vigorous attitude towards the scientific research, which is helpful in my following career. I sincerely thank him for his engagement for revising and correcting this report.

I would also like to thank Dr. Lionel Desgranges and Dr. Jose Ignacio Marquez Damian for their many suggestions given to my work.

I would also like to thank all my colleagues in SPRC for their technical supports and advices, especially Jean-Christophe Bosq, Philippe Dardé, Véronique Bellanger-Villard, Cyrille de Saint Jean, Olivier Bouland, David Bernard and so on. Special thanks to Pierre Tamagno for providing his GPUs for test. I am also grateful to Sandrine Poulain and Florence Aubert for their help and suggestions during the competition *Thèse & Vous 3 minutes*.

I would also like to thank all the colleagues at ILL for their kindly help for our experiments.

I would also like to thank all the fellows I met in Beijing during the ND2019. It was a memorable experience for me.

I would also like to thank all the Chinese community at Cadarache and all my friends in France, who accompany me to spend these three wonderful years.

Finally, I must express my very profound gratitude to my family: my parents and to my older sister Xiangmin, my younger sister Xiangrong and my younger brother Shuzhong for providing me with unfailing support and continuous encouragement throughout my years of study.

Contents

List of Figures

List of Tables

List of acronyms

AK

Asymptotic Kernel. 30, 32, 118, 121–124, 128, 138, 141

BCC

body-centered cubic. 71, 72

CM

center-of-mass. 121, 122, 124

CUDA

Compute Unified Device Architecture. 70

DBRC

Doppler Broadening Rejection Correction. 30, 120

DDXS

double differential cross section. 30, 34, 35, 56, 62, 64

DFT

density functional theory. 48, 71

FCC

face-centered cubic. 71, 72

FGM

Free Gas Model. 29, 30, 63, 94, 120, 133, 138, 141

GGA

generalized gradient approximation. 49

GPU

graphics processing unit. 67, 70

HB

hydrogen bond. 58, 60

HCP

hexagonal close packed. 71, 72

HWHM

half width at half maximum. 51, 60

ILL

Institut Laue–Langevin. 36, 50, 94, 95, 97, 116, 118

JIT

Just-in-Time. 70

LAB

laboratory. 118, 121, 123, 124

M-B

Maxwell-Boltzmann. 30, 61, 118, 123, 125–128, 141

MD

molecular dynamics. 50, 57, 65, 125

MSD

mean-squared displacement. 39, 41, 51, 52, 67, 68

PDOS

phonon density of states. 30, 36, 40, 48–50, 54, 57, 58, 65, 68, 71, 95, 138

RJD

random jump diffusion. 50, 60

SCT

short collision time. 34, 63–65, 67, 120, 133, 138, 140, 141

SVT

Sampling the Velocity of the Target nucleus. 30, 32, 118–125, 127, 128, 133, 138, 140, 141

TR

target-at-rest. 121–124

TSLs

thermal scattering laws. 30, 32, 34, 48, 56, 67, 68, 70, 71, 76, 98, 118, 127, 133, 138

VACF

velocity autocorrelation function. 52, 57, 127

VDOS

vibrational density of states. 54, 57, 58, 64

WCM

Weight Correction Method. 30, 120

1. Introduction

Summary

1.1. Context

Nuclear energy contributes over 10% of the global electricity production in 2019 (Schneider, Froggatt, Hazemann, et al. 2020), which helps to reduce tremendously the greenhouse gas emissions. The energy is released mainly thanks to the fission of heavy nuclides (e.g., uranium) induced by neutrons. Therefore, the behaviors of neutrons must be well understood and controlled in order to exploit the nuclear reactors safely and securely. To this end, neutronic calculation codes have been developed at French Alternative Energies and Atomic Energy Commission –or *Commissariat à l'Énergie Atomique et aux Énergies Alternatives*–(CEA), such as the Monte-Carlo neutron transport code TRIPOLI-4® (E. Brun, F. Damian, Diop, et al. 2015). The neutronic simulations performed by using the TRIPOLI-4® code rely on the knowledge of the neutron cross sections, which allow to quantify the neutron-nucleus interactions in the nuclear reactors.

For most nuclear power reactors, uranium has been used as fuels in the form of uranium dioxide (UO_2). In the Monte-Carlo neutron transport simulations, the total cross section is a key quantity for computing the distance traveled by the neutron between two interactions. The total neutron cross sections of uranium (U$\equiv^{238}$U) and oxygen (O$\equiv^{16}$O) in UO_2 as a function of the incident neutron energy E are the sum of the partial neutron cross sections:

$$\sigma_{t_{\mathrm{U}}}(E) = \sigma_{\gamma_{\mathrm{U}}}(E) + \sigma_{f_{\mathrm{U}}}(E) + \sigma_{n_{\mathrm{U}}}(E), \tag{1.1}$$

$$\sigma_{t_{\mathrm{O}}}(E) = \sigma_{\gamma_{\mathrm{O}}}(E) + \sigma_{n_{\mathrm{O}}}(E), \tag{1.2}$$

where the indexes γ, f and n are related to the radiative capture, fission and scattering reactions, respectively. In the neutronic simulations of nuclear power reactors, the neutron induced capture, fission and scattering reactions on uranium and oxygen are routinely calculated in the framework of the R-Matrix theory (Lane and Thomas 1958) and Doppler broadened at a given temperature T with a Free Gas Model (FGM), whose validity of the formalism is discussed in Ref. (Noguere, Maldonado, and De Saint Jean 2018).

In this work, special attentions are given to the scattering cross section $\sigma_n(E)$ as a function of temperature. Three distinct models are routinely implemented in the Monte-Carlo neutron transport code TRIPOLI-4®, to treat the neutron-nucleus elastic scattering according to the incident neutron energy E (Coveyou, Bate, and Osborn 1956; Zoia, Emeric Brun, Jouanne, et al. 2013). For E lower than a few eV, the neutron scattering cross section has to be divided in an elastic and inelastic parts, with coherent and incoherent terms. In the case of neutron induced scattering reactions on UO_2, the incoherent elastic cross section is negligible and the neutron scattering cross section reduces to:

$$\sigma_{n_j}(E) = \sigma^{\mathrm{el}}_{\mathrm{coh}}(E) + \sigma^{\mathrm{inel}}_{j}(E), \tag{1.3}$$

where j represents the uranium or oxygen atoms in UO_2. The first term in Eq. (1.3) is the coherent elastic scattering cross section which accounts for the crystalline

structure of UO_2. The second term is the inelastic scattering cross section which can be calculated by integrating its double differential form over the scattered energy E_f and solid angle Ω:

$$\sigma_j^{\text{inel}}(E) = \iint \frac{\mathrm{d}^2\sigma_j^{\text{inel}}(E)}{\mathrm{d}\Omega \mathrm{d}E_f} \mathrm{d}E_f \mathrm{d}\Omega, \tag{1.4}$$

where $\frac{\mathrm{d}^2\sigma_j^{\text{inel}}(E)}{\mathrm{d}\Omega \mathrm{d}E_f}$ is the inelastic double differential cross section (DDXS) of the atom j in UO_2, which can be obtained by the scattering function or dynamic structure factor $S_j(\vec{Q}, \omega)$. $S_j(\vec{Q}, \omega)$, as a function of the momentum transfer $\hbar\vec{Q}$ and energy transfer $\hbar\omega$, account for atomic vibration behaviors of the atom j (Squires 2012; Schober 2014). The dimensionless scattering function or dynamic structure factor $S(\alpha, \beta)$ is adopted in the neutron scattering data library used by the TRIPOLI-4® code, in the place of $S(\vec{Q}, \omega)$. $S(\alpha, \beta)$ is called thermal scattering laws (TSLs) with α and β representing the dimensionless momentum and energy transfers, respectively. The temperature-dependent $\sigma_{\text{coh}}^{\text{el}}(E)$ and $S_j(\alpha, \beta)$ of UO_2 can be calculated from the phonon density of states (PDOS) which characterize the atomic movements and structural dynamics of UO_2. The computed $\sigma_{\text{coh}}^{\text{el}}(E)$ and $S_j(\alpha, \beta)$ are stored in ascii files by following the ENDF-6 format requirements for TSLs (Trkov and D. A. Brown 2018), to prepare the neutron scattering data libraries used by TRIPOLI-4®.

For E between a few eV and $400k_BT$ (epithermal energy range), where k_B is the Boltzmann constant and T represents the temperature of material, the Sampling the Velocity of the Target nucleus (SVT) algorithm is used in the Monte-Carlo simulations, which samples the velocities of the target nuclides from a Maxwell-Boltzmann (M-B) distribution (Coveyou, Bate, and Osborn 1956; Lux 2018). Nevertheless, the SVT treatment for heavy nuclides with strong scattering resonances (e.g., ^{238}U) is reported to be inadequate (Dagan and Broeders 2006; Becker, R. Dagan, and Lohnert 2009). Stochastic correction methods such as Doppler Broadening Rejection Correction (DBRC) (Rothenstein and R. Dagan 1995) and Weight Correction Method (WCM) (Lee, Smith, and Rhodes 2009) have been adopted in the TRIPOLI-4® code to improve the SVT algorithm.

For E above $400k_BT$, the Asymptotic Kernel (AK) approximation is used in the TRIPOLI-4® code. The AK treatment considers the target nuclides at rest, when the velocities of the nuclides are negligible compared to the incident neutron velocities.

1.2. Motivations

The components of the neutron scattering cross section (Eq. (1.3)) are shown in Fig. 1.1 as a function of E for T = 300 K. The principles of the calculations implemented in the `CINEL` code (cf. Chapter 3) are presented in Chapter 2. The comparison with the neutron elastic scattering cross sections calculated with a FGM approximation (black curve) highlights the large differences between the formalism (red curve), which may introduce biases in neutronic calculations. For example, the use of the FGM

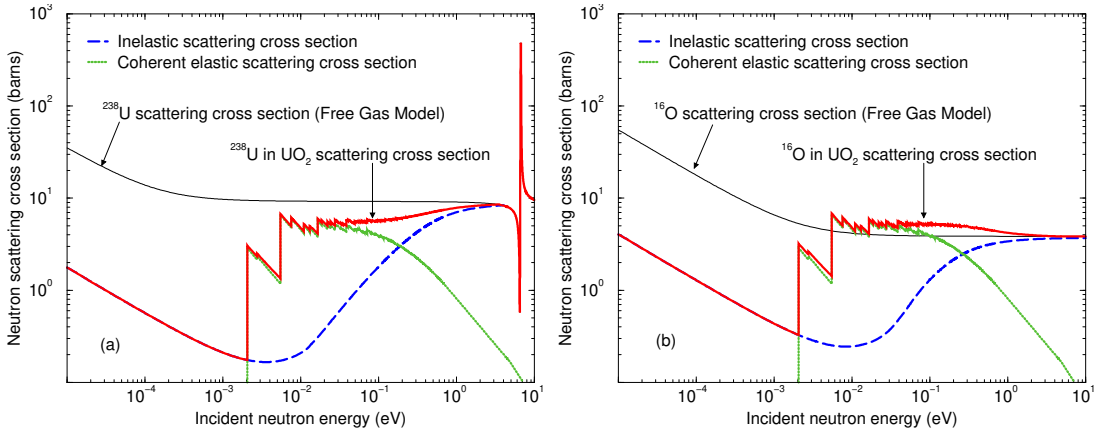

Figure 1.1.: Neutron scattering cross sections of ^{238}U in UO_2 (a) and ^{16}O in UO_2 (b) as a function of the incident neutron energy at $T = 300$ K. The coherent elastic and inelastic scattering cross sections were calculated with the CINEL code by using equations presented in Sections 2.2.3 and 2.2.5. The neutron cross sections calculated with the Free Gas Model are plotted for comparison. The structure observed at 6.6 eV corresponds to the first s-wave ^{238}U resonance.

approximation, instead of $S(\alpha,\beta)$ below a few eV, can imply a bias of about 100 pcm (0.1%) on the neutron multiplication factor k_{eff} calculated for integral benchmarks with UOX fuel. Such a bias cannot be seen as a negligible source of uncertainties, given that the total uncertainty on the calculated k_{eff} should be lower than 500 pcm (0.5%). Therefore, validating the crystalline effects at the microscopic level is still a necessity to motivate an update of the neutron scattering treatment in neutronic simulation schemes.

The atom binding effects can be taken into account by the effective temperature T_{eff} (Lamb 1939). In the epithermal energy range where the thermal scattering laws are not available, the important role of T_{eff} needs to be investigated.

1.3. Objectives

The first key point in the present study is to prepare and validate the coherent elastic neutron scattering cross sections and thermal scattering laws of UO_2 as a function of temperature in ENDF-6 format which can be used in the Monte-Carlo neutron transport code TRIPOLI-4®.

The second issue is to investigate the neutron scattering treatments involving the effective temperature in the epithermal energy range by using the TRIPOLI-4® code.

1.4. Report description

Chapter 2 is dedicated to present the theory of low energy neutron scattering. The general formalisms of the double differential neutron scattering cross section are given. The equations allowing to calculate the TSLs for solid crystalline, liquid and free gas materials are presented.

In Chapter 3, the development of the data processing tool CINEL is shortly presented. CINEL has been developed in this work to prepare the TSLs of materials in ENDF-6 format. The numerical validations of CINEL performed by using various types of crystal materials are also presented.

In Chapter 4, the Monte-Carlo neutron transport code TRIPOLI-4® is used to simulate neutron powder diffraction data on stoichiometric uranium dioxide (UO_2) measured up to 1664 K with the D4 and D20 diffractometers of the Institut Laue-Langevin. The TSLs of UO_2 required for the simulation are calculated by using the CINEL code. The performances of the Monte-Carlo calculations with the tabulated TSLs are illustrated with the comparison between the experimental and simulated diffraction patterns and atomic pair distribution functions.

Chapter 5 is devoted to investigate the neutron scattering with light nuclides having a non-resonant neutron scattering cross section below 10 eV. The formalisms of AK and SVT are reviewed and validated. Numerical validations of several neutron scattering treatments with the TRIPOLI-4® code are performed at room temperature for ^{1}H in $^{1}H_2O$ and ^{16}O in UO_2. A special attention will be given to the important role of the effective temperature T_{eff}.

Finally, general conclusions and perspectives are given at the end of the document. Two approaches provide additional information on H_2O for temperatures varying from 284 K and 494 K, and UO_2 between 300 K and 1675 K.

2. Low energy neutron scattering theory

Summary

The low energy neutron scattering theory is well detailed in the literature (Schober 2014; Squires 2012; Cai and T. Kittelmann 2020). The formalism of the neutron scattering presented in this work is mainly based on these references. The general equations of the double differential neutron scattering cross section are presented in Section 2.1. The equations allowing to calculate the TSLs for solid crystalline, liquid and free gas materials are presented in Sections 2.2, 2.3 and 2.4. The short collision time (SCT) approximation is presented in Section 2.5. Preliminary conclusions are given in the last section.

2.1. General formalisms

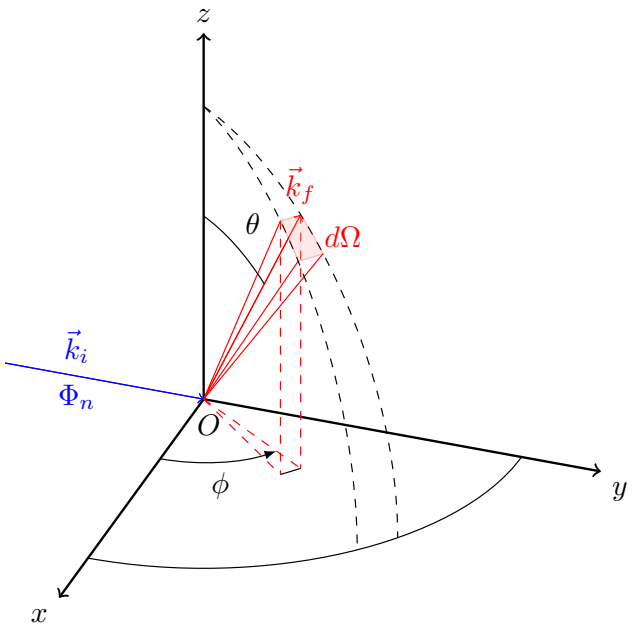

Figure 2.1.: Schematic representation of low energy neutron-nucleus scattering. The incident neutrons characterized by wave vector $\vec{k}_i$ and flux Φ_n arrive at points O and scatter with the target particles. After interaction, the outgoing neutrons travel into the direction of $\vec{k}_f$ with solid angle $\mathrm{d}\Omega = \sin(\theta)\mathrm{d}\theta\mathrm{d}\phi$.

In the low energy neutron range (usually less than a few eV), the scattering of neutron in materials can be described via the DDXS:

$$\frac{\mathrm{d}^2\sigma_{\vec{k}_i \Rightarrow \vec{k}_f}}{\mathrm{d}\Omega \mathrm{d}E_f} \equiv \frac{n(\mathrm{d}\Omega, \mathrm{d}E_f)}{\Phi_n \mathrm{d}\Omega \mathrm{d}E_f}, \tag{2.1}$$

where $\vec{k}_i$ and $\vec{k}_f$ are respectively the wave vectors of incident and scattered neutrons, $n(\mathrm{d}\Omega, \mathrm{d}E_f)$ represents the number of neutrons scattered per second into solid angle

$\mathrm{d}\Omega$ with final energy between E_f and $E_f + \mathrm{d}E_f$, and Φ_n represents the incident neutron flux. A schematic representation of the neutron-nucleus scattering is presented in Fig. 2.1.

For unpolarised neutrons and samples, based on Born approximation or Fermi's Golden rule, the DDXS can be obtained by (Schober 2014):

$$\frac{\mathrm{d}^2\sigma_{\vec{k}_i \Rightarrow \vec{k}_f}}{\mathrm{d}\Omega \mathrm{d}E_f} = \frac{k_f}{k_i} S(\vec{Q}, \omega), \tag{2.2}$$

where k_i and k_f represent the wavenumbers with $k = |\vec{k}|$, $\hbar\vec{Q}$ is the momentum transfer of neutron defined by $\hbar\vec{Q} \equiv \hbar(\vec{k}_i - \vec{k}_f)$ in which $\hbar$ is the Planck constant divided by 2π, $\hbar\omega$ is the energy transfer with $\hbar\omega \equiv E_i - E_f$ [1], and $S(\vec{Q}, \omega)$ is the scattering function or dynamic structure factor defined by:

$$S(\vec{Q}, \omega) \equiv \frac{1}{2\pi\hbar} \sum_{j, j'=1}^{N} \overline{b_{j'} b_j} \int_{-\infty}^{\infty} \langle j', j \rangle \exp(-i\omega t) \mathrm{d}t. \tag{2.3}$$

In Eq. (2.3), N is the number of particles in the scattering system under consideration, b_j represents the scattering length of the particle j, $\overline{b_j}$ is the average value, $\langle \boldsymbol{A} \rangle$ represents the operator expectation value in the scattering system, and $\langle j', j \rangle$ (notation taken from Ref. (Cai and T. Kittelmann 2020), which is referred as intermediate function in Ref. (Squires 2012)), represents the correlation between the position of the particle j at time t and the position of the particle j' at time 0:

$$\langle j', j \rangle \equiv \langle \exp\left(-i\vec{Q} \cdot \vec{\boldsymbol{R}}_{j'}(0)\right) \exp\left(i\vec{Q} \cdot \vec{\boldsymbol{R}}_j(t)\right) \rangle, \tag{2.4}$$

where $\vec{\boldsymbol{R}}(t)$ is the time-dependent Heisenberg operator.

It is assumed that there is no correlation between the scattering lengths and the positions of the particles in the scattering system (Schober 2014), then

$$\overline{b_{j'} b_j} = \begin{cases} \overline{b_{j'}} \cdot \overline{b_j} & j \neq j' \\ \overline{b_j^2} & j = j' \end{cases}. \tag{2.5}$$

Eq. (2.5) enables to decompose the scattering function in Eq. (2.3) into two distinct parts:

$$S(\vec{Q}, \omega) = S_{\mathrm{coh}}(\vec{Q}, \omega) + S_{\mathrm{inc}}(\vec{Q}, \omega), \tag{2.6}$$

where

$$S_{\mathrm{coh}}(\vec{Q}, \omega) \equiv \frac{1}{2\pi\hbar} \sum_{j, j'=1}^{N} \overline{b_{j'}} \cdot \overline{b_j} \int_{-\infty}^{\infty} \langle j', j \rangle \exp(-i\omega t) \mathrm{d}t, \tag{2.7}$$

[1] E_i represents the incident neutron energy, the subscript i is omitted in this work for the sake of clarity.

and

$$S_{\text{inc}}(\vec{Q},\omega) \equiv \frac{1}{2\pi\hbar}\sum_{j=1}^{N}\left(\overline{b_j^2}-(\overline{b_j})^2\right)\int_{-\infty}^{\infty}\langle j,\, j\rangle \exp(-i\omega t)\mathrm{d}t. \tag{2.8}$$

$S_{\text{coh}}(\vec{Q},\omega)$ is the coherent scattering function, representing the correlation between the positions of the same particle at different time (when $j = j'$) and the correlation between the positions of different particles at different time (when $j \neq j'$). Therefore, $S_{\text{coh}}(\vec{Q},\omega)$ gives interference effects (Squires 2012). $S_{\text{inc}}(\vec{Q},\omega)$ is the incoherent scattering function, which represents the correlation between the positions of the same particle at different time. The incoherent scattering does not give interference effects (there is no terms $\langle j',\, j\rangle$ for $j \neq j'$ in Eq. (2.8)).

Based on Eq. (2.3), the value of the scattering function $S(\vec{Q},\omega)$ increases with the number of particles in the scattering system. In practice, the normalization is performed with respect to the number of particles given by the chemical formula or the unit cell (Schober 2014). In addition, the principle of detailed balance must be fulfilled for the scattering function $S(\vec{Q},\omega)$ (Schober 2014):

$$S(\vec{Q},-\omega) = \exp\left(-\frac{\hbar\omega}{k_B T}\right)S(\vec{Q},\omega). \tag{2.9}$$

2.2. Scattering models for solid crystalline materials

In this section, the general equation of the scattering function $S(\vec{Q},\omega)$ is presented in the case of solid crystalline materials. Some basic crystallographic physical quantities are briefly presented in Section 2.2.1. Three approximations enabling to obtain the scattering functions are given in Section 2.2.2. Thanks to these approximations, the scattering functions for solid crystalline materials can be further decomposed into coherent elastic, incoherent elastic and inelastic parts, which are presented respectively in Sections 2.2.3, 2.2.4 and 2.2.5. In the last section, some PDOS of uranium dioxide (UO_2) calculated by first-principles are presented for illustration. The model presented in this section was applied to study the UO_2 data measured at the Institut Laue–Langevin (ILL) facilities (see appendix).

2.2.1. Basic crystallographic quantities

A crystal can be built up by periodically repeating a basic element along three dimensions in space. This basic element is referred as unit cell. For a given crystal, it is always possible to select a parallelepiped as its unit cell (Cai and T. Kittelmann 2020). Denote the basic vectors of the parallelepiped as $\vec{a}$, $\vec{b}$ and $\vec{c}$. Conventionally these vectors are defined by their lengths a, b and c, and the angles between them :

$$\alpha \equiv \widehat{(\vec{b},\vec{c})}, \quad \beta \equiv \widehat{(\vec{c},\vec{a})}, \quad \gamma \equiv \widehat{(\vec{a},\vec{b})}. \tag{2.10}$$

The number of atoms within the unit cell is denoted as $N_{\text{unit cell}}$. The position of the atom j with $1 \leq j \leq N_{\text{unit cell}}$ is defined by:

$$\vec{p}_j = x_j \vec{a} + y_j \vec{b} + z_j \vec{c}, \quad x_j, y_j, z_j \in [0,1]. \tag{2.11}$$

The set of positions of atoms in the unit cell is denoted as $\{\vec{p}_j\}$. A given crystal can thus be characterized by the above quantities : a, b, c, α, β, γ and $\{\vec{p}_j\}$.

For illustrating the above physical quantities, the unit cell of stoichiometric uranium dioxide (UO_2) in ideal fluorite structure with $Fm\bar{3}m$ symmetry (space group 225) is presented in Fig. 2.2a. Twelve atoms (four uranium atoms and eight oxygen atoms) are included in the cubic unit cell of UO_2, whose positions are listed in Table 2.1.

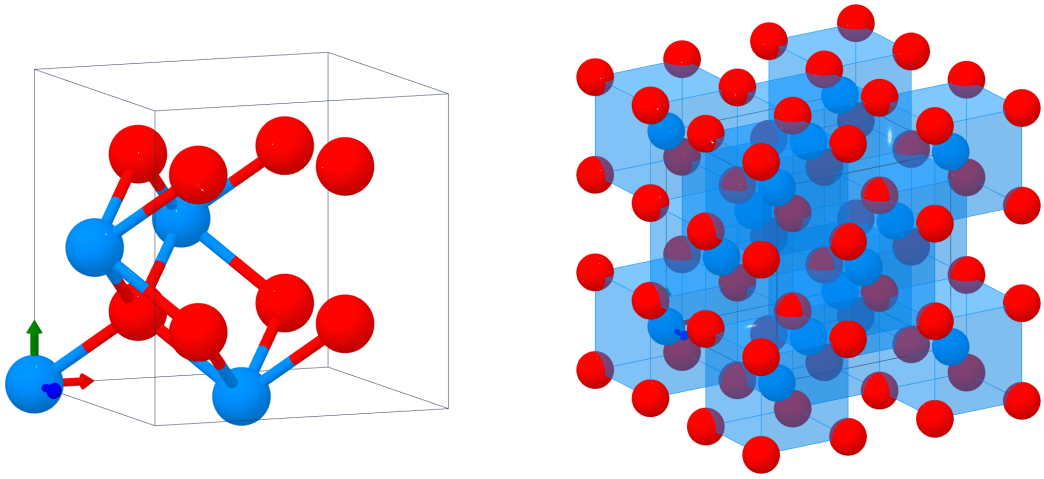

(a) UO_2 unit cell (b) UO_2 direct lattice

Figure 2.2.: Left hand plot presents the cubic unit cell of UO_2: $a = b = c$ and $\alpha = \beta = \gamma = 90°$. Blue and red spheres represent respectively uranium and oxygen atoms. The coordinations of U and O are presented: each U is surrounded by eight O atoms whereas each O is surrounded by four U atoms. UO_2 is in ideal fluorite structure with uranium atoms located in the vertices of twelve edges and in the center of six faces of the unit cell, and oxygen atoms located in the eight tetrahedral holes between the uranium atoms. Right hand plot shows the direct lattice of UO_2, which is further explained in the text. The drawings of these two figures are with the aid of the Crystal Toolkit in the Materials Project (Ong, Richards, Jain, et al. 2013).

As mentioned before, a crystal can be built up by repeating its unit cell along three dimensions, therefore it can be defined as a set of points at positions $\vec{p}_j + \vec{R}_{mno}$ with

$$\vec{R}_{mno} = m\vec{a} + n\vec{b} + o\vec{c}, \quad m, n, o \in \mathbb{Z}, \tag{2.12}$$

Table 2.1.: Positions of uranium and oxygen atoms in the unit cell of UO_2 with $Fm\bar{3}m$ symmetry (Ong, Richards, Jain, et al. n.d.).

Atom	j	$\vec{p}_j$		
		x	y	z
U	1	0	0	0
U	2	0	1/2	1/2
U	3	1/2	0	1/2
U	4	1/2	1/2	0
O	5	1/4	3/4	3/4
O	6	1/4	1/4	3/4
O	7	1/4	1/4	1/4
O	8	1/4	3/4	1/4
O	9	3/4	3/4	1/4
O	10	3/4	1/4	1/4
O	11	3/4	1/4	3/4
O	12	3/4	3/4	3/4

for $1 \leq j \leq N_{\text{unit cell}}$ and all integers m, n and o.

This set of points is referred as direct lattice. Plans passing through discrete points in the direct lattice are characterized by a unit vector $\vec{n}$ which is perpendicular to the plans, and the distance between two successive plans. This distance is called inter-planar spacing d in the literature. Fig. 2.2b shows the direct lattice of UO_2 with $Fm\bar{3}m$ symmetry for illustration. The horizontal plans passing through points occupied by oxygen atoms (red spheres) have inter-planar spacing which is equal to the O-O distance.

The classification of the plans passing through points in the direct lattice is crucial in the analysis of particle diffraction with crystal. To this end, the reciprocal lattice is introduced, which is the Fourier transform of the direct lattice. The basic vectors of the reciprocal lattice is given by:

$$\vec{\tau}_a = \frac{2\pi}{V_{\text{unit cell}}}(\vec{b} \times \vec{c}), \quad \vec{\tau}_b = \frac{2\pi}{V_{\text{unit cell}}}(\vec{c} \times \vec{a}), \quad \vec{\tau}_c = \frac{2\pi}{V_{\text{unit cell}}}(\vec{a} \times \vec{b}), \tag{2.13}$$

where $V_{\text{unit cell}} = \vec{a} \cdot (\vec{b} \times \vec{c})$ is the unit cell volume.

Points in the reciprocal lattice are discrete. For the point (h, k, l), we have:

$$\vec{\tau}_{hkl} = h\vec{\tau}_a + k\vec{\tau}_b + l\vec{\tau}_c, \tag{2.14}$$

and

$$\tau_{hkl} = \|\vec{\tau}_{hkl}\|. \tag{2.15}$$

It can be shown that $\vec{\tau}_{hkl}$ corresponds to the plan hkl in the direct lattice. The

interplanar spacing d_{hkl} of plan hkl satisfies

$$d_{hkl} = \frac{2\pi}{\tau_{hkl}}. \tag{2.16}$$

To illustrate the signification of the reciprocal lattice, the basic vectors presented in Eq.(2.13) for UO_2 are given by:

$$\vec{\tau}_a = \frac{2\pi}{a}\vec{e}_x, \quad \vec{\tau}_b = \frac{2\pi}{a}\vec{e}_y, \quad \vec{\tau}_c = \frac{2\pi}{a}\vec{e}_z, \tag{2.17}$$

where $\vec{e}_x$, $\vec{e}_y$ and $\vec{e}_z$ are orthonormal vectors along x, y and z direction, respectively.

2.2.2. Harmonic, incoherent and cubic approximations

For solid crystalline materials, the operator representing the position of atom $\vec{\boldsymbol{R}}(t)$ in the intermediate function (Eq. (2.4)) can be represented as the displacement of the atom $\vec{\boldsymbol{u}}(t)$ from its equilibrium position $\vec{d}$ at time t:

$$\vec{\boldsymbol{R}}(t) = \vec{d} + \vec{\boldsymbol{u}}(t). \tag{2.18}$$

In addition, the equilibrium position $\vec{d}$ is a simple vector, which commutes with all the operators. Hence, the intermediate function can be obtained by:

$$\langle j', j\rangle = \exp\Big(-i\vec{Q}\cdot(\vec{d}_{j'} - \vec{d}_j)\Big)\langle \exp\big(-i\vec{Q}\cdot\vec{\boldsymbol{u}}_{j'}(0)\big)\exp\big(i\vec{Q}\cdot\vec{\boldsymbol{u}}_j(t)\big)\rangle. \tag{2.19}$$

For practical purposes, it is desired to permute the exponential and the operator expectation in $\langle \exp\big(-i\vec{Q}\cdot\vec{\boldsymbol{u}}_{j'}(0)\big)\exp\big(i\vec{Q}\cdot\vec{\boldsymbol{u}}_j(t)\big)\rangle$ in Eq. (2.19). To this end, the harmonic approximation is supposed, in which atoms are assumed to have harmonic vibrations, i.e., the interatomic forces are linear with respect to the displacements of atoms and all the higher terms related to the anharmonic vibrations are neglected. The intermediate function $\langle j', j\rangle$ in Eq. (2.19) becomes:

$$\langle j', j\rangle = \exp\Big(-i\vec{Q}\cdot(\vec{d}_{j'} - \vec{d}_j)\Big)\exp\big(-W_{j'}(\vec{Q})\big)\exp\big(-W_j(\vec{Q})\big)\exp\big(\langle(\vec{Q}\cdot\vec{\boldsymbol{u}}_{j'}(0))(\vec{Q}\cdot\vec{\boldsymbol{u}}_j(t))\rangle\big), \tag{2.20}$$

where $W_j(\vec{Q})$ is the Debye-Waller function, which measures the mean-squared displacement (MSD) of the atom j along the direction $\vec{Q}$:

$$W_j(\vec{Q}) = \frac{1}{2}\langle(\vec{Q}\cdot\vec{\mathbf{u}}_j(0))^2\rangle. \tag{2.21}$$

Note that corrections related to the anharmonic effects can be lately introduced to the intermediate function in Eq. (2.20), in the case of small atomic displacements compared to interatomic distances.

In Eq. (2.20), $\langle(\vec{Q}\cdot\vec{\boldsymbol{u}}_{j'}(0))(\vec{Q}\cdot\vec{\boldsymbol{u}}_j(t))\rangle$ represents the correlation of linear displacement along $\vec{Q}$ of two atoms at different time. It is theoretically difficult to predict this

correlation for distinct atoms $j \neq j'$. Thus, in this work, a widely used approximation is utilized, called incoherent approximation, in which the correlation is neglected for inelastic scattering, i.e.,

$$\langle(\vec{Q}\cdot\vec{\boldsymbol{u}}_{j'}(0))(\vec{Q}\cdot\vec{\boldsymbol{u}}_j(t))\rangle = 0 \quad \text{if } j \neq j'. \tag{2.22}$$

For $j = j'$, the last term in Eq. (2.20) does not vanish. Its computation is quite difficult ($\langle(\vec{Q}\cdot\vec{\boldsymbol{u}}_j(0))(\vec{Q}\cdot\vec{\boldsymbol{u}}_j(t))\rangle$). To circumvent this difficulty, the cubic approximation is used in this work. It assumes that for atoms of a solid crystalline material under consideration, the interatomic forces along all directions are isotropic. Under the cubic approximation, we have:

$$\langle(\vec{Q}\cdot\vec{\boldsymbol{u}}_j(0))(\vec{Q}\cdot\vec{\boldsymbol{u}}_j(t))\rangle = \frac{\hbar Q^2}{2M_j}\int_0^\infty \frac{\rho_j(\omega)}{\omega}\left(\coth\left(\frac{\hbar\omega}{2k_BT}\right)\cos(\omega t) + i\sin(\omega t)\right)\mathrm{d}\omega, \tag{2.23}$$

where M_j is the mass of the atom j, k_B is the Boltzmann constant, T is the temperature of the material under consideration, $\rho_j(\omega)$ represents the PDOS of the atom j satisfying

$$\int_0^\infty \rho_j(\omega)\mathrm{d}\omega = 1. \tag{2.24}$$

The cubic approximation has the considerable merit that it enables to connect the PDOS of atoms to their dynamics. By utilizing the symmetry of the PDOS versus ω, i.e., $\rho_j(-\omega) = \rho_j(\omega)$, Eq. (2.23) can be rewritten as:

$$\langle(\vec{Q}\cdot\vec{\boldsymbol{u}}_j(0))(\vec{Q}\cdot\vec{\boldsymbol{u}}_j(t))\rangle = \frac{\hbar^2 Q^2}{2M_j k_B T}\int_{-\infty}^{\infty} P_j(\omega)\exp(i\omega t)\mathrm{d}\omega, \tag{2.25}$$

where

$$P_j(\omega) = \frac{\rho_j(\omega)}{\frac{2\hbar\omega}{k_BT}\sinh\left(\frac{\hbar\omega}{2k_BT}\right)}\exp\left(\frac{\hbar\omega}{2k_BT}\right). \tag{2.26}$$

An important condition emerges from Eqs. (2.25) and (2.26): $\rho_j(\omega)$ must vary as ω^2 as ω goes to zero, to ensure the convergence of the temperature-dependent function $P_j(\omega)$. The integral of $P_j(\omega)$ provokes the Debye-Waller coefficient $\Lambda_j(T)$ (Macfarlane, Muir, Boicourt, et al. 2017):

$$\Lambda_j(T) = \int_{-\infty}^{\infty} P_j(\omega)\mathrm{d}\omega. \tag{2.27}$$

Based on Eqs. (2.21) and (2.25), the Debye-Waller function $W_j(\vec{Q})$ represents the dynamics of the atom j at $t = 0$. In addition to Eq. (2.27), $W_j(\vec{Q})$ can be expressed by the corresponding Debye-Waller coefficient $\Lambda_j(T)$ as:

$$W_j(\vec{Q}) = \frac{\hbar^2 Q^2}{4M_j k_B T}\Lambda_j(T). \tag{2.28}$$

Another widely used physical quantities representing the atomic dynamics are the MSD and the B-factor. The MSD and the B-factor B_j of the atom j are respectively given by:

$$\mathrm{MSD}_j = \frac{\hbar^2}{2M_j k_B T}\Lambda_j(T), \tag{2.29}$$

and

$$B_j = 8\pi^2 \mathrm{MSD}_j = \frac{4\pi^2\hbar^2}{M_j k_B T}\Lambda_j(T). \tag{2.30}$$

Thus, under the cubic approximation, the Debye-Waller function $W_j(\vec{Q})$ can be determined by:

$$W_j(\vec{Q}) = \frac{\hbar^2 Q^2}{4M_j k_B T}\Lambda_j(T) = \frac{Q^2}{2}\mathrm{MSD}_j = \frac{Q^2}{16\pi^2}B_j. \tag{2.31}$$

Based on the incoherent and cubic approximations, the dynamic term $\langle(\vec{Q}\cdot\vec{\boldsymbol{u}}_j(0))(\vec{Q}\cdot\vec{\boldsymbol{u}}_j(t))\rangle$ and the Debye-Waller function $W_j(\vec{Q})$ in the intermediate function (Eq. (2.20)) can be obtained with Eqs. (2.25) and (2.31), respectively. The following step consists of expanding $\exp\big(\langle(\vec{Q}\cdot\vec{\boldsymbol{u}}_j(0))(\vec{Q}\cdot\vec{\boldsymbol{u}}_j(t))\rangle\big)$ in Eq. (2.20) in a Taylor series:

$$\exp\big(\langle(\vec{Q}\cdot\vec{\boldsymbol{u}}_j(0))(\vec{Q}\cdot\vec{\boldsymbol{u}}_j(t))\rangle\big) = \sum_{n=0}^{\infty}\frac{1}{n!}\big(\langle(\vec{Q}\cdot\vec{\boldsymbol{u}}_j(0))(\vec{Q}\cdot\vec{\boldsymbol{u}}_j(t))\rangle\big)^n. \tag{2.32}$$

Eq. (2.32) is referred to phonon expansion, originally introduced by Sjölander (Sjolander 1958). The first term $n = 0$ corresponds to elastic scattering (no energy exchange between the incident neutron and the system under consideration). The terms $n \geq 1$ represent inelastic scattering contributions.

The cross sections of the coherent elastic scattering, incoherent elastic scattering and inelastic scattering are presented in the following sections.

2.2.3. Coherent elastic scattering

This part presents the coherent elastic scattering function $S^{\mathrm{el}}_{\mathrm{coh}}(\vec{Q},\omega)$, which corresponds to the zero phonon term in Eq. (2.32). Given that the Fourier transform of a constant function is a Dirac delta function:

$$\int_{-\infty}^{\infty}\exp(-i\omega t)\mathrm{d}t = 2\pi\delta(\omega), \tag{2.33}$$

and thanks to Eqs. (2.7), (2.20) and (2.32), the coherent elastic scattering function $S^{\mathrm{el}}_{\mathrm{coh}}(\vec{Q},\omega)$ is given by:

$$S^{\mathrm{el}}_{\mathrm{coh}}(\vec{Q},\omega) = \frac{\delta(\omega)}{\hbar}\sum_{j,j'=1}^{N_{\mathrm{unit\,cell}}}\overline{b_j}\cdot\overline{b_{j'}}\exp\Big(-i\vec{Q}\cdot(\vec{d}_{j'}-\vec{d}_j)\Big)\exp\big(-W_{j'}(\vec{Q})\big)\exp\big(-W_j(\vec{Q})\big). \tag{2.34}$$

Considering a crystal with the notations presented in Section 2.2.1, $S^{\text{el}}_{\text{coh}}(\vec{Q},\omega)$ can be rewritten as:

$$S^{\text{el}}_{\text{coh}}(\vec{Q},\omega) = \frac{(2\pi)^3\delta(\omega)}{\hbar V_{\text{unit cell}}} \sum_{hkl} \delta(\vec{Q}-\vec{\tau}_{hkl}) \left|F(\vec{\tau}_{hkl})\right|^2, \tag{2.35}$$

where $V_{\text{unit cell}}$ is the unit cell volume, $\vec{\tau}_{hkl}$ corresponds to the plan hkl in the direct lattice, which can be obtained by Eqs. (2.13) and (2.14), respectively. $F(\vec{\tau}_{hkl})$ is the form factor of the unit cell, given by:

$$F(\vec{\tau}_{hkl}) = \sum_{j=1}^{N_{\text{unit cell}}} \overline{b_j} \exp\left(-W_j(\vec{\tau}_{hkl})\right) \exp\left(i\vec{\tau}_{hkl}\cdot\vec{p}_j\right), \tag{2.36}$$

where $\vec{p}_j$ represents the positions of atoms in the unit cell.

In this work, crystal powders in which the grains are uniformly and randomly oriented are considered. For a given lattice plan indexed hkl, $\vec{\tau}_{hkl}$ is hence isotropic to the momentum transfer $\vec{Q}$. Then

$$\delta(\vec{Q}-\vec{\tau}_{hkl}) = \frac{1}{4\pi}\int d\Omega\delta(\vec{Q}-\vec{\tau}_{hkl}). \tag{2.37}$$

Thanks to the property of the Dirac function $\int d\Omega\delta(\vec{r}-\vec{a}) = 2a^{-1}\delta(r^2-a^2)$ and Eq. (2.16), Eq. (2.37) can be rewritten as:

$$\delta(\vec{Q}-\vec{\tau}_{hkl}) = \frac{d_{hkl}}{(2\pi)^2}\delta(Q^2-\tau^2_{hkl}). \tag{2.38}$$

Based on Eqs. (2.35) and (2.38), the coherent elastic scattering function $S^{\text{el}}_{\text{coh}}(\vec{Q},\omega)$ is isotropic along the azimuthal direction ϕ for crystal powders with randomly oriented grains. Then $S^{\text{el}}_{\text{coh}}(\vec{Q},\omega) = S^{\text{el}}_{\text{coh}}(Q,\omega)$ and

$$S^{\text{el}}_{\text{coh}}(Q,\omega) = \frac{2\pi\delta(\omega)}{\hbar V_{\text{unit cell}}} \sum_{hkl} \delta(Q^2-\tau^2_{hkl}) d_{hkl} \left|F(\vec{\tau}_{hkl})\right|^2. \tag{2.39}$$

For elastic neutron scattering, the wavenumber and the energy of neutron remain the same. Then we have: $k = k_i = k_f$ and $E = E_f$. If θ is the angle between the incident wave vector $\vec{k}_i$ and the scattered wave vector $\vec{k}_f$, we have:

$$Q = 2k\sin\left(\frac{\theta}{2}\right). \tag{2.40}$$

Eq. (2.39) shows that the coherent elastic neutron scattering by a given lattice plan indexed by hkl can only happen ($S^{\text{el}}_{\text{coh}}(Q,\omega) > 0$) when the momentum transfer Q satisfies $Q = \tau_{hkl}$. Therefore, the happening of the coherent elastic scattering in the plan hkl for a given neutron with wavenumber k necessitates that the maximum

momentum transfer $Q_{\max}$ is larger than τ_{hkl}, i.e.,

$$Q_{\max} \geq \tau_{hkl}. \tag{2.41}$$

Based on Eq. (2.40), $Q_{\max} = 2k$ when the neutron moves in the opposite direction after scattering ($\theta = \pi$). Hence, Eq. (2.41) can be rewritten as:

$$2k \geq \tau_{hkl}. \tag{2.42}$$

The coherent elastic scattering described by Eq. (2.35) is referred to Bragg diffraction, and the condition in Eq. (2.42) is referred to Bragg condition.

Since $E = \hbar^2 k^2/(2m)$ where m is the neutron mass, Eq. (2.42) can be rewritten as:

$$E \geq E_{hkl}, \tag{2.43}$$

where

$$E_{hkl} = \hbar^2 \tau_{hkl}^2/(8m), \tag{2.44}$$

represents the “Bragg Edges" for the plan hkl.

Since we have:

$$\begin{aligned} Q^2 =& 4k^2 \sin^2(\frac{\theta}{2}), \\ =& 2k^2(1-\cos(\theta)), \\ =& 2k^2(1-\mu), \\ =& \frac{4m}{\hbar^2}E(1-\mu), \end{aligned} \tag{2.45}$$

where $\mu = \cos(\theta)$, then

$$\delta(Q^2 - \tau_{hkl}^2) = \delta\left(\frac{4m}{\hbar^2}E(1-\mu) - \frac{8m}{\hbar^2}E_{hkl}\right). \tag{2.46}$$

In addition to the property of the Dirac function $\delta(ax) = |a|^{-1}\delta(x)$, we have:

$$\delta(Q^2 - \tau_{hkl}^2) = \frac{\hbar^2}{4mE}\delta(\mu - \mu_{hkl}), \tag{2.47}$$

where μ_{hkl} is the cosine of the diffraction angle θ_{hkl} for plan (hkl), which can be obtained by:

$$\mu_{hkl} = \cos(\theta_{hkl}) = 1 - 2E_{hkl}/E. \tag{2.48}$$

By replacing Eq. (2.47) in Eq. (2.39), then by replacing Eq. (2.39) in (2.2) and integrating along the azimuthal direction ϕ, the double differential coherent elastic scattering

cross section per atom is given by:

$$\frac{\mathrm{d}^2\sigma^{\mathrm{el}}_{\mathrm{coh}}}{\mathrm{d}\mu\mathrm{d}E_f} = \frac{\pi^2\hbar\delta(\omega)}{mNV_{\mathrm{unit\ cell}}E}\sum_{hkl}^{E\geq E_{hkl}}\delta(\mu-\mu_{hkl})d_{hkl}\left|F(\vec{\tau}_{hkl})\right|^2. \tag{2.49}$$

By integrating Eq. (2.49) over E_f, the angular differential coherent elastic scattering cross section is given by:

$$\frac{\mathrm{d}\sigma^{\mathrm{el}}_{\mathrm{coh}}}{\mathrm{d}\mu}(E) = \frac{\pi^2\hbar^2}{mNV_{\mathrm{unit\ cell}}E}\sum_{hkl}^{E\geq E_{hkl}}\delta(\mu-\mu_{hkl})d_{hkl}\left|F(\vec{\tau}_{hkl})\right|^2. \tag{2.50}$$

By integrating Eq. (2.50) over $\mu=\cos(\theta)$, the integrated coherent elastic cross section per atom for crystal powder in which the grains are randomly distributed is:

$$\sigma^{\mathrm{el}}_{\mathrm{coh}}(E) = \frac{\pi^2\hbar^2}{mNV_{\mathrm{unit\ cell}}E}\sum_{hkl}^{E\geq E_{hkl}}d_{hkl}\left|F(\vec{\tau}_{hkl})\right|^2, \tag{2.51}$$

where $F(\vec{\tau}_{hkl})$ can be written by inserting in Eq. (2.36) the Debye-Waller function (Eq. (2.28)) obtained thanks to the cubic approximation:

$$F(\vec{\tau}_{hkl}) = \sum_{j=1}^{N_{\mathrm{unit\ cell}}}\overline{b_j}\exp\left(-\frac{\hbar^2\tau^2_{hkl}}{4M_jk_BT}\Lambda_j(T)\right)\exp\left(i\vec{\tau}_{hkl}\cdot\vec{p}_j\right). \tag{2.52}$$

The coherent elastic neutron scattering cross section $\sigma^{\mathrm{el}}_{\mathrm{coh}}(E)$ for uranium dioxide (UO_2) is illustrated in Fig. 1.1 (green curves). $\sigma^{\mathrm{el}}_{\mathrm{coh}}(E)$ is zero until the incident neutron energy E reaches the value of the first Bragg Edge E_{hkl} (Bragg condition Eq.(2.43)). The first Bragg Edge (determined by the lattice plans indexed (111) of UO_2) appears at about 2 meV for UO_2. After the first Bragg Edge, $\sigma^{\mathrm{el}}_{\mathrm{coh}}(E)$ begins to decrease with the $1/E$ tendency until the second Bragg Edge. $\sigma^{\mathrm{el}}_{\mathrm{coh}}(E)$ is increased at this energy thanks to the contributions of new lattice plans of UO_2. This kind of behavior continues until E reaches a threshold (around 1 eV for UO_2). After this energy, $\sigma^{\mathrm{el}}_{\mathrm{coh}}(E)$ reaches the asymptotic $1/E$ decrease.

2.2.4. Incoherent elastic scattering

The incoherent elastic scattering function $S^{\mathrm{el}}_{\mathrm{inc}}(\vec{Q},\omega)$ is obtained thanks to Eqs. (2.8), (2.20), (2.28), (2.32) and (2.33), which is given by:

$$S^{\mathrm{el}}_{\mathrm{inc}}(\vec{Q},\omega) = \sum_{j=1}^{N_{\mathrm{unit\ cell}}}S^{\mathrm{el}}_{\mathrm{inc},\,j}(\vec{Q},\omega), \tag{2.53}$$

where $S^{\text{el}}_{\text{inc},j}(\vec{Q},\omega)$ represents the incoherent elastic scattering function of the atom j:

$$S^{\text{el}}_{\text{inc},j}(\vec{Q},\omega) = \frac{\delta(\omega)}{\hbar}\left(\overline{b_j^2} - (\overline{b_j})^2\right)\exp\left(-\frac{\hbar^2 Q^2}{2M_j k_B T}\Lambda_j(T)\right). \tag{2.54}$$

Eqs. (2.53) and (2.54) indicate that the incoherent elastic scattering function of a solid crystalline material can be obtained by summing the partial scattering functions of all the atoms in the unit cell. In addition, under the cubic approximation, $S^{\text{el}}_{\text{inc},j}(\vec{Q},\omega)$ is a function of Q^2, therefore, $S^{\text{el}}_{\text{inc},j}(\vec{Q},\omega) = S^{\text{el}}_{\text{inc},j}(Q,\omega)$. $S^{\text{el}}_{\text{inc},j}(Q,\omega)$ is isotropic along the azimuthal direction ϕ (Eq. (2.45)). By replacing Eq. (2.45) in Eq. (2.54), then by replacing the obtained equation in Eq. (2.2) and finally integrating over ϕ, the double differential incoherent elastic scattering cross section of the atom j is given by:

$$\frac{\mathrm{d}^2\sigma^{\text{el}}_{\text{inc},j}}{\mathrm{d}\mu\mathrm{d}E_f} = \frac{2\pi}{\hbar}\delta(\omega)\left(\overline{b_j^2} - (\overline{b_j})^2\right)\exp\left(-\frac{2E(1-\mu)}{A_j k_B T}\Lambda_j(T)\right), \tag{2.55}$$

where $A_j = M_j/m$ is ratio of the mass of the atom j to the neutron mass.

The angular differential incoherent elastic scattering cross section can be obtained by integrating the Eq. (2.55) over E_f:

$$\frac{\mathrm{d}\sigma^{\text{el}}_{\text{inc},j}}{\mathrm{d}\mu}(E) = \int_0^\infty \mathrm{d}E_f \frac{2\pi}{\hbar}\delta(\omega)\left(\overline{b_j^2} - (\overline{b_j})^2\right)\exp\left(-\frac{2E(1-\mu)}{A_j k_B T}\Lambda_j(T)\right), \tag{2.56}$$

$$= \frac{\sigma_{\text{inc},j}}{2}\exp\left(-\frac{2E(1-\mu)}{A_j k_B T}\Lambda_j(T)\right), \tag{2.57}$$

where $\sigma_{\text{inc},j}$ is the bound incoherent scattering cross section of the atom j:

$$\sigma_{\text{inc},j} = 4\pi\left(\overline{b_j^2} - (\overline{b_j})^2\right). \tag{2.58}$$

Then the total incoherent elastic scattering cross section of the atom j can be obtained by integrating Eq. (2.57) over μ:

$$\sigma^{\text{el}}_{\text{inc},j}(E) = \int_{-1}^{1}\mathrm{d}\mu\frac{\sigma_{\text{inc},j}}{2}\exp\left(-\frac{2E(1-\mu)}{A_j k_B T}\Lambda_j(T)\right), \tag{2.59}$$

$$= \frac{A_j k_B T}{4E\Lambda_j(T)}\left(1-\exp\left(-\frac{4E\Lambda_j(T)}{A_j k_B T}\right)\right)\sigma_{\text{inc},j}. \tag{2.60}$$

Eq. (2.60) shows that the incoherent elastic scattering cross section of a given atom j is determined by its Debye-Waller coefficient $\Lambda_j(T)$. The incoherent elastic scattering cross section $\sigma^{\text{el}}_{\text{inc}}(E)$ of H in ice I_h at 233 K (red curve) taken from the JEFF-3.3 evaluations (Plompen, Cabellos, De Saint Jean, et al. 2020) is presented in Fig. 2.3 for illustration. $\sigma^{\text{el}}_{\text{inc}}(E)$ of H in ice I_h varies smoothly with the incident neutron energy.

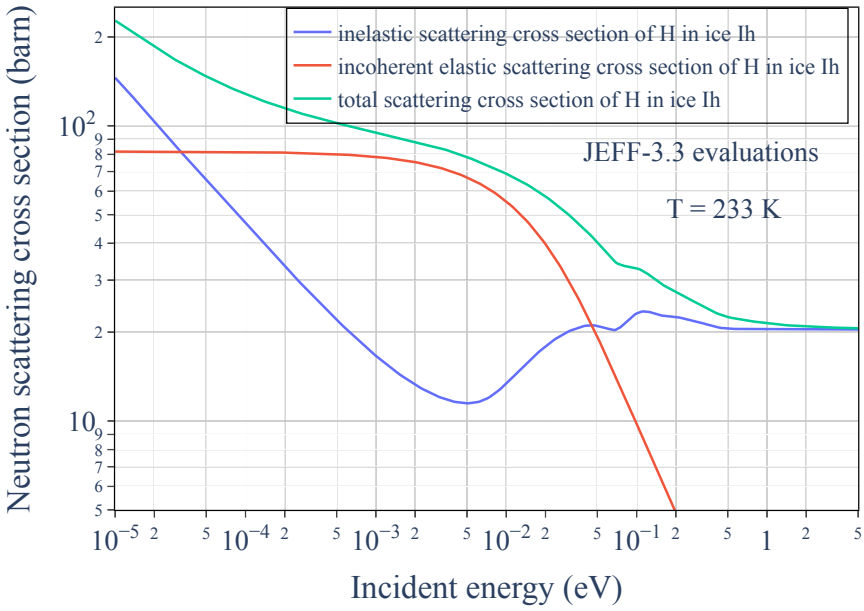

Figure 2.3.: JEFF-3.3 incoherent elastic (red curve), inelastic (blue curve) and total (green curve) neutron scattering cross sections for H in ice I_h at 233 K (Plompen, Cabellos, De Saint Jean, et al. 2020).

2.2.5. Inelastic scattering

The inelastic scattering function $S^{\text{inel}}(\vec{Q},\omega)$ can be obtained by summing the coherent and incoherent inelastic scattering functions, under the incoherent approximation and cubic approximations and thanks to Eqs. (2.7), (2.8), (2.20) and (2.32). $S^{\text{inel}}(\vec{Q},\omega)$ is given by:

$$S^{\text{inel}}(\vec{Q},\omega) = S^{\text{inel}}_{\text{coh}}(\vec{Q},\omega) + S^{\text{inel}}_{\text{inc}}(\vec{Q},\omega), \tag{2.61}$$

$$= \sum_{j=1}^{N_{\text{unit cell}}} S^{\text{inel}}_{j}(\vec{Q},\omega), \tag{2.62}$$

where $S^{\text{inel}}_{j}(\vec{Q},\omega)$ is the inelastic scattering function of the atom j:

$$\begin{aligned} S^{\text{inel}}_{j}(\vec{Q},\omega) = & \frac{1}{2\pi\hbar}\overline{b_j^2}\exp\left(-\frac{\hbar^2Q^2}{2M_jk_BT}\Lambda_j(T)\right)\times \\ & \sum_{n=1}^{\infty}\frac{1}{n!}\int_{-\infty}^{\infty}\left(\frac{\hbar^2Q^2}{2M_jk_BT}\int_{-\infty}^{\infty}P_j(\omega')\exp\left(i\omega' t\right)\mathrm{d}\omega'\right)^n\exp(-i\omega t)\mathrm{d}t. \end{aligned} \tag{2.63}$$

Eqs. (2.62) and (2.63) indicate that under the incoherent approximation, the inelastic scattering function $S^{\text{inel}}(\vec{Q},\omega)$ of a solid crystalline material can be obtained by summing the partial scattering function of all the atoms in the unit cell. In addition, $S^{\text{inel}}_{j}(\vec{Q},\omega)$ is a function of Q^2 based on the cubic approximation. Thus $S^{\text{inel}}_{j}(\vec{Q},\omega)$ is

isotropic for the momentum transfer, i.e., $S_j^{\text{inel}}(\vec{Q},\omega) = S_j^{\text{inel}}(Q,\omega)$. $S_j^{\text{inel}}(Q,\omega)$ is given by:

$$S_j^{\text{inel}}(Q,\omega) = \frac{1}{\hbar}\overline{b_j^2}\exp\left(-\frac{\hbar^2Q^2}{2M_jk_BT}\Lambda_j(T)\right)\sum_{n=1}^{\infty}\frac{1}{n!}\left(\frac{\hbar^2Q^2}{2M_jk_BT}\Lambda_j(T)\right)^n\mathcal{T}_{j,n}(\omega), \tag{2.64}$$

where

$$\mathcal{T}_{j,n}(\omega) = \frac{1}{2\pi}\int_{-\infty}^{\infty}\eta_j^n(t)\exp(-i\omega t)\mathrm{d}t, \tag{2.65}$$

where

$$\eta_j(t) = \frac{1}{\Lambda_j(T)}\int_{-\infty}^{\infty}P_j(\omega')\exp\left(i\omega' t\right)\mathrm{d}\omega'. \tag{2.66}$$

The double integral terms $\mathcal{T}_{j,n}(\omega)$ is computed by recurrence (Sjolander 1958). For $n=1$,

$$\mathcal{T}_{j,1}(\omega) = \frac{1}{\Lambda_j(T)}\int_{-\infty}^{\infty}P_j(\omega')\left(\frac{1}{2\pi}\int_{-\infty}^{\infty}\exp\left(-i(\omega-\omega')t\right)\mathrm{d}t\right)\mathrm{d}\omega' = \frac{1}{\Lambda_j(T)}P_j(\omega). \tag{2.67}$$

Thus

$$S_{j,n=1}^{\text{inel}}(Q,\omega) = \frac{1}{\hbar}\overline{b_j^2}\exp\left(-\frac{\hbar^2Q^2}{2M_jk_BT}\Lambda_j(T)\right)\frac{\hbar^2Q^2}{2M_jk_BT}P_j(\omega). \tag{2.68}$$

For $n\geq 2$, $\eta^n(t) = \eta(t)\eta^{n-1}(t)$, and by applying the convolution theorem for Fourier transform,

$$\mathcal{T}_{j,n}(\omega) = \int_{-\infty}^{\infty}\mathcal{T}_{j,1}(\omega')\mathcal{T}_{j,n-1}(\omega-\omega')\mathrm{d}\omega'. \tag{2.69}$$

The integral of $\mathcal{T}_{j,1}(\omega)$ over $[-\infty;\infty]$ is equal to 1 (Eqs. (2.27) and (2.67)). By applying the Fubini's theorem, the integral of $\mathcal{T}_{j,n}(\omega)$ in Eq. (2.69) is also equal to 1 for $n\geq 2$. This property is referred as normalization condition (Macfarlane, Muir, Boicourt, et al. 2017), which serves for the verification of calculation. $\mathcal{T}_{j,n}(\omega)$ is computed until a given order N_{phonon}, which is referred to phonon expansion order.

Note that based on Eq. (2.66), we have:

$$\eta_j(-t) = \eta_j(t+\frac{i\hbar}{k_BT}). \tag{2.70}$$

By replacing Eq. (2.70) in Eq. (2.65), we obtain:

$$\mathcal{T}_{j,n}(-\omega) = \exp\left(-\frac{\hbar\omega}{k_BT}\right)\mathcal{T}_{j,n}(\omega). \tag{2.71}$$

By replacing Eq.(2.71) in Eq. (2.64), we have:

$$S_j^{\text{inel}}(Q,-\omega) = \exp\left(-\frac{\hbar\omega}{k_BT}\right)S_j^{\text{inel}}(Q,\omega). \tag{2.72}$$

Therefore, the principle of detailed balance (Eq. (2.9)) is satisfied. The double

differential inelastic scattering cross section of the atom j is given by:

$$\frac{\mathrm{d}^2\sigma_j^{\mathrm{inel}}}{\mathrm{d}\Omega \mathrm{d}E_f} = \sqrt{\frac{E_f}{E}} S_j^{\mathrm{inel}}(Q,\omega). \tag{2.73}$$

In Monte-Carlo neutron transport codes (Goorley, James, Booth, et al. 2012; E. Brun, F. Damian, Diop, et al. 2015; Leppänen, Pusa, Viitanen, et al. 2015), dimensionless TSLs $S(\alpha,\beta)$ are used in the place of $S(\vec{Q},\omega)$. Eq. (2.73) can be rewritten as:

$$\frac{\mathrm{d}^2\sigma_j^{\mathrm{inel}}}{\mathrm{d}\Omega \mathrm{d}E_f} = \frac{\sigma_{b,j}}{4\pi k_B T}\sqrt{\frac{E_f}{E}} S_j^{\mathrm{inel}}(\alpha_j,\beta), \tag{2.74}$$

where $\sigma_{b,j} = 4\pi\overline{b_j^2}$ is the bound scattering cross section of the atom j and

$$S_j^{\mathrm{inel}}(\alpha_j,\beta) = \exp\left(-\alpha_j \Lambda_j(T)\right) \sum_{n=1}^{N_{\mathrm{phonon}}} \frac{1}{n!}(\alpha_j \Lambda_j(T))^n \mathscr{T}_{j,n}(\beta), \tag{2.75}$$

with

$$\alpha_j = \frac{\hbar^2 Q^2}{2M_j k_B T} = \frac{E + E_f - 2\mu\sqrt{EE_f}}{A_j k_B T}, \tag{2.76}$$

$$\beta = -\frac{\hbar\omega}{k_B T} = \frac{E_f - E}{k_B T}, \tag{2.77}$$

where A_j is ratio of the mass of the atom j to the neutron mass.

2.2.6. Phonon density of states of uranium dioxide calculated by *ab initio* lattice dynamics method

In the previous sections, it is noted that the PDOS is the key element for the determination of the coherent elastic neutron scattering cross section $\sigma_{\mathrm{coh}}^{\mathrm{el}}(E)$ and the TSLs $S(\alpha,\beta)$ for solid crystalline materials in the framework of the harmonic, incoherent and cubic approximations with the phonon expansion method.

In this part, special attention will be given to stoichiometric uranium dioxide (UO_2) in solid crystalline phase, and above the Néel temperature ($T_N = 30.8$).

Until recently, TSLs for reactor applications were obtained with the PDOS of uranium in uranium dioxide (U in UO_2) and that of oxygen in uranium dioxide (O in UO_2), resulting from the semi-empirical lattice dynamics model developed by Dolling et al. in the 1960s (Dolling, Cowley, and Woods 1965). To improve the description of the atomic vibrational motions of UO_2, Wormald et al. generate the PDOSs of U in UO_2 and O in UO_2 for the latest ENDF/B-VIII.0 database, via *ab initio* lattice dynamic methods (Wormald, N. C. Fleming, A. I. Hawari, et al. 2021). They use a method that relies on electronic structure calculations of UO_2 via the spin-polarized density functional

theory (DFT) using the generalized gradient approximation (GGA) with a Hubbard model in the VASP code (Kresse and Furthmüller 1996b; Kresse and Furthmüller 1996a). The obtained interatomic forces are then utilized in the lattice dynamics code PHONON (K. Parlinski, Li, and Kawazoe 1997; Krzysztof Parlinski 1999). *Ab initio* calculations of PDOS of UO_2 were also performed by Maldonado et al. at the Uppsala University by using the VASP code within the GGA and Hubbard correction (Noguere, Maldonado, and De Saint Jean 2018). The lattice dynamics calculations were performed with the finite-displacement method by using the PHONONPY code (Togo and Tanaka 2015).

The PDOS of UO_2 obtained by Wormald et al. (Wormald, J. L. and Hawari, A. I. 2016) and Maldonado et al. (Noguere, Maldonado, and De Saint Jean 2018) are presented in Fig. 2.4. The first two peaks of the PDOS of UO_2 correspond to the acoustic modes of the uranium atoms. The peak at nearly 10 meV corresponds to the transverse acoustic (TA) mode while the peak at nearly 20 meV corresponds to the longitudinal acoustic (LA) mode. The peaks at nearly 30 meV, 55 meV and 70 meV are dominated by the optical modes of the oxygen atoms. The peak at roughly 30 meV stems from the transverse and longitudinal (TO1, LO1) optical modes. The peak at nearly 55 meV corresponds to the transverse optical mode (TO2) and the last peak at nearly 70 meV corresponds to the longitudinal optical mode (LO2).

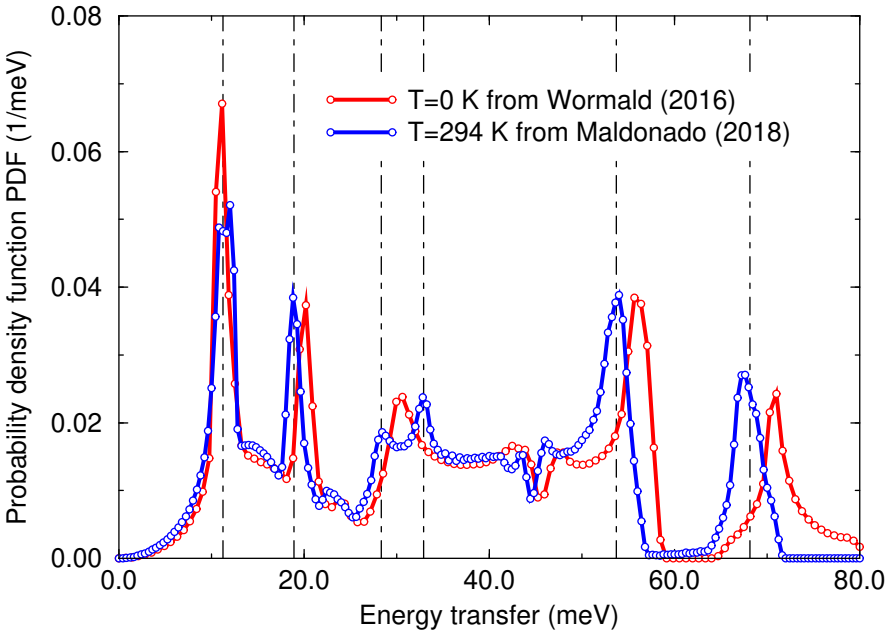

Figure 2.4.: *Ab initio* phonon density of states (PDOS) of UO_2 at $T = 0$ K (Wormald, J. L. and Hawari, A. I. 2016) and $T = 294$ K (Noguere, Maldonado, and De Saint Jean 2018). The corresponding modes of the peaks of the PDOS are presented in the text.

Compared to the semi-empirical lattice dynamics model developed by Dolling et al. (Dolling, Cowley, and Woods 1965), *ab initio* lattice dynamics calculations enable to achieve

a better agreement with the experimental phonon dispersion curves and the PDOS of UO_2 at room temperature (Wormald, N. C. Fleming, A. I. Hawari, et al. 2021). At elevated temperatures, the theoretical descriptions of the anharmonicity effects are still an issue debated in the literature.

2.3. Scattering models for liquid materials

In this section, the general equation of the scattering function $S(\vec{Q}, \omega)$ is presented in the case of liquid materials. The approximations that enable to connect the scattering function $S(\vec{Q}, \omega)$ to the width function $w(t)$ are discussed in Section 2.3.1. In Section 2.3.2, the width function $w(t)$ is further separated as a diffusive and a vibrational parts to take into account different atomic motions of liquid materials. On one hand, the separated diffusive scattering function $S_{\text{diff}}(\vec{Q}, \omega)$ based on the Egelstaff-Schofield diffusion model is presented. On the other hand, the calculations of the vibrational scattering function $S_{\text{vib}}(\vec{Q}, \omega)$ by using the phonon expansion method are summarized by analogy with solid crystalline materials. At the end of Section 2.3.2, the recombination of the diffusive and vibrational scattering functions is presented. The PDOS of hydrogen bound in water molecule (H in H_2O) obtained by molecular dynamics (MD) calculations is presented in Section 2.3.3. The last section is devoted to present the corrections of random jump diffusion (RJD) and rotational diffusion applied to water molecules. The model presented in this section was applied to study a few water data measured at the ILL facilities (see appendix).

2.3.1. Incoherent and Gaussian approximations

The double differential neutron scattering cross section as a function of the scattering function $S(\vec{Q}, \omega)$ in Eq. (2.2) is introduced by Van Hove (Van Hove 1954), as well as the generalized pair distribution function $G(\vec{r}, t)$. For the sake of clarity, the scattering system is supposed to be composed of one single type of particles in Ref. (Van Hove 1954). Although the monatomic scattering system is a simplified model, the obtained results can be easily extended to the liquid materials with multiple types of atoms.

By distinguishing the contribution from the same particle to different particles, Van Hove split $G(\vec{r}, t)$ into a self part $G_s(\vec{r}, t)$ and a distinct part $G_d(\vec{r}, t)$:

$$G(\vec{r}, t) = G_s(\vec{r}, t) + G_d(\vec{r}, t). \tag{2.78}$$

For a given particle at position $\vec{r}$ and time t, $G_s(\vec{r}, t)\mathrm{d}\vec{r}\mathrm{d}t$ represents the probability of finding the same particle between $\vec{r}$ and $\vec{r} + \mathrm{d}\vec{r}$ in a time interval t and $t + \mathrm{d}t$. Similarly, $G_d(\vec{r}, t)\mathrm{d}\vec{r}\mathrm{d}t$ is the probability of finding a distinct particle between $\vec{r}$ and $\vec{r} + \mathrm{d}\vec{r}$ in a time interval t and $t + \mathrm{d}t$.

The scattering function $S(\vec{Q}, \omega)$ is a two-fold Fourier transform of the generalized pair distribution function $G(\vec{r}, t)$ (Van Hove 1954). As introduced in Section 2.1, the coherent scattering includes the interference effects among different particles.

Hence, the distinct part $G_d(\vec{r},\, t)$ will only appear in the coherent scattering function $S_{\text{coh}}(\vec{Q},\, \omega)$. Eqs. (2.7), (2.8) and (2.78) enable to obtain the coherent and incoherent scattering functions for liquid materials composed of a single type of atoms:

$$S_{\text{coh}}(\vec{Q},\, \omega) = \frac{N}{2\pi\hbar}(\overline{b})^2 \int_{-\infty}^{\infty} \left(\int_V (G_s(\vec{r},\, t) + G_d(\vec{r},\, t)) \exp\left(i\vec{Q}\cdot\vec{r}\right) \mathrm{d}\vec{r} \right) \exp(-i\omega t)\mathrm{d}t, \quad (2.79)$$

and

$$S_{\text{inc}}(\vec{Q},\, \omega) = \frac{N}{2\pi\hbar}\left(\overline{b^2} - (\overline{b})^2\right) \int_{-\infty}^{\infty} \left(\int_V G_s(\vec{r},\, t) \exp\left(i\vec{Q}\cdot\vec{r}\right) \mathrm{d}\vec{r} \right) \exp(-i\omega t)\mathrm{d}t, \quad (2.80)$$

where V is the volume of the scattering system.

Since it is difficult to predict theoretically the contribution from the distinct part, we use the incoherent approximation, as for solid crystalline materials:

$$G_d(\vec{r},\, t)) \cong 0. \quad (2.81)$$

Under the incoherent approximation, $G_d(\vec{r},\, t)$ vanishes and hence Eqs. (2.79) and (2.80) can be combined to obtain the normalized scattering function for liquid materials $S(\vec{Q},\, \omega)$:

$$S(\vec{Q},\, \omega) = \frac{1}{2\pi\hbar}\overline{b^2} \int_{-\infty}^{\infty} \langle j,\, j\rangle_s \exp(-i\omega t)\mathrm{d}t, \quad (2.82)$$

where $\langle j,\, j\rangle_s$ is the self intermediate function (Squires 2012):

$$\langle j,\, j\rangle_s = \int_V G_s(\vec{r},\, t) \exp\left(i\vec{Q}\cdot\vec{r}\right)\mathrm{d}\vec{r}. \quad (2.83)$$

To obtain an analytical form of $G_s(\vec{r},\, t)$, Vineyard (Vineyard 1958) suggests an approximation, called Gaussian approximation, which enables to decouple $\vec{r}$ and t:

$$G_s(\vec{r},\, t) \cong (2\pi)^{-3/2} w^{-3}(t) \exp\left(-r^2/2w^2(t)\right). \quad (2.84)$$

Under the Gaussian approximation, with respect to a given particle at $\vec{r}$ and t, the probability of finding the same particle at position $\vec{r}'$ follows a Gaussian distribution. This Gaussian distribution is a function of $\left\|\vec{r}-\vec{r}'\right\|$ and its half width at half maximum (HWHM) $\sqrt{2\ln 2}w(t)$ is a function of t. $w(t)$ is the width function and $3w^2(t)$ is the MSD of the particle after time t.

By replacing Eq. (2.84) in Eq. (2.83) and by applying the theorem for Fourier transform of Gaussian functions, the self intermediate function for liquid materials $\langle j,\, j\rangle_s$ is given by:

$$\langle j,\, j\rangle_s = \exp\left(-Q^2 w^2(t)/2\right). \quad (2.85)$$

Eq. (2.85) shows that $S(\vec{Q},\, \omega)$ under the Gaussian approximation is a function of Q^2, thus the self part is isotropic for the momentum transfer, i.e., $S(\vec{Q},\, \omega) = S(Q,\, \omega)$.

As shown in Eq. (2.85), the width function $w(t)$ is the key ingredient to determine the intermediate function and then the scattering function. The width functions

for several simple models such as perfect gas and diffusing atom are reported in Vineyard's paper (Vineyard 1958). Later, Rahman, Singwi and Sjölander suggest in their co-authored paper (Rahman, Singwi, and A. Sjölander 1962) an approximated width function for $G_s(\vec{r}, t)$:

$$w^2(t) = \frac{\hbar}{M}\int_0^\infty \frac{f(\omega)}{\omega}\left(\coth\left(\frac{\hbar\omega}{2k_BT}\right)(1-\cos(\omega t)) - i\sin(\omega t)\right)\mathrm{d}\omega, \tag{2.86}$$

where M is the mass of the nucleus, k_B is the Boltzmann constant, T is the temperature of the liquid. Eq.(2.86) is based on the fluctuation-dissipation theorem obtained by Schofield (Schofield 1960), which relates the real and imaginary parts of the generalized pair distribution function. In Ref. (Rahman, Singwi, and A. Sjölander 1962), $f(\omega)$ is named the frequency spectrum of the velocity autocorrelation function (VACF) in analogy with the case of a solid, which is referred to eigen-frequency function in the literature (Yuwei Zhu 2018), satisfying:

$$\int_0^\infty f(\omega)d\omega = 1. \tag{2.87}$$

2.3.2. Separation and recombination of diffusive and vibrational scattering functions

Eqs. (2.82), (2.85) and (2.86) indicate that under the Gaussian approximation, the scattering function $S(Q, \omega)$ of a liquid can be calculated via the eigen-frequency function $f(\omega)$. Nevertheless, it is difficult to determine $f(\omega)$ analytically for a liquid system. To solve this problem, a separation technique is conventionally used, by decomposing the square of the width function, i.e., the MSD, into a diffusive and a vibrational parts

$$w^2(t) = w^2_{\mathrm{diff}}(t) + w^2_{\mathrm{vib}}(t). \tag{2.88}$$

The diffusive scattering function $S_{\mathrm{diff}}(Q, \omega)$ and the vibrational scattering function $S_{\mathrm{vib}}(Q, \omega)$ can thus be determined respectively by using Eqs. (2.82) and (2.85):

$$S_{\mathrm{diff}}(Q, \omega) = \frac{1}{2\pi\hbar}\overline{b^2}\int_{-\infty}^{\infty}\exp\left(-Q^2w^2_{\mathrm{diff}}(t)/2\right)\exp(-i\omega t)\mathrm{d}t, \tag{2.89}$$

and

$$S_{\mathrm{vib}}(Q, \omega) = \frac{1}{2\pi\hbar}\overline{b^2}\int_{-\infty}^{\infty}\exp\left(-Q^2w^2_{\mathrm{vib}}(t)/2\right)\exp(-i\omega t)\mathrm{d}t. \tag{2.90}$$

Then $S(Q, \omega)$ is obtained by recombining these two components. According to the convolution theorem for Fourier transform, the recombined scattering function can be obtained by convoluting the diffusive with the vibrational scattering functions:

$$S(Q, \omega) = \frac{\hbar}{\overline{b^2}}\int_{-\infty}^{\infty} S_{\mathrm{diff}}(Q, \omega')S_{\mathrm{vib}}(Q, \omega - \omega')\mathrm{d}\omega' \tag{2.91}$$

where $\hbar/\overline{b^2}$ is a scale coefficient.

For the diffusive part, it exists several representative models in the literature (Squires 2012; Vineyard 1958; P. A. Egelstaff and Schofield 1962; Márquez Damián, J. Granada, Cantargi, et al. 2016). For each of these models, an analytical width function $w_{\text{diff}}(t)$ is proposed to interpret the diffusion behavior of the liquid. In this work, the Egelstaff-Schofield diffusion model (P. A. Egelstaff and Schofield 1962) is investigated, in which

$$w^2_{\text{diff}}(t) = \frac{2\hbar D}{k_B T}\left(\sqrt{\left(\frac{tk_B T}{\hbar}\right)^2 + c^2 + \frac{1}{4}} - c\right), \tag{2.92}$$

where D represents the diffusion coefficient (m^2/s) of the liquid and c is a dimensionless diffusion constant

$$c = \frac{MD}{\hbar\zeta_{\text{diff}}}, \tag{2.93}$$

where ζ_{diff} represents diffusive weight.

By replacing Eq. (2.92) in Eq. (2.89), we have:

$$S_{\text{diff}}(Q,\omega) = \frac{1}{2\pi\hbar}\overline{b^2}\int_{-\infty}^{\infty}\exp\left(-\frac{\hbar DQ^2}{k_B T}\left(\sqrt{\left(\frac{tk_B T}{\hbar}\right)^2 + c^2 + \frac{1}{4}} - c\right)\right)\exp(-i\omega t)\mathrm{d}t. \tag{2.94}$$

According to the property of exponential functions:

$$\exp\left(-2\sqrt{AB}\right) = \sqrt{\frac{A}{\pi}}\int_{-\infty}^{\infty}\exp\left(-Ax^2\right)\exp\left(-B/x^2\right)\mathrm{d}x, \tag{2.95}$$

we have:

$$\begin{aligned}&\exp\left(-\frac{\hbar DQ^2}{k_B T}\left(\sqrt{\left(\frac{tk_B T}{\hbar}\right)^2 + c^2 + \frac{1}{4}} - c\right)\right)\\ &= \frac{DQ^2}{\sqrt{\pi}}\exp\left(\frac{c\hbar DQ^2}{k_B T}\right)\int_{-\infty}^{\infty}\exp\left(-(DQ^2)^2x^2\right)\exp\left(-\frac{1}{4x^2}\left(t^2 + (\frac{\hbar}{k_B T})^2(c^2+\frac{1}{4})\right)\right)\mathrm{d}x.\end{aligned} \tag{2.96}$$

Since we have:

$$\begin{aligned}&\int_{-\infty}^{\infty}\exp\left(-\frac{1}{4x^2}\left(t^2 + (\frac{\hbar}{k_B T})^2(c^2+\frac{1}{4})\right)\right)\exp(-i\omega t)\mathrm{d}t\\ &= \exp\left(-\frac{1}{4x^2}\left((\frac{\hbar}{k_B T})^2(c^2+\frac{1}{4})\right)\right)\exp\left(-x^2\omega^2\right)\int_{-\infty}^{\infty}\exp\left(-\frac{1}{4x^2}(t+2ix^2\omega)^2\right)\mathrm{d}t,\end{aligned} \tag{2.97}$$

and according to the property of Gaussian integrals:

$$\int_{-\infty}^{\infty}\exp\left(-A(t+B)^2\right)\mathrm{d}t = \sqrt{\frac{\pi}{A}}, \tag{2.98}$$

then Eq. (2.94) becomes:

$$S_{\text{diff}}(Q,\omega) = \frac{\overline{b^2}DQ^2}{2\sqrt{\pi}\pi\hbar}\exp\left(\frac{c\hbar DQ^2}{k_BT}\right)\times \int_{-\infty}^{\infty}\exp\left(-\frac{1}{4x^2}\left((\frac{\hbar}{k_BT})^2(c^2+\frac{1}{4})\right)\right)\exp\left(-(\omega^2+(DQ^2)^2)x^2\right)\sqrt{4\pi x^2}\mathrm{d}x. \tag{2.99}$$

By performing a change of variable $y = x^2$, Eq. (2.99) becomes:

$$S_{\text{diff}}(Q,\omega) = \frac{\overline{b^2}DQ^2}{\pi\hbar}\exp\left(\frac{c\hbar DQ^2}{k_BT}\right)\times \int_{0}^{\infty}\exp\left(-\frac{1}{4y}\left((\frac{\hbar}{k_BT})^2(c^2+\frac{1}{4})\right)\right)\exp\left(-(\omega^2+(DQ^2)^2)y\right)\mathrm{d}y. \tag{2.100}$$

According to the property of exponential functions:

$$\int_0^{\infty}\exp\left(-\frac{B}{4y}-Ay\right)\mathrm{d}y = \sqrt{\frac{B}{A}}K_1(\sqrt{AB}), \tag{2.101}$$

where $K_1(x)$ is a modified Bessel function of the second kind. Thus, Eq. (2.100) becomes:

$$S_{\text{diff}}(Q,\omega) = \frac{\overline{b^2}}{k_BT}\frac{\hbar DQ^2}{\pi k_BT}\exp\left(\frac{MD^2Q^2}{\zeta_{\text{diff}}k_BT}\right)\frac{\sqrt{c^2+1/4}}{\frac{\hbar}{k_BT}\sqrt{\omega^2+(DQ^2)^2}}K_1\left(\frac{\hbar}{k_BT}\sqrt{c^2+1/4}\sqrt{\omega^2+(DQ^2)^2}\right). \tag{2.102}$$

Nevertheless, the principle of detailed balance is violated in Eq. (2.102). Thus, $S_{\text{diff}}(Q,\omega)$ is corrected to $\widetilde{S_{\text{diff}}}(Q,\omega)$ by:

$$\widetilde{S_{\text{diff}}}(Q,\omega) = \exp\left(\frac{\hbar\omega}{2k_BT}\right)S_{\text{diff}}(Q,\omega). \tag{2.103}$$

The PDOS of the diffusive part can be obtained from Eq. (2.103):

$$\rho_{\text{diff}}(\omega) = \frac{4\hbar c\zeta_{\text{diff}}}{\pi k_BT}\sqrt{c^2+1/4}\sinh\left(\frac{\hbar\omega}{2k_BT}\right)K_1\left(\frac{\hbar\omega}{k_BT}\sqrt{c^2+1/4}\right). \tag{2.104}$$

For the vibrational part, which takes into account the vibrational behavior of the liquid, the width function is given by (Sjolander 1958):

$$w^2_{\text{vib}}(t) = \frac{\hbar}{M}\int_0^{\infty}\frac{\rho_{\text{vib}}(\omega)}{\omega}\left(\coth\left(\frac{\hbar\omega}{2k_BT}\right)(1-\cos(\omega t))-i\sin(\omega t)\right)\mathrm{d}\omega, \tag{2.105}$$

where $\rho_{\text{vib}}(\omega)$ represents the PDOS of the vibrational part, which is referred to vibra-

tional density of states (VDOS), with

$$\int_0^\infty \rho_{\text{vib}}(\omega)\mathrm{d}\omega = \zeta_{\text{vib}}, \tag{2.106}$$

where ζ_{vib} represents the vibrational weight.

The diffusive and vibrational weights satisfy:

$$\zeta_{\text{diff}} + \zeta_{\text{vib}} = 1. \tag{2.107}$$

The vibrational width function $w_{\text{vib}}(t)$ (Eq. (2.105)) is replaced in the intermediate function (Eq. (2.85)). The obtained equation is compared with the intermediate function for solid crystalline materials (Eq. (2.20)), which is obtained thanks to the cubic approximation (Eq. (2.23)). The equations of the intermediate function for solid crystalline and liquid materials are exactly the same for inelastic scattering of neutrons in monatomic systems. This result indicates that the harmonic approximation is equivalent to the Gaussian approximation, and the width function of liquid materials (Eq.(2.105)) can be regarded as the application of the cubic approximation to liquid, with interpretation that atoms in liquid materials are isotropic.

By analogy with the physical quantities used in the phonon expansion method presented in Section 2.2.5, the vibrational width function in Eq. (2.105) can be rewritten as

$$w^2_{\text{vib}}(t) = \frac{\hbar^2}{Mk_BT}\Lambda_{\text{vib}}(T)(1-\eta_{\text{vib}}(t)), \tag{2.108}$$

where $\Lambda_{\text{vib}}(T)$ represents the temperature-dependent Debye-Waller coefficient of the vibrational part:

$$\Lambda_{\text{vib}}(T) = \int_{-\infty}^{\infty} P_{\text{vib}}(\omega)\mathrm{d}\omega, \tag{2.109}$$

and

$$\eta_{\text{vib}}(t) = \frac{1}{\Lambda_{\text{vib}}(T)}\int_{-\infty}^{\infty} P_{\text{vib}}(\omega)\exp(i\omega t)\mathrm{d}\omega, \tag{2.110}$$

with

$$P_{\text{vib}}(\omega) = \frac{\rho_{\text{vib}}(\omega)}{\frac{2\hbar\omega}{k_BT}\sinh\left(\frac{\hbar\omega}{2k_BT}\right)}\exp\left(\frac{\hbar\omega}{2k_BT}\right). \tag{2.111}$$

By following the same phonon expansion method as in Section 2.2.5, the vibrational scattering function $S_{\text{vib}}(Q,\omega)$ is given by:

$$S_{\text{vib}}(Q,\omega) = \frac{1}{\hbar}\overline{b^2}\exp\left(-\frac{\hbar^2Q^2}{2Mk_BT}\Lambda_{\text{vib}}(T)\right)\sum_{n=0}^{\infty}\frac{1}{n!}\left(\frac{\hbar^2Q^2}{2Mk_BT}\Lambda_{\text{vib}}(T)\right)^n \mathcal{T}_{\text{vib},n}(\omega), \tag{2.112}$$

where

$$\mathcal{T}_{\text{vib},n}(\omega) = \frac{1}{2\pi}\int_{-\infty}^{\infty}\eta^n_{\text{vib}}(t)\exp(-i\omega t)\mathrm{d}t. \tag{2.113}$$

The vibrational scattering function in Eq. (2.112) can be split into the vibrational

elastic scattering function $S_{\text{vib}}^{\text{el}}(Q,\omega)$ (which corresponds to the $n=0$ term), and the vibrational inelastic scattering function $S_{\text{vib}}^{\text{inel}}(Q,\omega)$ (with $n \geq 1$):

$$S_{\text{vib}}(Q,\omega) = S_{\text{vib}}^{\text{el}}(Q,\omega) + S_{\text{vib}}^{\text{inel}}(Q,\omega). \tag{2.114}$$

For $n=0$,

$$\mathcal{T}_{\text{vib},0}(\omega) = \frac{1}{2\pi}\int_{-\infty}^{\infty} \exp(-i\omega t)\mathrm{d}t = \delta(\omega), \tag{2.115}$$

thus

$$S_{\text{vib}}^{\text{el}}(Q,\omega) = \frac{\delta(\omega)}{\hbar}\overline{b^2}\exp\left(-\frac{\hbar^2 Q^2}{2Mk_BT}\Lambda_{\text{vib}}(T)\right). \tag{2.116}$$

The vibrational elastic scattering function $S_{\text{vib}}^{\text{el}}(Q,\omega)$ in Eq. (2.116) has the same form as the incoherent elastic scattering function for solid crystalline materials (Eq. (2.54)), except for the scattering length. This difference indicates that the incoherent approximation is applied only to the inelastic scattering for solid crystalline materials while it is adopted to both elastic and inelastic scattering for liquid materials. Therefore, the scattering function can be calculated separately for each type of atoms in the liquid materials under the incoherent approximation. Hence, the obtained results for monatomic liquid materials can be extended to polyatomic liquid materials.

Based on Eqs. (2.91), (2.114) and (2.116), the recombined scattering function is given by:

$$S(Q,\omega) = \exp\left(-\frac{\hbar^2 Q^2}{2Mk_BT}\Lambda_{\text{vib}}(T)\right)\widetilde{S_{\text{diff}}}(Q,\omega) + \frac{\hbar}{\overline{b^2}}\int_{-\infty}^{\infty}\widetilde{S_{\text{diff}}}(Q,\omega')S_{\text{vib}}^{\text{inel}}(Q,\omega-\omega')\mathrm{d}\omega'. \tag{2.117}$$

The principle of detailed balance for $S(Q,\omega)$ in Eq. (2.117) is satisfied. The DDXS is given by:

$$\frac{\mathrm{d}^2\sigma}{\mathrm{d}\Omega\mathrm{d}E_f} = \sqrt{\frac{E_f}{E}}S(Q,\omega). \tag{2.118}$$

The DDXS can also be rewritten in terms of the dimensionless TSLs $S(\alpha,\beta)$:

$$\frac{\mathrm{d}^2\sigma}{\mathrm{d}\Omega\mathrm{d}E_f} = \frac{\sigma_b}{4\pi k_BT}\sqrt{\frac{E_f}{E}}S(\alpha,\beta), \tag{2.119}$$

with

$$S(\alpha,\beta) = \exp(-\alpha\Lambda_{\text{vib}}(T))\widetilde{S_{\text{diff}}}(\alpha,\beta) + \int_{-\infty}^{\infty}\widetilde{S_{\text{diff}}}(\alpha,\beta')S_{\text{vib}}^{\text{inel}}(\alpha,\beta-\beta')\mathrm{d}\beta', \tag{2.120}$$

where

$$\widetilde{S_{\text{diff}}}(\alpha,\beta) = \frac{2c\zeta_{\text{diff}}\alpha}{\pi}\exp\left(2c^2\zeta_{\text{diff}}\alpha-\beta/2\right)\frac{\sqrt{c^2+1/4}}{\sqrt{\beta^2+4c^2\zeta_{\text{diff}}^2\alpha^2}}K_1\left(\sqrt{c^2+1/4}\sqrt{\beta^2+4c^2\zeta_{\text{diff}}^2\alpha^2}\right), \tag{2.121}$$

and

$$S_{\text{vib}}^{\text{inel}}(\alpha,\beta) = \exp(-\alpha\Lambda_{\text{vib}}(T)) \sum_{n=1}^{N_{\text{phonon}}} \frac{1}{n!}(\alpha\Lambda_{\text{vib}}(T))^n \mathcal{T}_{\text{vib},n}(\beta). \tag{2.122}$$

2.3.3. Phonon density of states of hydrogen bound in the water molecule calculated by molecular dynamics code GROMACS

To determine the scattering function $S(Q,\omega)$ for liquid materials under the incoherent and Gaussian approximations, the separation of the diffusive scattering function $S_{\text{diff}}(Q,\omega)$ and vibrational scattering function $S_{\text{vib}}(Q,\omega)$ presented in Section 2.3.2 enables to circumvent the difficulty of directly determining the eigen-frequency function. The Egelstaff-Schofield diffusion model presented in Section 2.3.2 provides an analytical formula of $S_{\text{diff}}(Q,\omega)$, parameterized in terms of diffusion coefficient D and diffusive weight ζ_{diff}. $S_{\text{vib}}(Q,\omega)$ can be calculated from the VDOS $\rho_{\text{vib}}(\omega)$ of the liquid, with the phonon expansion method presented in Section 2.3.2. These parameters can be obtained from theoretical models and/or experimental results.

In this work, special attention is given to the PDOS of hydrogen bound in the water molecule (H in H_2O). The investigation of the PDOS of H in H_2O is based on the CAB model whose description is detailed in Refs. (J. I. Marquez Damian, D. C. Malaspina, and J. R. Granada 2013; Márquez Damián, J. Granada, and D. Malaspina 2014). In the CAB model, the diffusive weight ζ_{diff} is obtained from literature. The other parameters will be computed from MD calculations by using the MD code `GROMACS` (Van Der Spoel, Lindahl, Hess, et al. 2005) with the TIP4P/2005f potential for water (González and Abascal 2011).

The main steps are summarized in this part. A detail description can be found in Ref. (Márquez Damián, J. Granada, and D. Malaspina 2014). First of all, the trajectory file which includes the positions and velocities of H in H_2O is obtained from `GROMACS` calculations. Then, the VACF of H in H_2O is computed by:

$$\text{VACF}(\tau) = \langle \vec{v}(t)\cdot\vec{v}(t+\tau)\rangle, \tag{2.123}$$

where $\vec{v}(t)$ represents the velocity vector of H in H_2O at time t, and $\langle . \rangle$ is the average over all hydrogen atoms in the trajectory file.

The generalized PDOS or generalized frequency spectrum of H in H_2O obtained by MD calculations $\rho_{\text{MD}}(\omega)$ can thus be computed by performing the cosine transform to the VACF:

$$\rho_{\text{MD}}(\omega) = \frac{2M}{3\pi k_B T}\int_0^\infty \text{VACF}(\tau)\cos(\omega\tau)d\tau. \tag{2.124}$$

The generalized PDOS $\rho_{\text{MD}}(\omega)$ is composed of the diffusive PDOS and VDOS:

$$\rho_{\text{MD}}(\omega) = \rho_{\text{diff}}(\omega) + \rho_{\text{vib}}(\omega). \tag{2.125}$$

It should be noticed that the integral of the diffusive PDOS $\rho_{\text{diff}}(\omega)$ over the whole

range of ω is equal to the diffusive weight ζ_{diff} and that of the VDOS is equal to the vibrational weight ζ_{vib} as indicated in Eqs. (2.104) and (2.106). Hence, if the diffusive PDOS and the VDOS are pre-normalized to 1 for practical purposes, Eq. (2.125) can be written as:

$$\rho_{\text{MD}}(\omega) = \zeta_{\text{diff}}\rho_{\text{diff}}^{\text{norm}}(\omega) + \zeta_{\text{vib}}\rho_{\text{vib}}^{\text{norm}}(\omega). \tag{2.126}$$

Based on Eq. (2.104), the diffusion coefficient D is given by:

$$D = \frac{\pi k_B T \rho_{\text{diff}}(0)}{2M}. \tag{2.127}$$

Since $\rho_{\text{vib}}(\omega)$ varies as ω^2 as ω goes to zero, then $\rho_{\text{vib}}(0) = 0$. Eq.(2.127) can be rewritten as:

$$D = \frac{\pi k_B T \rho_{\text{MD}}(0)}{2M}. \tag{2.128}$$

The generalized PDOS of H in H_2O at 300 K is presented in Fig. 2.5. At 300 K, the diffusive weight ζ_{diff} is fixed to 0.008605 according to Ref. (Márquez Damián, J. Granada, and D. Malaspina 2014). The diffusive PDOS can thus be determined according to Eq. (2.104), as well as the VDOS. They are also presented in Fig. 2.5 for illustration. These PDOSs are given as a function of the energy transfer $\varepsilon = E_f - E = -\hbar\omega$.

The description of water dynamics can be split into two parts : diffusive dynamics and vibrational dynamics (Amann-Winkel, Marie-Claire Bellissent-Funel, Bove, et al. 2016). The contribution of the diffusive motion to the generalized PDOS $\rho_{\text{MD}}(\varepsilon)$ is dominant in the nearby of zero energy transfer of neutrons, as indicated in the bottom plot of Fig. 2.5. For the CAB model, the diffusive dynamics are represented by the Egelstaff-Schofield diffusion model detailed in Section 2.3.2.

The contribution to $\rho_{\text{vib}}(\varepsilon)$ is due to the vibrational dynamics. Below 150 meV, the contribution comes mainly from intermolecular motions. The peak at around 6 meV (indicated in the bottom plot of Fig. 2.5) is observed by different experimental techniques such as incoherent neutron scattering and Raman spectroscopies (Ohmine and Saito 1999). The peak at around 6 meV and the shoulder-like region from 20 to 40 meV are attributed to hydrogen bond (HB) bending and stretching modes whose contribution (green dotted line) is well reproduced by the calculations of Lerbret et al. (Lerbret, Hédoux, Annighöfer, et al. 2013). However, their microscopic origin is the subject of debates in the literature(Joan Àngel Padró and Martí 2003; De Santis, Ercoli, and Rocca 2004; Joań Àngel Padró and Martí 2004). The intense band from 50 to 130 meV is due to the librational motion of water molecules. For energy range above 150 meV, the contribution to $\rho_{\text{vib}}(\omega)$ comes from intramolecular motions. The band at around 200 meV represents the O-H bending. The two bands near 400 meV are due to the O-H stretching.

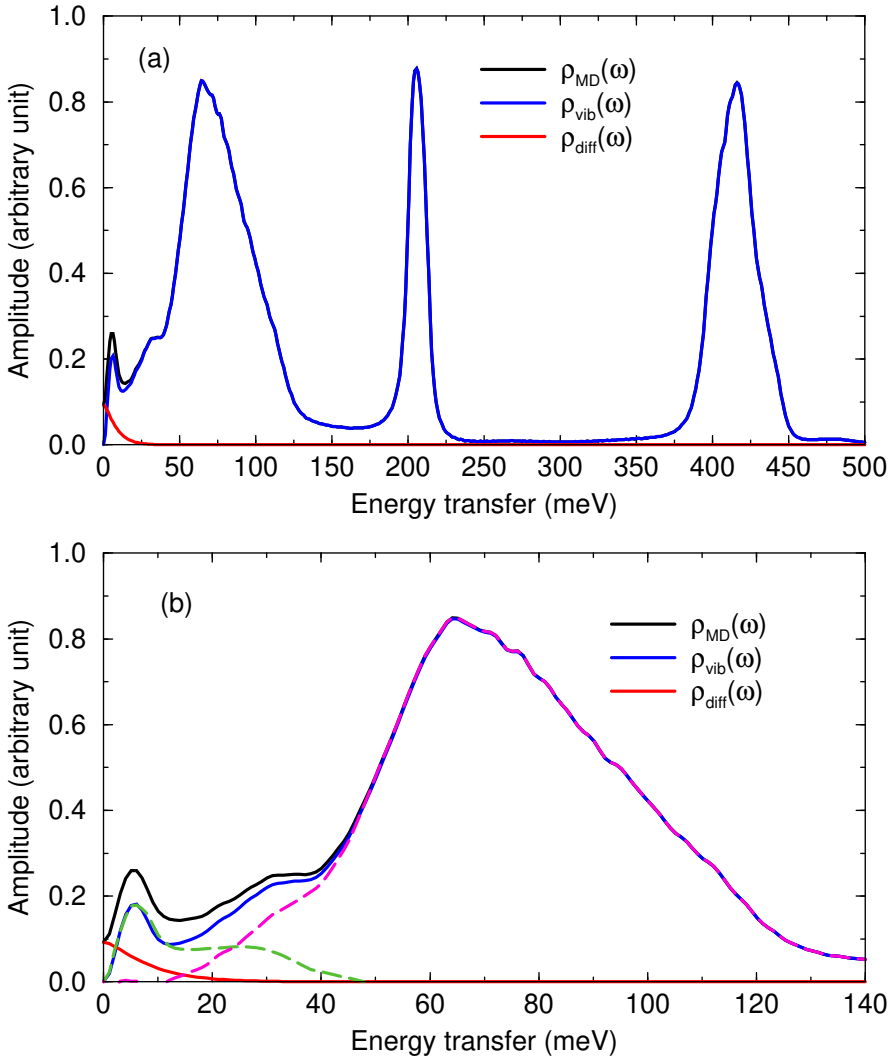

Figure 2.5.: Top plot presents generalized PDOS $\rho_{\mathrm{MD}}(\varepsilon)$, diffusive PDOS $\rho_{\mathrm{diff}}(\varepsilon)$ and VDOS $\rho_{\mathrm{vib}}(\varepsilon)$ for H in H_2O at 300 K of CAB model (Márquez Damián, J. Granada, and D. Malaspina 2014). $\varepsilon \equiv E_f - E = -\hbar\omega$ represents the energy transfer of neutrons. $\rho_{\mathrm{MD}}(\varepsilon)$ is obtained from MD calculations. $\rho_{\mathrm{diff}}(\varepsilon)$ and $\rho_{\mathrm{vib}}(\varepsilon)$ are calculated with diffusive weight $\zeta_{\mathrm{diff}} = 0.008605$ from CAB model. Bottom plot is a zoom of the top plot for low energy part. Dotted lines separate the contribution of the broad librational band to the hydrogen bond bending and stretching modes (Lerbret, Hédoux, Annighöfer, et al. 2013).

2.3.4. Random jump diffusion and rotational diffusion corrections to liquid water

The particularity of liquid water is the presence of HB. HB and the related local tetrahedral structure directly affect the water diffusion dynamics at the molecular level (Amann-Winkel, Marie-Claire Bellissent-Funel, Bove, et al. 2016). The water diffusion dynamics can be interpreted by the coupling of translational and rotational diffusion motions. Therefore, due to the presence of HB, a translational and a rotational corrections are to be applied to the Egelstaff-Schofield diffusion model presented in Section 2.3.2.

In the nearby of the quasi-elastic peak, Q and ω tend to zero. Since $K_1(x) \sim 1/x$ for $x \to 0$, the diffusive scattering function $\widetilde{S_{\text{diff}}}(Q,\omega)$ in formula (2.103) can be approximated by:

$$\widetilde{S_{\text{diff}}}(Q,\omega) = \frac{\overline{b^2}}{\hbar}\frac{1}{\pi}\frac{\Gamma(Q)}{\omega^2+\Gamma(Q)^2}, \tag{2.129}$$

where $\Gamma(Q) = DQ^2$.

Eq. (2.129) indicates that in the quasi-elastic region, $\widetilde{S_{\text{diff}}}(Q,\omega)$ is a Lorentzian with a HWHM $\Gamma(Q)$ equal to DQ^2. The linearity of $\Gamma(Q)$ with Q^2 is strictly valid for a system where Fick's law is satisfied (Márquez Damián, J. Granada, Cantargi, et al. 2016). In the case of liquid water, the movements of the molecules are non-continuous, and the non-linearity of $\Gamma(Q)$ with Q^2 can be easily observed in inelastic neutron scattering experiments. The mechanism of this behavior is still under discussion and it exists different models in the literature (Singwi and Alf Sjölander 1960; Hall and Ross 1981; Teixeira, M.-C. Bellissent-Funel, Chen, et al. 1985; González Sánchez, Jurányi, Gimmi, et al. 2008; Qvist, Schober, and Halle 2011).

In this work, a RJD model is investigated for the translational correction of the Egelstaff-Schofield diffusion model, in which an analytical non-linear equation of $\Gamma(Q)$ is given by:

$$\Gamma(Q) = \frac{DQ^2}{1+DQ^2\tau_0}, \tag{2.130}$$

where τ_0 is the residence time between jumps.

In this case, the Egelstaff-Schofield diffusion model with RJD correction becomes:

$$\begin{aligned} S_{\text{RJD, diff}}(Q,\omega) = &\frac{\overline{b^2}}{k_BT}\frac{\hbar D(Q)Q^2}{\pi k_BT}\exp\left(\frac{MD(Q)^2Q^2}{\zeta_{\text{diff}}k_BT}+\frac{\hbar\omega}{2k_BT}\right)\times \\ &\frac{\sqrt{c(Q)^2+1/4}}{\frac{\hbar}{k_BT}\sqrt{\omega^2+(D(Q)Q^2)^2}}K_1\left(\frac{\hbar}{k_BT}\sqrt{c(Q)^2+1/4}\sqrt{\omega^2+(D(Q)Q^2)^2}\right), \end{aligned} \tag{2.131}$$

with

$$D(Q) = \frac{D}{1+DQ^2\tau_0}, \tag{2.132}$$

and

$$c(Q) = \frac{MD(Q)}{\hbar\zeta_{\text{diff}}}. \tag{2.133}$$

Eqs. (2.132) and (2.133) enable to obtain a jump diffusion correction for Eqs. (2.102) and (2.104), respectively.

In this work, a rotational correction is also applied to the diffusion model. The rotational diffusion scattering function $S_{\text{rot, diff}}(Q,\omega)$ is obtained though the Sears expansion (Sears 1966):

$$S_{\text{rot, diff}}(Q,\omega) = j_0^2(Qa)\delta(\omega) + \frac{1}{\pi}\sum_{n=1}^{\infty}(2n+1)j_n^2(Qa)\frac{n(n+1)(\hbar/6\tau_r)}{\omega^2 + (n(n+1)(\hbar/6\tau_r))^2} \tag{2.134}$$

where a is the radius of the molecular rotation which is fixed to the O-H distance, $j_l(Qa)$ represents the spherical Bessel function of order l and τ_r is the rotational relaxation time.

The scattering function of Egelstaff-Schofield diffusion model with translational and rotational corrections is obtained by convoluting $S_{\text{RJD, diff}}(Q,\omega)$ and $S_{\text{rot, diff}}(Q,\omega)$ as follows:

$$S_{\text{diff}}^{\text{corr}}(Q,\omega) = \int_{-\infty}^{\infty} S_{\text{RJD, diff}}(Q,\omega')S_{\text{rot, diff}}(Q,\omega-\omega')\mathrm{d}\omega'. \tag{2.135}$$

2.4. Scattering models for free gas materials

The momentum transfer $\hbar\vec{Q}$ and the energy transfer $\hbar\omega$ are large when neutrons scatter with free gas particles. Hence, the interaction time is short and the time dependent Heisenberg operator $\vec{\boldsymbol{R}}(t)$ which represents the position of the particle in the intermediate function (Eq. (2.4)) can be approximated by its first order term (Tammar et al. 2000):

$$\vec{\boldsymbol{R}}(t) = \vec{\boldsymbol{R}}(0) + \vec{v}t, \tag{2.136}$$

where $\vec{v}$ is the speed of the particle.

Since there is no inter-particle interaction for a free gas material, the incoherent approximation is automatically valid. Thus, only the self intermediate function $\langle j, j\rangle_s$ is considered and it is given by:

$$\langle j, j\rangle_s = \langle \exp\left(i\vec{Q}\cdot\vec{v}t\right)\rangle. \tag{2.137}$$

The free gas material is assumed to be monatomic. From the statistical point of view, the speeds of the free gas atoms $\vec{v}$ follow the M-B distribution with:

$$\vec{v} \propto \exp\left(-v^2/v_p^2\right), \tag{2.138}$$

where $v_p^2 = 2k_BT/M$ is the square of the most probable speed, T represents the temperature of the gas and M is the mass of the gas atom.

By replacing the M-B distribution (Eq. (2.138)) in Eq. (2.137), the intermediate

function for monatomic free gas is given by:

$$\langle j,\, j\rangle_s = \frac{\int_{-\infty}^{\infty} \exp\left(-v^2/v_p^2\right) \exp\left(i\vec{Q}\cdot\vec{v}\,t\right) \mathrm{d}\vec{v}}{\int_{-\infty}^{\infty} \exp\left(-v^2/v_p^2\right) \mathrm{d}\vec{v}}, \tag{2.139}$$

$$= \frac{\int_{-\infty}^{\infty} \exp\left(-v^2/v_p^2\right) \exp(iQvt)\mathrm{d}v}{\int_{-\infty}^{\infty} \exp\left(-v^2/v_p^2\right) \mathrm{d}v}. \tag{2.140}$$

Thanks to the Gaussian integral property $\int_{-\infty}^{\infty} \exp\left(-x^2\right) dx = \sqrt{\pi}$ and the Fourier transform of the Gaussian function $\int_{-\infty}^{\infty} \exp\left(-x^2/(2a^2)\right) \exp(-ibx)dx = a\sqrt{2\pi}\exp\left(-a^2b^2/2\right)$, Eq. (2.140) can be rewritten as:

$$\langle j,\, j\rangle_s = \exp\left(-Q^2 w^2(t)/2\right), \tag{2.141}$$

where $w(t)$ is the width function of the free gas:

$$w(t) = t\sqrt{\frac{k_B T}{M}}. \tag{2.142}$$

$w(t)$ in Eq. (2.142) should be corrected to account for quantum effects (P. Egelstaff 1962; Turner 1961):

$$\widetilde{w}(t) = \sqrt{w^2(t) - \frac{i\hbar}{M}t}. \tag{2.143}$$

Based on Eqs. (2.3), (2.141), (2.142) and (2.143), the normalized scattering function for monatomic free gas can be obtained by:

$$S(Q,\omega) = \frac{1}{\hbar}\overline{b^2}\sqrt{\frac{M}{2\pi k_B T Q^2}} \exp\left(-\frac{M}{2k_B T Q^2}\left(\omega - \frac{\hbar Q^2}{2M}\right)^2\right). \tag{2.144}$$

By putting $-\omega$ in Eq. (2.144), we have:

$$S(Q,-\omega) = \exp\left(-\frac{\hbar\omega}{k_B T}\right) S(Q,\omega), \tag{2.145}$$

thus the principle of the detailed balance (Eq. (2.9)) is satisfied.

The DDXS of monatomic free gas can thus be given by:

$$\frac{\mathrm{d}^2\sigma}{\mathrm{d}\Omega \mathrm{d}E_f} = \sqrt{\frac{E_f}{E}} S(Q,\omega). \tag{2.146}$$

The DDXS can be obtained with the dimensionless $S(\alpha,\beta)$:

$$\frac{\mathrm{d}^2\sigma}{\mathrm{d}\Omega \mathrm{d}E_f} = \frac{\sigma_b}{4\pi k_B T}\sqrt{\frac{E_f}{E}} S(\alpha,\beta), \tag{2.147}$$

with

$$S(\alpha,\beta)=\sqrt{\frac{1}{4\pi\alpha}}\exp\left(-\frac{(\beta+\alpha)^2}{4\alpha}\right). \tag{2.148}$$

The use of the FGM in neutronic calculations is discussed in Section 5.3 and compared with other scattering models in Section 5.4.

2.5. Short collision time approximation

The computations of the inelastic scattering function (Eq. (2.64)) for solid crystalline materials and the vibrational scattering function $S_{\text{vib}}(Q,\omega)$ for liquid materials (Eq. (2.112)) necessitate a large phonon expansion order for large momentum transfer $\hbar Q$ and energy transfer $\hbar\omega$ to ensure the convergence of the sum. To reduce the computational time, the SCT approximation is used in many codes such as the `LEAPR` module of `NJOY` code (Macfarlane, Muir, Boicourt, et al. 2017).

Since the SCT is an approximation of the scattering function for large momentum and energy transfers, only the inelastic scattering is concerned. As analyzed in Section 2.3.2, the harmonic approximation for solid crystalline materials and the Gaussian approximation for liquid materials are equivalent. Therefore, a monatomic liquid material can be assumed to obtain a formula for the SCT approximation.

Based on the incoherent and Gaussian approximations, the vibrational scattering function $S_{\text{vib}}(Q,\omega)$ of the considered monatomic liquid material can be obtained as a function of the vibrational width function $w_{\text{vib}}(t)$ (Section 2.3.2):

$$S_{\text{vib}}(Q,\omega)=\frac{1}{2\pi\hbar}\overline{b^2}\int_{-\infty}^{\infty}\exp\left(-Q^2w_{\text{vib}}^2(t)/2\right)\exp(-i\omega t)\mathrm{d}t, \tag{2.149}$$

and

$$w_{\text{vib}}^2(t)=\frac{\hbar}{M}\int_0^{\infty}\frac{\rho_{\text{vib}}(\omega)}{\omega}\left(\coth\left(\frac{\hbar\omega}{2k_BT}\right)(1-\cos(\omega t))-i\sin(\omega t)\right)\mathrm{d}\omega. \tag{2.150}$$

For large momentum and energy transfers, the collision time is small compared to the periods of atomic motions. Thus, the trigonometric functions in Eq. (2.150) can be approximated by their Taylor expansions up to the second-order terms in t (Borgonovi 1970), i.e., $\cos(\omega t)\approx 1-\omega^2t^2/2$ and $\sin(\omega t)\approx\omega t$, then:

$$w_{\text{vib}}^2(t)=\frac{\hbar}{M}\int_0^{\infty}\frac{\rho_{\text{vib}}(\omega)}{\omega}\left(\coth\left(\frac{\hbar\omega}{2k_BT}\right)\frac{\omega^2t^2}{2}-i\omega t\right)\mathrm{d}\omega, \tag{2.151}$$

$$=\frac{\hbar}{M}\left(\frac{t^2}{2}\int_0^{\infty}\omega\rho_{\text{vib}}(\omega)\coth\left(\frac{\hbar\omega}{2k_BT}\right)\mathrm{d}\omega-it\int_0^{\infty}\rho_{\text{vib}}(\omega)\mathrm{d}\omega\right). \tag{2.152}$$

The effective temperature T_{eff} is defined by (Borgonovi 1970; Macfarlane, Muir,

Boicourt, et al. 2017):

$$T_{\text{eff}} \equiv \frac{\hbar}{2k_B\zeta_{\text{vib}}}\int_0^\infty \omega\rho_{\text{vib}}(\omega)\coth\left(\frac{\hbar\omega}{2k_BT}\right)\mathrm{d}\omega. \tag{2.153}$$

Based on Eq. (2.106), the integral of the VDOS is equal to the vibrational weight ζ_{vib}. Then the vibrational width function in Eq. (2.152) can be given by:

$$w^2_{\text{vib}}(t) = \zeta_{\text{vib}}\left(\frac{k_BT_{\text{eff}}}{M}t^2 - \frac{i\hbar}{M}t\right). \tag{2.154}$$

By inserting the vibrational width function $w_{\text{vib}}(t)$ (Eq. (2.154)) in Eq. (2.149) and by applying the Fourier transform to the Gaussian function, the vibrational scattering function based on the SCT approximation is given by:

$$S_{\text{vib}}(Q,\omega) = \frac{1}{\hbar}\overline{b^2}\sqrt{\frac{M}{2\pi\zeta_{\text{vib}}k_BT_{\text{eff}}Q^2}}\exp\left(-\frac{M}{2\zeta_{\text{vib}}k_BT_{\text{eff}}Q^2}\left(\omega-\frac{\zeta_{\text{vib}}\hbar Q^2}{2M}\right)^2\right). \tag{2.155}$$

The principle of the detailed balance in Eq. (2.155) is violated. Since the SCT approximation is dedicated to large momentum and energy transfers in which the up-scattering is negligible, the vibrational scattering function $S_{\text{vib}}(Q,\omega)$ in Eq. (2.155) becomes:

$$\widetilde{S_{\text{vib}}}(Q,\omega) = \begin{cases} S_{\text{vib}}(Q,\omega) & \text{if } \omega \geq 0 \\ \exp\left(\dfrac{\hbar\omega}{k_BT}\right)S_{\text{vib}}(Q,-\omega) & \text{if } \omega < 0 \end{cases}. \tag{2.156}$$

Eq. (2.156) can be rewritten in a compact form:

$$\widetilde{S_{\text{vib}}}(Q,\omega) = \frac{1}{\hbar}\overline{b^2}\sqrt{\frac{M}{2\pi\zeta_{\text{vib}}k_BT_{\text{eff}}Q^2}}\exp\left(-\frac{M}{2\zeta_{\text{vib}}k_BT_{\text{eff}}Q^2}\left(|\omega|-\frac{\zeta_{\text{vib}}\hbar Q^2}{2M}\right)^2+\frac{\hbar}{2k_BT}(\omega-|\omega|)\right). \tag{2.157}$$

The SCT enables to compute the vibrational scattering function $\widetilde{S_{\text{vib}}}(Q,\omega)$ by using an analytical formula, which reduces the computational time. For liquid materials, the diffusive behavior is essential and the recombined scattering function $S(Q,\omega)$ can be obtained by convoluting the diffusive and vibrational scattering functions as follows:

$$S(Q,\omega) = \frac{\hbar}{\overline{b^2}}\int_{-\infty}^{\infty}\widetilde{S_{\text{diff}}}(Q,\omega')\widetilde{S_{\text{vib}}}(Q,\omega-\omega')\mathrm{d}\omega', \tag{2.158}$$

where $\widetilde{S_{\text{diff}}}(Q,\omega')$ is the diffusive scattering function based on Egelstaff-Schofield diffusion model presented in Section 2.3.2.

The DDXS can be obtained by:

$$\frac{\mathrm{d}^2\sigma}{\mathrm{d}\Omega\mathrm{d}E_f} = \sqrt{\frac{E_f}{E}}S(Q,\omega) \tag{2.159}$$

and in terms of $S(\alpha, \beta)$:

$$\frac{\mathrm{d}^2\sigma}{\mathrm{d}\Omega \mathrm{d}E_f} = \frac{\sigma_b}{4\pi k_B T} S(\alpha, \beta), \tag{2.160}$$

where

$$S(\alpha, \beta) = \int_{-\infty}^{\infty} \widetilde{S_{\mathrm{diff}}}(\alpha, \beta') \widetilde{S_{\mathrm{vib}}}(\alpha, \beta - \beta') \mathrm{d}\beta', \tag{2.161}$$

with

$$\widetilde{S_{\mathrm{vib}}}(\alpha, \beta) = \sqrt{\frac{1}{4\pi\zeta_{\mathrm{vib}}\alpha T_{\mathrm{eff}}/T}} \exp\left(-\frac{(|\beta| - \zeta_{\mathrm{vib}}\alpha)^2}{4\zeta_{\mathrm{vib}}\alpha T_{\mathrm{eff}}/T} - \frac{\beta + |\beta|}{2}\right). \tag{2.162}$$

Since the incoherent approximation is assumed, the SCT approximation (Eq. (2.162)) can be extended to polyatomic materials. Note that for a material approximated by a free gas, its PDOS is a Dirac function (P. A. Egelstaff and Schofield 1962). By inserting a Dirac function and $\zeta_{\mathrm{vib}} = 1$ in Eq. (2.153), the effective temperature is equal to the thermodynamic temperature of material:

$$T_{\mathrm{eff}} = \frac{\hbar}{2k_B} \int_0^{\infty} \omega\delta(\omega) \coth\left(\frac{\hbar\omega}{2k_B T}\right) \mathrm{d}\omega = T. \tag{2.163}$$

Then by replacing $T_{\mathrm{eff}} = T$ and $\zeta_{\mathrm{vib}} = 1$ in Eq. (2.162), we obtain the same formula as for free gas (cf. Eq. (2.148)). The use of the SCT formalism in neutronic calculations will be discussed in Section 5.4.

2.6. Preliminary conclusions

This chapter is dedicated to present the theory of low energy neutron scattering. As presented in Section 2.1, the neutron-nucleus scattering can be described via the double differential neutron scattering cross section, which can be obtained from the scattering function $S(\vec{Q}, \omega)$. Considering the correlations among isotopes, the scattering function can be further decomposed as a coherent and an incoherent parts. These formalisms are valid for different types of materials. Based on the general formalisms, scattering models are given respectively for solid crystalline, liquid and free gas materials in Sections 2.2, 2.3 and 2.4. The PDOS is the key ingredient to determine the scattering function. The PDOS of uranium dioxide presented in Section 2.2.6 is obtained by first-principles calculations. The PDOS of hydrogen bound in water molecule (H in H_2O) presented in Section 2.3.3 is calculated with MD method. These PDOSs are presented for illustration. To reduce the computational time compared to the phonon expansion method, the SCT approximation is presented in Section 2.5.

3. Data processing tool CINEL

Summary

This chapter presents the data processing tool CINEL. CINEL has been developed to calculate the coherent and incoherent elastic neutron scattering cross sections of solid crystalline materials within the cubic approximation (cf. Eq. (2.23)). The module implemented to fulfill this task is called Cubic. A second module named INELastic has been implemented to calculate the TSLs $S(\alpha, \beta)$ by taking into account graphics processing unit (GPU) accelerations.

In Section 3.1, some widely used codes or platforms capable of computing the coherent and incoherent elastic cross sections and $S(\alpha, \beta)$ are outlined. The CINEL code is presented in Section 3.2. The numerical validations of CINEL by mainly using some solid crystalline materials are presented in Section 3.3. The results provided by CINEL are compared to those available in the ENDF/B-VIII.0 database (D. Brown, Chadwick, Capote, et al. 2018) and the NJOY-NCrystal library (Ramic, Jose Ignacio Marquez Damian, Thomas Kittelmann, et al. 2021). Preliminary conclusions are given in the last section.

3.1. Overview of data processing codes

TSLs which take into account the atomic motions of bound isotopes in materials can be computed by a few codes: the LEAPR module (MacFarlane 1994) of NJOY code (Macfarlane, Muir, Boicourt, et al. 2017), the SAB module (Jaiswal 2018) of GAIA code (Ferran, Haeck, and Gonin 2014), the Monte-Carlo based library NCrystal (Cai, T. Kittelmann, Klinkby, et al. 2019; Cai and T. Kittelmann 2020), the OCLIMAX platform (Cheng, Daemen, Kolesnikov, et al. 2019; Cheng and Ramirez-Cuesta 2020) and the full law analysis scattering system hub (FLASSH) (Zhu and Ayman I Hawari 2018).

LEAPR (MacFarlane 1994) is a module integrated in the nuclear data processing system NJOY (Macfarlane, Muir, Boicourt, et al. 2017) which is developed at Los Alamos National Laboratory. The LEAPR module, written in Fortran, is based on the British code LEAP+ADDELT. LEAPR enables to generate the TSLs for various types of materials in ENDF-6 format (Trkov and D. A. Brown 2018). The models rely on the harmonic or Gaussian, incoherent and cubic approximations (cf. Chapter 2). In addition, to reduce the computational time and/or for coding convenience, the SCT approximation (Section 2.5) and the atom site approximation in which the MSD are the same for different types of atoms in the same material, are also adopted in LEAPR.

SAB (Jaiswal 2018) is a module of a nuclear data processing code GAIA (Ferran, Haeck, and Gonin 2014) which is developed at *Institut de Radioprotection et de Sûreté Nucléaire* (IRSN). SAB has been developed to ease the generation of TSLs. The TSLs formalism implemented in the GAIA code is close to the LEAPR formalism.

NCrystal (Cai, T. Kittelmann, Klinkby, et al. 2019; Cai and T. Kittelmann 2020) is a Monte-Carlo based library developed at the European Spallation Source. The NCrystal library, written in C++, was originally designed to be used with the Monte-Carlo packages such as Geant4 (Allison, Amako, Apostolakis, et al. 2016) and McStas (Willendrup and Lefmann 2020). The harmonic or Gaussian, incoherent and cubic approximations (cf. Chapter 2) are employed in NCrystal. TSLs in ENDF-

6 format are not directly produced by NCrystal. They can be obtained by linking NCrystal and LEAPR (J.-I. M. Damian n.d.). The combination of these two codes allows to produce TSLs for many crystal structures. The atom site approximation was removed in LEAPR+NCrystal, because the MSD of a given atom can be computed in NCrystal from its PDOS.

OCLIMAX (Cheng, Daemen, Kolesnikov, et al. 2019; Cheng and Ramirez-Cuesta 2020) is a platform developed at Oak Ridge National Laboratory for inelastic neutron scattering simulations of solid crystalline and single-crystal materials. Compared to LEAPR and NCrystal, the OCLIMAX platform improves the calculations of the scattering functions or dynamic structure factors $S(\vec{Q}, \omega)$, by introducing the coherent one-phonon correction (Squires 2012) to the incoherent approximation and eliminating the cubic approximation. On one hand, the improvement of the coherent one-phonon correction is that the coherent effects of inelastic scattering are approximately calculated by the first term of the phonon expansion expressions, instead of being completely neglected within the incoherent approximation. On the other hand, the elimination of the cubic approximation allows to compute the MSD as a 3×3 matrix in which the anisotropic atomic motions along x, y, z directions are presented. The computation of the coherent one-phonon correction and the MSD matrix necessitate respectively the phonon dispersion relations and the partial PDOS. These physical qualities can be obtained by using the VASP (Kresse and Furthmüller 1996b; Kresse and Furthmüller 1996a) and PHONONPY (Togo and Tanaka 2015) codes.

FLASSH (Zhu and Ayman I Hawari 2018) is a code system developed by the Low Energy Interaction Physics group at North Carolina State University. The coherent one-phonon correction is adopted and the cubic approximation is eliminated in the FLASSH code system. Multiple programming languages are used such as Fortran, Python and C++ in different modules of FLASSH.

We started to develop CINEL because most of these systems were not available or mature at the beginning of our work.

3.2. Implementation of CINEL

The data flow presenting the generation of the TSLs in ENDF-6 format by CINEL is shown in Fig. 3.1. To generate the TSLs, various physical quantities are needed. The input files of CINEL are then separated in five different inputs: scattering length, positions of atom in the unit cell (only for solid crystalline materials), α and β grids, general settings and temperature-dependent parameters.

As mentioned before, CINEL consists of two modules Cubic and INELastic. Cubic calculates the Debye-Waller coefficients $\Lambda(T)$ and the coherent elastic scattering cross sections $\sigma^{\mathrm{el}}_{\mathrm{coh}}(E)$. $\Lambda(T)$ is computed from the PDOS (cf. Eq. (2.27)) since the cubic approximation is assumed. $\sigma^{\mathrm{el}}_{\mathrm{coh}}(E)$ is calculated by directly looping through the indexes hkl until the interplanar distance d_{hkl} of the corresponding plan is smaller than 0.1 Å. The default threshold value is chosen to be 0.1 Å because the contribution from plans with $d_{hkl} < 0.1$ Å to $\sigma^{\mathrm{el}}_{\mathrm{coh}}(E)$ can be neglected, as discussed in Ref. (Cai and

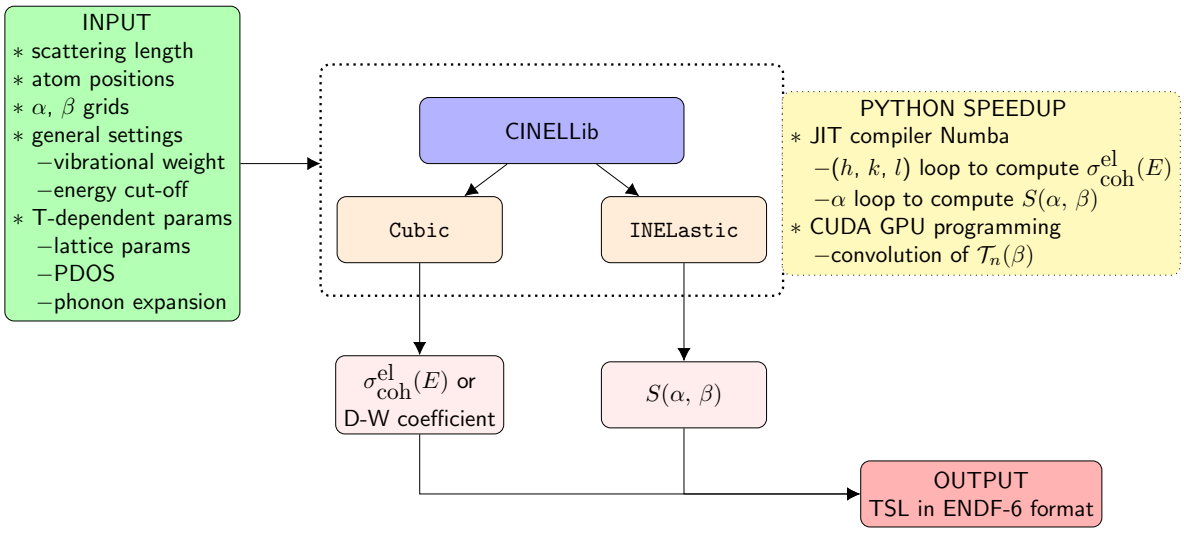

Figure 3.1.: Data flow presenting the generation of the thermal scattering laws in ENDF-6 format by CINEL.

T. Kittelmann 2020). Nonetheless, the threshold value can always be modified by the users. During the loop over hkl, plans with identical interplanar distance d_{hkl} and form factor $|F(\tau_{hkl})|$ are grouped together since they contribute equally to $\sigma^{el}_{coh}(E)$ (Eq. (2.51)). The number of identical plans (hkl) is referred to multiplicity M_{hkl}. These physical quantities are calculated by CINEL and stored in ascii file, as illustrated in Fig. 3.2. The diffraction angle θ_{hkl} can be determined when the incident neutron energy is provided (Eq. (2.48)). The orientation angle can be obtained if the preferred orientation of crystal is given in input. These two quantities are optional.

The INELastic module calculates the $S(\alpha, \beta)$ tables with the phonon expansion method. The Egelstaff-Schofield diffusion model and the recombination of the diffusive and vibrational parts are also implemented in INELastic. Physical constants such as Boltzmann constant and common functions used by Cubic and INELastic are available via the library CINELLib.

Table 3.1.: Comparison of the computational time of the TSLs of H in H_2O at room temperature with a phonon expansion order $N_{phonon} = 2000$.

	CPU	GPU K20	GPU K6000
GPU memory (gigabyte)	N/A	2	12
CUDA cores	N/A	384	2280
Computational time	~ 3 h	~ 15 min	< 2 min

CINEL is developed in Python by using JupyterLab (Granger and Grout 2016). JupyterLab is a new generation of user interface (Kluyver, Ragan-Kelley, Pérez, et al. 2016)

Multiplicity_UO2_298K.dat 〉 No Selection

1	1	0	0	5.46910	5.20849	90.00000	0.00000	6	6.8372889320e-04	0.0000000000e+00
2	1	1	0	3.86724	7.36846	90.00000	0.00000	12	1.3674577864e-03	0.0000000000e+00
3	1	1	1	3.15759	9.02760	54.73561	11.22064	8	2.0511866796e-03	5.9058119823e-03
4	2	0	0	2.73455	10.42779	90.00000	1.50106	6	2.7349155728e-03	5.1315863925e-04
5	2	1	0	2.44586	11.66266	90.00000	0.00000	24	3.4186444660e-03	0.0000000000e+00
6	2	1	1	2.23275	12.78024	65.90516	0.00000	24	4.1023733592e-03	0.0000000000e+00
7	2	2	0	1.93362	14.76761	90.00000	61.10716	12	5.4698311456e-03	2.9543439887e-02
8	3	0	0	1.82303	15.66888	90.00000	0.00000	30	6.1535600388e-03	0.0000000000e+00
9	3	1	0	1.72948	16.52222	90.00000	0.00000	24	6.8372889320e-03	0.0000000000e+00
10	3	1	1	1.64900	17.33471	72.45160	10.92040	24	7.5210178252e-03	9.0050540303e-03
11	2	2	2	1.57879	18.11185	54.73561	1.26397	8	8.2047467184e-03	3.3263522129e-04
12	3	2	0	1.51686	18.85803	90.00000	0.00000	24	8.8884756116e-03	0.0000000000e+00
13	3	2	1	1.46168	19.57678	74.49864	0.00000	48	9.5722045048e-03	0.0000000000e+00
14	4	0	0	1.36728	20.94320	90.00000	58.19803	6	1.0939662291e-02	9.9479194567e-03
15	4	1	0	1.32645	21.59537	90.00000	0.00000	48	1.1623391184e-02	0.0000000000e+00
16	4	1	1	1.28908	22.22931	76.36698	0.00000	36	1.2307120078e-02	0.0000000000e+00
17	3	3	1	1.25470	22.84654	76.73732	10.62820	24	1.2990848971e-02	6.6684827463e-03
18	4	2	0	1.22293	23.44836	90.00000	1.05556	24	1.3674577864e-02	6.4552440598e-04
19	4	2	1	1.19346	24.03596	77.39562	0.00000	48	1.4358306757e-02	0.0000000000e+00

Figure 3.2.: Screenshot of cross section file generated by the Cubic module of CINEL for uranium dioxide at 298 K. Columns 1 to 10 represent respectively: index h, k, l, interplanar distance d_{hkl} (in Å), diffraction angle θ_{hkl} (in degree), orientation angle (in degree), form factor square $|F(\tau_{hkl})|^2$ (in barn), multiplicity M_{hkl}, Bragg Edge E_{hkl} (in eV) and $E_{hkl}\sigma^{\text{el}}_{\text{coh}}(E_{hkl})$ (in eV.barn), which serve as calculations and verifications of the coherent elastic cross sections.

which is an open-source tool enabling to mix live code, texts, mathematical equations and interactive graphics. An example of JupyterLab interface is given in Fig. 3.3 for illustration. This interactive development environment facilitates the verification and visualization of the results.

To improve the performance of CINEL, a Just-in-Time (JIT) compiler named Numba (Lam, Pitrou, and Seibert 2015) is used. Numba allows to reduce the computational time by directly adding simple Python syntaxes to the initial functions without rewriting them in low-level languages. In addition, Numba supports Compute Unified Device Architecture (CUDA) GPU programming, which enables CINEL to benefit from the powerful computing capability of GPU.

GPU programming, has been introduced in the early 2000s and has been developed tremendously during the last two decades. In our work, the use of GPU enables to accelerate the phonon expansion calculation. To test the speedup with GPU, the TSLs of hydrogen bound in water molecule (H in H_2O) at room temperature were calculated with a phonon expansion order $N_{\text{phonon}} = 2000$. Two kinds of GPU are used: NVIDIA® QUADRO® K620 with 2 gigabyte memory and 384 cores; NVIDIA® QUADRO® K6000 with 12 gigabyte memory and 2880 cores. The comparisons of the computational time are presented in Table 3.1. High performing GPU allows to significantly reduce the computational time down to 2 minutes.

Approximations adopted in codes are summarized in Table 3.2. For strongly coherent crystalline materials such as pyrolytic graphite, the introduction of the coherent one-phonon correction (Squires 2012) to the incoherent approximation enables to better reproduce the experimental inelastic scattering cross sections as shown in Ref. (Al-Qasir 2008). The calculations of one-phonon coherent inelastic scattering

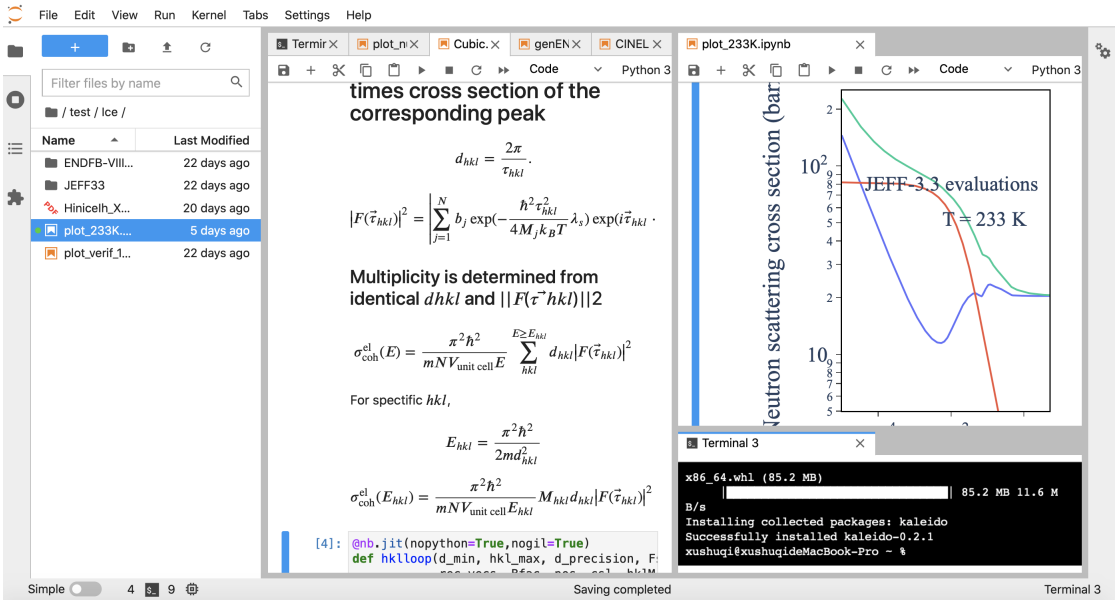

Figure 3.3.: JupyterLab interface. Live code, texts, mathematical equations and interactive graphics are mixed in Jupyter Notebooks which are integrated in JupyterLab together with blocks like terminal and text editor.

function necessitates the dispersion relations of materials. This correction will be implemented in the future version of CINEL. The cubic approximation will also be eliminated since it only necessitates the partial PDOSs which can be calculated by DFT codes.

3.3. Numerical validations of CINEL

The numerical validations of CINEL were performed by comparing the calculated TSLs of solid crystalline materials with the ENDF/B-VIII.0 database and the NJOY-NCrystal library. A few crystal structures were studied: beryllium (^{9}Be) metal (hexagonal close packed (HCP), space group P6$_3$/mmc), iron (^{56}Fe) (body-centered cubic (BCC), space group Im$\bar{3}$m), aluminum (^{27}Al) metal, uranium dioxide (UO_2) and lithium hydride (LiH) (face-centered cubic (FCC), space group Fm$\bar{3}$m), magnetism hydride (MgH_2) and magnetism deuteride (MgD_2) (tetragonal structure, space group P4$_2$/mnm). Ice I$_h$ is also investigated in this work. Inputs for CINEL were prepared by using the physical quantities available in the ENDF/B-VIII.0 database and the NJOY-NCrystal library.

Uranium dioxide (UO_2) is the major component of the UOX fuel. In the ENDF/B-VIII.0 database, UO_2 is in the ideal fluorite structure with Fm$\bar{3}$m symmetry. This crystal structure has been illustrated in Fig. 2.2. Beryllium is an important material which is widely used as neutron moderators and reflectors. Magnetism hydride (MgH_2) is a potential candidate for cold neutron reflectors (José Rolando Granada, Márquez Damián, Dawidowski, et al. 2021). Magnetism deuteride (MgD_2) shows improvements on neutron slowing down since the neutron capture cross section of deuterium is

Table 3.2.: Comparison of codes or platforms which enable to calculate the TSLs.

Codes/Platforms	LEAPR+NCrystal	OCLIMACX	FLASSH	CINEL(this work)
Harmonic approximation	Yes	Yes	Yes	Yes
1-p correction [a]	No	Yes	Yes	No
Cubic approximation	Yes	No	No	Yes
Support any material	Yes	Yes	Yes	Yes
SCT approximation	Yes	No	No	No
GPU speedup	No	not reported	not reported	Yes

[a] for coherent one-phonon correction to incoherent approximation

lower than that of hydrogen. MgH_2 and MgD_2 share the same crystal structure which is illustrated in Fig 3.4b. In terms of atoms in the unit cell, beryllium metal in HCP structure has two atoms, iron in BCC crystal structure has one single atom, aluminum in FCC crystal structure has one single atom. Lithium hydride (LiH) is in FCC crystal structure which is illustrated in Fig 3.4a. The PDOSs of the studied materials are presented in Figs. 3.5, 3.6 and 3.7.

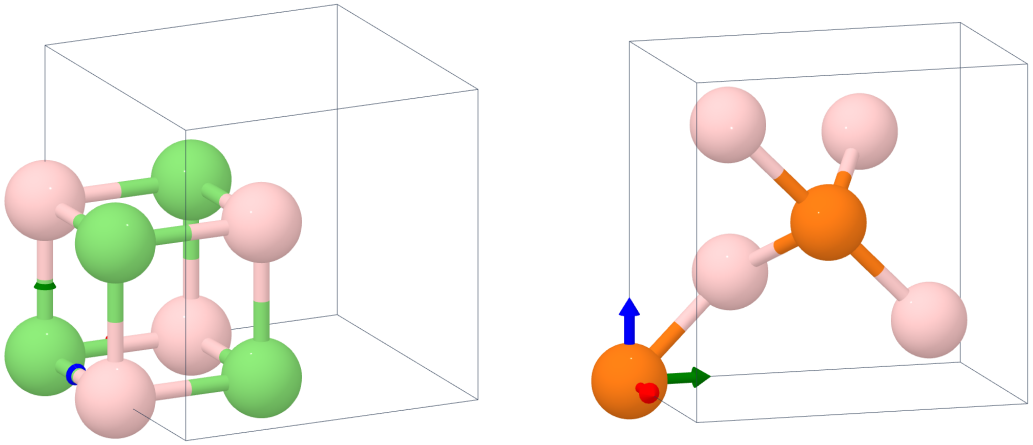

(a) LiH unit cell

(b) MgH_2 or MgD_2 unit cell

Figure 3.4.: Left hand plot presents the cubic unit cell of LiH: $a = b = c$ and $\alpha = \beta = \gamma = 90°$. Green and pink spheres represent respectively lithium and hydrogen atoms. Right hand plot presents the tetragonal unit cell of MgH_2 or MgD_2: $b = c$ and $\alpha = \beta = \gamma = 90°$. Orange spheres represent magnesium atoms. Pink spheres represent hydrogen or deuterium atoms. The drawings of these two figures are with the aid of the Crystal Toolkit in the Materials Project (Ong, Richards, Jain, et al. 2013).

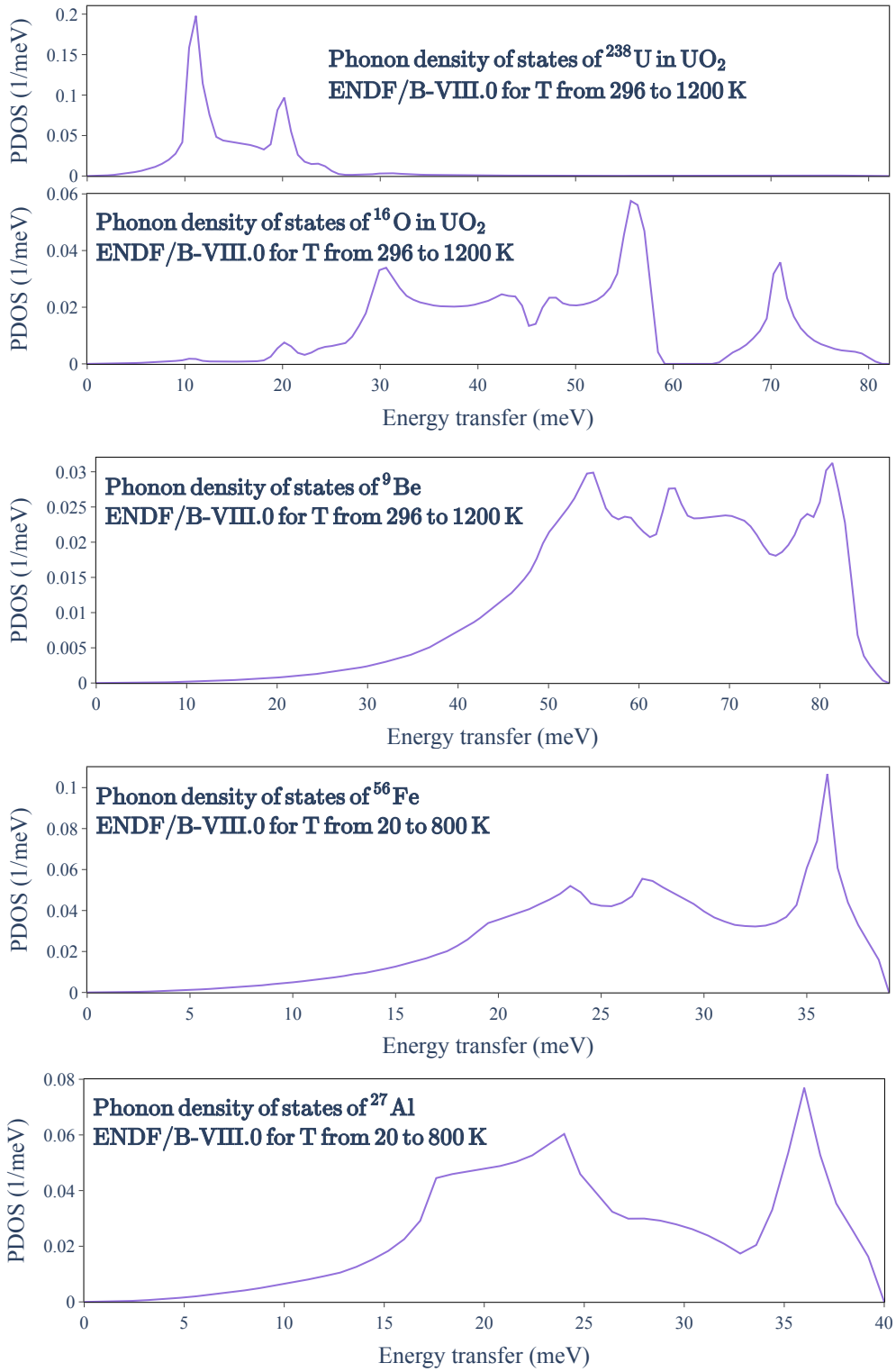

Figure 3.5.: PDOSs of ^{238}U in UO_2 and ^{16}O in UO_2, ^{9}Be, ^{56}Fe and ^{27}Al given by the ENDF/B-VIII.0 database. The PDOSs are utilized for the calculations of TSLs for temperatures between 296 K and 1200 K for UO_2 and ^{9}Be, between 20 K to 800 K for ^{56}Fe and ^{27}Al.

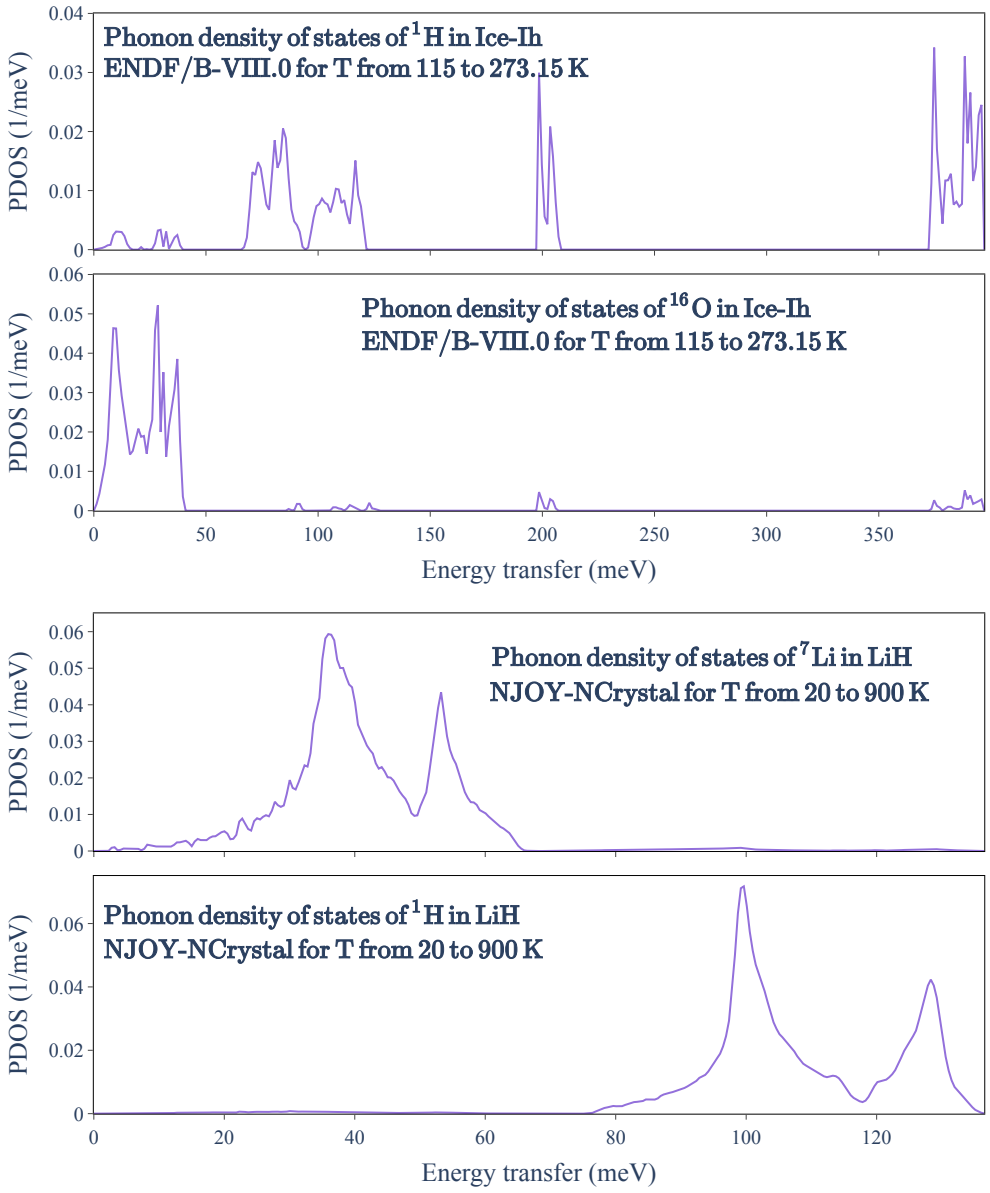

Figure 3.6.: The top plot presents the PDOSs of ^{1}H in ice I_h and ^{16}O in ice I_h for temperatures between 115 and 273.15 K, given in the ENDF/B-VIII.0 database. The bottom plot presents the PDOSs of ^{1}H in LiH and ^{7}Li in LiH for temperatures between 20 and 900 K, given in the `NJOY-NCrystal` library.

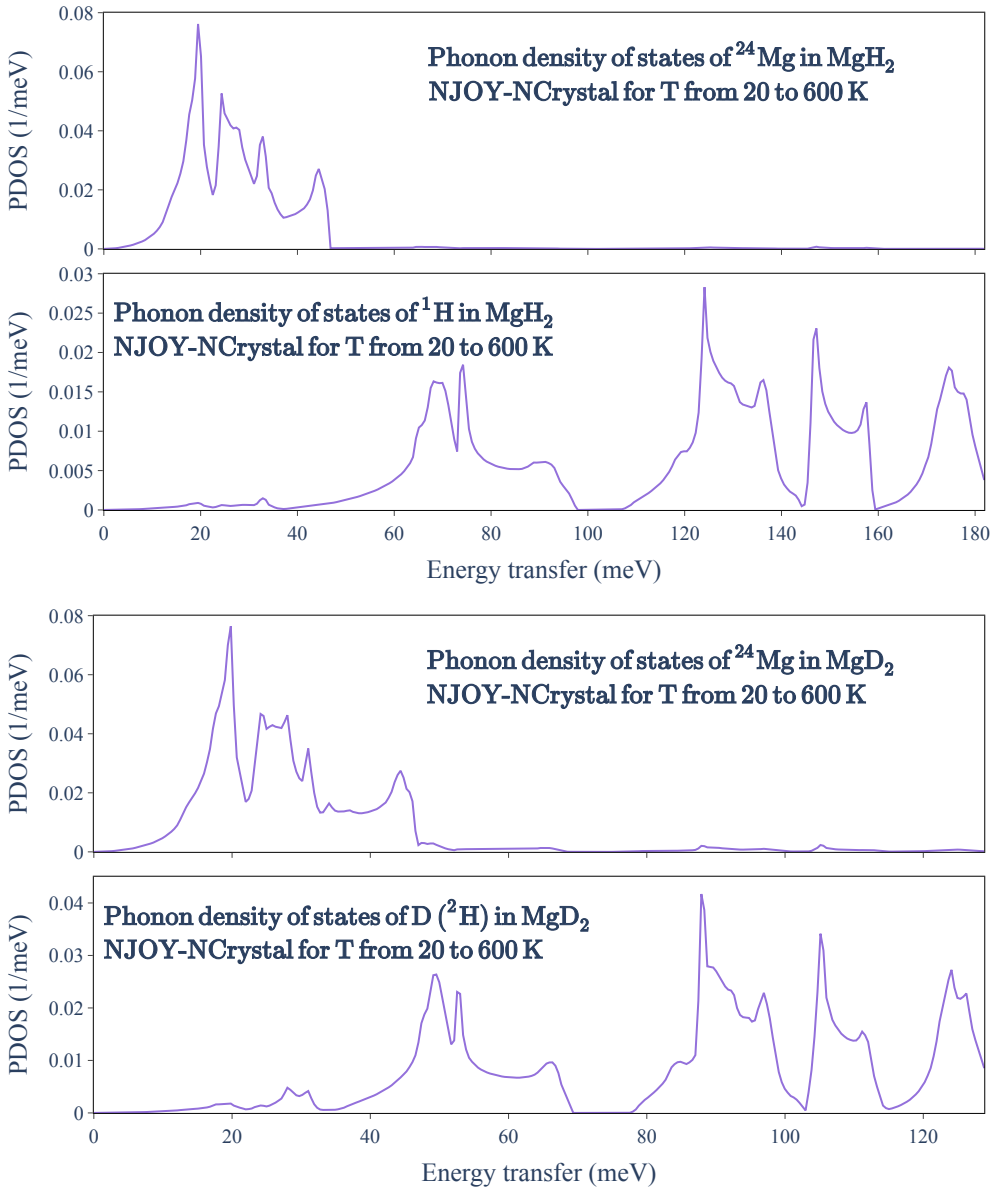

Figure 3.7.: PDOSs of ^{1}H in MgH_2, ^{24}Mg in MgH_2, D (^{2}H) in MgD_2, ^{24}Mg in MgD_2, given in the `NJOY-NCrystal` library. The PDOSs are utilized for the calculations of TSLs for temperatures between 20 K and 600 K.

The coherent and incoherent elastic, and inelastic neutron scattering cross sections ($\sigma^{\text{el}}_{\text{coh}}(E)$ and $\sigma^{\text{el}}_{\text{inc}}(E)$, and $\sigma^{\text{inel}}(E)$) of the studied materials calculated by CINEL are compared with the ENDF/B-VIII.0 database and the NJOY-NCrystal library (Figs. 3.8, 3.9, 3.10, 3.11, 3.12, 3.13, 3.14 and 3.15). Excellent agreement is obtained for $\sigma^{\text{el}}_{\text{coh}}(E)$, $\sigma^{\text{el}}_{\text{inc}}(E)$ and $\sigma^{\text{inel}}(E)$. $\sigma^{\text{el}}_{\text{coh}}(E)$ and $\sigma^{\text{el}}_{\text{inc}}(E)$ decrease with increasing temperature T, while $\sigma^{\text{inel}}(E)$ increase with T. The first Bragg peak of UO_2 appears at around 2 meV, which corresponds to the neutron diffraction on plan (111).

Symmetric TSLs $SS(\alpha, \beta)$ are used in the ENDF-6 format, which can be obtained by:

$$SS(\alpha, \beta) = \exp\left(\frac{\beta}{2}\right) S(\alpha, \beta). \tag{3.1}$$

The CINEL-calculated symmetric TSLs $SS(\alpha, \beta)$ of the studied materials at room temperature is compared with ENDF/B-VIII.0 database. The results are shown in Figs. 3.16 and 3.17. $SS(\alpha, \beta)$ as a function of the momentum transfers α for various values of energy transfers β are presented in Figs. 3.18 and 3.19. Excellent agreements are obtained.

3.4. Preliminary conclusions

In this chapter, several codes or platforms capable of calculating the TSLs of materials are overviewed. To generate the TSLs for uranium dioxide and liquid water, a flexible and efficient data processing tool CINEL has been developed in our work. The development of CINEL is shortly presented. Special attentions are given to its data flow and speedup with GPU. The numerical validations are performed by using various types of materials. An excellent agreement is obtained when compared to the ENDF/B-VIII.0 database and the NJOY-NCrystal library.

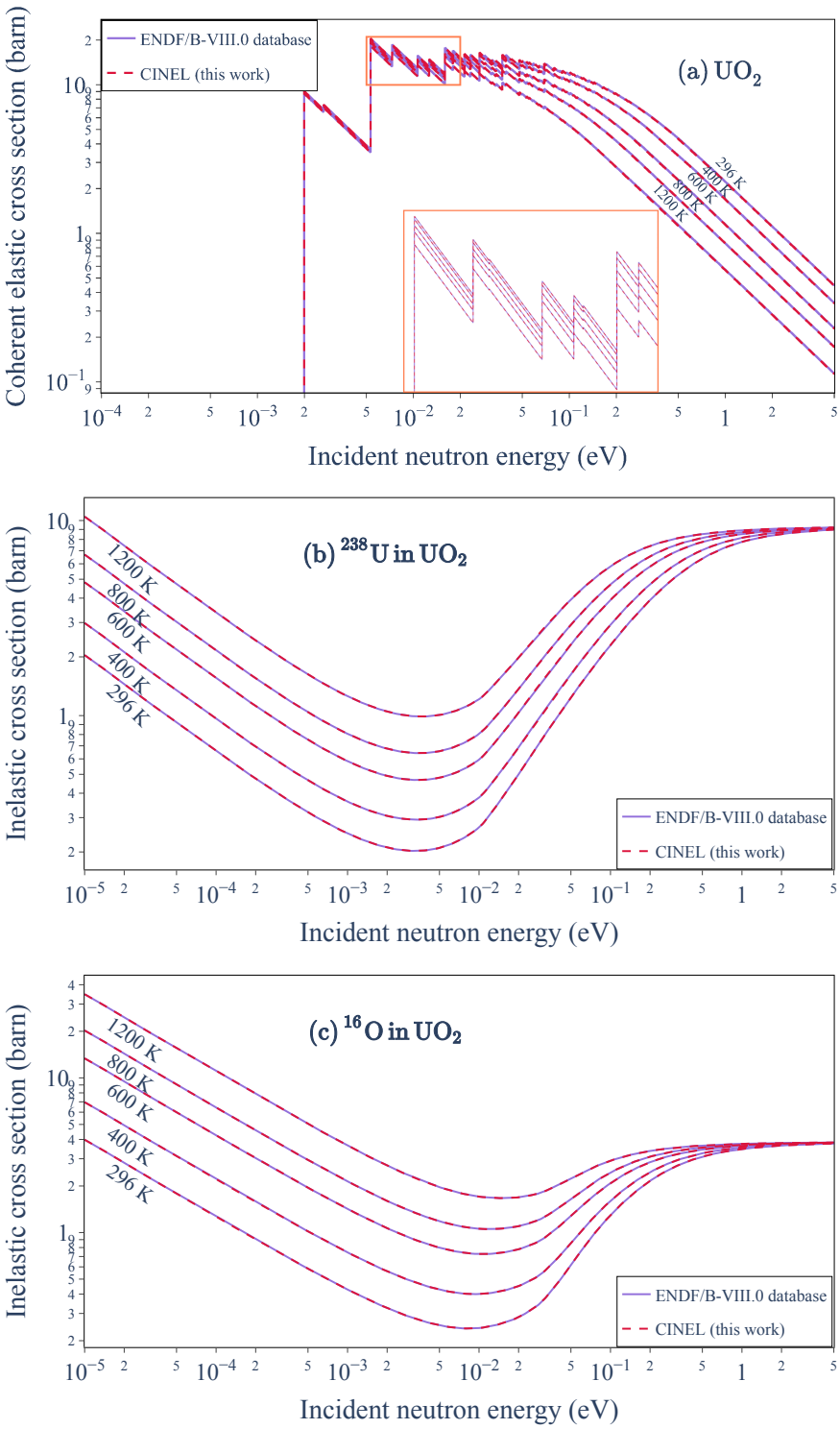

Figure 3.8.: Comparisons of CINEL-calculated coherent elastic and inelastic scattering cross section of UO_2 (dash curves) with the ENDF/B-VIII.0 database (solid curves) from 296 to 1200 K. The coherent elastic cross sections for incident energies are zoomed between 5 and 20 meV.

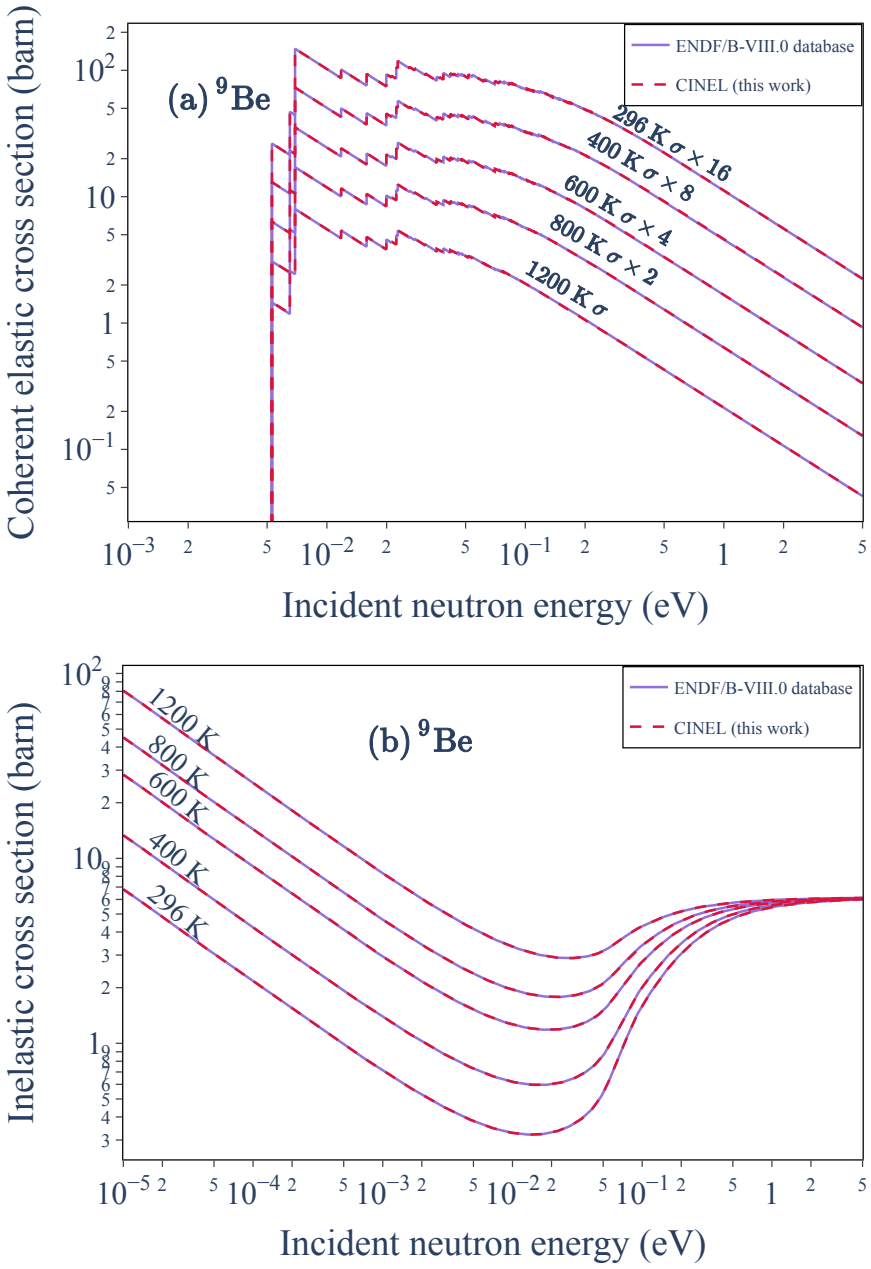

Figure 3.9.: Comparison of CINEL-calculated coherent elastic and inelastic scattering cross sections of ^{9}Be (dash curves) with the ENDF/B-VIII.0 database (solid curves) from 296 to 1200 K. The coherent elastic cross sections in Fig. (a) are multiplied with different factors for better visualization.

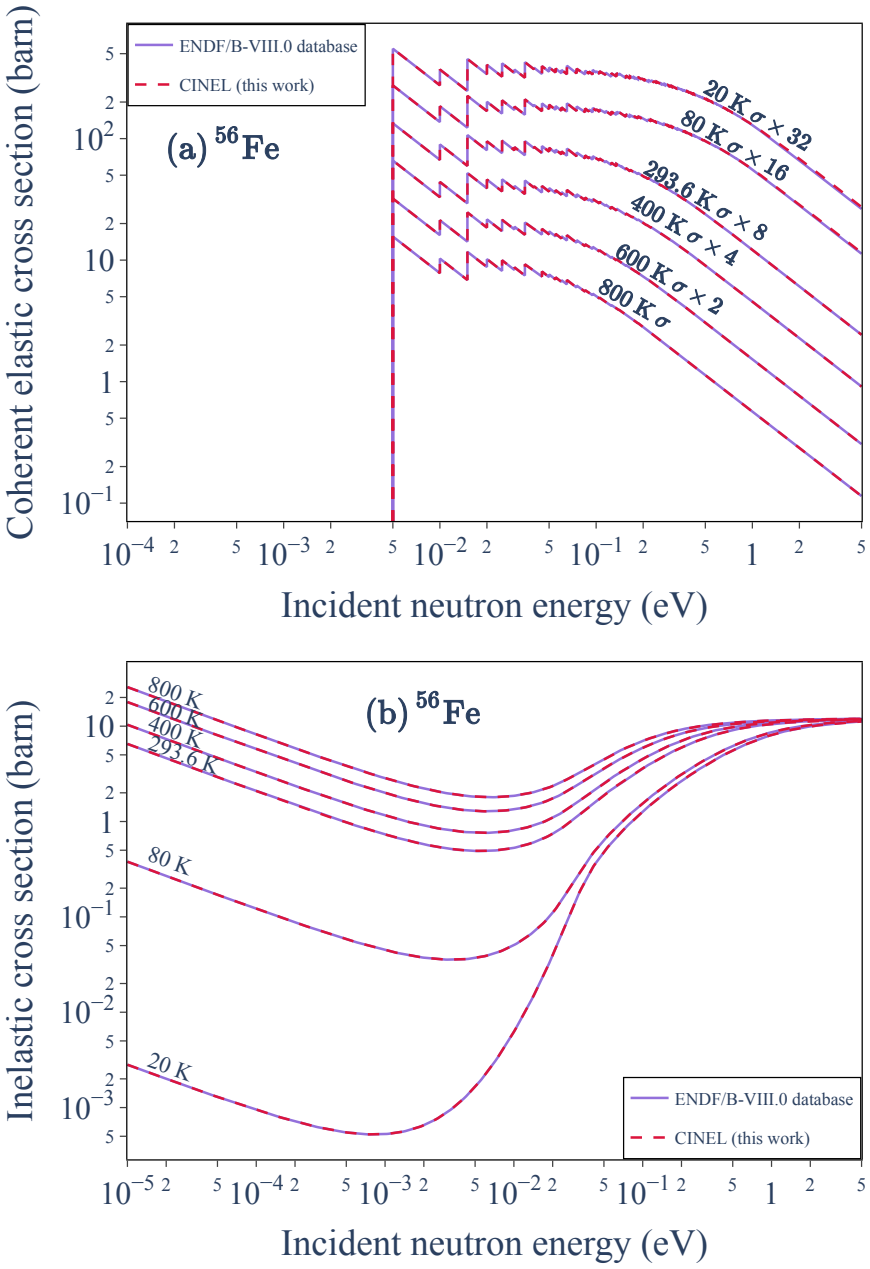

Figure 3.10.: Comparison of CINEL-calculated coherent elastic and inelastic scattering cross sections of ^{56}Fe (dash curves) with the ENDF/B-VIII.0 database (solid curves) from 20 to 800 K. The coherent elastic cross sections in Fig. (a) are multiplied with different factors for better visualization.

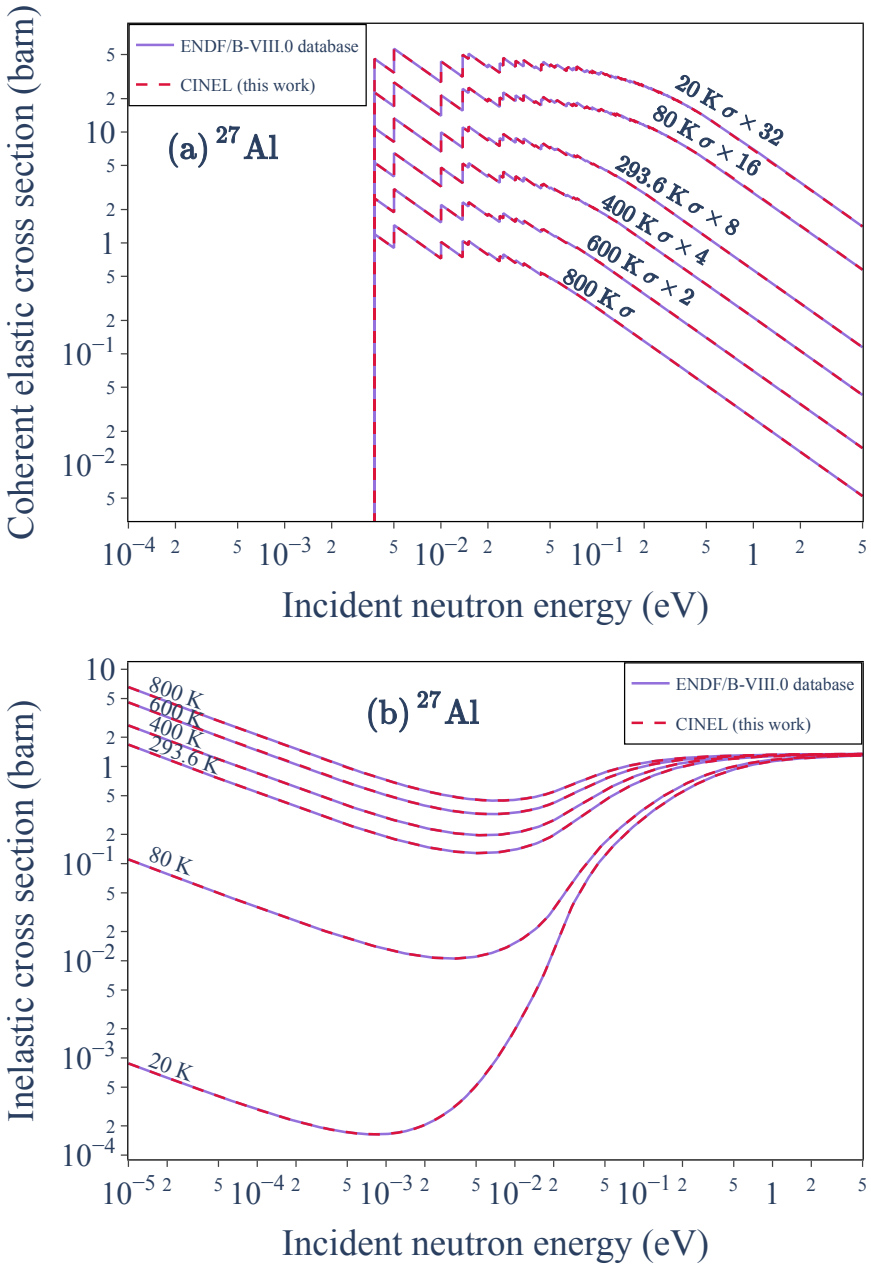

Figure 3.11.: Comparison of CINEL-calculated coherent elastic and inelastic scattering cross sections of ^{27}Al (dash curves) with the ENDF/B-VIII.0 database (solid curves) from 20 to 800 K. The coherent elastic cross sections in Fig. (a) are multiplied with different factors for better visualization.

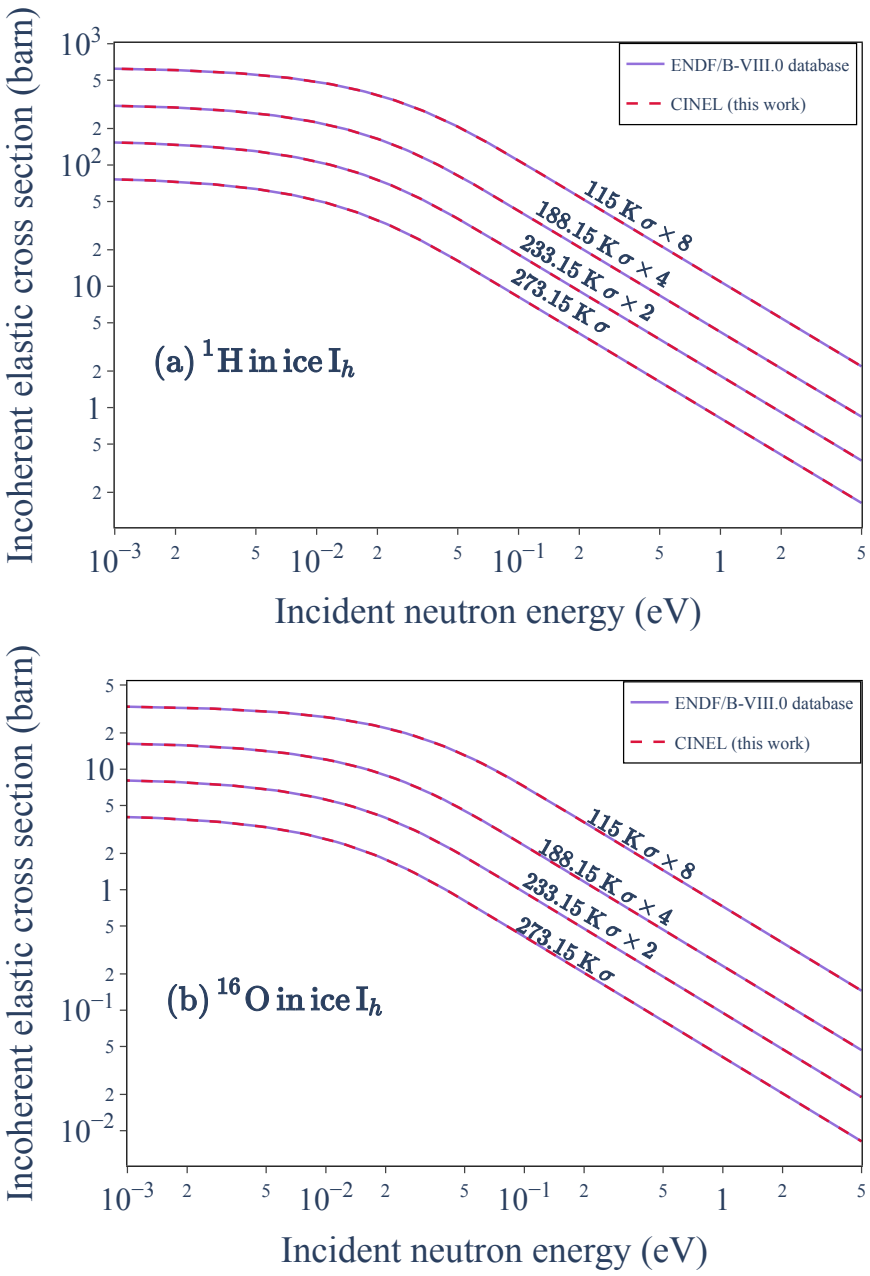

Figure 3.12.: Comparison of CINEL-calculated incoherent elastic scattering cross sections of ^{1}H in ice I_h and ^{16}O in ice I_h (dash curves) with the ENDF/B-VIII.0 database (solid curves) from 115 to 273.15 K.

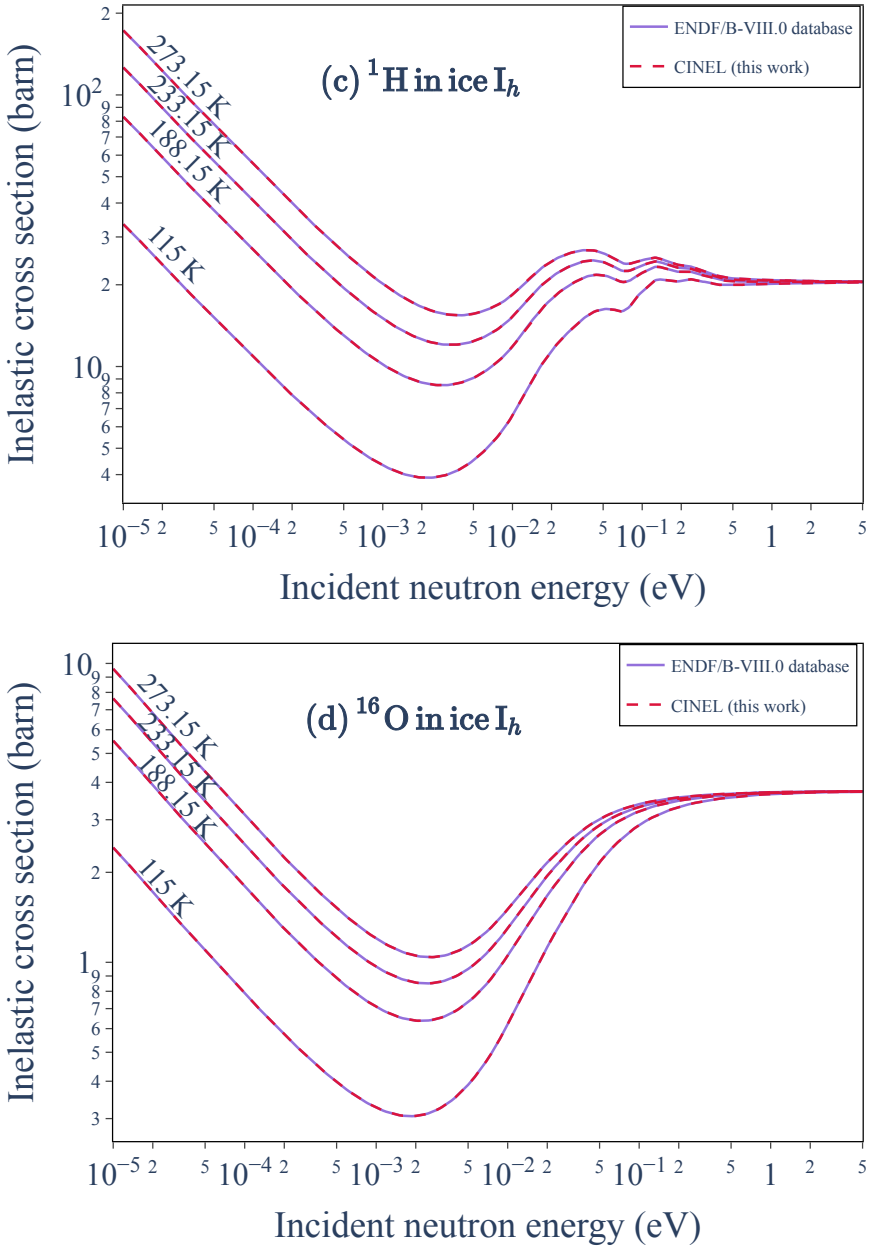

Figure 3.12.: (continued) Comparison of CINEL-calculated inelastic scattering cross sections of ^{1}H in ice I_h and ^{16}O in ice I_h (dash curves) with the ENDF/B-VIII.0 database (solid curves) from 115 to 273.15 K. The incoherent elastic cross sections in Figs. (a) and (b) are multiplied with different factors for better visualization.

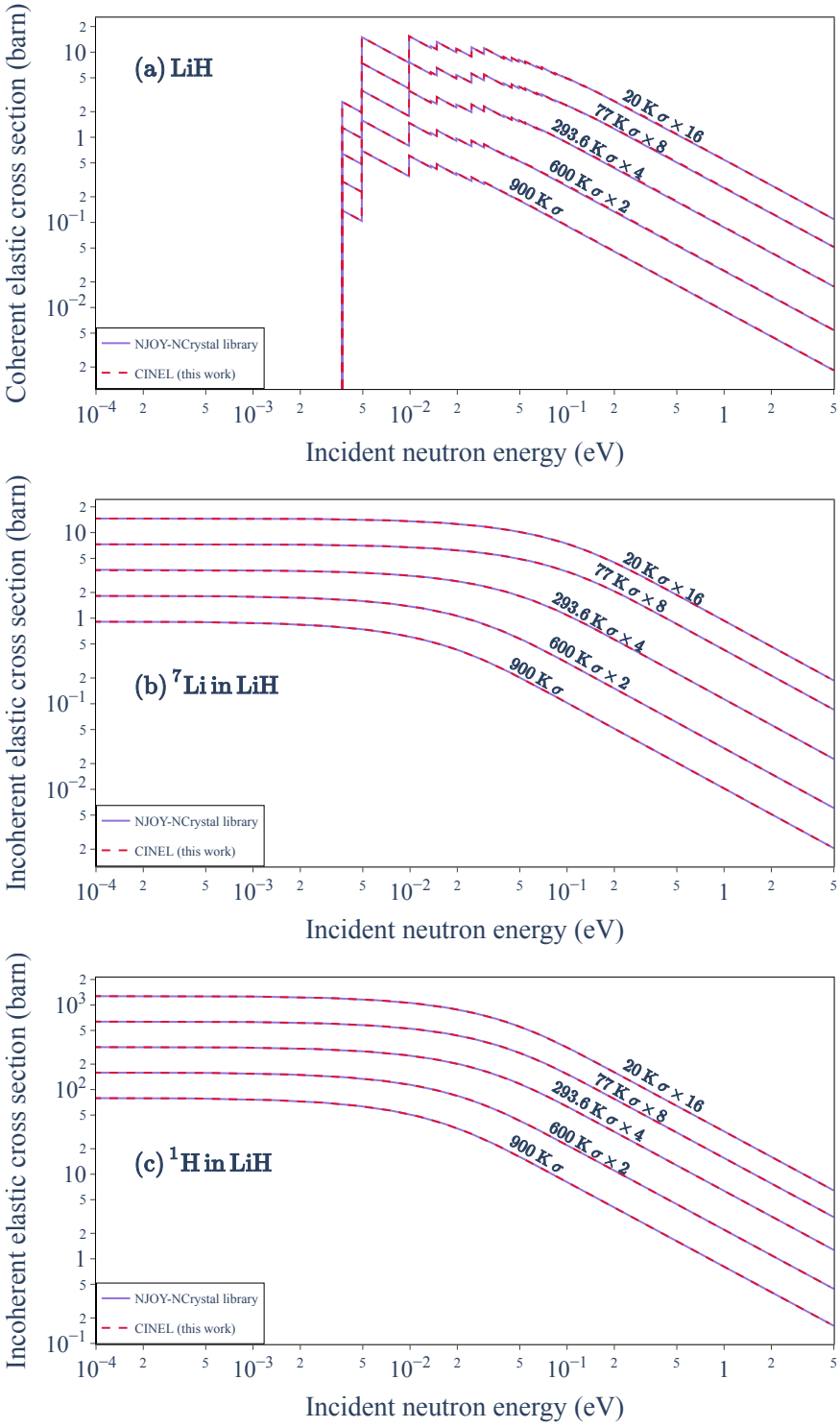

Figure 3.13.: Comparison of CINEL-calculated coherent elastic cross sections of LiH, and incoherent elastic scattering cross sections of ^{7}Li in LiH and ^{1}H in LiH (dash curves) with the NJOY-NCrystal library (solid curves) from 20 to 900 K.

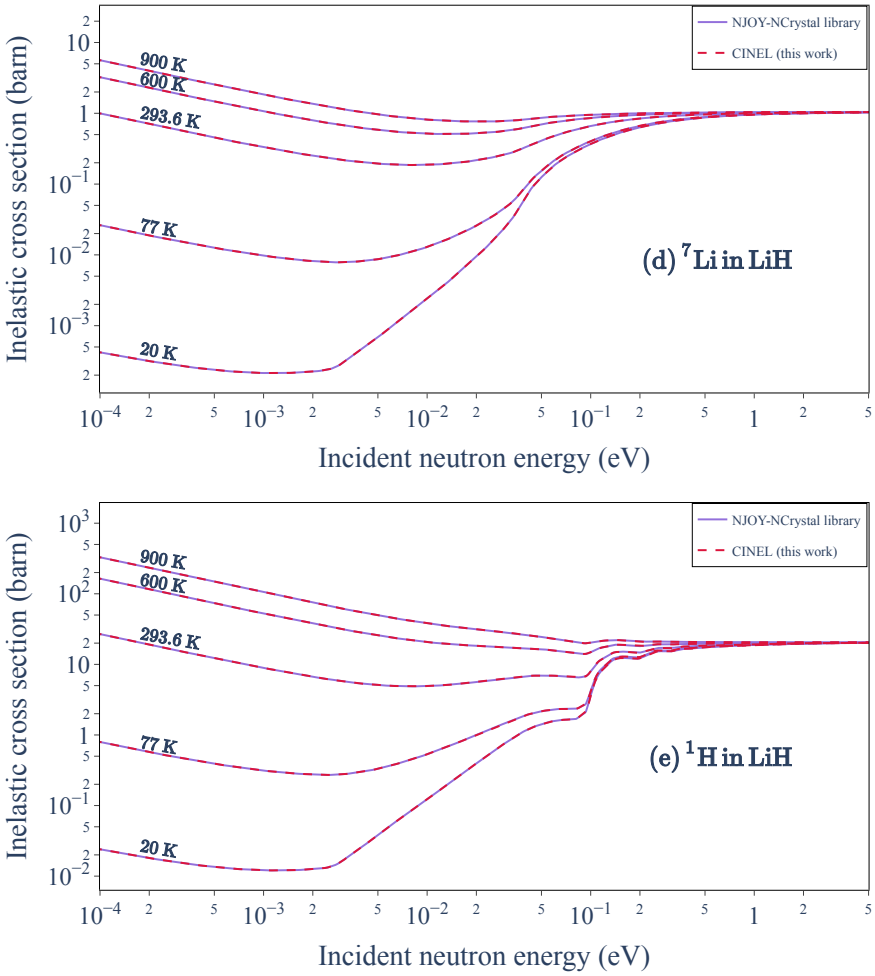

Figure 3.13.: (continued) Comparison of CINEL-calculated inelastic scattering cross sections of ^{7}Li in LiH and ^{1}H in LiH (dash curves) with the NJOY-NCrystal library (solid curves) from 20 to 900 K. The coherent and incoherent elastic cross sections in Figs. (a), (b) and (c) are multiplied with different factors for better visualization.

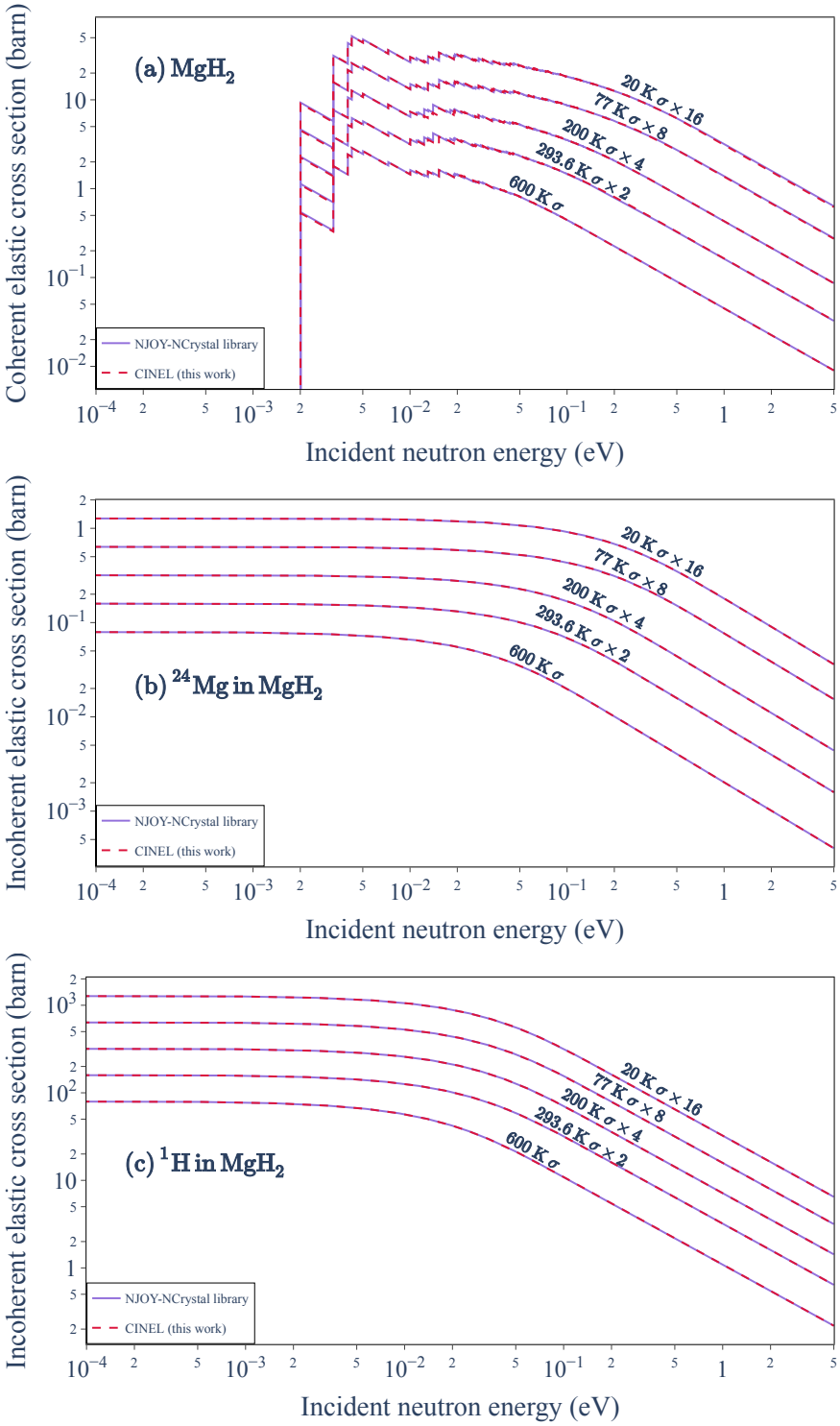

Figure 3.14.: Comparison of CINEL-calculated coherent elastic cross sections of MgH_2, and incoherent elastic scattering cross sections of ^{24}Mg in MgH_2 and ^{1}H in MgH_2 (dash curves) with the NJOY-NCrystal library (solid curves) from 20 to 600 K.

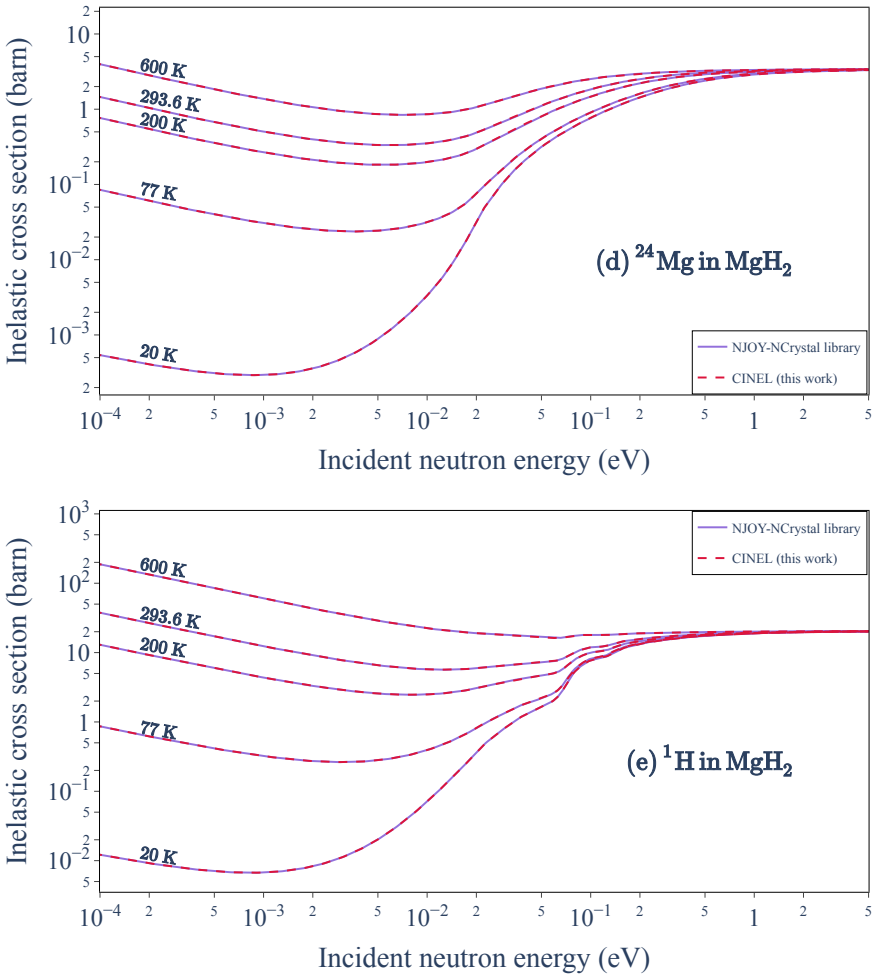

Figure 3.14.: (continued) Comparison of CINEL-calculated inelastic scattering cross sections of ^{24}Mg in MgH_2 and ^{1}H in MgH_2 (dash curves) with the NJOY-NCrystal library (solid curves) from 20 to 600 K. The coherent and incoherent elastic cross sections in Fig. (a), (b) and (c) are multiplied with different factors for better visualization.

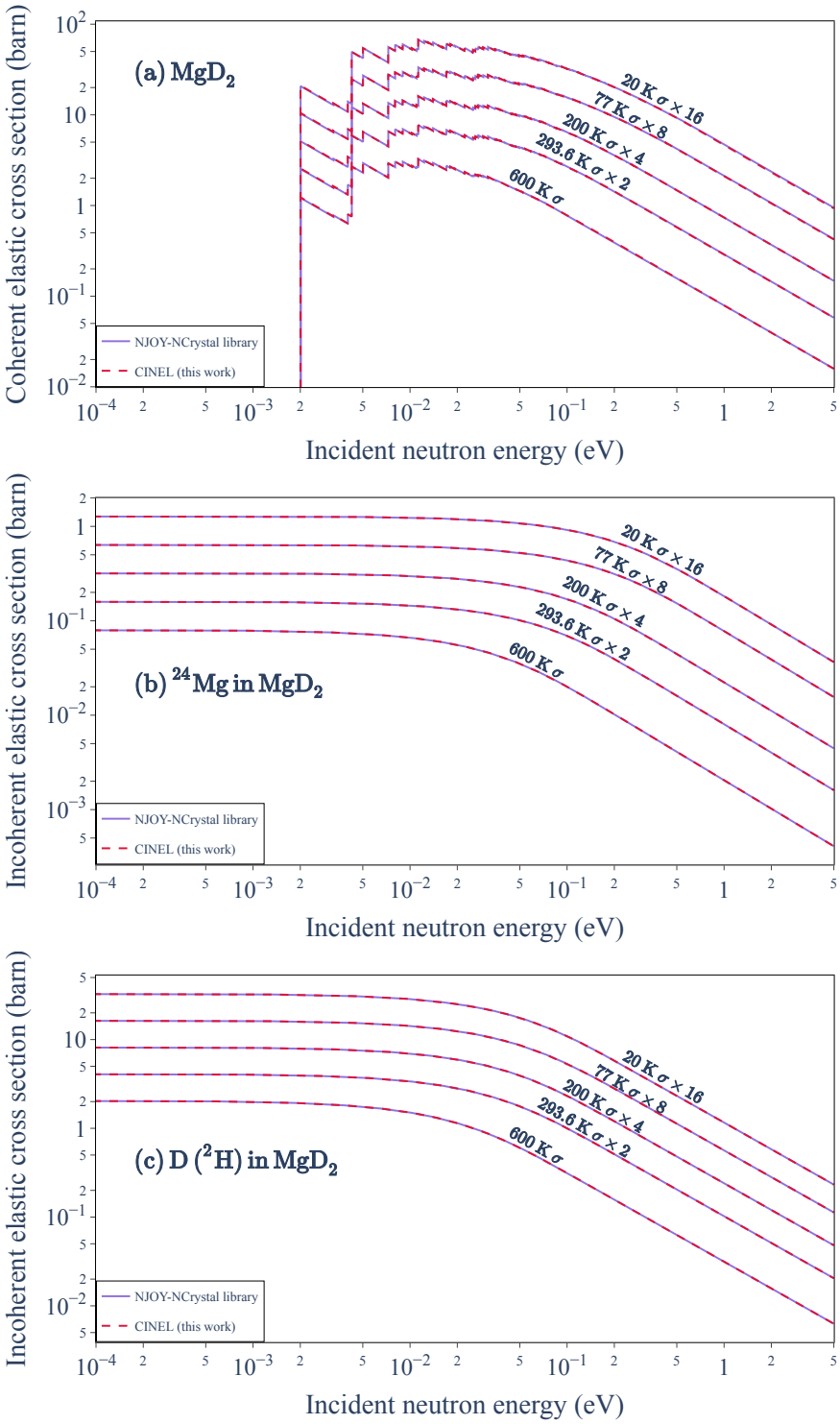

Figure 3.15.: Comparison of CINEL-calculated coherent elastic cross sections of MgD_2, and incoherent elastic scattering cross sections of ^{24}Mg in MgD_2 and D (^2H) in MgD_2 (dash curves) with the NJOY-NCrystal library (solid curves) from 20 to 600 K.

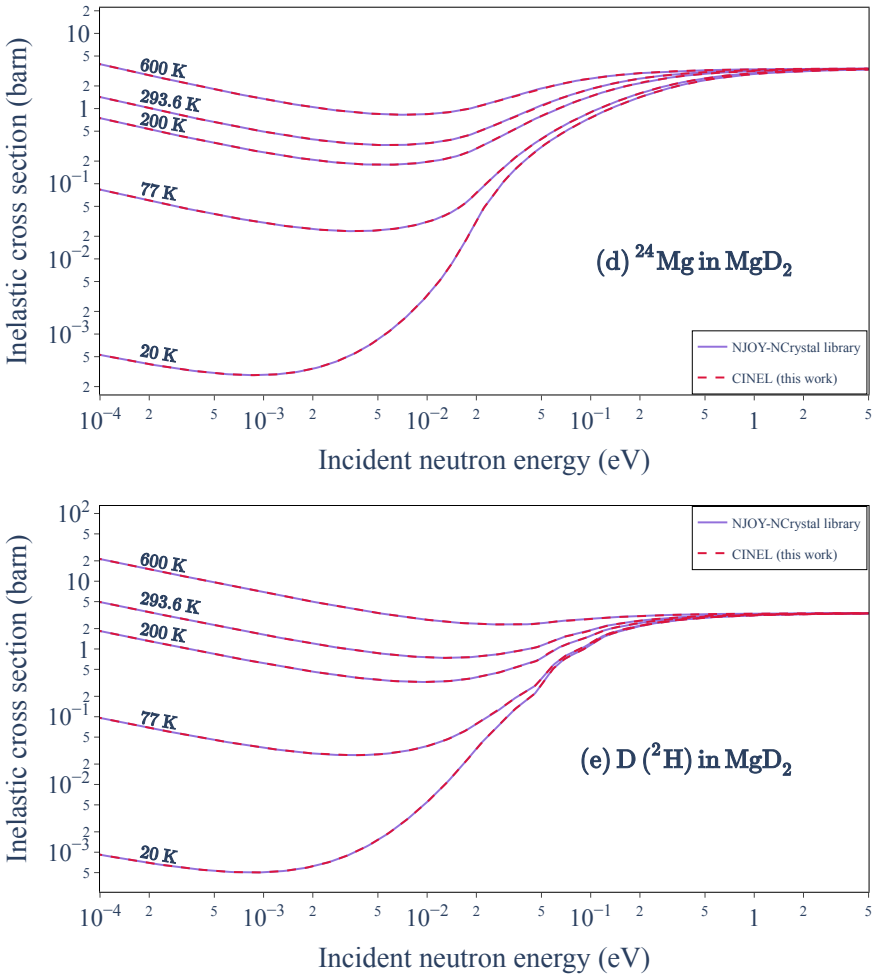

Figure 3.15.: (continued) Comparison of CINEL-calculated inelastic scattering cross sections of ^{24}Mg in MgD_2 and D (^{2}H) in MgD_2 (dash curves) with the NJOY-NCrystal library (solid curves) from 20 to 600 K. The coherent and incoherent elastic cross sections in Fig. (a), (b) and (c) are multiplied with different factors for better visualization.

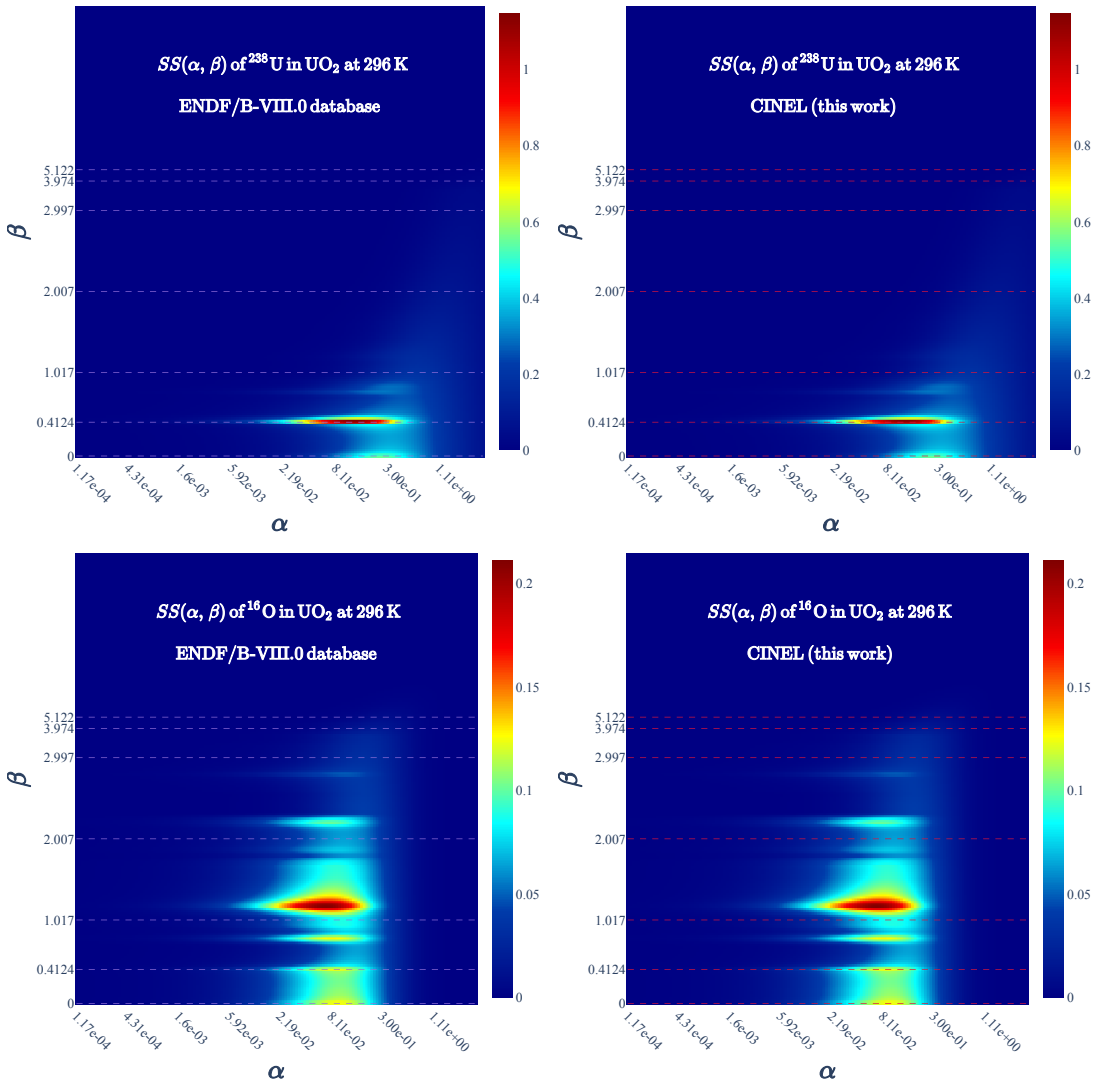

Figure 3.16.: CINEL calculated symmetric TSLs $SS(\alpha, \beta)$ (left column plots) compared to the ENDF/B-VIII.0 database (left column plots) of ^{238}U in UO_2 and ^{16}O in UO_2. A few horizontal dash curves represent: $SS(\alpha, \beta)$ as a function of the momentum transfer α for the given energy transfer β. The comparisons of these curves will be shown in Fig. 3.18.

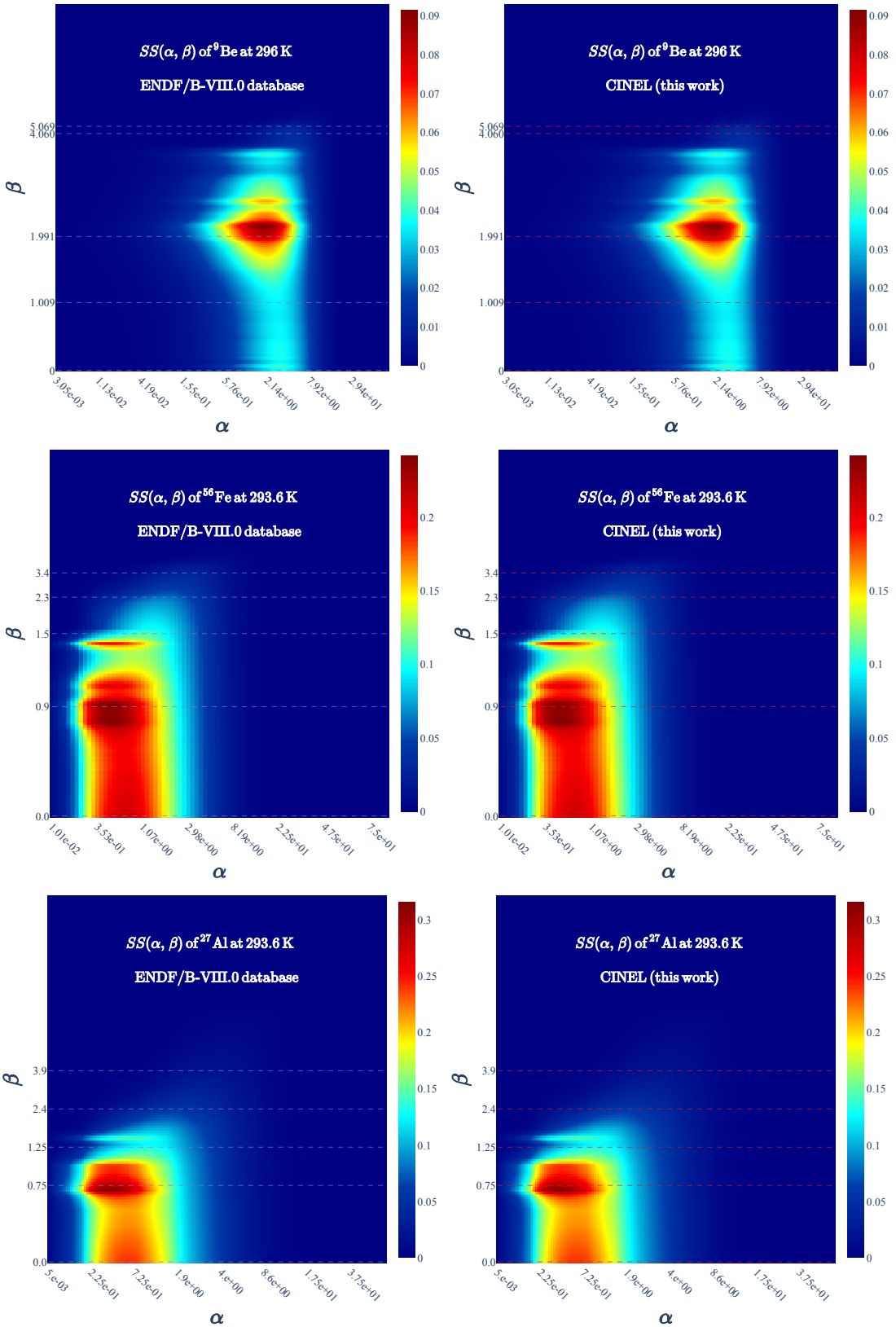

Figure 3.17.: CINEL calculated symmetric TSLs $SS(\alpha, \beta)$ (left column plots) compared to the ENDF/B-VIII.0 database (left column plots) of ^{9}Be, ^{56}Fe and ^{27}Al. A few horizontal dash curves represent: $SS(\alpha, \beta)$ as a function of the momentum transfer α for the given energy transfer β. The comparisons of these curves will be shown in Fig. 3.19.

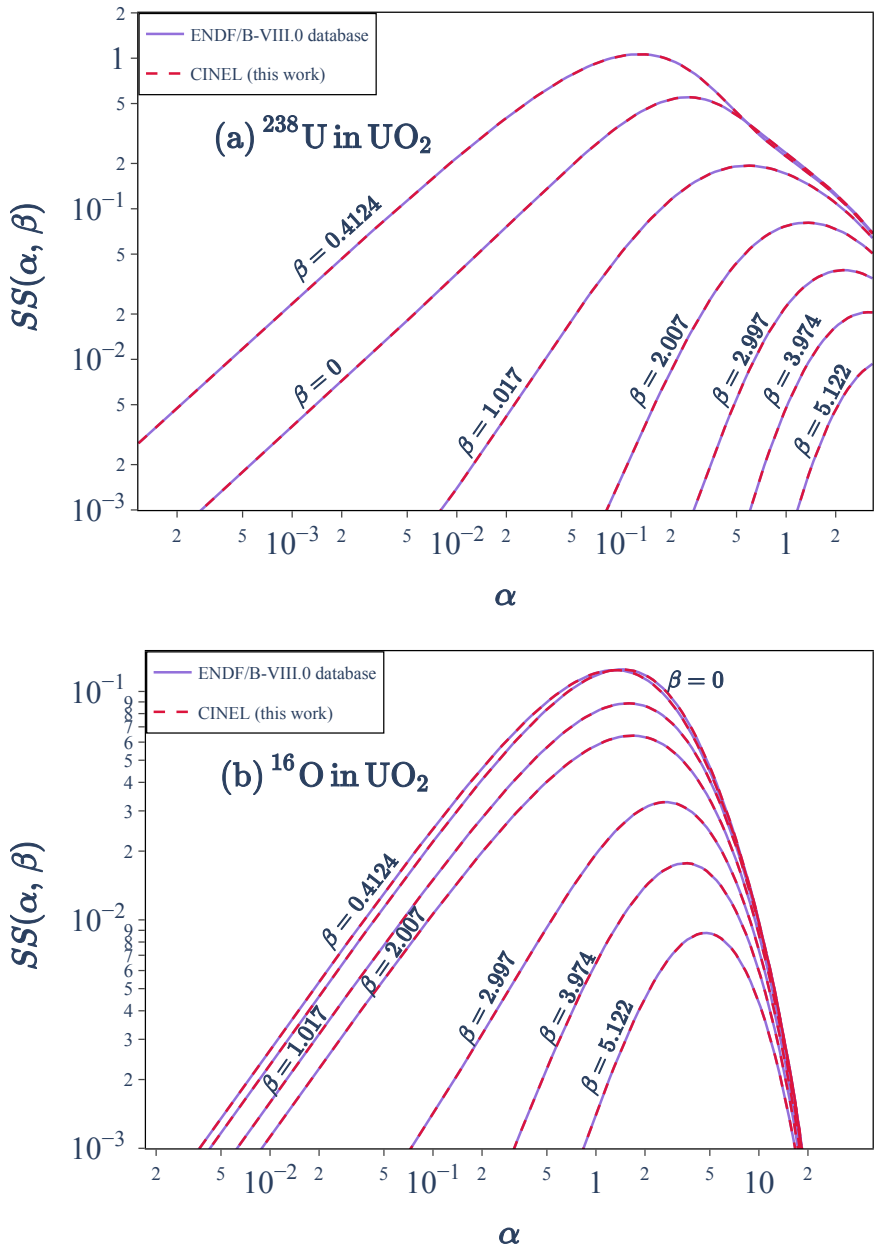

Figure 3.18.: CINEL-calculated symmetric TSL $SS(\alpha, \beta)$ as a function of the momentum transfer α for various values of energy transfer β (dash curves) are compared with the ENDF/B-VIII.0 database (solid curves) for ^{238}U in UO_2 and ^{16}O in UO_2 at 296 K.

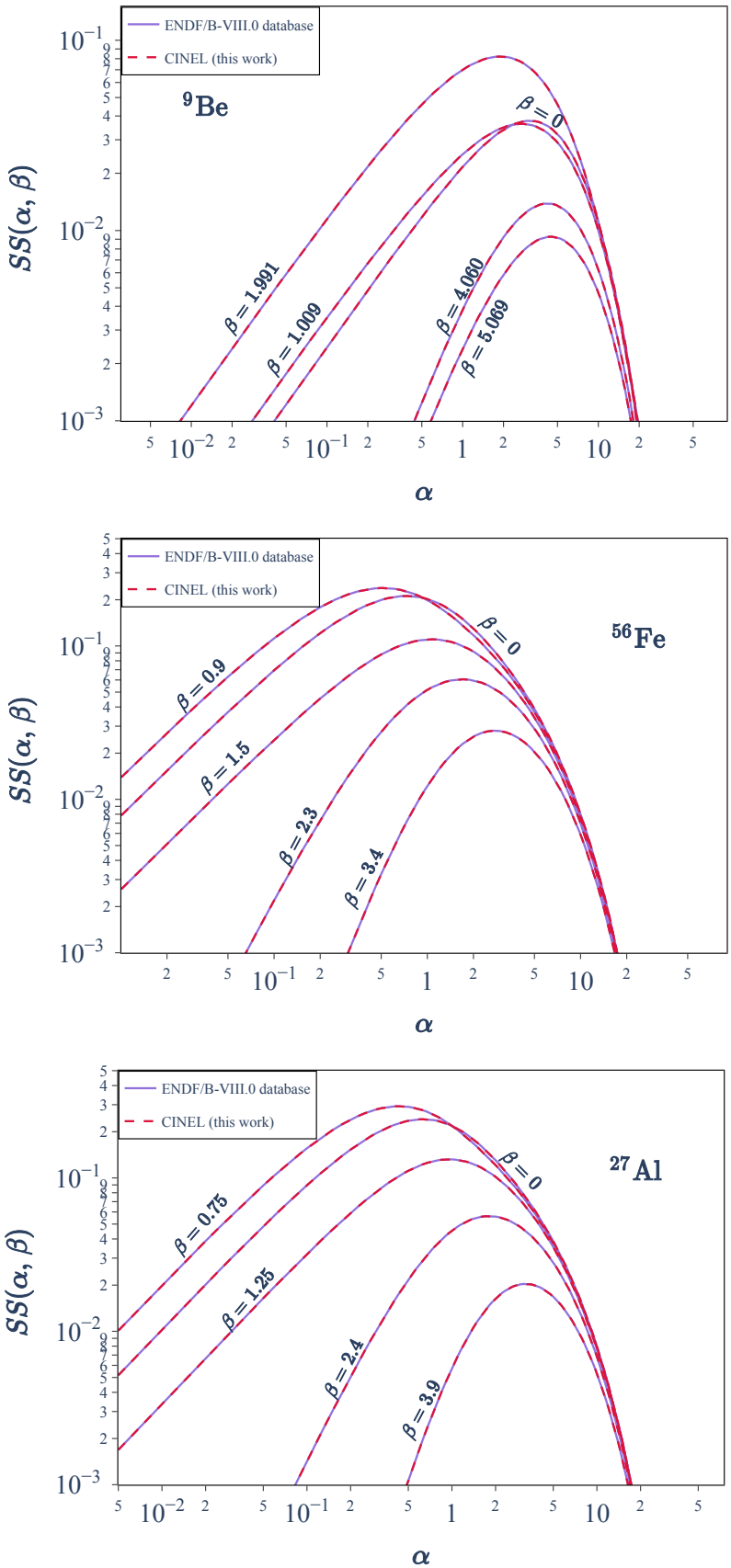

Figure 3.19.: CINEL-calculated symmetric TSL $SS(\alpha, \beta)$ as a function of the momentum transfer α for various values of energy transfer β (dash curves) are compared with the ENDF/B-VIII.0 database (solid curves) for ^{9}Be at 296 K, ^{56}Fe and ^{27}Al at 293.6 K.

4. Monte-Carlo simulations of neutron experiments for UO_2 at ILL (incident neutron energy lower than a few eV)

Summary

Low-energy neutrons (below a few eV) have been used since the sixties (Willis 1963a; Willis 1963b) to probe the crystalline structure of uranium dioxide (UO_2) from room temperature to normal nuclear reactors operating conditions. Despite these experimental and theoretical efforts, crystalline structure effects are not yet routinely taken into account in industrial neutronic simulation schemes of nuclear power reactors. Temperature effects are often calculated via a simple FGM. Therefore, validating the crystalline effects at the microscopic level is still a necessity to motivate an update of the neutron scattering treatment in neutronic simulation schemes.

The aim of the chapter is to show the performances of modern Monte-Carlo neutron transport codes for revisiting the analysis of neutron diffraction experiments measured at elevated temperatures, which were originally designed to study the temperature effects on the UO_2 lattice arrangement. Indeed, if the fluorite structure ($Fm\bar{3}m$ space group) of UO_2 is well established at room temperature, the understanding of the unusual relaxation with the increasing temperature of the oxygen atoms from their regular positions is still under discussion. Among the few neutron diffraction measurements on stoichiometric uranium dioxide reported in the literature, we have selected the works of Ruello (P. Ruello, Desgranges, Baldinozzi, et al. 2005) and Ma (Yue Ma 2017), whose data are still available at ILL of Grenoble (France). The experiments were performed on the D20 and D4 diffractometers, respectively. They consisted in measuring the temperature-dependent neutron scattering yield $Y^T_{\text{exp}}(\theta)$ as a function of the scattering angle θ. The two data sets cover a wide temperature range from room temperature to 1664 K (the melting point of UO_2 is around 3100 K (Hausner 1965)). The originality of our work relies on the use of the Monte-Carlo code TRIPOLI-4® (E. Brun, F. Damian, Diop, et al. 2015) to simulate the experimental diffraction patterns by taking into account the multiple neutron scattering effects and the multiphonon contribution. The experimental corrections, which are not introduced in the Monte-Carlo simulations, are the background correction, the angular offset and the angular response function of the diffractometer. They are deduced from the data by applying a Rietveld-type structure refinement (Rietveld 1969) on the neutron scattering yields simulated with the TRIPOLI-4® code. Final results mainly depend on the neutron scattering cross sections of uranium and oxygen in UO_2 which were introduced in the simulations.

In Section 4.1, the measurements performed at ILL and the calculation scheme developed in this work are briefly described. The interpretation of the data with the Monte-Carlo neutron transport code TRIPOLI-4® is presented in Section 4.2. Extensions of the `CINEL` model to account for anharmonic oxygen vibrations in the $Fm\bar{3}m$ space group or other crystalline symmetries for UO_2 at elevated temperatures are discussed in Section 4.3. Preliminary conclusions are given in the last section.

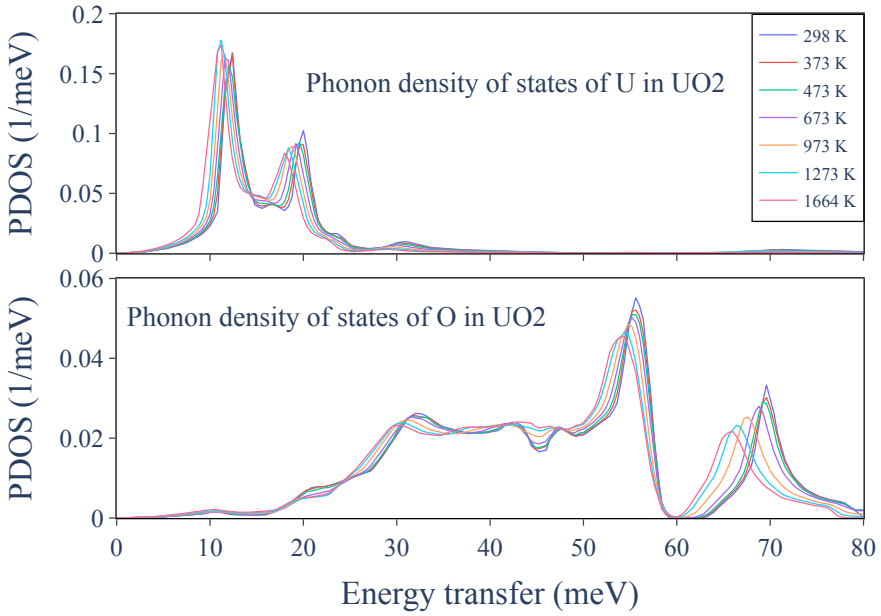

Figure 4.1.: Temperature-dependent phonon density of states of uranium and oxygen in uranium dioxide as a function of the energy transfer ε (G. Noguere, J. P. Scotta, Xu, Filhol, et al. 2020).

4.1. Presentation of experimental data

4.1.1. Time-of-flight spectrometers IN6 and IN4

As shown in Chapter 2, the PDOS $\rho_j(\omega)$ is the key physical quantity involved in the theoretical description of the double-differential inelastic scattering cross section. Results obtained from the analysis of inelastic scattering measurements performed at ILL (G. Noguere, J. P. Scotta, Xu, Filhol, et al. 2020) are shown in Fig. 4.1. The five normal modes of vibration of UO_2 can be distinguished around 10 meV, 20 meV, 30 meV, 55 meV and 70 meV. The two first peaks correspond to the translational and longitudinal acoustic phonon modes of the uranium atoms. The highest energy structures are dominated by the optical phonon modes of the oxygen atoms.

4.1.2. Diffractometers D20 and D4

The performances of the TRIPOLI-4® code are illustrated with two sets of data measured at ILL on the D4 and D20 diffractometers. The description of the experiments and the results are reported in Refs (P. Ruello, Desgranges, Baldinozzi, et al. 2005; Desgranges, Y. Ma, Garcia, et al. 2017). The detailed characteristics of each instrument can be found elsewhere (Laue-Langevin n.d.; Fischer, Cuello, Palleau, et al. 2002).

The left hand side of Fig. 4.2 shows schematic top views of the D4 and D20 spectrometers. The right hand drawings represent the simplified geometries introduced in the Monte-Carlo code TRIPOLI-4®. From the point of view of the neutron transport

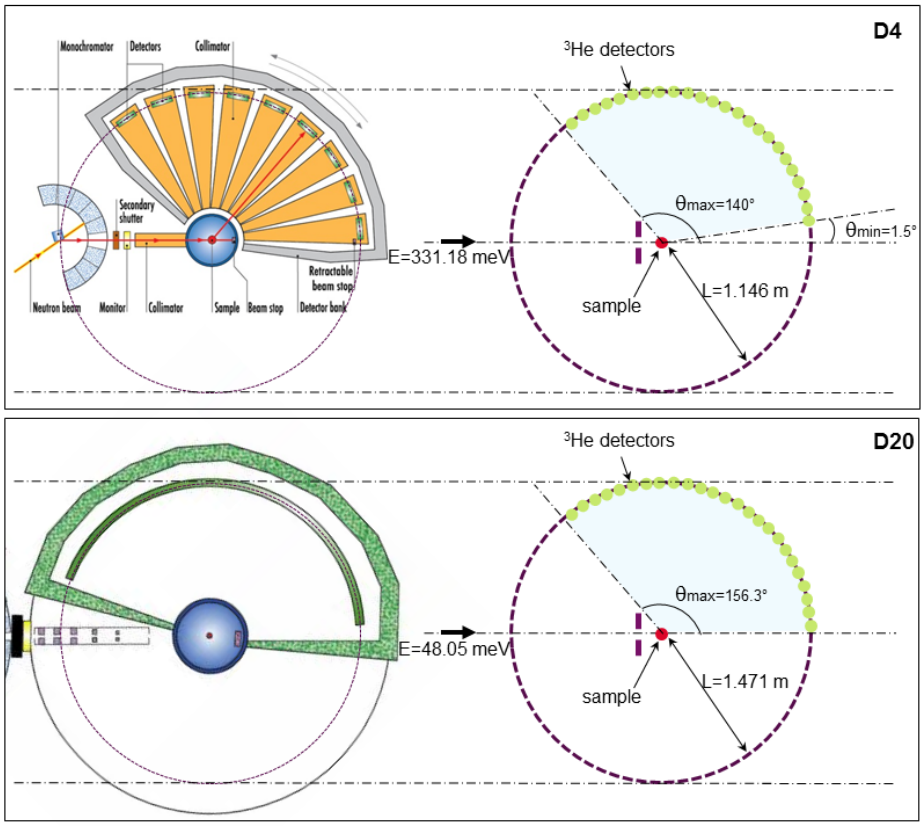

Figure 4.2.: The left hand drawings represent simplified top view of the D4 and D20 diffractometers of the Institut Laue-Langevin (ILL). Those on the right hand side show the geometries introduced in the Monte-Carlo calculations.

physics, both spectrometers share the same basic design. The experimental technique consists in measuring the neutron scattering yield $Y^T_{\text{exp}}(\theta)$ as a function of the scattering angle θ and temperature T.

For D4, the distance between the sample and the ^{3}He detectors is 1.146 m. The detector array covers scattering angles ranging from 1.5° to 140° with an angular resolution of 0.125°. The monoenergetic neutron beam of 331.18 meV (λ = 0.4970 Å) emerges from a Cu (220) monochromator. The neutron beam was focused to the sample, which was mounted in a furnace placed at the center of the spectrometer. The sample consisted in a stack of two UO_2 pellets of 8.3 mm in diameter and 14 mm in height sealed under vacuum in a quartz tube. The density of the pellets is 10.76 g/cm^3 which corresponds to 98.2% of the theoretical density. The measurements were performed with temperatures ranging from 298 K to 1273 K.

For D20, the ^{3}He detector ring is located at 1.471 m from the sample. It covers scattering angles ranging from 0° to 156.3° with an angular resolution of 0.1°. The energy of the incident neutrons, coming from a Cu (200) monochromator, was equal to 48.05 meV (λ = 1.3048 Å). Two UO_2 pellets (with a diameter of 8 mm and a height of

10 mm) were placed in a niobium tube on the bottom of a niobium furnace, allowing to investigate a wide temperature range from 292 K to 1664 K.

The experiments consisted in a sequence of UO_2 and empty-sample measurements. The data reduction steps were handled with ILL in-house codes, whose major issues could come from the background subtraction. The background is mainly due to neutrons scattered by the sample-holder and its environment. It is removed by subtracting the neutron scattering yield measured during the empty-sample sequence times an empirical determined effective sample transmission factor. In the present work, the background subtraction was only revisited in the case of the Ruello's data measured on D20. Fig. 4.3 shows neutron diffraction patterns at $T = 292$ K, in which many structures due to the large amount of niobium can be observed. Most of them were removed by using an effective transmission factor of 0.87.

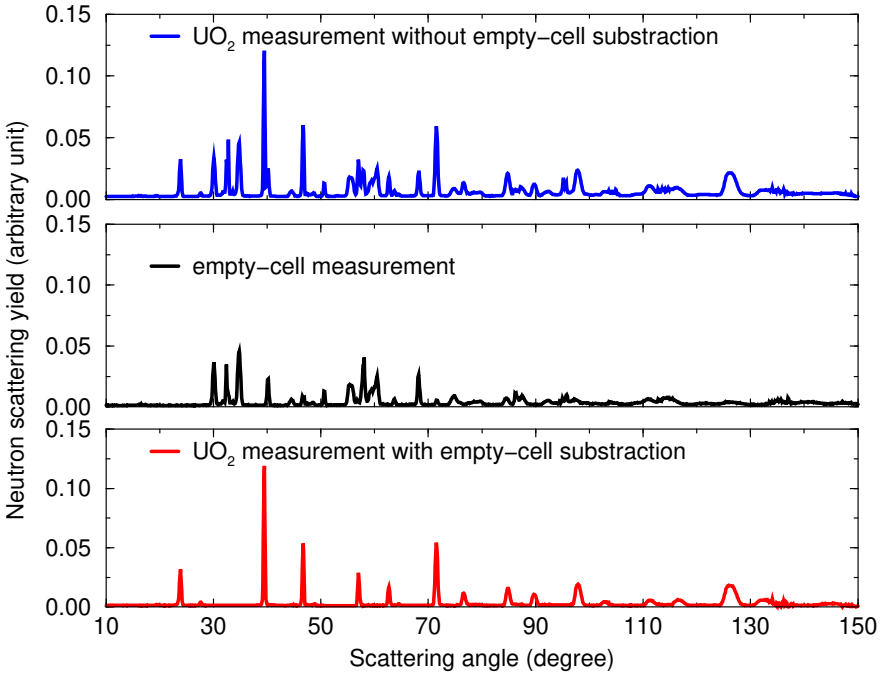

Figure 4.3.: Examples of neutron diffraction patterns measured on D20 at $T = 292$ K ($E = 48.05$ meV).

As shown in Fig. 2.2, the UO_2 unit cell contains $N_{\text{unit cell}} = 12$ atoms, with 4 atoms of uranium and 8 atoms of oxygen. The cubic symmetry leads to cell parameters $a = b = c$ and angles $\alpha = \beta = \gamma = 90°$. The positions of the uranium and oxygen atoms are reported in Table 2.1. Fig. 4.4 shows the two sets of temperature-dependent cell parameters (Pascal Ruello 2001; Desgranges, Y. Ma, Garcia, et al. 2017) which were used to simulate the neutron diffraction patterns measured at ILL. The observed differences are discussed in Section 4.2.

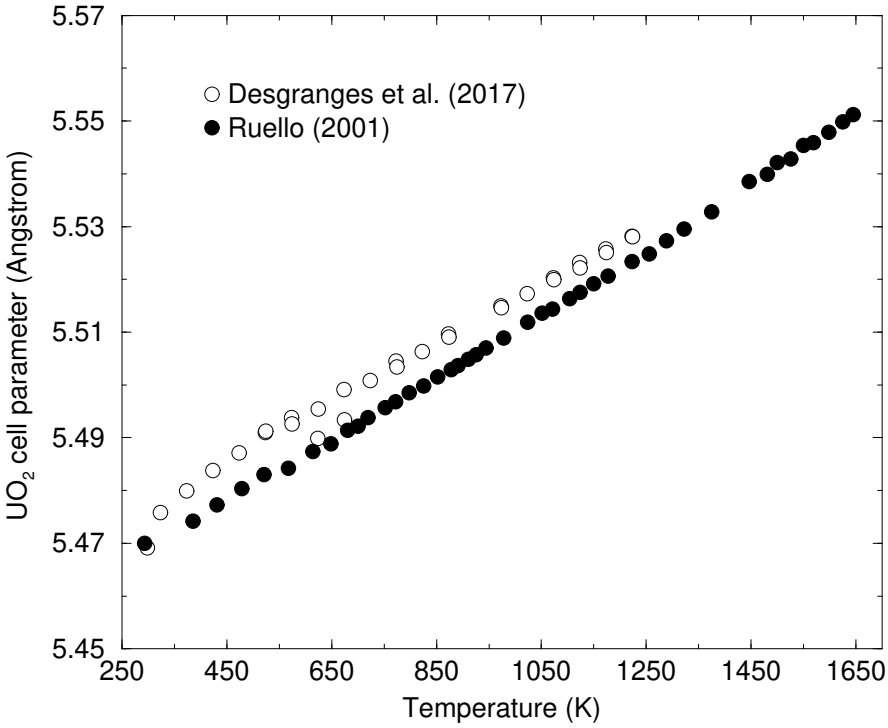

Figure 4.4.: Temperature-dependent cell parameters for UO_2 obtained by Ruello (Pascal Ruello 2001) and Desgranges (Desgranges, Y. Ma, Garcia, et al. 2017) from the Rietveld refinement of neutron diffraction patterns measured on the D20 and D4 diffractometers, respectively.

4.2. Experimental validations

4.2.1. Calculation scheme

The calculation scheme used in this work are summarized in Fig. 4.5. The first step consists in producing with the CINEL processing tool an application library that contains temperature-dependent neutron scattering cross sections, which are stored in ascii files by following the ENDF-6 format requirements for TSLs (Trkov and D. A. Brown 2018). The second step consists in simulating the neutron diffraction experiments with the Monte-Carlo code TRIPOLI-4®. The high performance computing capabilities allow to reach a relative statistical uncertainty of about ±0.5% on the top of the Bragg peaks (and ±5.0% in between) in a few minutes for a given temperature. The last step is devoted to account for experimental corrections not introduced in the Monte-Carlo simulations. The theoretical neutron yield Y_{th}^{T} as a function of the scattering angle θ is calculated from the neutron yields Y_{T4}^{T} provided by TRIPOLI-4® as follows:

$$Y_{\text{th}}^{T}(\theta) = \int_{0}^{2\pi} R_{\theta}(\theta')\, Y_{\text{T4}}^{T}(\theta' + \Delta\theta)\, \mathrm{d}\theta' + C_{\text{bkg}}, \tag{4.1}$$

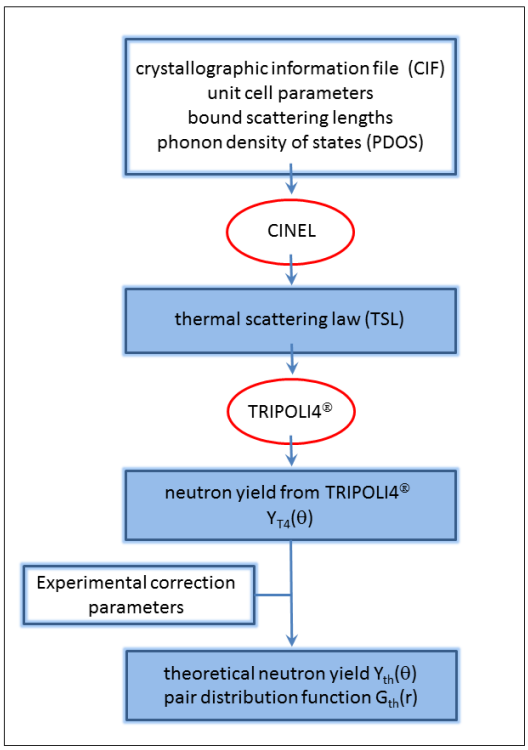

Figure 4.5.: Flow chart presenting the processing steps from the crystallographic information file to the theoretical neutron scattering yield and atomic pair distribution function.

in which C_{bkg} represents a constant background, $\Delta\theta$ accounts for a non-zero angular offset and $R_\theta(\theta')$ stands for the angular response function of the diffractometer. The angular offset is given by (McCusker, Von Dreele, Cox, et al. 1999):

$$\Delta\theta = C + \frac{x\sin(\theta) - y\cos(\theta)}{L}, \tag{4.2}$$

where C is a constant angular shift and (x, y) accounts for the sample displacement from the center of the diffractometer of radius L. In this work, the angular response function of the instrument is approximated by a Gaussian, whose full width at half maximum (FWHM) is given by the Caglioti expression (Caglioti, Paoletti, and Ricci 1958):

$$\text{FWHM}^2(\theta) = U_1 \tan^2\left(\frac{\theta}{2}\right) + U_2 \tan\left(\frac{\theta}{2}\right) + U_3. \tag{4.3}$$

Fig. 4.6 shows the effect of the response function broadening in the case of the D4 diffractometer. For UO_2, only a few Bragg peaks are expected to be well resolved at forward scattering angles.

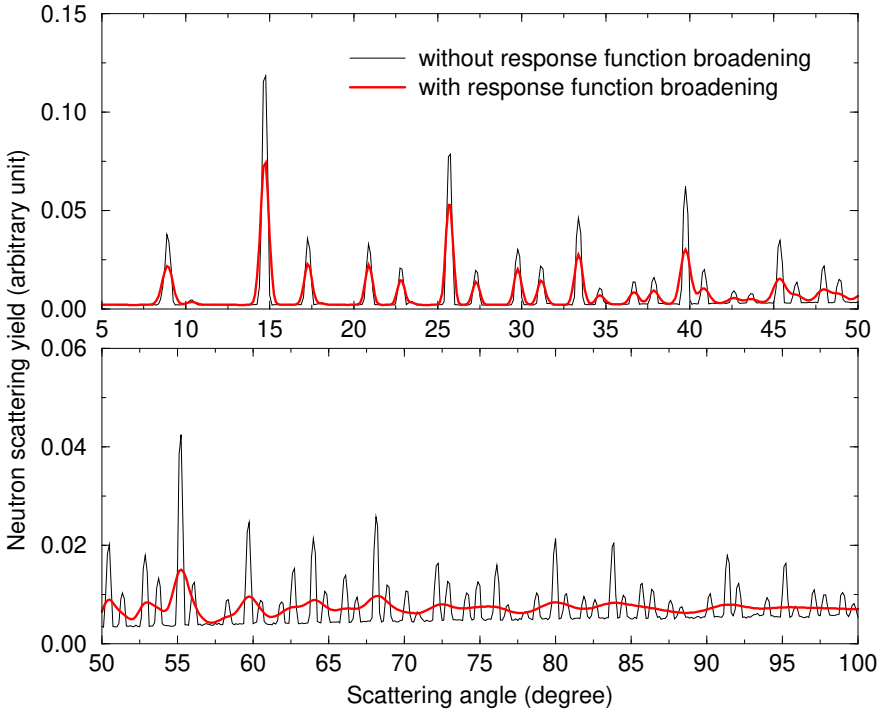

Figure 4.6.: Examples of theoretical neutron diffraction patterns simulated with the TRIPOLI-4® code at $T = 298$ K for an incident neutron energy of 331.18 meV before and after broadening with the angular response function of the D4 diffractometer.

4.2.2. Validation of the coherent elastic scattering formalism

The experimental validation of our calculation scheme (Fig. 4.5) was performed thanks to the neutron diffraction patterns of Ruello et al. (P. Ruello, Desgranges, Baldinozzi, et al. 2005) measured with the D20 diffractometer by using an incident neutron energy of $E = 48.05$ meV. As shown in Fig. 1.1, the contribution of the inelastic scattering cross sections around this energy is rather low. Therefore, the Ruello's data are suited to verify the implementation of the coherent elastic scattering formalism (cf. Eq. (2.51)) in the `CINEL` processing code and its subsequent use in TRIPOLI-4®.

No attempt was made to determine the UO_2 cell parameters as a function of the temperature. Such a work was already performed by Ruello (Pascal Ruello 2001). His results are shown in Fig. 4.4. Only experimental correction parameters involved in Eqs. (4.1), (4.2) and (4.3) were adjusted on the experimental data by using the non-linear least-squares minimization module `LMFIT` (Newville, Stensitzki, Allen, et al. 2014). The selection of the most sensitive parameters was achieved by using the Python module `SALib` (Herman and Usher 2017). The sensitivity analysis indicates that the constant shift C and the displacement x can be omitted from the fitting procedure. We have used $C = 0$ and $x = 0$ over the full temperature range of interest for this work.

Table 4.1.: Experimental correction parameters adjusted with the `LMFIT` module (Newville, Stensitzki, Allen, et al. 2014) on the diffraction patterns measured by Ruello et al. (P. Ruello, Desgranges, Baldinozzi, et al. 2005) on D20 at 292 K.

Parameters	Values	Correlation matrix				
y/L	-0.075(3)	100				
C_{bkg}	0.0024(1)	0	100			
U_1	1.49(5)	0	-14	100		
U_2	-1.01(7)	1	8	-96	100	
U_3	0.25(2)	-1	-6	91	-98	100

Table 4.2.: Final values of the experimental correction parameters used in this work to describe the diffraction patterns measured by Ruello et al. (P. Ruello, Desgranges, Baldinozzi, et al. 2005) on D20 up to 1664 K.

Parameters	Temperatures	Values
U_1	292-1664 K	1.49(5)
U_2	292-1664 K	-1.01(7)
U_3	292-1664 K	0.25(2)
y/L	292-1664 K	-0.081(1)
C_{bkg}	292 K	0.00245(8)
C_{bkg}	478 K	0.00233(8)
C_{bkg}	614 K	0.00204(8)
C_{bkg}	752 K	0.00234(8)
C_{bkg}	891 K	0.00217(8)
C_{bkg}	1051 K	0.00214(8)
C_{bkg}	1223 K	0.00195(9)
C_{bkg}	1375 K	0.00192(8)
C_{bkg}	1500 K	0.00192(8)
C_{bkg}	1664 K	0.00172(9)

The posterior values for the ratio y/L, the constant background C_{bkg} and U_i (i = 1,2,3) are reported in Table 4.1 for T = 292 K. The correlation matrix shows that negligible correlation coefficients exist between the angular offset, the background corrections and the response function parameters involved in the Caglioti expression. In first approximation, the experimental corrections can be assumed as independent from each other. Consequently, we decided to use the response function parameters U_i (i=1,2,3) established at 292 K for all the measured temperatures, in order to no longer smooth out possible temperature effects with the experimental broadening. The angular offset ratio y/L is a free parameter common to all the neutron diffraction patterns. Only the background correction C_{bkg} is a temperature-dependent free parameter.

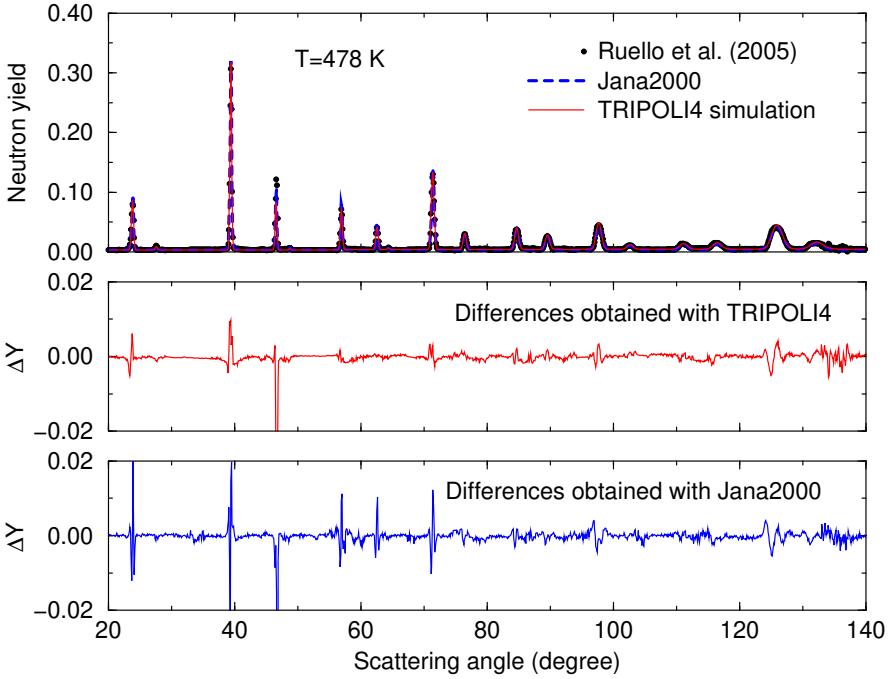

Figure 4.7.: Examples of theoretical results obtained with the TRIPOLI-4® code and the Jana2000 refinement software (Petříček, Dušek, and Palatinus 2014) in the case of the UO_2 diffraction pattern measured on D20 (E = 48.05 meV) at 478 K. ΔY represents the difference between the theory and the experiment.

The final values of the parameters are listed in Table 4.2. The average angular offset ratio of -0.081 is slightly lower than the values obtained at T = 292 K (-0.075). This trend can be explained by the displacement of the sample during the temperature rise or by a temperature-compensating bias introduced during the determination of the cell parameters. The mismatch between these two sources of uncertainties as well as the sample environment which is not the same between the D4 and D20 experiments may explain the differences observed between the two sets of cell parameters shown in

Fig. 4.4. The peak-shift obtained by Rietveld refinements is discussed in Ref. (Tsubota, Paik, and Kitagawa 2019) through the review of discrepant cell parameters reported in the literature.

The result obtained at $T = 478$ K with our calculation scheme is compared in Fig. 4.7 with the diffraction pattern obtained by G. Baldinozzi (Baldinozzi 2021) with the crystallographic computing system Jana2000 (Petříček, Dušek, and Palatinus 2014). In both cases, the treatment of the experimental corrections relies on the same steps as presented through Eqs. (4.1) to (4.3). In the case of the Jana2000 calculations, the asymmetry of the diffraction-lines was tentatively accounted by applying the anisotropic microstrain model formulated by Stephens (Stephens 1999) for a cubic symmetry. The quality of each fitting procedure is illustrated by the difference $\Delta Y = Y^T_{\text{th}}(\theta) - Y^T_{\text{exp}}(\theta)$ between the theory and the experiment. The amplitude of the differences located at the Bragg peak positions is nearly similar between the two approaches. It highlights the difficulty to define an asymmetric response function at the forward angles which smoothly becomes symmetric with increasing scattering angles. Various solutions are reported in the literature which distinguish the diffraction optic contributions to the crystallite size and strain components.

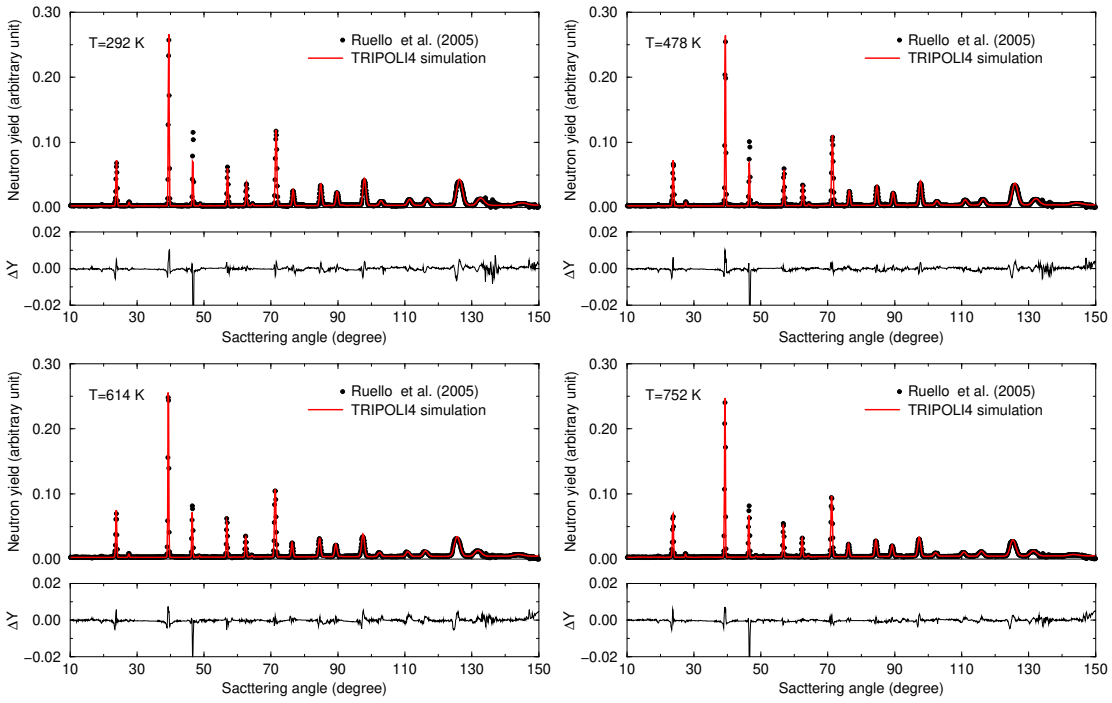

Figure 4.8.: Experimental and theoretical UO_2 diffraction patterns for D20 from 292 to 1664 K ($E = 48.05$ meV).

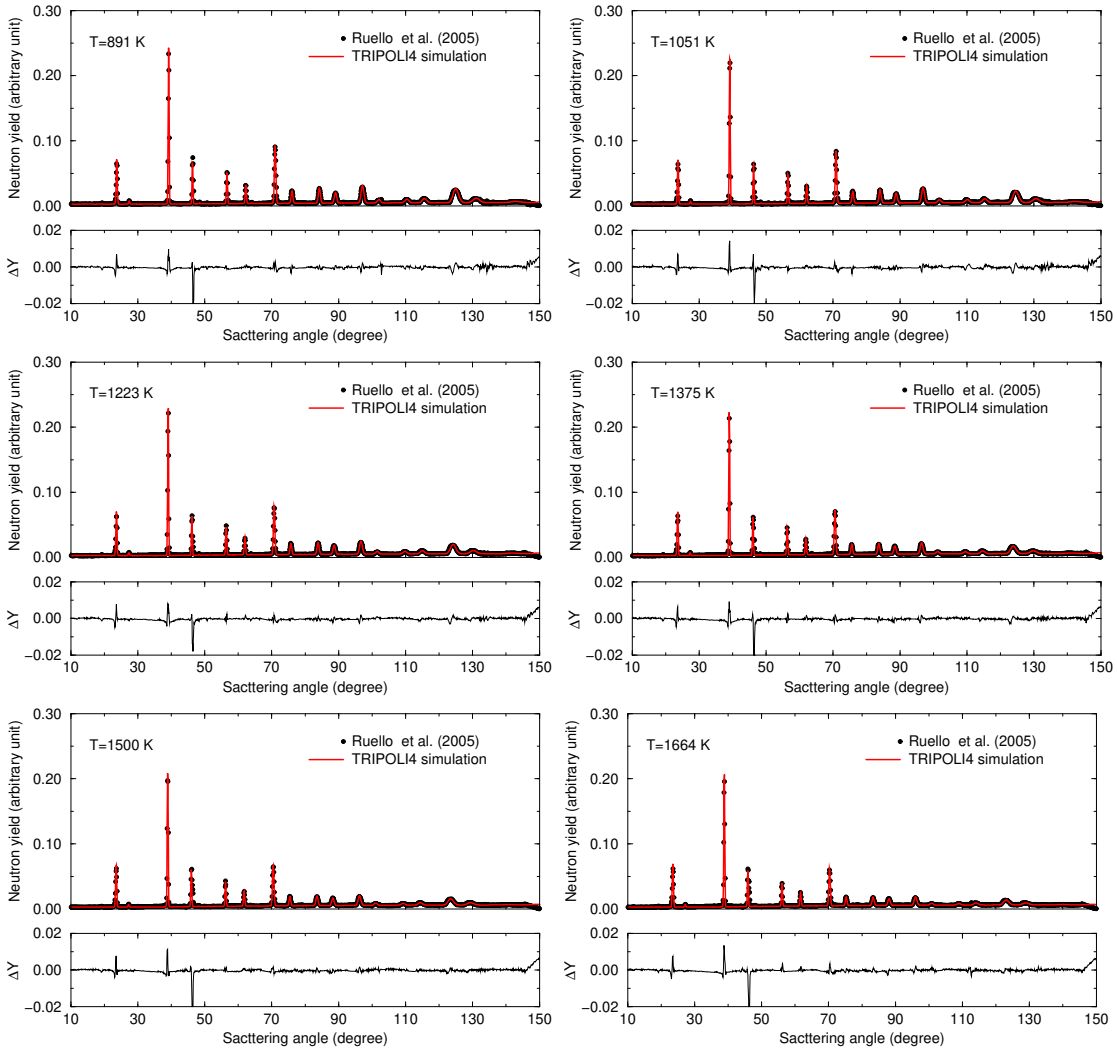

Figure 4.9.: (continued) Experimental and theoretical UO_2 diffraction patterns for D20 from 292 to 1664 K (E = 48.05 meV). A comparison of the results obtained at these two temperatures is shown in Fig. 4.10. ΔY stands for the difference between the theory and the experiment.

Final calculated curves are compared to the experimental results in Fig. 4.9 up to 1664 K. No meaningful anomalies with increasing temperatures were observed through the behavior of ΔY as a function of the scattering angles. Nearly equivalent ΔY variations are obtained whatever the temperature is. The theoretical shape of the Bragg edges at the forward scattering angles could be improved by introducing an anisotropic diffraction-line model, as proposed in Rietveld structure refinement softwares. Despite such an additional correction, which is not taken into account in the present work, the closer comparison of the experimental and theoretical diffraction patterns, shown in Fig. 4.10, confirms that the TRIPOLI-4® code is suitable for a quantitative analysis of the diffraction data by using a few numbers of free parameters. The same figure also shows that the increasing contribution of the inelastic scatter-

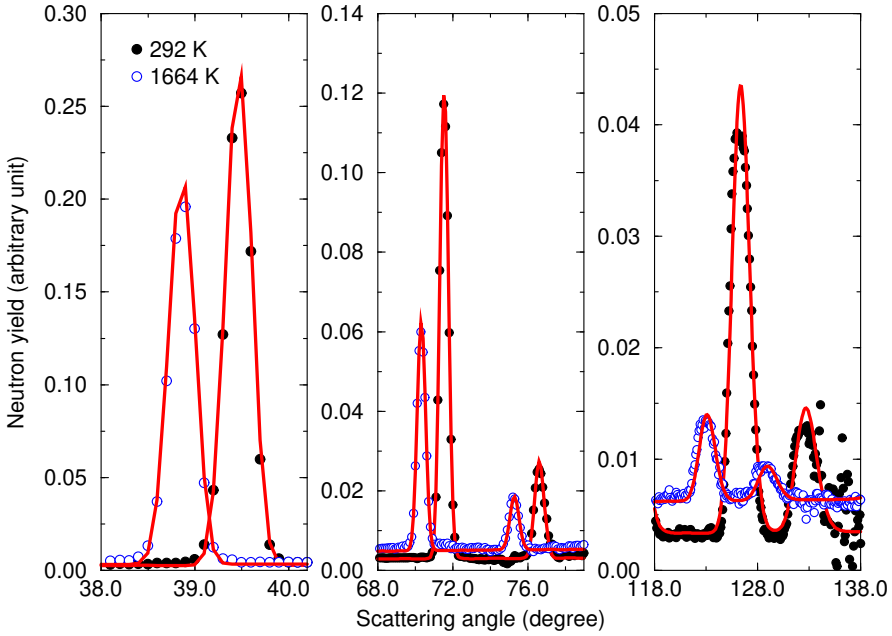

Figure 4.10.: Examples of experimental and theoretical UO_2 diffraction patterns (D20, $E = 48.05$ meV) obtained at 292 and 1664 K over three scattering angle ranges. The red solid lines represent the TRIPOLI-4® results.

ing with the temperature is pretty well reproduced by the Monte-Carlo calculations. However, this scattering component is rather low in the case of the D20 experiment which was performed with neutrons of energy $E = 48.05$ meV (Fig. 1.1). Such an issue is discussed in the next section thanks to results obtained with the D4 instrument.

4.2.3. Validation of the inelastic scattering formalism

The neutron diffraction patterns measured by Desgranges et al. (Desgranges, Y. Ma, Garcia, et al. 2017) on D4 are of great interest for testing the contribution of the inelastic scattering cross sections of uranium and oxygen in UO_2 on a dense temperature grid ranging from 298 to 1273 K. Fig. 1.1 shows that $\sigma_j^{\text{inel}}(E)$ is no longer negligible around $E = 331.18$ meV. As shown in Fig. 4.11, its contribution looks like a smooth background below the Bragg edges.

The strategy used to analyse the Ruello's data was also applied to the Desgranges' data. The cell parameters introduced in the neutron cross section formalism are shown in Fig. 4.4. Experimental parameters whose values were optimized on the neutron diffraction patterns are listed in Table 4.3. The response function parameters involved in the Caglioti expression (Eq. (4.3)) were determined at 298 K and kept fixed up to 1273 K. The fitting procedure provided correlation coefficients between U_i ($i = 1,2,3$) as strong as those obtained for D20 (Table 4.1). In the case of D4, an average angular offset was determined over the full temperature range by fitting both the constant shift C and displacement x (Eq. (4.2)).

Table 4.3.: Final values of the experimental correction parameters used in this work to describe the diffraction patterns measured by Desgranges et al. (Desgranges, Y. Ma, Garcia, et al. 2017) on D4 up to 1273 K.

Parameters	Temperatures	Values
U_1	298-1273 K	9.49(33)
U_2	298-1273 K	-3.80(19)
U_3	298-1273 K	0.53(3)
C	298-1273 K	0.106(2)
x/L	298-1273 K	0.210(4)
C_{bkg}	298 K	0.00119(3)
C_{bkg}	323 K	0.00146(3)
C_{bkg}	373 K	0.00162(3)
C_{bkg}	423 K	0.00172(4)
C_{bkg}	473 K	0.00179(4)
C_{bkg}	523 K	0.00183(4)
C_{bkg}	573 K	0.00185(4)
C_{bkg}	623 K	0.00189(4)
C_{bkg}	673 K	0.00182(4)
C_{bkg}	723 K	0.00177(4)
C_{bkg}	773 K	0.00174(4)
C_{bkg}	823 K	0.00170(5)
C_{bkg}	873 K	0.00171(5)
C_{bkg}	973 K	0.00161(5)
C_{bkg}	1023 K	0.00158(5)
C_{bkg}	1073 K	0.00149(5)
C_{bkg}	1123 K	0.00150(5)
C_{bkg}	1173 K	0.00145(5)
C_{bkg}	1223 K	0.00144(6)
C_{bkg}	1273 K	0.00128(6)

Fig. 4.12 compares the experimental and theoretical neutron diffraction patterns for D4, in which the lin-log representation highlights the increasing inelastic scattering contribution with the scattering angle. For the sake of clarity, only a few sets of temperature are shown. As already illustrated with Fig. 4.6, the response function of the D4 instrument makes it difficult the individual identification of the Bragg peaks above scattering angles greater than a few tens of degrees. Below $\theta = 60°$, a satisfactory agreement is achieved between the experimental and theoretical structures observed over the entire temperature range (Fig. 4.13).

Interesting differences between the experimental values and the theoretical curves are observed at the forward scattering angles (see green arrows in Fig. 4.12). They indicate that the constant background C_{bkg} introduced in Eq. (4.1) is not able to provide an accurate description of the data. The origin of such non-zero background

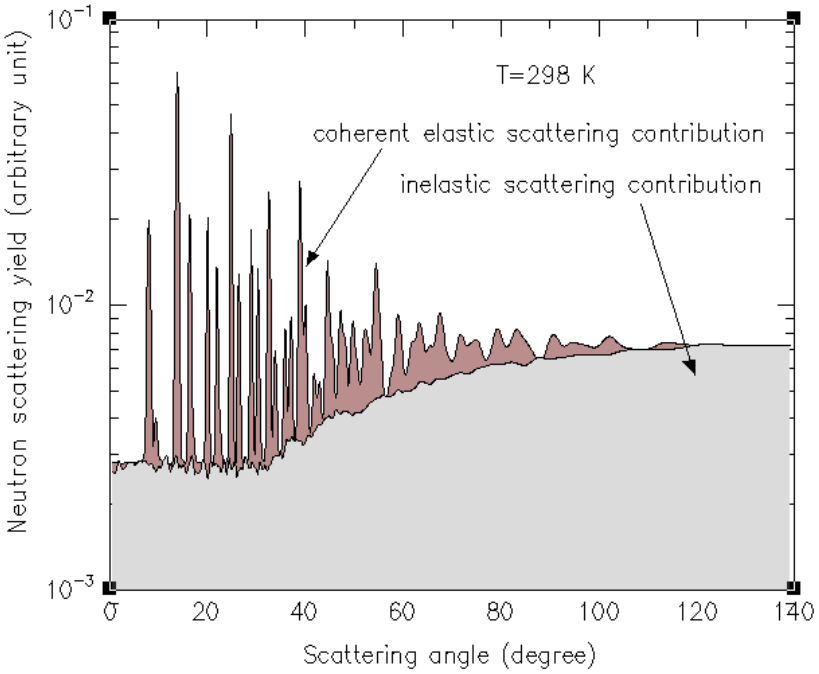

Figure 4.11.: Inelastic and coherent elastic scattering contributions simulated with the TRIPOLI-4® code at $T = 298$ K for D4 ($E = 331.18$ meV).

correction issues as a function of the scattering angle is not well understood and needs further investigations. This result confirms that, in complement to inelastic neutron scattering instruments, the characteristics of the D4 diffractometer are suited to challenge the angular anisotropy of the neutron inelastic scattering calculated under the harmonic or Gaussian, incoherent and cubic approximations (cf. Section (2.2.2)), of which the accuracy of the Gaussian approximation as a function of the momentum transfer is discussed in Refs. (Nijboer and Rahman 1966; Schober 2014).

4.2.4. From neutron diffraction patterns to atomic pair distribution functions

The experimental program carried out on the D4 diffractometer was originally designed to investigate the validity of the $Fm\bar{3}m$ symmetry as a function of the temperature. Deviations from the average structure of UO_2 have been analyzed via atomic pair distribution functions $G(r)$, which give the probability of finding an atom at a distance r from a given atom. The expression of $G(r)$ depends on the total scattering structure factor $S(Q)$:

$$G(r) = \frac{2}{\pi} \int_{Q_{\min}}^{Q_{\max}} Q(S(Q) - 1) \sin(Qr) dQ. \tag{4.4}$$

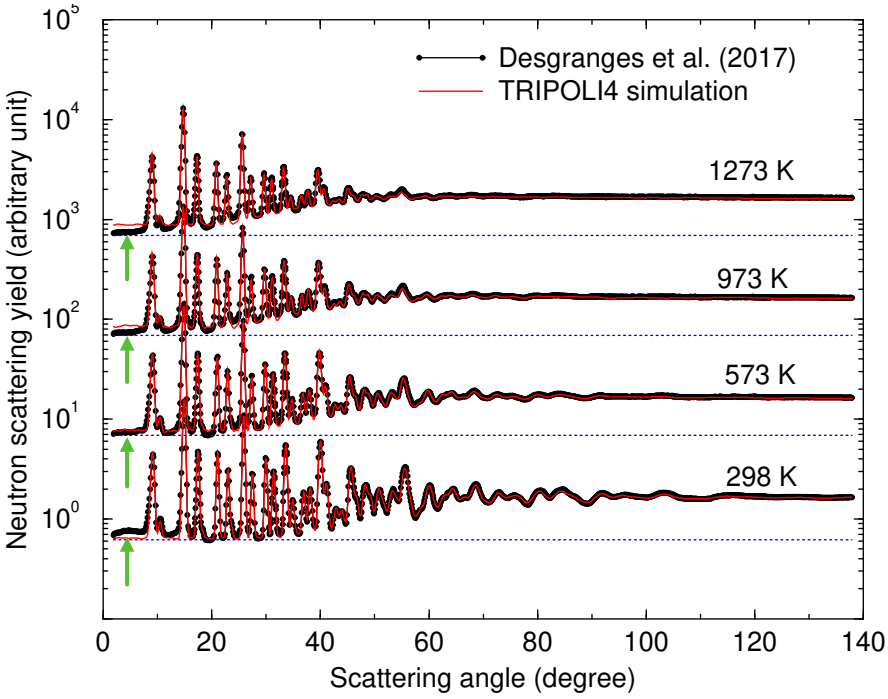

Figure 4.12.: Experimental and theoretical UO_2 diffraction patterns for D4 from 298 to 1273 K (E = 331.18 meV). A comparison of the results obtained at these two temperatures is shown in Fig. 4.13. The green arrows highlight the differences observed between the experiment and the theory at the forward scattering angles. The dotted blue lines show the increasing inelastic scattering contribution with the scattering angle.

For neutron diffraction experiments, $S_{\text{exp}}(Q)$ is defined as follow:

$$S_{\text{exp}}(Q) = \frac{Y^T_{\text{exp}}(Q)\,(1-\mathscr{P}(Q)) - \sum_{j=1}^{N_{\text{unit cell}}} c_j |b_j|^2}{|\sum_{j=1}^{N_{\text{unit cell}}} c_j b_j|^2} + 1, \tag{4.5}$$

where $c_j = 1/N_{\text{unit cell}}$ and b_j represent the concentration and the bound scattering length of the j-th atom in the unit cell of the studied material. The inelasticity correction $1-\mathscr{P}(Q)$ was taken form the work of Desgranges, in which a Placzek-type analytical correction (Placzek 1952) was applied to the normalized experimental neutron scattering yields. The proposed correction is well appropriate to the D4 experiment that involves heavy atoms and an incident neutron energy of E = 331.18 meV. These conditions allow to assume that the average amount of energy exchanged with the scattering system is small compared to the excitation energies of that system.

The experimental and theoretical atomic pair distribution functions for UO_2 are compared in Fig. 4.14 from room temperature to 1273 K. The Monte-Carlo simulations were performed by using the $Fm\bar{3}m$ group space with harmonic atomic vibrations. The first three peaks mainly correspond to the U-O, O-O and U-U bonds (Palomares,

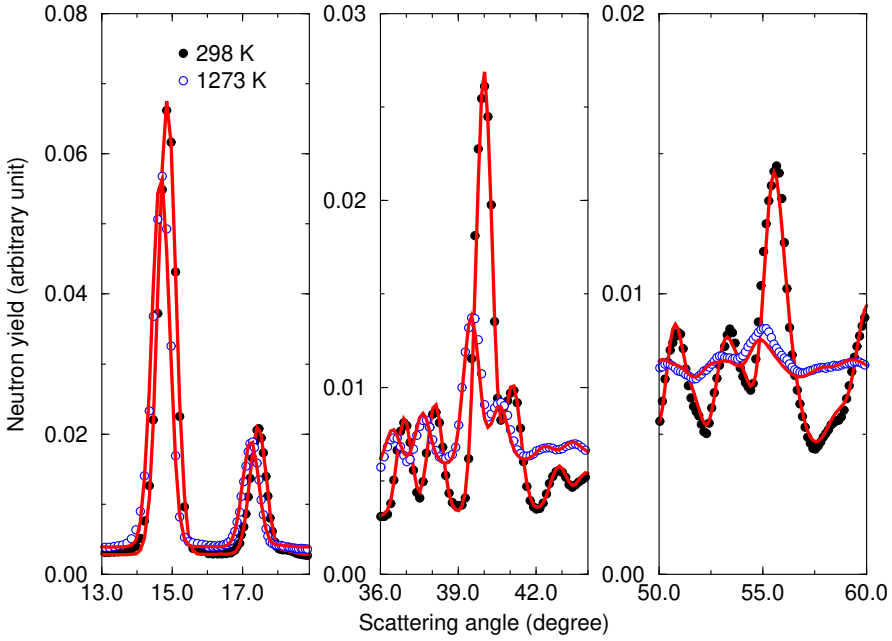

Figure 4.13.: Examples of experimental and theoretical UO_2 diffraction patterns (D4, $E = 331.18$ meV) obtained at 298 and 1273 K over three scattering angle ranges. The red solid lines represent the TRIPOLI-4® results.

McDonnell, Yang, et al. 2019). A closer inspection of the experimental results indicates a negative peak-shift of -0.010(5) Å for the U-O bond from 298 K to 1273 K, while the peak position of the U-U bond increases by +0.020(5) Å. By contrast, the Monte-Carlo simulations provide positive peak-shifts which are close to +0.040(5) Å for both U-O and U-U bonds.

Our calculations agree with past works reported in the literature. They all conclude that the arrangement of the uranium and oxygen atoms cannot be described in term of an ideal fluorite structure at elevated temperature. The observed differences between the experiment and the theory correspond to an unexpected shortening of the U-O distance with increasing temperature. The underlying mechanism is not well understood. It is the subject of debates in the literature. Willis interprets the temperature effects on the lattice arrangement in terms of anharmonic atomic vibrations (Willis 1963b; Willis, B.T.M. 1964; Willis and Hazell 1980). Similarly, Skinner et al. (Skinner, Benmore, Weber, et al. 2014) favor atomic disorder mechanisms in the $Fm\bar{3}m$ group space for explaining the U-O and U-U bond lengths deduced from X-ray diffraction patterns measured up to the UO_2 melting point. By contrast, the existence of a local symmetry (such as $Pa\bar{3}$) is suggested by Desgranges et al. (Desgranges, Y. Ma, Garcia, et al. 2017) for explaining the shortening of the U-O distance at 1273 K (Fig. 4.14). These different approaches are discussed in the next section.

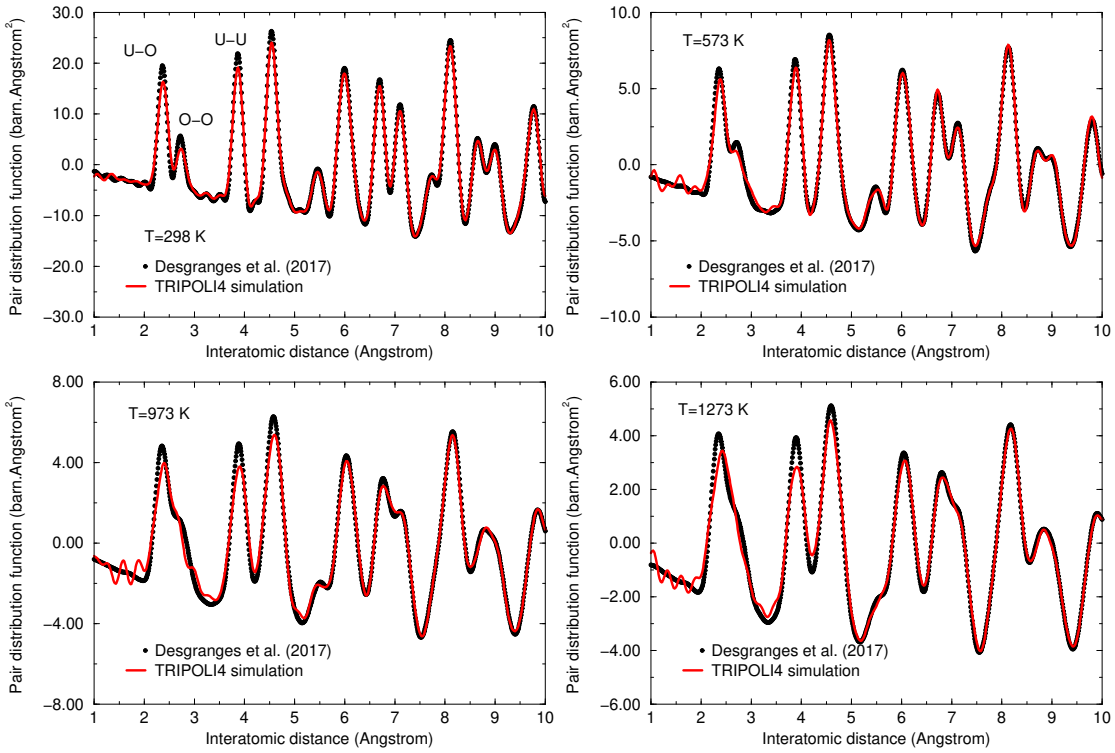

Figure 4.14.: Experimental and theoretical atomic pair distribution functions for UO_2 (D4, E = 331.18 meV). The TRIPOLI-4® simulation were performed by using the Fm$\bar{3}$m space group with harmonic atomic vibrations. The first three peaks mainly corresponds to the U-O, O-O and U-U bonds (Palomares, McDonnell, Yang, et al. 2019).

4.3. Perspectives for improving the CINEL calculations

4.3.1. Investigation of a four-site model for the oxygen atoms

On the basis of single-crystal neutron diffraction data on UO_2 measured from 293 to 1373 K, Willis notices that a better agreement between the calculated and the experimental data is obtained by relaxing the oxygen atoms from their regular positions in the ideal fluorite structure (Willis 1963b). In this model, the uranium atoms remain in the same positions (0, 0, 0), (0, 1/2, 1/2), (1/2, 0, 1/2) and (1/2, 1/2, 0), while every single oxygen atom is split into four 1/4 atom and they are located in the (111) directions toward the four neighbored interstices with a relaxation term δ. Detailed positions of the oxygen atoms in the four-site model are presented in Table 4.4.

As all the coordinates of the atom position are known, the form factor given by Eq. (2.52) can be explicitly expressed for the four-site model as follow:

Table 4.4.: Oxygen site occupancy in the UO_2 unit cell in the case of the ideal fluorite structure and four-site model.

Ideal fluorite structure			Four-site model		
x	y	z	x	y	z
1/4	1/4	1/4	$1/4+\delta$	$1/4+\delta$	$1/4+\delta$
			$1/4+\delta$	$1/4-\delta$	$1/4-\delta$
			$1/4-\delta$	$1/4+\delta$	$1/4-\delta$
			$1/4-\delta$	$1/4-\delta$	$1/4+\delta$
1/4	3/4	3/4	$1/4+\delta$	$3/4+\delta$	$3/4+\delta$
			$1/4+\delta$	$3/4-\delta$	$3/4-\delta$
			$1/4-\delta$	$3/4+\delta$	$3/4-\delta$
			$1/4-\delta$	$3/4-\delta$	$3/4+\delta$
3/4	1/4	3/4	$3/4+\delta$	$1/4+\delta$	$3/4+\delta$
			$3/4+\delta$	$1/4-\delta$	$3/4-\delta$
			$3/4-\delta$	$1/4+\delta$	$3/4-\delta$
			$3/4-\delta$	$1/4-\delta$	$3/4+\delta$
3/4	3/4	1/4	$3/4+\delta$	$3/4+\delta$	$1/4+\delta$
			$3/4+\delta$	$3/4-\delta$	$1/4-\delta$
			$3/4-\delta$	$3/4+\delta$	$1/4-\delta$
			$3/4-\delta$	$3/4-\delta$	$1/4+\delta$
3/4	3/4	3/4	$3/4-\delta$	$3/4-\delta$	$3/4-\delta$
			$3/4-\delta$	$3/4+\delta$	$3/4+\delta$
			$3/4+\delta$	$3/4-\delta$	$3/4+\delta$
			$3/4+\delta$	$3/4+\delta$	$3/4-\delta$
3/4	1/4	1/4	$3/4-\delta$	$1/4-\delta$	$1/4-\delta$
			$3/4-\delta$	$1/4+\delta$	$1/4+\delta$
			$3/4+\delta$	$1/4-\delta$	$1/4+\delta$
			$3/4+\delta$	$1/4+\delta$	$1/4-\delta$
1/4	3/4	1/4	$1/4-\delta$	$3/4-\delta$	$1/4-\delta$
			$1/4-\delta$	$3/4+\delta$	$1/4+\delta$
			$1/4+\delta$	$3/4-\delta$	$1/4+\delta$
			$1/4+\delta$	$3/4+\delta$	$1/4-\delta$
1/4	1/4	3/4	$1/4-\delta$	$1/4-\delta$	$3/4-\delta$
			$1/4-\delta$	$1/4+\delta$	$3/4+\delta$
			$1/4+\delta$	$1/4-\delta$	$3/4+\delta$
			$1/4+\delta$	$1/4+\delta$	$3/4-\delta$

$$F_{4s}(\vec{\tau}_{hkl}) = \begin{cases} 4b_U \exp\left(-\frac{\hbar^2\tau_{hkl}^2}{4M_U k_B T}\Lambda_U(T)\right) + 8b_O \exp\left(-\frac{\hbar^2\tau_{hkl}^2}{4M_O k_B T}\Lambda_O(T)\right) f_1 & \text{if } h+k+l=4n \text{ and } h,k,l \text{ all even} \\ 4b_U \exp\left(-\frac{\hbar^2\tau_{hkl}^2}{4M_U k_B T}\Lambda_U(T)\right) + 8b_O \exp\left(-\frac{\hbar^2\tau_{hkl}^2}{4M_O k_B T}\Lambda_O(T)\right) f_2 & \text{if } h+k+l=4n+1 \text{ and } h,k,l \text{ all odd} \\ 4b_U \exp\left(-\frac{\hbar^2\tau_{hkl}^2}{4M_U k_B T}\Lambda_U(T)\right) - 8b_O \exp\left(-\frac{\hbar^2\tau_{hkl}^2}{4M_O k_B T}\Lambda_O(T)\right) f_1 & \text{if } h+k+l=4n+2 \text{ and } h,k,l \text{ all even} \\ 4b_U \exp\left(-\frac{\hbar^2\tau_{hkl}^2}{4M_U k_B T}\Lambda_U(T)\right) - 8b_O \exp\left(-\frac{\hbar^2\tau_{hkl}^2}{4M_O k_B T}\Lambda_O(T)\right) f_2 & \text{if } h+k+l=4n+3 \text{ and } h,k,l \text{ all odd} \\ 0 & \text{otherwise} \end{cases}, \quad (4.6)$$

in which $f_1 = \cos(2\pi\delta h)\cos(2\pi\delta k)\cos(2\pi\delta l)$ and $f_2 = \sin(2\pi\delta h)\sin(2\pi\delta k)\sin(2\pi\delta l)$. Willis proposed to rewrite Eq. (4.6) in the following compact form:

$$F_{4s}(\vec{\tau}_{hkl}) = \begin{cases} 4b_U \exp\left(-\frac{\hbar^2\tau_{hkl}^2}{4M_U k_B T}\Lambda_U(T)\right) + 8b_O \exp\left(-\frac{\hbar^2\tau_{hkl}^2}{4M_O k_B T}\Lambda_O(T)\right) f_{4s} & \text{if } h,k,l \text{ all odd or all even} \\ 0 & \text{otherwise} \end{cases}, \quad (4.7)$$

with

$$f_{4s} = \cos\left(2\pi h\left(\frac{1}{4}+\delta\right)\right)\cos\left(2\pi k\left(\frac{1}{4}+\delta\right)\right)\cos\left(2\pi l\left(\frac{1}{4}+\delta\right)\right). \quad (4.8)$$

The implementation of the four-site model in the CINEL code leads to the theoretical results shown in Fig 4.15a, which were obtained in the case of the D4 experiment for $T = 1273$ K with a relaxation term $\delta = 0.0177$ given in Ref. (Desgranges, Y. Ma, Garcia, et al. 2017). Compared to the ideal fluorite structure, no improvement is observed at elevated temperature when the four-site model is introduced in the fitting procedure. The differences with the experimental values increase with the hkl values in the scattering angle range shown in Fig 4.15a.

In the case of an ideal fluorite structure ($\delta = 0$), Eq. (4.6) shows that the intensity of the form factor for $h+k+l = 4n$ is more important than that of $h+k+l = 4n \pm 1$ and $h+k+l = 4n+2$, because in such a case the uranium and oxygen atoms scatter in-phase. For $h+k+l = 4n+2$, the intensity of the form factor is weak because they scatter out-of-phase. For $h+k+l = 4n \pm 1$, the intensity is medium since only the uranium atoms contribute to the scattering. The introduction of the relaxation term $\delta \neq 0$ not only weaken the strongest in-phase scattering, but also strengthen the weakest out-of-phase scattering. Such an effect increases with the hkl values until its peak value, and decreases for large hkl values because of the dominance of the exponential term in Eq. (4.7) which involves $-\tau_{hkl}^2$. As a consequence, the four-site model proposed by Willis is not an adequate solution to introduce an oxygen disorder mechanism in the CINEL model.

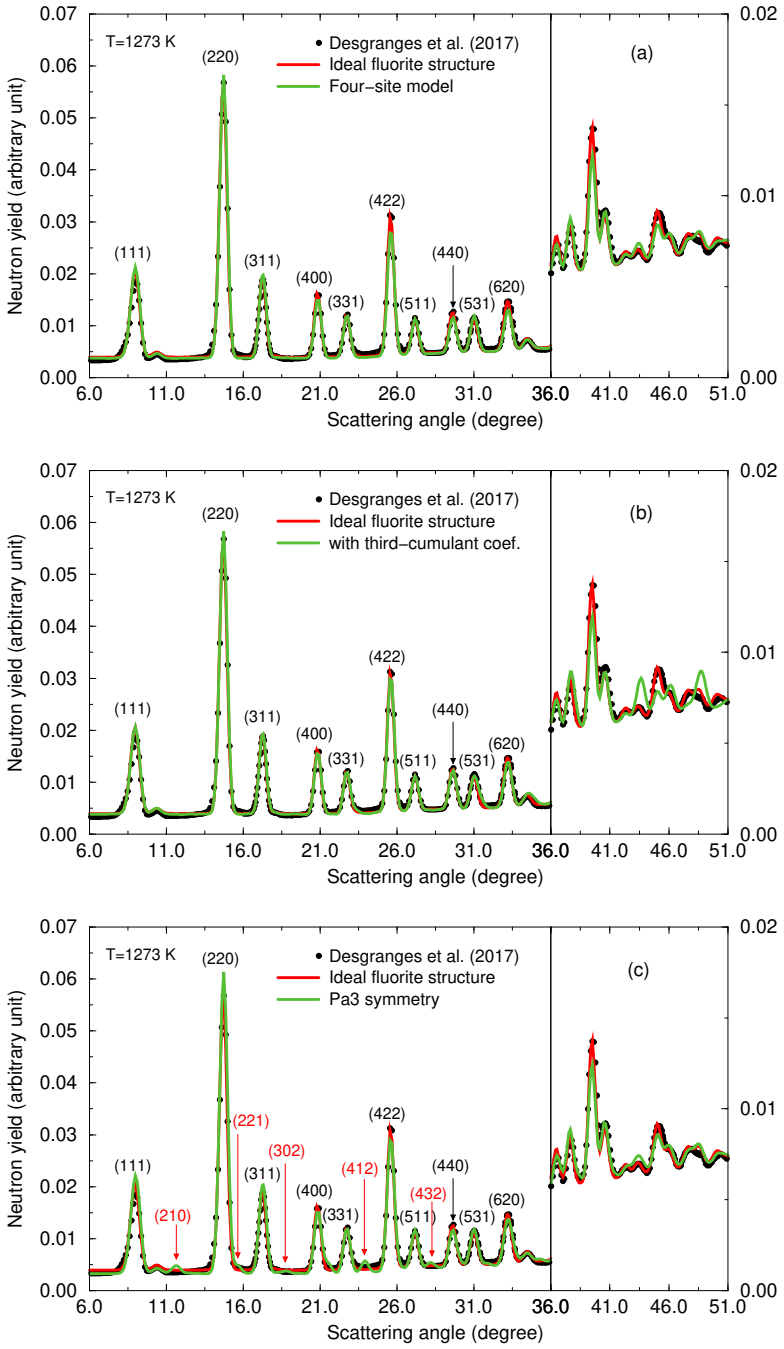

Figure 4.15.: The experimental diffraction patterns measured on D4 at $T = 1273$ K ($E = 331.18$ meV) and theoretical results obtained with the ideal fluorite structure are compared to results obtained with (a) a four-site model for the oxygen atoms with a relaxation term $\delta = 0.0177$, (b) a structure factor equation with a non-zero anharmonic third-cumulant coefficient for the oxygen atoms ($c^{O}_{123} = 0.0017$ and (c) a $Pa\bar{3}$ symmetry with the same relaxation term as in the four-site model ($\delta = 0.0177$). The (hkl) plans for the fluorite structure are indicated in black for the well resolved peaks observed below $\theta = 36°$. The additional (hkl) peaks due to the $Pa\bar{3}$ symmetry are indicated in red.

4.3.2. Investigations of a non-zero anharmonic third-cumulant coefficient for the oxygen atoms

In order to favor anharmonic oxygen vibrations in the fluorite structure instead of a disorder mechanism only based on the displacement of the oxygen atoms from their equilibrium positions, Willis and Hazell (Willis and Hazell 1980) re-analyzed the single-crystal diffraction data on UO_2 (Section 4.3.1) by introducing third-cumulant coefficients in the form factor $F(\vec{\tau}_{hkl})$ (Eq. (2.52)). In theory, there are up to ten third-cumulant coefficients for each atom j. However, Willis and Hazell concluded that only the third-cumulant coefficient of the oxygen atoms c^{O}_{123} is non-vanishing when using the symmetry properties of the ideal fluorite structure. According to their work, the anharmonic form factor becomes:

$$F_{\mathrm{anhar}}(\vec{\tau}_{hkl}) = \sum_{j=1}^{N_{\mathrm{unit\,cell}}} b_j \exp\left(-\frac{\hbar^2\tau^2_{hkl}}{4M_j k_B T}\Lambda_j(T)\right)\exp\left(i\vec{\tau}_{hkl}\cdot\vec{p}_j - i\delta_{j\mathrm{O}}c^{\mathrm{O}}_{123}\tau^3_{hkl}\right), \quad (4.9)$$

where $\delta_{j\mathrm{O}}$ is the Kronecker delta function which is equal to 1 if atom j is oxygen and 0 for uranium. By analogy with Eq. (4.7), $F_{\mathrm{anhar}}(\vec{\tau}_{hkl})$ can be rewritten as

$$F_{\mathrm{anhar}}(\vec{\tau}_{hkl}) = \begin{cases} 4b_U \exp\left(-\frac{\hbar^2\tau^2_{hkl}}{4M_U k_B T}\Lambda_U(T)\right) + 8b_O \exp\left(-\frac{\hbar^2\tau^2_{hkl}}{4M_O k_B T}\Lambda_O(T)\right) f_{\mathrm{anhar}} & \text{if } h, k, l \text{ all odd or all even} \\ 0 & \text{otherwise} \end{cases}, \quad (4.10)$$

with

$$f_{\mathrm{anhar}} = \exp\left(-ic^{\mathrm{O}}_{123}\tau^3_{hkl}\right)\cos\left(\pi\frac{h}{2}\right)\cos\left(\pi\frac{k}{2}\right)\cos\left(\pi\frac{l}{2}\right). \quad (4.11)$$

For (hkl) peaks satisfying $h+k+l = 4n\pm1$, anharmonicity vanishes ($f_{\mathrm{anhar}} = 0$) when uranium atoms contribute to the scattering. For (hkl) peaks satisfying $h+k+l = 4n$ or $h+k+l = 4n+2$, $f_{\mathrm{anhar}} = \pm\exp\left(-ic^{\mathrm{O}}_{123}\tau^3_{hkl}\right)$ and $|F_{\mathrm{anhar}}(\vec{\tau}_{hkl})|^2$ is given by:

$$|F_{\mathrm{anhar}}(\vec{\tau}_{hkl})|^2 = |F(\vec{\tau}_{hkl})|^2 \mp 128 b_U b_O \exp\left(-\frac{\hbar^2\tau^2_{hkl}}{4k_B T}\left(\frac{\Lambda_U(T)}{M_U} + \frac{\Lambda_O(T)}{M_O}\right)\right)\sin^2\left(\frac{c^{\mathrm{O}}_{123}\tau^3_{hkl}}{2}\right), \quad (4.12)$$

in which $|F(\vec{\tau}_{hkl})|^2$ represents the square of the form factor in the case of an ideal fluorite structure.

Fig. 4.15b shows the theoretical results calculated at $T = 1273$ K in the case of the D4 experiment with an anharmonic third-cumulant coefficient c^{O}_{123} equal to 0.0017. This value was obtained from the interpolation of the results reported in Ref. (Willis and Hazell 1980). The agreement with the experiment is not improved by using $c^{\mathrm{O}}_{123} \neq 0$. On the contrary, significant differences are observed for scattering angles greater than 40°. According to Eq. (4.12), the intensity of the strongest U-O in-phase scattering will be weakened, while the weakest out-of-phase scattering will be strengthened. The present result indicates that the term $c^{\mathrm{O}}_{123}\tau^3_{hkl}$ in Eq. (4.12) is not able to simulate the anharmonic behavior of the oxygen atoms in our calculation scheme at elevated temperatures.

Table 4.5.: Oxygen site occupancy in the UO_2 unit cell in the case of the $Fm\bar{3}m$ and $Pa\bar{3}$ symmetries.

$Fm\bar{3}m$ symmetry			$Pa\bar{3}$ symmetry		
x	y	z	x	y	z
1/4	1/4	1/4	$1/4+\delta$	$1/4+\delta$	$1/4+\delta$
1/4	3/4	3/4	$1/4-\delta$	$3/4-\delta$	$3/4+\delta$
3/4	1/4	3/4	$3/4+\delta$	$1/4-\delta$	$3/4-\delta$
3/4	3/4	1/4	$3/4-\delta$	$3/4+\delta$	$1/4-\delta$
3/4	3/4	3/4	$3/4-\delta$	$3/4-\delta$	$3/4-\delta$
3/4	1/4	1/4	$3/4+\delta$	$1/4+\delta$	$1/4-\delta$
1/4	3/4	1/4	$1/4-\delta$	$3/4+\delta$	$1/4+\delta$
1/4	1/4	3/4	$1/4+\delta$	$1/4-\delta$	$3/4+\delta$

4.3.3. Investigations of the $Pa\bar{3}$ symmetry

The experimental results measured on the D4 instrument have been originally analyzed by Desgranges et al. (Desgranges, Y. Ma, Garcia, et al. 2017). They investigated the possibility of using the $Pa\bar{3}$ crystalline symmetry as a local configuration in UO_2, instead of the ideal fluorite structure, for explaining the shortening of the U-O distance with increasing temperature. In this section, we show how the theoretical diffraction patterns change when the $Pa\bar{3}$ symmetry is used as an average configuration for UO_2.

Compared to the ideal fluorite structure, the positions of the uranium atoms in the $Pa\bar{3}$ symmetry remain the same while those of oxygen are modified with a relaxation term δ (Table 4.5). The oxygen cage is thus distorted to form two long U-O distances and six short U-O distances. Such an oxygen site occupancy can be regarded as a specific configuration of the four-site model (Table 4.4). Desgranges et al. show that the first few peaks observed in the pair distribution function of UO_2 at 1273 K (Fig. 4.14) are better reproduced by distinguishing these two U-O distances.

The theoretical diffraction pattern calculated at 1273 K in the case of the D4 experiment under the assumption of the $Pa\bar{3}$ symmetry is reported in Fig. 4.15c. The differences between the experiment and the theory are nearly of the same order of magnitude than those obtained with the four-site model. The main problem compared to the ideal fluorite structure is the presence of new (hkl) peaks in the theoretical diffraction pattern which are not observed in the experimental one. According to Eq. (4.6), the Bragg diffractions in the ideal fluorite structure occur for (hkl) plan when h, k, l are all odd or all even. The distortion of the oxygen cage in the $Pa\bar{3}$ symmetry allows Bragg diffractions in (hkl) plan even if h, k, l are not all odd and not all even. In response to this drawback, outgoing experimental and theoretical works are in progress for exploring other alternative symmetries that will satisfy the average and local structures of UO_2 at elevated temperatures.

4.4. Preliminary conclusions

The results reported in this chapter indicate that the Monte-Carlo neutron transport code TRIPOLI-4® is able to reproduce neutron diffraction patterns measured at ILL up to 1664 K thanks to the newly developed processing tool `CINEL`. The neutron cross section formalism implemented in `CINEL` allows to calculate the inelastic and coherent elastic scattering contributions by using an ideal fluorite structure for UO_2 over the full temperature range. A few numbers of experimental parameters were optimized on the data to account for the angular offset, the response function of the diffractometer and a background correction. The good agreement between the experimental and theoretical neutron diffraction patterns validates our TRIPOLI-4® calculation scheme for UO_2. However some limited issues remain in the interpretation of the background correction. Biases due to theoretical approximations would need to be investigated.

The performance of our calculation scheme was also investigated by simulating atomic pair distribution functions to probe the structure of UO_2 at elevated temperature. The differences observed at 1273 K between the experiment and the theory confirm that the local deviations of the oxygen atoms from the average structure of UO_2 are not compatible with an ideal fluorite structure. We show that the `CINEL` processing tool offers the possibility of testing atomic disorder configurations, anharmonic models or space groups which are suggested in the literature for exploring the unexpected shortening of the U-O distance with increasing temperature.

5. Investigation of neutron scattering treatments in the epithermal energy range (incident neutron energy greater than a few eV)

Summary

In Chapter 4, the Monte-Carlo neutron transport code TRIPOLI-4® (E. Brun, F. Damian, Diop, et al. 2015) is used to simulate neutron powder diffraction data on stoichiometric uranium dioxide (UO_2) measured up to 1664 K with the D4 and D20 diffractometers of the ILL. The TSLs of UO_2 required for the simulation are calculated by using the data processing tool `CINEL` (cf. Chapter 3). It should be pointed out that the incident neutron energies of D4 ($E = 331.18$ meV) and D20 ($E = 48.05$ meV) are both below 1 eV. At such low energy range, the performances of the Monte-Carlo calculations with the tabulated TSLs are illustrated with the comparison between the experimental and simulated diffraction patterns and atomic pair distribution functions. In this chapter, we will investigate the neutron scattering treatments with TRIPOLI-4® for neutron energies above a few eV.

5.1. Introduction of problems

Three distinct models are routinely implemented in Monte-Carlo neutron transport codes such as `MCNP5` (Team 2003), to treat the neutron-nucleus (elastic) [1] scattering according to the incident neutron energy (Coveyou, Bate, and Osborn 1956; Zoia, Emeric Brun, Jouanne, et al. 2013). Tabulated TSLs or $S(\alpha, \beta)$ account for atomic vibration and/or diffusion behaviors of the target nuclides (Squires 2012; Schober 2014). The SVT algorithm is used to sample the velocities of the target nuclides from a M-B distribution (Coveyou, Bate, and Osborn 1956; Lux 2018). The AK approximation considers the target nuclides at rest, when the velocities of the nuclides are negligible compared to the incident neutron velocities.

The energy thresholds of the above listed neutron scattering treatments in the Monte-Carlo neutron transport code TRIPOLI-4® are illustrated in Fig. 5.1 in the case of the total cross section of ^{1}H and ^{1}H bound in ^1H_2O. Below the energy threshold near 5 eV, $S(\alpha, \beta)$ are used to determine the energies and momenta of the scattered neutrons. If $S(\alpha, \beta)$ are not available, the SVT algorithm is used instead. From 5 eV to $400 k_B T$, where k_B is the Boltzmann constant and T represents the temperature of the target nuclides, the SVT algorithm is applied to simulate the neutron-nucleus scattering. Above $400 k_B T$, the AK treatment is used.

The neutron-nucleus scattering is approximated by the two-body collision kinetics within the SVT algorithm. During each collision, the scalar velocity of the target nucleus V in the laboratory (LAB) frame can be sampled from a M-B distribution $\mathcal{M}_T(V)$ with T the temperature of the nuclei. The cosine of the angle between incident neutron and target nucleus in the LAB frame μ is sampled uniformly on the interval $[-1; 1]$. The velocity of the incident neutron is denoted as v. Then the relative velocity v_{rel} between the incident neutron and the target nucleus can be obtained by $v_{\text{rel}} = \sqrt{v^2 + V^2 - 2vV\mu}$. In the SVT algorithm, it is assumed that the neutron-nucleus

[1] Here, the term "elastic" indicates that the kinetic energies of the incident neutron and the target nucleus are conserved before and after scattering. It is different than the notion presented in Chapter 2, in which elastic scattering refers that the energy of neutron does not change before and after scattering. In order to avoid confusion, the term "elastic" will be omitted hereafter.

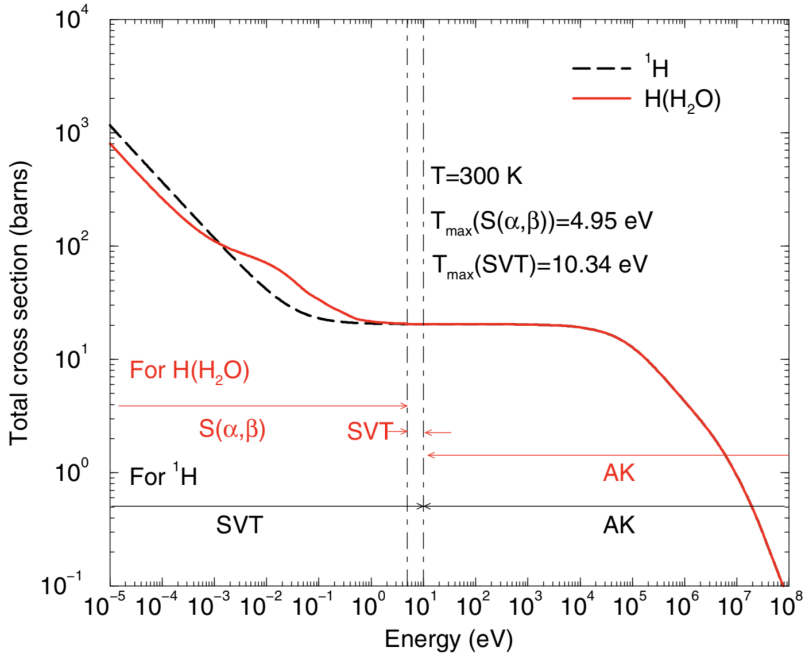

Figure 5.1.: Comparison of the hydrogen total cross-sections for free gas model (^{1}H) and hydrogen bound in water molecule (denoted as H(H_2O) in the figure) calculated at $T = 300$ K. The energy thresholds for $S(\alpha, \beta)$ and SVT are respectively 4.95 eV and $400 k_B T$, that is 10.34 eV for $T = 300$ K (Scotta, Juan Pablo, Noguere, Gilles, Bernard, David, et al. 2016).

scattering cross section at zero temperature σ_0^s is invariant with the relative velocity v_{rel}, i.e., $\sigma_0^s(v_{\text{rel}}) \approx$ constant (Carter and Cashwell 1975). The constant scattering cross section approximation is justified by the arguments that for light nuclides, $\sigma_0^s(v_{\text{rel}})$ vary slowly with the energy.

The SVT treatment for heavy nuclides with strong scattering resonances is reported to be inadequate (Dagan and Broeders 2006; Becker, R. Dagan, and Lohnert 2009). As illustrated in Fig. 5.2, the scattering and radiative capture cross sections of ^{238}U rise with several magnitudes at specific neutron energies. These abrupt variations correspond to nuclear resonances. Furthermore, it is proven that the target velocity V and the cosine of the angle between incident neutron and target nucleus μ are correlated (Rothenstein and R. Dagan 1995; Rothenstein 1996; Rothenstein and R. Dagan 1998). Thus V and μ cannot be sampled independently as performed in the SVT algorithm. To overcome the shortcomings of the application of the SVT algorithm to heavy nuclides with pronounced resonances, two options can be employed in Monte-Carlo simulations: analytical $S(\alpha, \beta)$ tables and stochastic correction.

The first option consists of directly utilizing $S(\alpha, \beta)$ tables to determine the energies and momenta of the scattered neutrons instead of using the sampling scheme as presented in the SVT algorithm. The $S(\alpha, \beta)$ tables can be calculated by the Doppler broadening double differential scattering kernel which is developed by Rothenstein

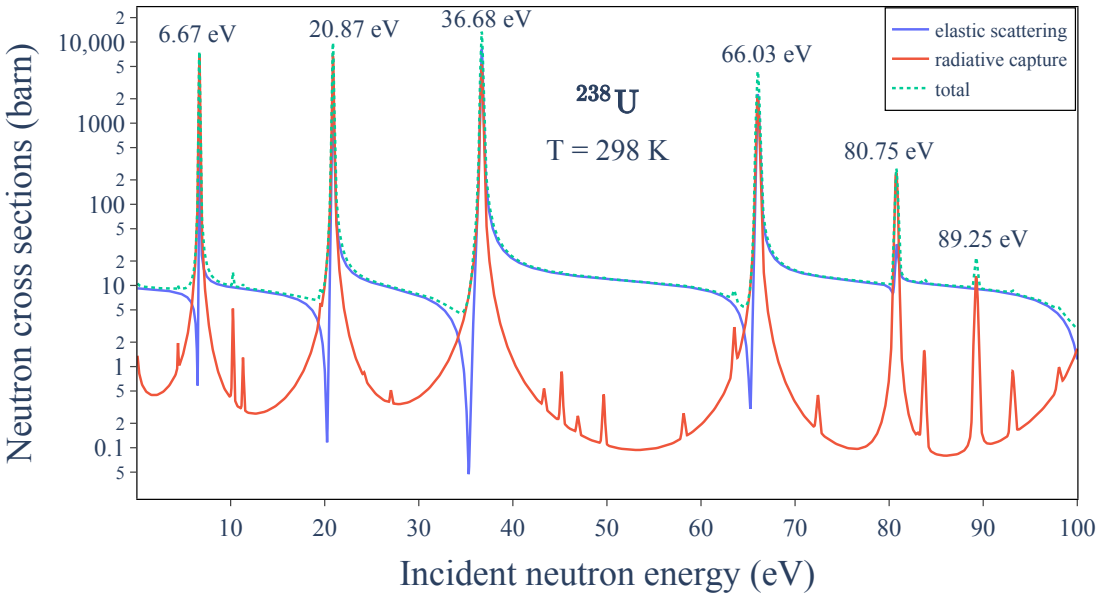

Figure 5.2.: Elastic scattering, radiative capture and total cross sections of ^{238}U at 298 K from the ENDF/B-VIII.0 database (D. Brown, Chadwick, Capote, et al. 2018).

and Dagan (Rothenstein and R. Dagan 1998; Rothenstein 2004).

The second option is to eliminate the approximation of $\sigma_0^s(v_{\text{rel}}) \approx$ constant by adding a rejection step in the SVT algorithm. For each simulation, the sampled V and μ will be rejected whenever the supplementary rejection criteria are fulfilled. Therefore, this approach is based solely on stochastic consideration. So far, two rejection models are implemented in TRIPOLI-4®: DBRC which is developed by Rothenstein and Dagan (Rothenstein and R. Dagan 1995) and WCM developed by Lee *et al.* (Lee, Smith, and Rhodes 2009). Nevertheless, this option induces a large number of rejection in the vicinity of the resonances, which increases the computational time for the Monte-Carlo simulations.

In this work, we focus on the neutron scattering with light nuclides having a non-resonant neutron scattering cross section below 10 eV. The formalism of the SVT algorithm and its numerical validations at room temperature T are presented in Section 5.2. In Section 5.3, we investigate several neutron scattering treatments with the Monte-Carlo neutron transport code TRIPOLI-4® in the energy range between 5 eV and 10 eV. The studied scattering models are the SVT algorithm, the $S(\alpha, \beta)$ tables calculated with simplified models: Free Gas Model (FGM) and Short Collision Time approximation (SCT), and the PDOS-based $S(\alpha, \beta)$ tables. In Section 5.4, the SVT algorithm at the effective temperature T_{eff} and the SCT scattering treatment are compared to results obtained with the PDOS-based $S(\alpha, \beta)$ tables. Preliminary conclusions are given in the last section.

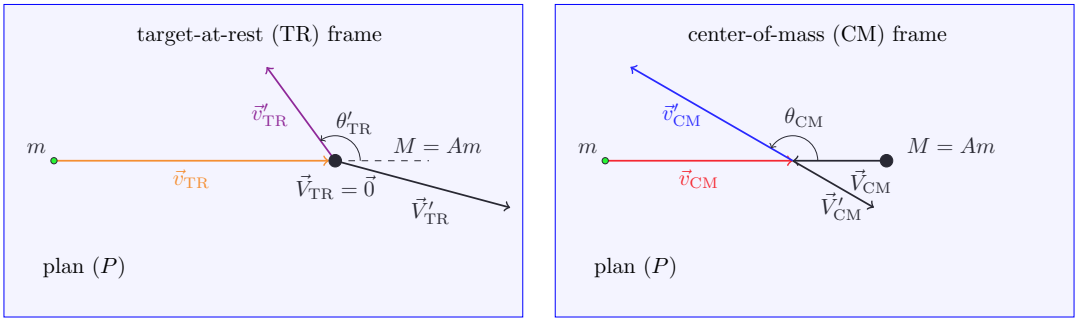

Figure 5.3.: Schematic representation of the neutron-nucleus scattering in the AK treatment from the point of view in target-at-rest (TR) frame (left hand plot) and center-of-mass (CM) frame (right hand plot). Detail explanations are presented in the text.

5.2. Numerical validations of the SVT algorithm at room temperature T

The neutron-nucleus scattering in the AK treatment or the SVT algorithm is approximated by the two-body collision kinetics, whose formalisms are presented in Sections 5.2.1 and 5.2.2, respectively. The numerical validations of the SVT algorithm are shown in Section 5.2.3.

5.2.1. Asymptotic Kernel

The AK treatment of TRIPOLI-4® is applied in the neutron scattering Monte-Carlo simulations when the incident neutron energies exceed $400\,k_B\,T$. In the AK treatment, the neutron-nucleus scattering is approximated by the two-body collision kinetics with target nuclei at rest in the LAB frame, as illustrated in Fig. 5.3. Hence, the LAB frame will hereafter be referred to as target-at-rest (TR) frame in the AK treatment. The neutron-target system is first transformed from the TR frame to the center-of-mass (CM) frame, as shown in Fig. 5.3, from the left hand plot to the right hand plot. The speeds of the neutron and the target nucleus before collision in the CM frame are $\vec{v}_{\mathrm{CM}}$ and $\vec{V}_{\mathrm{CM}}$, respectively. The kinematics of the collision in the CM frame are computed to obtain the post-collision speeds $\vec{v}'_{\mathrm{CM}}$ and $\vec{V}'_{\mathrm{CM}}$, as shown in the right hand plot. Finally the post-collision neutron-target system is transformed back to the TR frame to calculate the velocity v'_{TR} and the cosine of angle $\mu'_{\mathrm{TR}} = \cos(\theta'_{\mathrm{TR}})$ of the scattered neutron, as shown in the left hand plot. The derivation of v'_{TR} and μ'_{TR} are presented as follows.

The neutron mass and the mass of target nucleus are respectively m and M with $M = Am$. The speeds of neutron and target nucleus are respectively $\vec{v}$ and $\vec{V}$ with subscripts indicating the belonging frame. In the AK treatment, the target nucleus is assumed to be at rest in the TR frame, i.e., $\vec{V}_{\mathrm{TR}} = \vec{0}$. The speed of the CM frame in the

TR frame $\vec{c}_{TR}$ can be computed by:

$$\vec{c}_{TR} = \frac{m\vec{v}_{TR} + M\vec{V}_{TR}}{m+M} = \frac{\vec{v}_{TR}}{1+A}. \tag{5.1}$$

Then the speeds of neutron and target in the CM frame $\vec{v}_{CM}$ and $\vec{V}_{CM}$ can be obtained respectively by subtracting the speed of the CM frame $\vec{c}_{TR}$

$$\vec{v}_{CM} = \vec{v}_{TR} - \vec{c}_{TR} = \frac{A\vec{v}_{TR}}{1+A}, \tag{5.2}$$

and

$$\vec{V}_{CM} = \vec{V}_{TR} - \vec{c}_{TR} = -\frac{\vec{v}_{TR}}{1+A}. \tag{5.3}$$

The neutron-target collision is assumed to be isotropic in the CM frame. Thus the cosine of the scattering angle $\mu_{CM} = \cos(\theta_{CM})$ is sampled uniformly on the interval $[-1;1]$. Since the total momentum and the kinetic energy of the neutron-target system is conserved before and after the collision, it can be easily shown that the scalar velocities of the neutron and the target remain invariant in the CM frame, i.e., $v_{CM} = v'_{CM}$ and $V_{CM} = V'_{CM}$. The speed of the post-collision neutron in the TR frame $\vec{v}'_{TR}$ and that of the target $\vec{V}'_{TR}$ can thus be calculated by adding the speed of the CM frame, i.e.,

$$\vec{v}'_{TR} = \vec{v}'_{CM} + \vec{c}_{TR}, \tag{5.4}$$

and

$$\vec{V}'_{TR} = \vec{V}'_{CM} + \vec{c}_{TR}. \tag{5.5}$$

Plan P presented in the right hand plot of Fig. 5.3 is determined by the speeds of neutron before and after collision $\vec{v}_{CM}$ and $\vec{v}'_{CM}$. It can be obtained from Eqs. (5.1), (5.4) and (5.5) that the speeds of target $\vec{v}'_{TR}$ and $\vec{V}'_{TR}$ are in the same plan P. Furthermore, based on geometric relations, the scalar velocity of the post-collision neutron v'_{TR} and the cosine of the scattering angle μ'_{TR} in the TR frame can be respectively calculated by:

$$v'_{TR} = \sqrt{\left(\frac{1+\mu_{CM}A}{1+A}\right)^2 + \frac{A^2(1-\mu_{CM}^2)}{(1+A)^2}}\, v_{TR}, \tag{5.6}$$

and

$$\mu'_{TR} = \begin{cases} 1 & \text{if } \mu_{CM} = -1 \text{ and } A = 1 \\ \dfrac{1+\mu_{CM}A}{\sqrt{(1+\mu_{CM}A)^2 + A^2(1-\mu_{CM}^2)}} & \text{otherwise} \end{cases}. \tag{5.7}$$

5.2.2. Sampling the velocity of the target nucleus

The neutron-nucleus scattering is approximated by the two-body kinetics in the SVT algorithm, which is illustrated in Fig. 5.4. Same conventions for the notations of speed and angle are used in the SVT and AK treatments, e.g., the superscript $'$ represents the

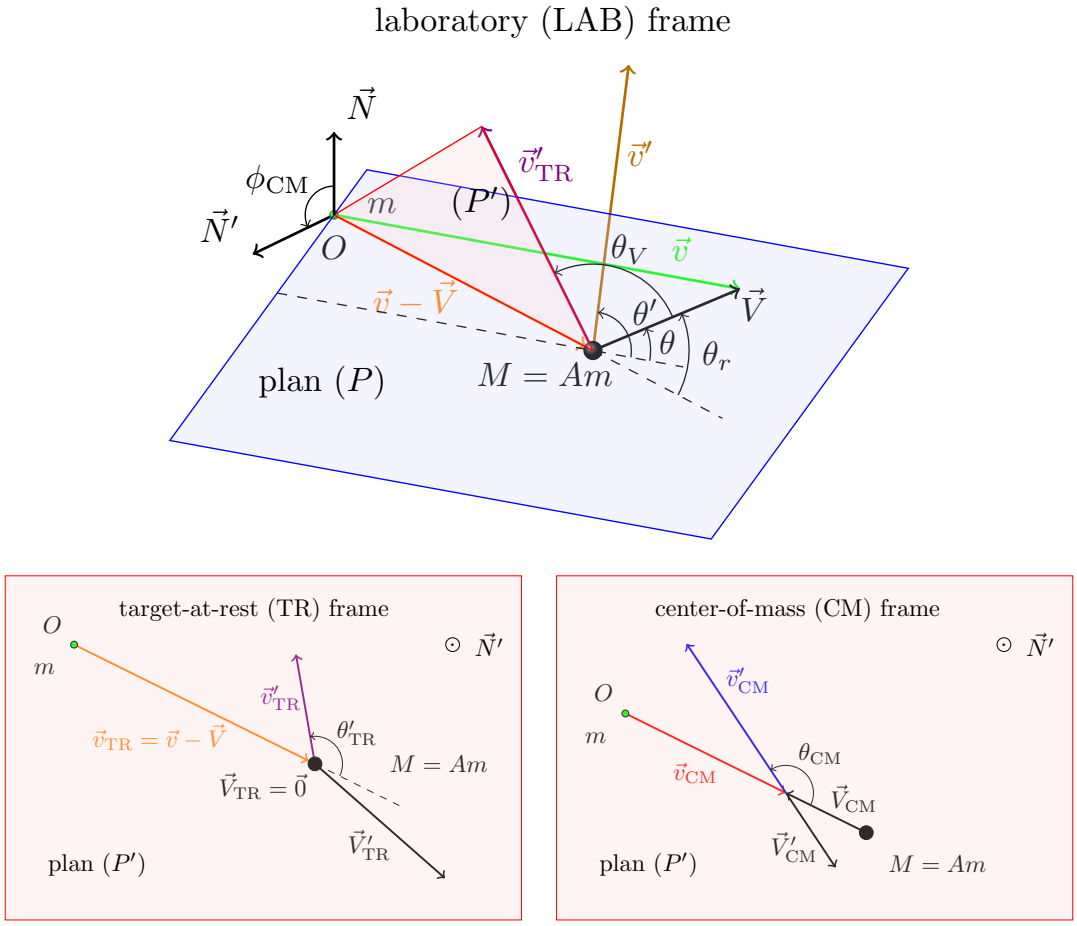

Figure 5.4.: Schematic representation of neutron-nucleus scattering in LAB (top plot), TR (bottom left plot) and CM (bottom right plot) frames. Detail descriptions can be found in the text.

physical quantities after the scattering while the subscripts indicate the belonging frames. In the SVT algorithm, the subscripts of quantities in the LAB frame are omitted for the sake of clarity.

Unlike the AK treatment in which the target nuclei are assumed to be at rest, the velocities of the target nuclei V in the LAB frame in the SVT algorithm can be sampled from a M-B distribution $\mathscr{M}_T(V)$ with T the temperature of the nuclei. The cosine of the angle between the incident neutron and the target nucleus $\mu = \cos(\theta)$ before collision can be sampled uniformly on $[-1;1]$. After the sampling of V and μ, the relative speed between the incident neutron and the target nucleus $\vec{v} - \vec{V}$ can be computed. This step enables to transform the neutron-target system from the LAB frame to the TR frame, as shown in Fig. 5.4, from the top plot to the bottom left plot. Then, by using Eqs. (5.6) and (5.7) obtained in the AK treatment, the velocity v'_{TR} and the cosine of angle μ'_{TR} can be computed. The final step consist of transforming the neutron-target system back to the LAB frame to calculate v' and $\mu' = \cos(\theta')$.

Based on the results obtained in the AK treatment, the speed vectors in the TR or CM frame lie on the same plan (P') (pink color), as shown in the two bottom plots of Fig. 5.4. While the target speed $\vec{V}$ does not generally lie on the same plan except for $\mu = \pm 1$. Thus, compared to the AK treatment, an additional azimuthal angle ϕ_{CM} is sampled in the SVT algorithm. ϕ_{CM} is sampled uniformly on the interval $]-\pi;\pi]$ based on the assumption that the neutron scattering is isotropic in the CM frame. Therefore, there are four variables sampled in the SVT algorithm (Rothenstein 1996): V and μ are related to the motion of target nuclei, and μ_{CM} and ϕ_{CM} are used in the collision kinematics. The derivation of the velocity v' and the cosine of angle $\mu' = \cos(\theta')$ of the post-collision neutron is summarized as follows.

The relative speed between the incident neutron and the target nucleus $\vec{v}_{\mathrm{ref}}$ is computed by:

$$\vec{v}_{\mathrm{ref}} = \vec{v} - \vec{V}. \tag{5.8}$$

The cosine of the angle between the relative speed $\vec{v}_{\mathrm{ref}}$ and the speed of the target nucleus $\vec{V}$ is denoted as $\mu_r = \cos(\theta_r)$, which is determined by:

$$\mu_r = \frac{\vec{v}_{\mathrm{ref}} \cdot \vec{V}}{v_{\mathrm{ref}} V} = \frac{v\mu - V}{\sqrt{v^2 + V^2 - 2vV\mu}}. \tag{5.9}$$

Then, the speed of scattered neutron in the TR frame $\vec{v}'_{\mathrm{TR}}$ is decomposed into two components with one parallel to the relative speed $\vec{v}_{\mathrm{ref}}$ and the other perpendicular to it, i.e., $\vec{v}'_{\mathrm{TR}} = \vec{v}'_{\mathrm{TR},\parallel} + \vec{v}'_{\mathrm{TR},\perp}$. Equally, the speed of the target nucleus is decomposed into $\vec{V} = \vec{V}_{\parallel} + \vec{V}_{\perp}$. Hence, the speed of scattered neutron in the LAB frame $\vec{v}'$ can be expressed by:

$$\vec{v}' = \vec{v}'_{\mathrm{TR}} + \vec{V} = \vec{v}'_{\mathrm{TR},\parallel} + \vec{v}'_{\mathrm{TR},\perp} + \vec{V}_{\parallel} + \vec{V}_{\perp}. \tag{5.10}$$

Based on geometric relations, the velocity of the scattered neutron in the LAB frame v' can be obtained by:

$$v' = (v'_{\mathrm{TR}})^2 + V^2 + 2v'_{\mathrm{TR}} V \mu_V, \tag{5.11}$$

where $\mu_V = \cos(\theta_V)$ represents the cosine of the angle between v'_{TR} and $\vec{V}$, which is obtained thanks to the decompositions of $\vec{v}'_{\mathrm{TR}}$ and $\vec{V}$ in Eq. (5.10) and

$$\mu_V = \mu'_{\mathrm{TR}}\mu_r + \sqrt{1-(\mu'_{\mathrm{TR}})^2}\sqrt{1-\mu_r^2}\cos(\phi_{\mathrm{CM}}). \tag{5.12}$$

μ_V can be computed thanks to the calculations of μ'_{TR} and μ_r from Eqs. (5.7) and (5.9). Since v'_{TR} can be obtained from Eq. (5.6), the velocity of scattered neutron in the LAB frame v' in Eq.(5.11) can be obtained. Finally, the expression of the cosine of the scattering angle $\mu' = \cos(\theta')$ can be calculated by:

$$\mu' = \frac{\vec{v}\cdot\vec{v}'}{vv\prime} = \frac{(\vec{v}_{\mathrm{ref}} + \vec{V})\cdot(\vec{v}'_{\mathrm{TR}} + \vec{V})}{vv'} = \frac{v'_{\mathrm{TR}} v_{\mathrm{ref}} \mu'_{\mathrm{TR}} + v_{\mathrm{ref}} V \mu_r + v'_{\mathrm{TR}} V \mu_V + V^2}{vv'}. \tag{5.13}$$

5.2.3. Numerical validations of the SVT algorithm

In this part, the SVT algorithm presented in Section 5.2.2 is validated by sampling the velocities of ^{1}H in ^1H_2O from M-B distributions and trajectory files provided by the MD code GROMACS (Abraham, Murtola, Schulz, et al. 2015).

The M-B probability distribution function of velocities is explicitly expressed as:

$$\mathscr{M}_T(V) = \frac{4}{\sqrt{\pi}} B^3 V^2 \exp\left(-B^2 V^2\right), \tag{5.14}$$

where

$$B = \sqrt{\frac{M}{2k_B T}}. \tag{5.15}$$

The M-B probability distribution function of the velocities $\mathscr{M}_T(V)$ is characterized by the mass M and the temperature T. The mean velocity $\overline{V}$ of the M-B distribution can be calculated by:

$$\overline{V} = \frac{2}{\sqrt{\pi} B} = \sqrt{\frac{8k_B T}{\pi M}}. \tag{5.16}$$

The generation of the trajectory files for water by using GROMACS is described in Scotta's thesis (J. Scotta 2017). The physical model used in the GROMACS simulation consists of in total 512 water molecules within a cubic box with side length equal to 2.48 nm. A water potential named TIP4P/2005f (González and Abascal 2011) is adopted to quantify the forces between atoms. The TIP4P/2005f model is a flexible water potential model which enables to take into account the intermolecular and intramolecular interactions. Thanks to this potential, the positions and velocities [2] of the hydrogen and oxygen atoms in the water molecules can be obtained for a given time step and they are stored in trajectory files.

In this work, the trajectory files are obtained with a time duration of 100 ps with a time step of 0.6 fs. Each water molecule is composed of two hydrogen atoms and one oxygen atom. For each time step, the partial velocities are denoted as $V_{j,x}$, $V_{j,y}$ and $V_{j,z}$, along the x, y and z directions with j denotes the oxygen atom O or two hydrogen atoms H – 1 and H – 2. The velocities V_j can thus be computed via the partial components as follows:

$$V_j = \sqrt{V_{j,x}^2 + V_{j,y}^2 + V_{j,z}^2}. \tag{5.17}$$

After calculating the velocities V_j of atoms O, H – 1 and H – 2 for all the time frames, the mean values V_j^{avg} can be obtained by directly averaging V_j. The results are presented in Table 5.1. The mean velocities of H – 1 and H – 2 are quite close and they are almost 4 times bigger than the mean velocity of O.

The velocity distributions of the oxygen and two hydrogen atoms for the time frames up to 100 ps are shown in Fig. 5.5. The velocity distributions are fitted with M-B model

[2] More precisely, the momenta of atoms are stored in the trajectory files. While the velocities can be directly obtained by dividing the atomic mass. Hence, we mention directly the velocities in this work.

Table 5.1.: Mean velocities of atoms O, H – 1 and H – 2 for all the time frames up to 100 ps.

Atom	Mean velocity V_j^{avg} (m/s)
O	625.24
H-1	2488.1
H-2	2488.9

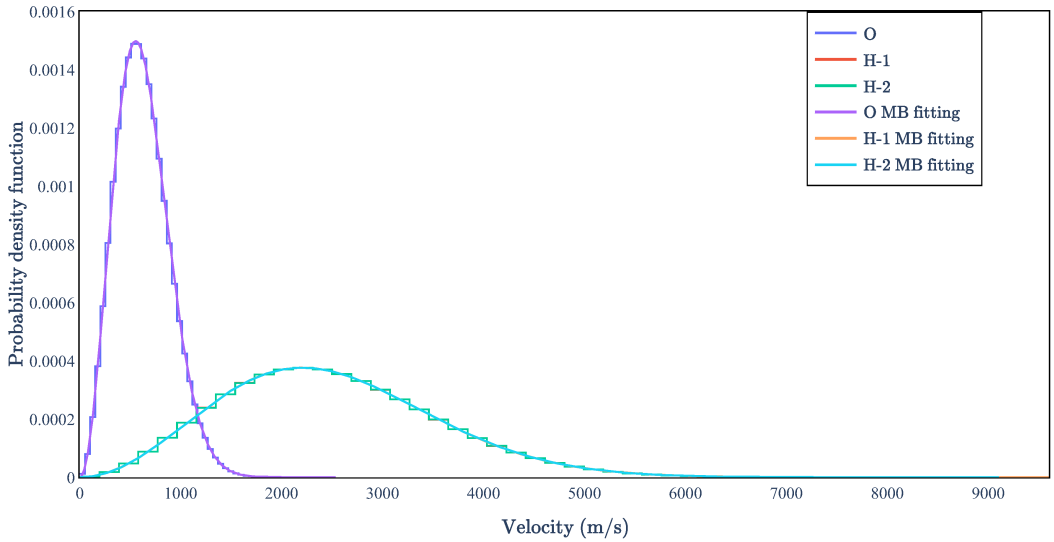

Figure 5.5.: Distributions of the velocities of oxygen and hydrogen during the time frames up to 100 ps. The velocity distributions are fitted with the M-B model.

by using the Python module `SciPy` (Virtanen, Gommers, Oliphant, et al. 2020). The fitted temperatures are presented in Table 5.2.

The temperature of each atom can also be calculated with the mean velocities V_j^{avg} presented in Table 5.1. The temperatures obtained with Eq. (5.16) are denoted as T_{calc}. The comparison of T_{fit} and T_{calc} are presented in Table 5.2. The fitted and calculated temperatures are the same, which confirms that the velocities follow M-B distributions during the simulation time of 100 ps.

The cosine of the angle between the z components $V_{j,z}$ and the velocities V_j for oxygen and hydrogen atoms, μ_j can be computed by:

$$\mu_j = \frac{V_{j,z}}{V_j}. \tag{5.18}$$

The distribution of μ_j is presented in Figure 5.6. The mean value and the standard deviation of μ_j is shown in Table 5.3. The results confirm that μ_j is equiprobable on the interval $[-1;1]$.

Table 5.2.: Fitted and calculated temperature of atoms of all the time frames up to 100 ps.

Atom	Fitted temperature T_{fit} (K)	Calculated temperature T_{calc} (K)
O	295.41	295.41
H-1	294.51	294.51
H-2	294.72	294.72

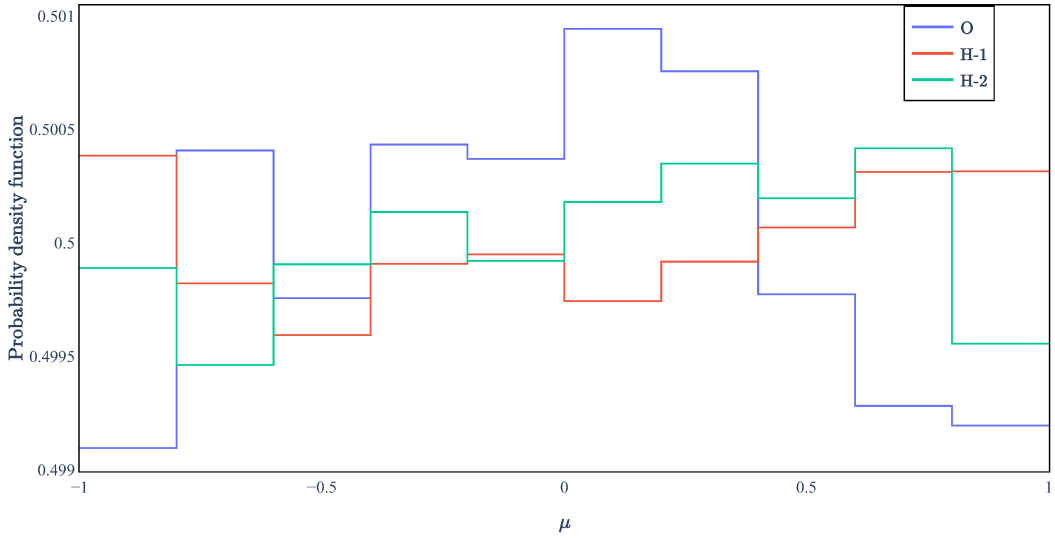

Figure 5.6.: Distributions of cosine of theta $\mu_j = \cos(\theta_j)$ of oxygen and hydrogen atoms for all the time frames up to 100 ps. μ_j is equiprobable on the interval $[-1;1]$.

So far, the velocity distributions provided by the water trajectory files are confirmed to be M-B distribution. Nevertheless, strong correlations appear between time steps, which are illustrated via the VACF (J. Scotta 2017). However, these correlations are not taken into account in the SVT algorithm.

To validate the SVT algorithm, the velocities of the target nuclei are sampled from the M-B distribution at 294 K based on Eq. (5.14), and from the velocities of H−1 of the GROMACS trajectory files. The obtained neutron yields (distributions of scattered neutrons as a function of energy) at $\theta' = 10°, 45°, 90°$ for incident neutron energies $E = 1, 5, 10$ eV are respectively presented from Fig. 5.7 to Fig. 5.9. These results are also compared to neutron yields obtained with TSLs $S(\alpha, \beta)_{\text{FGM}}$ calculated in the free gas approximation (cf. Section 2.4).

These results show that the neutron yields obtained by the SVT algorithm are in excellent agreement with the analytical $S(\alpha, \beta)_{\text{FGM}}$ results at temperature $T = 294$ K for incident neutron energy above 5 eV. The derivation of $S(\alpha, \beta)_{\text{FGM}}$ is based on the assumption that the target nuclei are free gas with velocities that follow a M-B distribution. Therefore, the SVT must be applied above the threshold near 5 eV for

Table 5.3.: Mean and standard deviation of the cosine of angle of atoms of all the time frames up to 100 ps.

Atom	Mean cosine of angle	Standard deviation
O	0.500	6.40×10^{-4}
H-1	0.500	2.51×10^{-4}
H-2	0.500	3.00×10^{-4}

hydrogen, as presented in Fig. 5.1. The neutron yields obtained with the velocities sampled from the M-B and the GROMACS trajectory files are the same because the correlations between velocities presented in the trajectory files are not included.

The energy distributions of scattered neutrons for incident neutron energies E = 1, 10, 100 eV are presented in Fig. 5.10. For AK, since target nuclei are at rest, neutrons can only loss their energy after the collisions. The loss of energy is referred to neutron down-scattering. Furthermore, according to the two body kinematics, the energy distribution of the scattered neutrons is uniform for AK. While for the SVT algorithm, target nuclei have velocities following a M-B distribution. Based on the two body collision treatment, scattered neutrons having an energy gain becomes possible. The gain of energy is referred to neutron up-scattering. The percentage of "up-scattering" for different incident neutron energies are presented in Table 5.4 and Fig. 5.10. Since the percentage of up-scattering is less than 0.3 % for incident neutron energy equal to 10 eV, the threshold of 10 eV can be chosen for hydrogen to apply AK in the neutron scattering simulation.

Table 5.4.: Percentage of up-scattering for incident neutron energies equal to 1, 10 and 100 eV. The velocities of target nuclei are sampled from the M-B distribution at 294 K and from the velocities of the H – 1 atom of the GROMACS trajectory files.

E (eV)	1	10	100
M-B up-scat. (%)	2.47	0.252	0.0258
MD up-scat. (%)	2.49	0.251	0.0253

5.3. Numerical validations of the neutron scattering treatments with TRIPOLI-4® at room temperature T

In this section, the neutron-nucleus scattering in the energy range between 5 eV and 10 eV at room temperature T is investigated by using the Monte-Carlo code TRIPOLI-4®.

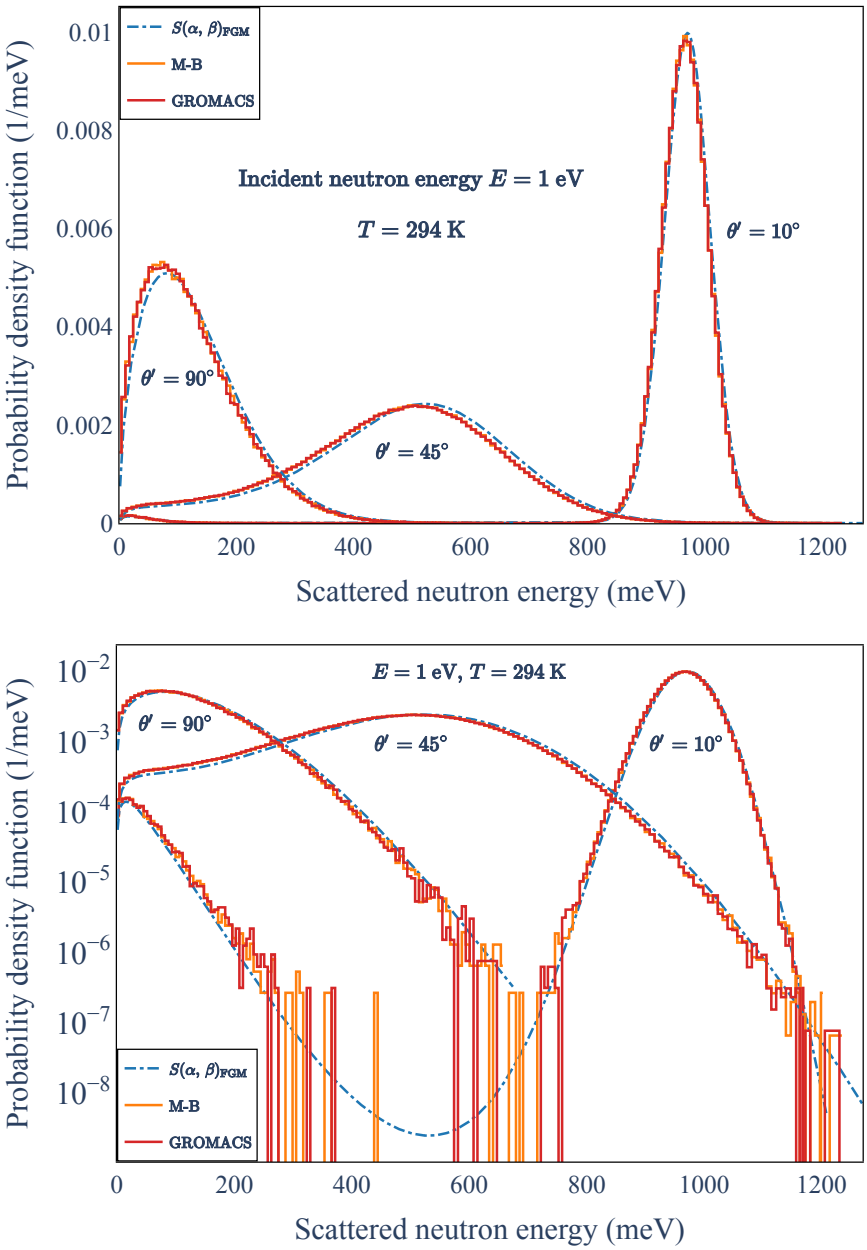

Figure 5.7.: Energy distributions of scattered neutrons at $\theta' = 10°, 45°, 90°$ computed by thermal scattering laws for free gas model $S(\alpha, \beta)_{\text{FGM}}$ and from Sampling the Velocity of the Target nucleus (SVT) at temperature $T = 294$ K for incident neutron energy equal to 1 eV. The target nucleus is hydrogen. The velocities of hydrogen are sampled from the M-B distribution at 294 K and from the velocities of the H – 1 atom in the GROMACS files. The y axis of the bottom plot is in log scale for a better visualization.

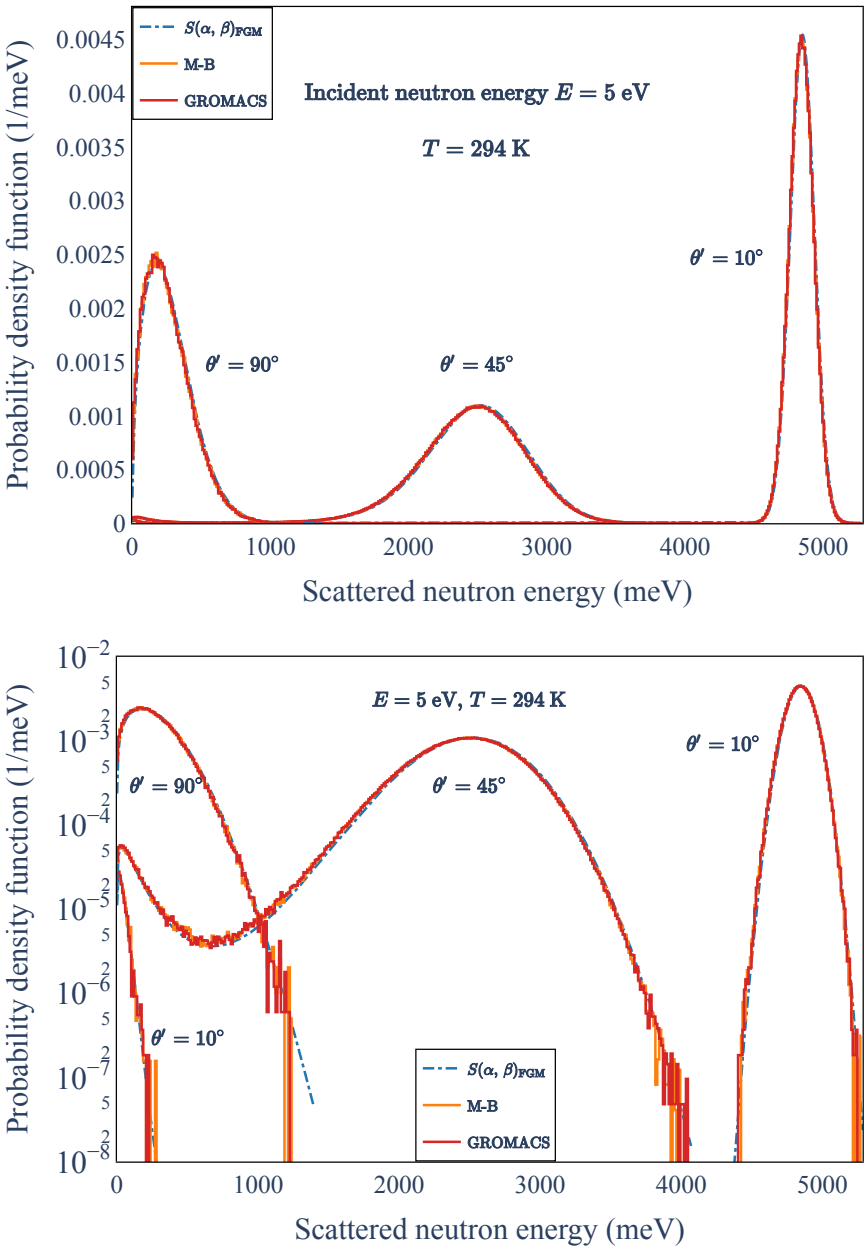

Figure 5.8.: Energy distributions of scattered neutrons at $\theta' = 10°, 45°, 90°$ computed by thermal scattering laws for free gas model $S(\alpha, \beta)_{\text{FGM}}$ and from Sampling the Velocity of the Target nucleus (SVT) at temperature $T = 294$ K for incident neutron energy equal to 5 eV. The target nucleus is hydrogen. The velocities of hydrogen are sampled from the M-B distribution at 294 K and from the velocities of the H – 1 atom in the GROMACS files. The y axis of the bottom plot is in log scale for a better visualization.

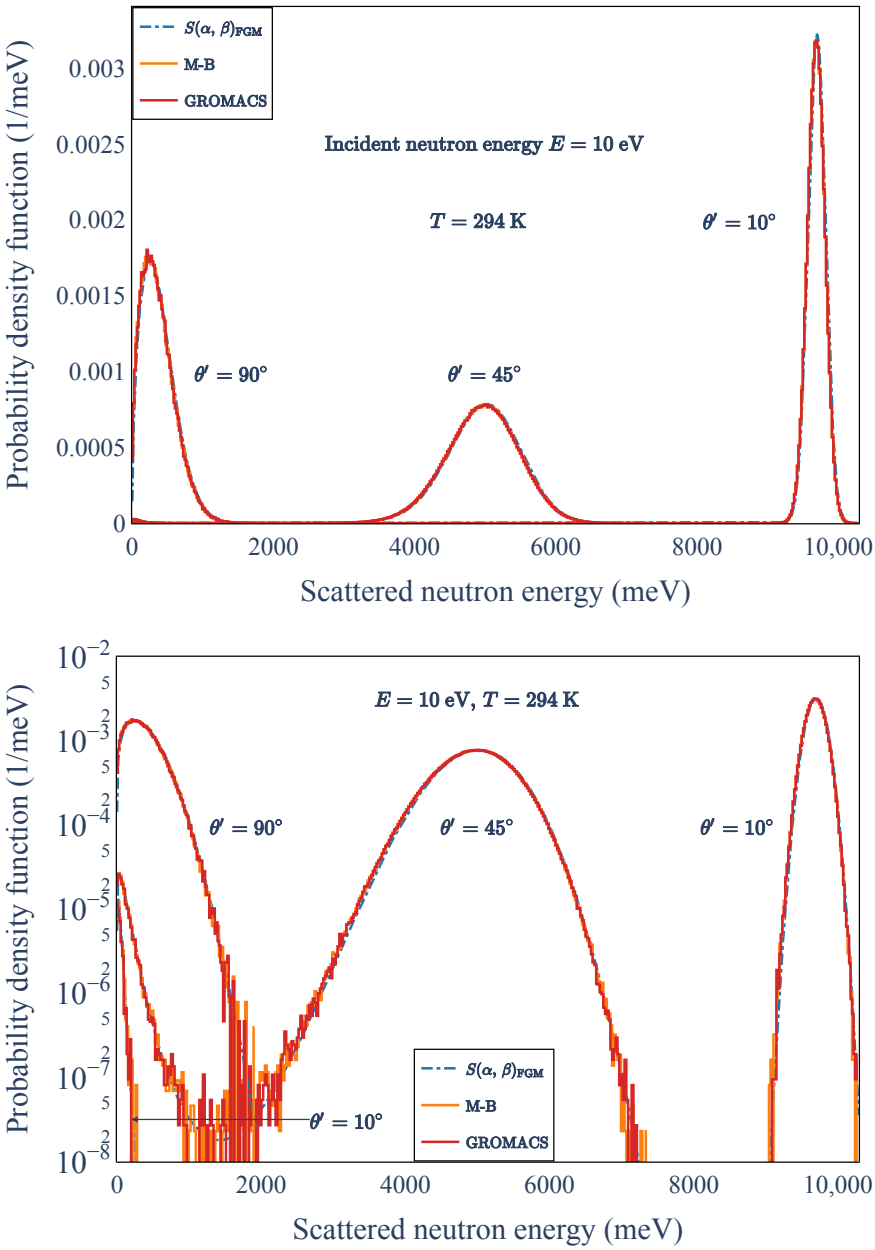

Figure 5.9.: Energy distributions of scattered neutrons at $\theta' = 10°, 45°, 90°$ computed by thermal scattering laws for free gas model $S(\alpha, \beta)_{\text{FGM}}$ and from Sampling the Velocity of the Target nucleus (SVT) at temperature $T = 294$ K for incident neutron energy equal to 10 eV. The target nucleus is hydrogen. The velocities of hydrogen are sampled from the M-B distribution at 294 K and from the velocities of the H – 1 atom in the GROMACS files. The y axis of the bottom plot is in log scale for a better visualization.

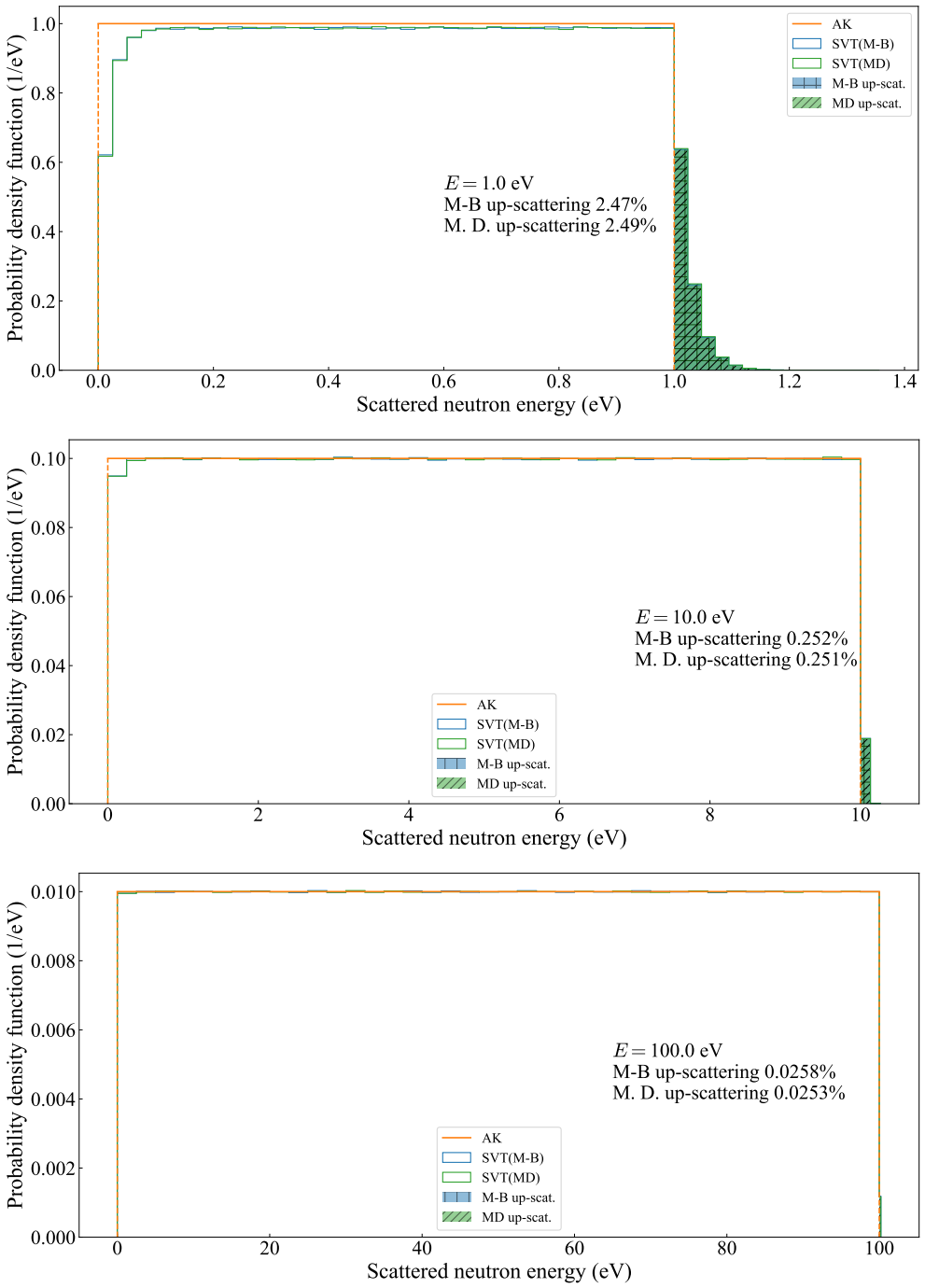

Figure 5.10.: Energy distributions computed by Asymptotic Kernel (AK) and Sampling the Velocity of the Target nucleus (SVT) for incident neutron energy equal to 1, 10 and 100 eV. The target nucleus is hydrogen. The velocities of hydrogen are sampled from the Maxwell-Boltzmann (M-B) distribution at 294 K and from the velocities of the H – 1 atom of the GROMACS trajectory files.

In total four neutron scattering treatments are studied: SVT algorithm implemented in TRIPOLI-4®, the tabulated TSLs $S(\alpha, \beta)$ based on PDOS, the $S(\alpha, \beta)$ tables based on the FGM and SCT approximation. These $S(\alpha, \beta)$ tables are prepared with the data processing tool `CINEL` (cf. Chapter 3). The listed neutron scattering treatments will be validated by comparing the neutron yields obtained by the TRIPOLI-4® simulations to the analytical results. These numerical validations are illustrated with the case of ^{1}H in $^{1}H_2O$ and ^{16}O in UO_2. The simulations performed with TRIPOLI-4® are summarized in Table 5.5.

Table 5.5.: Simulations performed by using the Monte-Carlo neutron transport code TRIPOLI-4® for ^{1}H in $^{1}H_2O$ and ^{16}O in UO_2 at room temperatures T.

Target nucleus	E (eV)	Temperature T (K)	Scattering treatments
^{1}H in $^{1}H_2O$	5	294	SVT $S(\alpha, \beta)_{\text{FGM}}$ $S(\alpha, \beta)_{\text{SCT}}$ $S(\alpha, \beta)$
^{16}O in UO_2	6.67	298	

The physical model employed in the TRIPOLI-4® simulations is briefly presented. A capillary sample with a radius equal to 5 µm and a height of 10 µm is placed in the center of the simulation model. The dimensions are chosen to minimize the impact of multiple scattering. The incident neutron energy is monoenergetic which is set to be 5 eV for ^{1}H in $^{1}H_2O$ and 6.67 eV for ^{16}O in UO_2. The outgoing neutrons are detected at $\theta' = 10°$, 45° and 90°. The TRIPOLI-4® simulations are performed at room temperature with $T = 294$ K for ^{1}H in $^{1}H_2O$ and $T = 298$ K for ^{16}O in UO_2.

The neutron yields of ^{1}H in $^{1}H_2O$ at $T = 294$ K at $\theta' = 10°$, 45° and 90° obtained by the SVT algorithm of TRIPOLI-4®and the $S(\alpha, \beta)_{\text{FGM}}$ tables are compared to the analytical results computed from Eqs. (2.147) and (2.148). These results are presented in Fig. 5.11. The TRIPOLI-4® simulated neutron yields are in excellent agreement with the analytical results. The neutron yields obtained by TRIPOLI-4® simulations for ^{16}O in UO_2 at $T = 298$ K are also in excellent agreement with the analytical results, as presented in Fig. 5.12.

The neutron yields at $\theta' = 10°$, 45° and 90° obtained by using the $S(\alpha, \beta)_{\text{SCT}}$ tables with TRIPOLI-4® are compared to the analytical results computed by Eqs. (2.160) and (2.162). Excellent agreement is obtained for ^{1}H in $^{1}H_2O$ with $E = 5$ eV at $T = 294$ K and ^{16}O in UO_2 with $E = 6.67$ eV at $T = 298$ K, as shown in Fig. 5.13. The final investigation consists of the comparison of the neutron yields calculated from the $S(\alpha, \beta)$ tables and the analytical results. The simulation results are in excellent agreement with the analytical results as shown in Fig. 5.14.

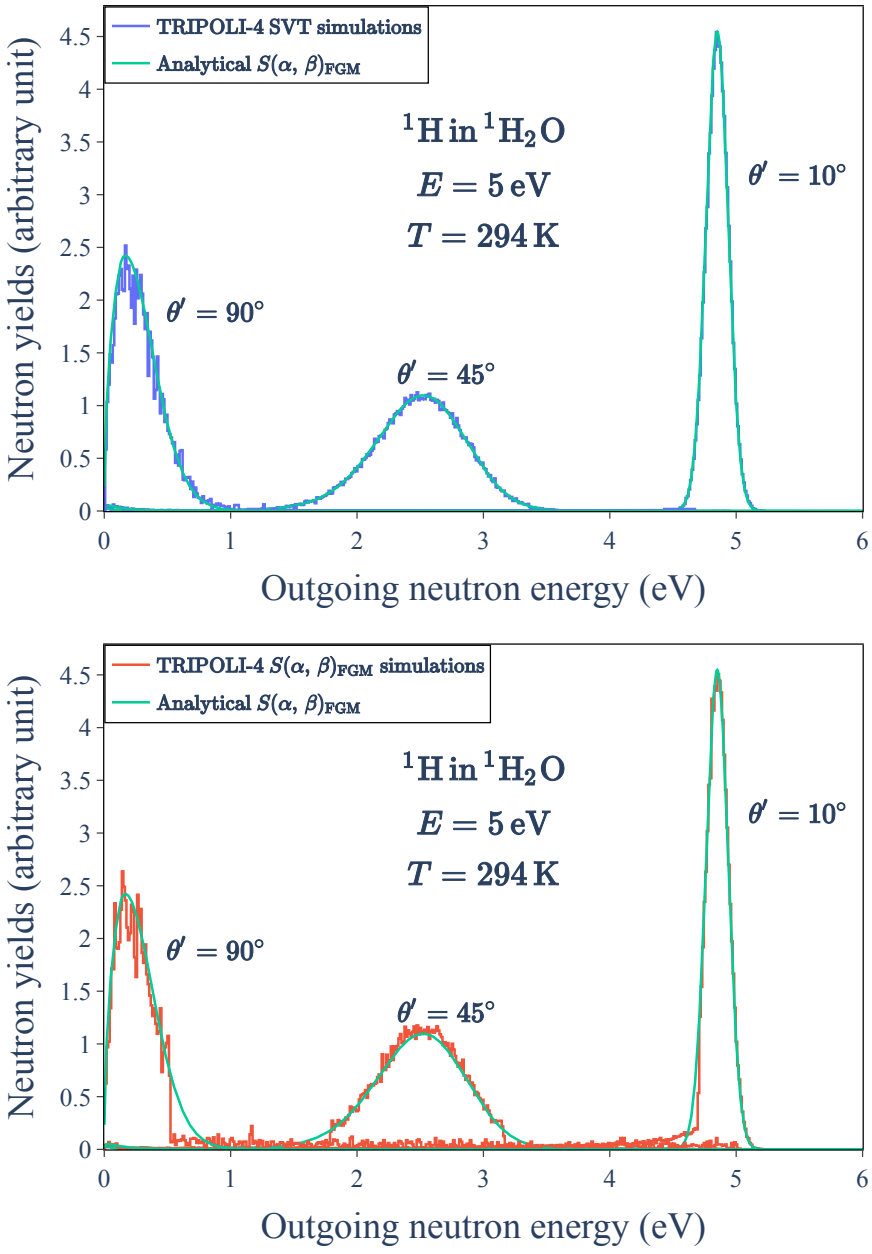

Figure 5.11.: Neutron yields at $\theta' = 10°$, 45° and 90° obtained by using the Monte-Carlo neutron transport code TRIPOLI-4® for scattering treatments: SVT (blue lines) and tabulated $S(\alpha, \beta)_{FGM}$ with free gas approximation (red lines). Excellent agreement with the analytical results computed from Eqs. (2.147) and (2.148) (green lines), for ^1H in ^1H_2O with incident neutron energy $E = 5$ eV at temperature $T = 294$ K.

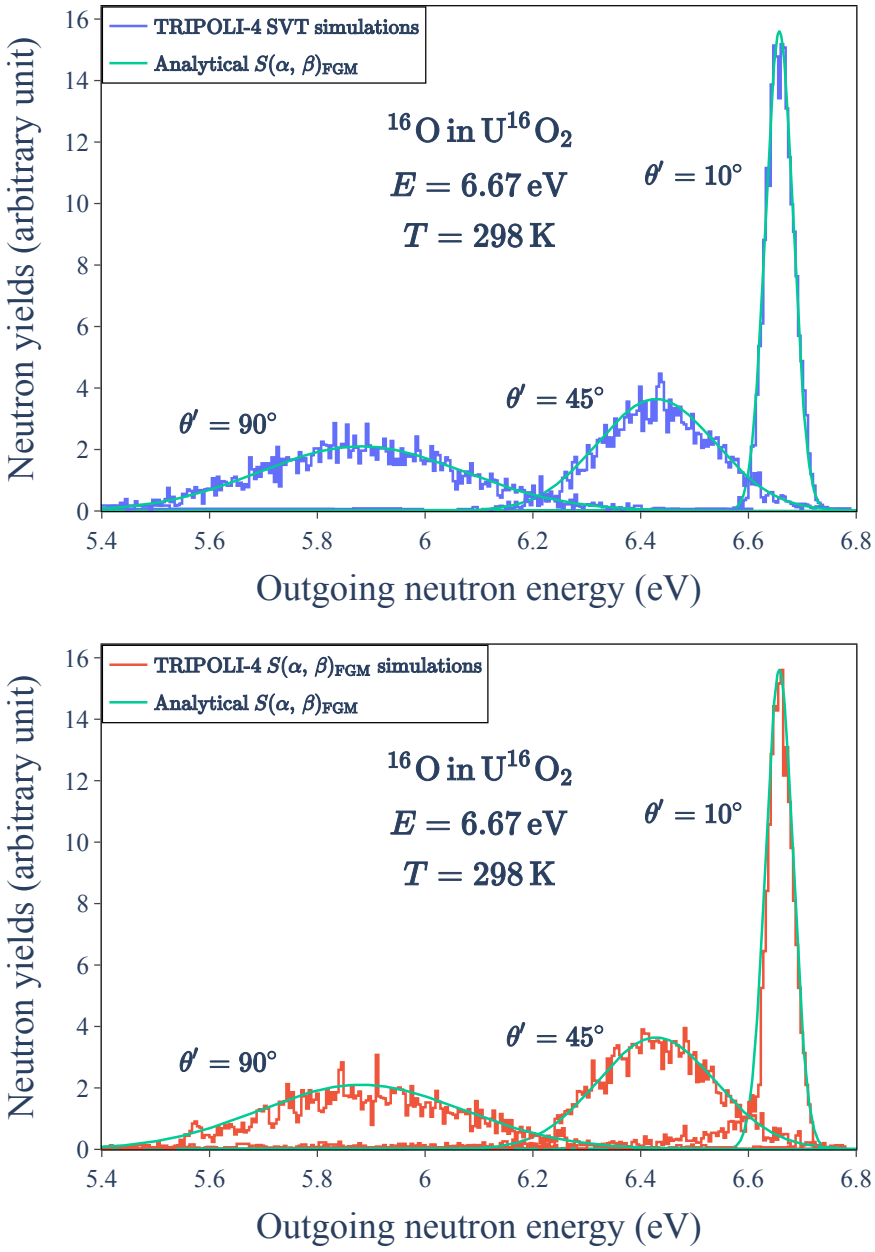

Figure 5.12.: Neutron yields at $\theta' = 10°$, 45° and 90° obtained by using the Monte-Carlo neutron transport code TRIPOLI-4® for scattering treatments: SVT (blue lines) and tabulated $S(\alpha, \beta)_{FGM}$ with free gas approximation (red lines). Excellent agreement with the analytical results computed from Eqs. (2.147) and (2.148) (green lines), for ^{16}O in UO_2 with incident neutron energy $E = 6.67$ eV at temperature $T = 298$ K.

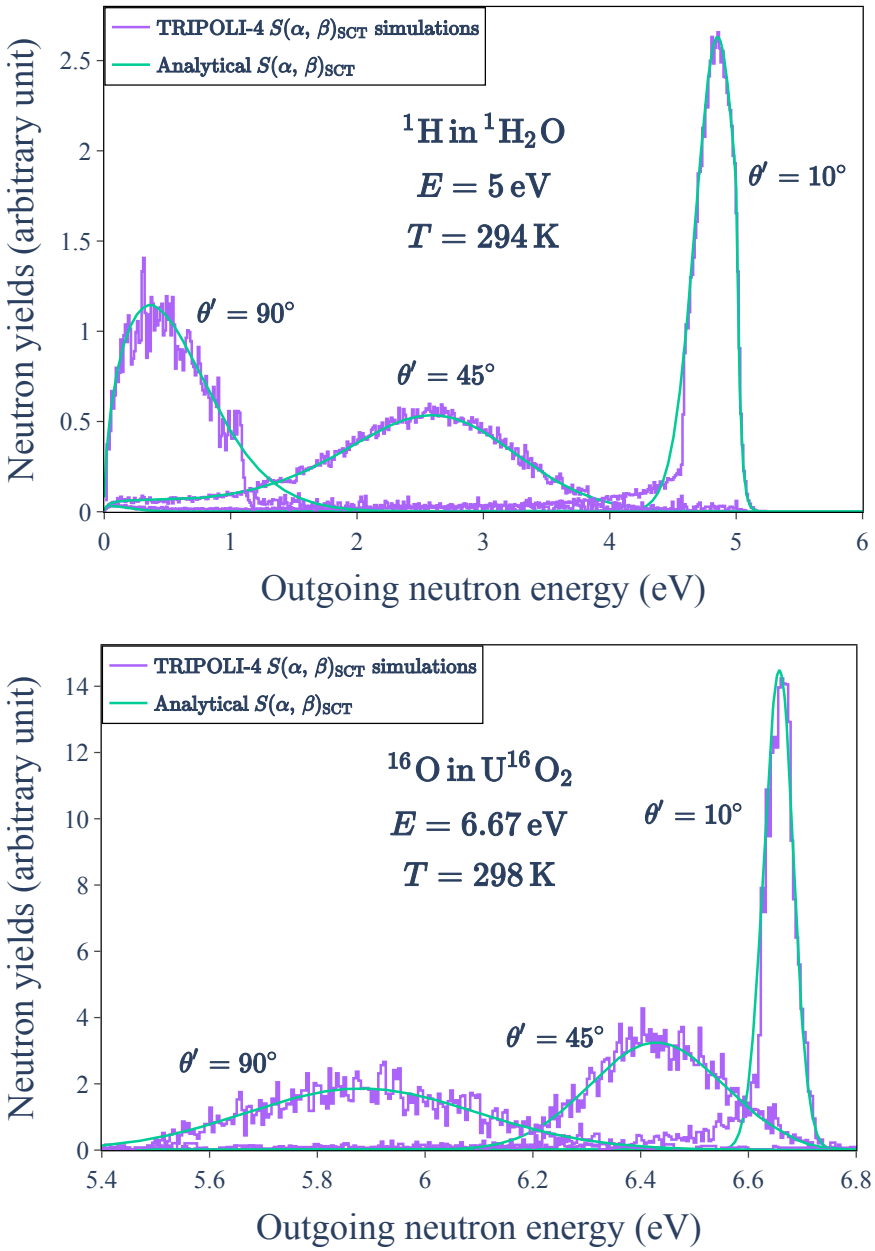

Figure 5.13.: Neutron yields at $\theta' = 10°$, 45° and 90° obtained by using the Monte-Carlo neutron transport code TRIPOLI-4® for tabulated $S(\alpha, \beta)_{SCT}$ with short collision time approximation (purple lines). Excellent agreement with the analytical results computed from Eqs. (2.160) and (2.162) (green lines), for ^{1}H in $^{1}H_2O$ with incident neutron energy $E = 5$ eV at temperature $T = 294$ K and ^{16}O in UO_2 with incident neutron energy $E = 6.67$ eV at temperature $T = 298$ K.

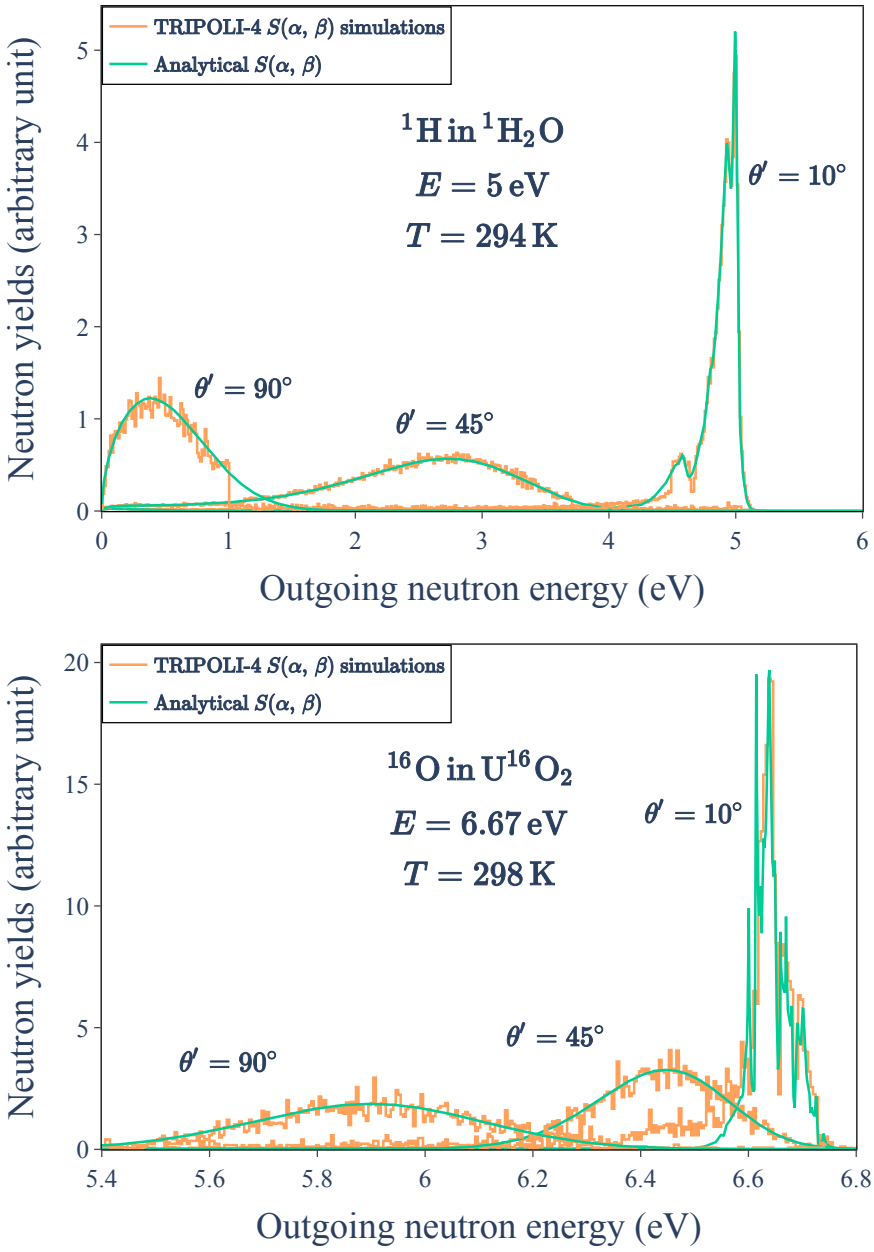

Figure 5.14.: Neutron yields at $\theta' = 10°$, 45° and 90° obtained by using the Monte-Carlo neutron transport code TRIPOLI-4® for tabulated $S(\alpha, \beta)$ (orange lines). Excellent agreement with the analytical results (green lines), for ^{1}H in ^1H_2O with incident neutron energy $E = 5$ eV at temperature $T = 294$ K and ^{16}O in UO_2 with incident neutron energy $E = 6.67$ eV at temperature $T = 298$ K.

5.4. Comparison of neutron scattering treatments with TRIPOLI-4® in the epithermal energy range

This final section is devoted to study with the TRIPOLI-4® code a few alternative neutron scattering treatments between 5 eV and 10 eV where the $S(\alpha, \beta)$ approach is no longer used in the neutronic calculations schemes for reactor applications. This study is limited to nuclides having a non-resonant neutron scattering cross section below 10 eV. The discussion is illustrated with the case of ^{1}H in $^{1}H_2O$ and ^{16}O in UO_2.

We have shown in the previous sections that $S(\alpha, \beta)$ tables are correctly used by the TRIPOLI-4® code to simulate the transport of neutrons with energies lying below a few eV. The analytical and simulated results obtained with the scattering models, called AK (for Asymptotic Kernel), SVT (for Sampling the Velocity of the Target nucleus), SCT (for Short Collision Time approximation) and FGM (for Free Gas Model), will be compared to those obtained with the $S(\alpha, \beta)$ treatment. A special attention will be given to the important role of the effective temperature T_{eff} (Eq. 2.153).

The effective temperature T_{eff}, which can be calculated from the PDOS via Eq. (2.153), takes into account the atom binding effects in the molecules (Lamb 1939). It is shown in the previous section that the SVT algorithm of TRIPOLI-4® and the neutron scattering treatment with $S(\alpha, \beta)_{\text{FGM}}$ tables are equivalent above 5 eV. Therefore, the SVT algorithm at T_{eff} will be investigated. The effective temperature is also involved in the SCT approximation formalism (Eq.(2.162)). T_{eff} is used to take into account the atom binding effects for the neutron down-scattering calculations. While T is used for the neutron up-scattering calculations to fulfill the principle of detail balance (Eq.(2.9)). Hence, the neutron scattering treatment with $S(\alpha, \beta)_{\text{SCT}}$ tables is expected to improve the up-scattering simulation compared to the SVT algorithm at T_{eff}. The neutron yields obtained by using the TRIPOLI-4® code for the SVT algorithm at T_{eff} and the $S(\alpha, \beta)_{\text{SCT}}$ tables will be compared to the results obtained with tabulated TSLs $S(\alpha, \beta)$. These comparisons are illustrated in the case of ^{1}H in $^{1}H_2O$ and ^{16}O in UO_2. The physical model has been presented in the previous section. The simulations performed with TRIPOLI-4® are summarized in Table 5.6.

Table 5.6.: Simulations performed by using the Monte-Carlo neutron transport code TRIPOLI-4® for ^{1}H in $^{1}H_2O$ and ^{16}O in UO_2. The effective temperature T_{eff} of ^{1}H in $^{1}H_2O$ is computed via the PDOS of the CAB model (Márquez Damián, J. Granada, and D. Malaspina 2014). T_{eff} of ^{16}O in UO_2 is obtained via the PDOS of (G. Noguere, J. P. Scotta, Xu, Filhol, et al. 2020).

Target nucleus	E (eV)	T (K)	T_{eff} (K)	Scattering treatments
^{1}H in $^{1}H_2O$	5	294	1184	SVT at T SVT at T_{eff} $S(\alpha, \beta)_{\text{SCT}}$ $S(\alpha, \beta)$ at T
^{16}O in UO_2	6.67	298	381	

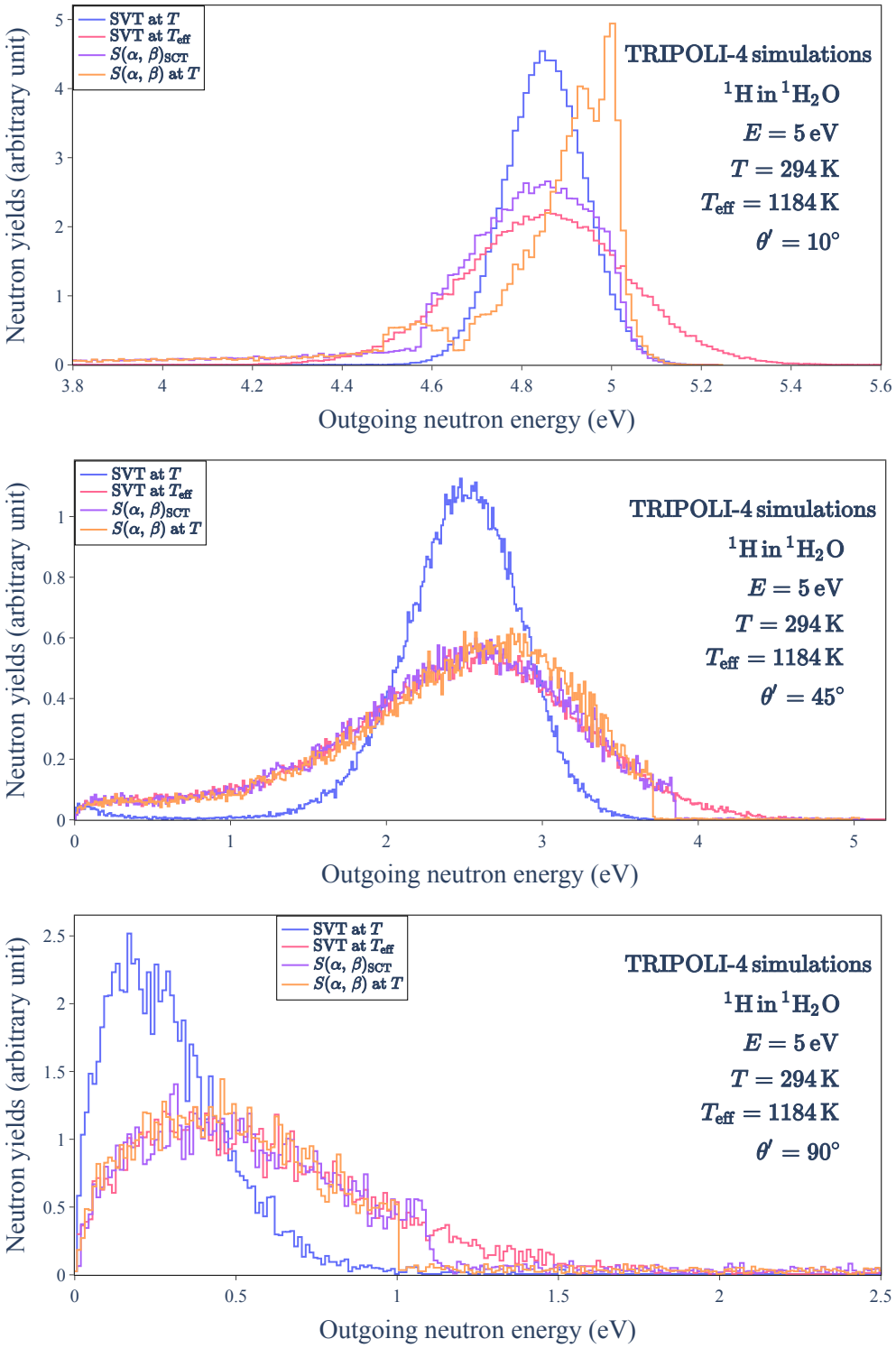

Figure 5.15.: Neutron yields of ^{1}H in ^1H_2O at $\theta' = 10°$, 45° and 90° obtained by using the Monte-Carlo neutron transport code TRIPOLI-4® for different scattering treatments: SVT at $T = 294$ K (blue lines), SVT at $T_{eff} = 1184$ K (pink lines), $S(\alpha, \beta)_{SCT}$ tables (purple lines), tabulated $S(\alpha, \beta)$ at T (orange lines).

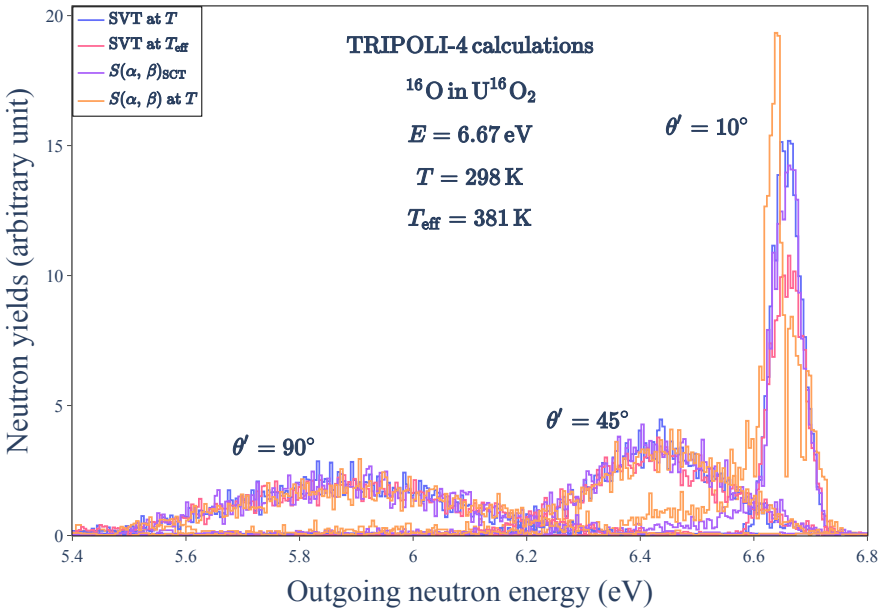

Figure 5.16.: Neutron yields of ^{16}O in UO_2 at $\theta' = 10°$, 45° and 90° obtained by using the Monte-Carlo neutron transport code TRIPOLI-4® for different scattering treatments: SVT at $T = 298$ K (blue lines), SVT at $T_{\text{eff}} = 381$ K (pink lines), $S(\alpha, \beta)_{\text{SCT}}$ tables (purple lines), tabulated $S(\alpha, \beta)$ at T (orange lines).

The neutron yields of ^{1}H in $^{1}H_2O$ at $\theta' = 10°$, 45° and 90° obtained by using the TRIPOLI-4® code for scattering treatments: SVT at T, SVT at T_{eff} and $S(\alpha, \beta)_{\text{SCT}}$ tables are compared with the results simulated by the tabulated $S(\alpha, \beta)$ at T. The comparisons of the results are shown in Fig. 5.15. At small scattering angle ($\theta' = 10°$), all three investigated treatments fail to reproduce the quasi-elastic peak and the associated structures. The treatment with $S(\alpha, \beta)_{\text{SCT}}$ tables reproduces better the neutron yields related to the up-scattering, compared to the SVT at T_{eff}. At large θ', the neutron up-scattering can be neglected. Therefore, the treatments of the $S(\alpha, \beta)_{\text{SCT}}$ tables and the SVT at T_{eff} are equivalent. These two treatments reproduce better the neutron yields, compared to the SVT at T.

Same comparisons are performed in the case of ^{16}O in UO_2. The obtained results are presented in Fig. 5.16. At small θ', all three investigated scattering treatments are incapable of reproducing the structures related to the atomic motions of the oxygen atoms bound in UO_2. This result is in consistency with the case of ^{1}H in $^{1}H_2O$. The effective temperature of ^{16}O in UO_2 ($T_{\text{eff}} = 381$ K) is close to $T = 298$ K. Therefore, at large θ', the neutron yields obtained by the SVT algorithm at T_{eff} show no significant difference with the results obtained by the SVT algorithm at T. It is recommended to add a new scattering option in the TRIPOLI-4® code that allows to compute in real time $S(\alpha, \beta)$ tables with the SCT formalism by taking into account T and T_{eff} in the calculations. This new option will be of great interest to test the impact of different scattering models on integral benchmarks.

These results show the importance of using the effective temperature to take into account the atomic motions of atoms bound in molecules. They also confirm the improvement of the SCT treatment for the up-scattering calculations, compared to the SVT at T_{eff}.

5.5. Preliminary conclusions

This chapter is devoted to investigate the neutron scattering with light nuclides having a non-resonant neutron scattering cross section below 10 eV. The neutron scattering treatments studied are: AK (for Asymptotic Kernel), SVT (for Sampling the Velocity of the Target nucleus) at T and T_{eff}, FGM (for Free Gas Model), SCT (for Short Collision Time approximation), and tabulated $S(\alpha, \beta)$. The formalisms of AK and SVT are reviewed. The SVT algorithm is validated by sampling the velocities of hydrogen atoms from a M-B distribution and trajectory files obtained from molecular dynamics calculations with the GROMACS code. Numerical validations of the listed neutron scattering treatments with the TRIPOLI-4® code are performed at room temperature for ^{1}H in $^{1}H_2O$ and ^{16}O in UO_2. $S(\alpha, \beta)$ tables are correctly used by the TRIPOLI-4® code to simulate the transport of neutrons with energies lying below a few eV. Finally, importance of using the effective temperature and the improvement of the SCT treatment for the up-scattering calculations are confirmed.

General conclusions and perspectives

The present work concentrates on the data processing and validation of the coherent elastic neutron scattering cross sections $\sigma_{\text{coh}}^{\text{el}}(E)$ and thermal scattering laws (TSLs) or $S(\alpha, \beta)$ of UO_2 as a function of temperature.

The low energy neutron scattering formalism has been presented: equations allowing to calculate the TSLs for solid crystalline, liquid and gas materials are given. Based on these equations, the data processing tool `CINEL` has been developed to generate the TSLs in ENDF-6 format. `CINEL` is developed in Python by using an interactive development environment named JupyterLab. `CINEL` enables to use graphics processing unit (GPU) to accelerate the computation of the TSLs. The numerical validations of `CINEL` are performed by using various types of crystal materials. An excellent agreement is obtained when compared to the ENDF/B-VIII.0 database and the `NJOY-NCrystal` library. Nevertheless, the incoherent approximation adopted in the `CINEL` code is reported to be inadequate for strongly coherent crystalline materials such as pyrolytic graphite. Therefore, the coherent one-phonon correction will be implemented in the future version of `CINEL` to improve the incoherent approximation. The cubic approximation used in the current version of `CINEL` will also be eliminated.

Thanks to the phonon density of states (PDOS) of UO_2 measured at the IN4 and IN6 time-of-flight spectrometers of the Institut Laue-Langevin (ILL) up to 1675 K, the TSLs of UO_2 for a wide temperature range can be calculated by using the `CINEL` code. An ideal fluorite structure for UO_2 over the full temperature range has been adopted to calculate $\sigma_{\text{coh}}^{\text{el}}(E)$. Results provided by `CINEL` are stored in ENDF-6 format, which can be further processed to be used as neutron scattering library in the Monte-Carlo neutron transports code TRIPOLI-4®. Two data sets of neutron diffraction experiments performed at the D4 and D20 diffractometers of ILL up to 1664 K, have been simulated by using the TRIPOLI-4® code. A few numbers of experimental parameters were optimized on the data to account for the angular offset, the response function of the diffractometer and a background correction. The good agreement between the experimental and theoretical neutron diffraction patterns validates our TRIPOLI-4® calculation scheme for UO_2. The obtained results indicate that TRIPOLI-4® is able to reproduce these neutron diffraction patterns thanks to the developed `CINEL` code. However some limited issues remain in the interpretation of the background correction. Biases due to theoretical approximations would need to be investigated.

The performance of our calculation scheme was also investigated by simulating atomic pair distribution functions to probe the structure of UO_2 at elevated temperature. The differences observed at 1273 K between the experiment and the theory con-

firm that the local deviations of the oxygen atoms from the average structure of UO_2 are not compatible with an ideal fluorite structure. We show that the CINEL processing tool offers the possibility of testing atomic disorder configurations, anharmonic models or space groups which are suggested in the literature for exploring the unexpected shortening of the U-O distance with increasing temperature.

The TRIPOLI-4® calculation scheme for UO_2 has been validated for incident neutron energy above a few eV. In the epithermal energy range where the TSLs are not available, the neutron scattering with light nuclides having a non-resonant neutron scattering cross section has been investigated. The studied neutron scattering treatments are: AK (for Asymptotic Kernel), SVT (for Sampling the Velocity of the Target nucleus) at thermodynamic temperature T and effective temperature T_{eff}, FGM (for Free Gas Model), SCT (for Short Collision Time approximation), and tabulated $S(\alpha, \beta)$. The SVT algorithm has been validated by sampling the velocities of hydrogen atoms from a Maxwell-Boltzmann (M-B) distribution and trajectory files obtained from molecular dynamics calculations with the GROMACS code. Numerical validations of the above neutron scattering treatments with the TRIPOLI-4® code are performed at room temperature for ^{1}H in $^{1}H_2O$ and ^{16}O in UO_2. The obtained results indicate that $S(\alpha, \beta)$ tables are correctly used by the TRIPOLI-4® code to simulate the transport of neutrons with energies lying between a few eV and $400 k_B T$. The importance of using the effective temperature and the improvement of the SCT treatment for the up-scattering calculations are confirmed. The obtained results for light nuclides will be further investigated for ^{238}U in UO_2.

Bibliography

[Abr+15] Mark James Abraham, Teemu Murtola, Roland Schulz, et al. "GROMACS: High performance molecular simulations through multi-level parallelism from laptops to supercomputers". In: *SoftwareX* 1-2 (2015), pp. 19–25. ISSN: 2352-7110. DOI: https://doi.org/10.1016/j.softx.2015.06.001. URL: https://www.sciencedirect.com/science/article/pii/S2352711015000059 (cit. on p. 125).

[All+16] J. Allison, K. Amako, J. Apostolakis, et al. "Recent developments in Geant4". In: *Nuclear Instruments and Methods in Physics Research Section A: Accelerators, Spectrometers, Detectors and Associated Equipment* 835 (2016), pp. 186–225. ISSN: 0168-9002. DOI: https://doi.org/10.1016/j.nima.2016.06.125. URL: https://www.sciencedirect.com/science/article/pii/S0168900216306957 (cit. on p. 67).

[Ama+16] Katrin Amann-Winkel, Marie-Claire Bellissent-Funel, Livia E. Bove, et al. "X-ray and Neutron Scattering of Water". In: *Chemical Reviews* 116.13 (2016). PMID: 27195477, pp. 7570–7589. DOI: 10.1021/acs.chemrev.5b00663. eprint: https://doi.org/10.1021/acs.chemrev.5b00663. URL: https://doi.org/10.1021/acs.chemrev.5b00663 (cit. on pp. 58, 60).

[Bal21] G. Baldinozzi. *private communication*. 2021 (cit. on p. 103).

[BDL09] B. Becker, R. Dagan, and G. Lohnert. "Proof and implementation of the stochastic formula for ideal gas, energy dependent scattering kernel". In: *Annals of Nuclear Energy* 36.4 (2009), pp. 470–474. ISSN: 0306-4549. DOI: https://doi.org/10.1016/j.anucene.2008.12.001. URL: https://www.sciencedirect.com/science/article/pii/S0306454908003186 (cit. on pp. 30, 119, 190).

[Bor70] GM Borgonovi. *NEUTRON SCATTERING KERNELS CALCULATIONS AT EPITHERMAL ENERGIES*. Tech. rep. Gulf General Atomic, Inc., San Diego, Calif., 1970 (cit. on p. 63).

[Bro+18] D.A. Brown, M.B. Chadwick, R. Capote, et al. "ENDF/B-VIII.0: The 8^{th} Major Release of the Nuclear Reaction Data Library with CIELO-project Cross Sections, New Standards and Thermal Scattering Data". In: *Nuclear Data Sheets* 148 (2018). Special Issue on Nuclear Reaction Data, pp. 1–142. ISSN: 0090-3752. DOI: https://doi.org/10.1016/j.nds.2018.02.001. URL: https://www.sciencedirect.com/science/article/pii/S0090375218300206 (cit. on pp. 67, 120, 193).

[Bru+15] E. Brun, F. Damian, C.M. Diop, et al. "TRIPOLI-4®, CEA, EDF and AREVA reference Monte Carlo code". In: *Annals of Nuclear Energy* 82 (2015). Joint International Conference on Supercomputing in Nuclear Applications and Monte Carlo 2013, SNA + MC 2013. Pluri- and Trans-disciplinarity, Towards New Modeling and Numerical Simulation Paradigms, pp. 151–160. ISSN: 0306-4549. DOI: https://doi.org/10.1016/j.anucene.2014.07.053. URL: https://www.sciencedirect.com/science/article/pii/S0306454914003843 (cit. on pp. 29, 48, 94, 118, 189, 199).

[CPR58] G. Caglioti, A. Paoletti, and F.P. Ricci. "Choice of collimators for a crystal spectrometer for neutron diffraction". In: *Nuclear Instruments* 3.4 (1958), pp. 223–228. ISSN: 0369-643X. DOI: https://doi.org/10.1016/0369-643X(58)90029-X. URL: https://www.sciencedirect.com/science/article/pii/0369643X5890029X (cit. on p. 99).

[CK20] X.-X. Cai and T. Kittelmann. "NCrystal: A library for thermal neutron transport". In: *Computer Physics Communications* 246 (2020), p. 106851. ISSN: 0010-4655. DOI: https://doi.org/10.1016/j.cpc.2019.07.015. URL: https://www.sciencedirect.com/science/article/pii/S0010465519302280 (cit. on pp. 34–36, 67, 68).

[Cai+19] X.-X. Cai, T. Kittelmann, E. Klinkby, et al. "Rejection-based sampling of inelastic neutron scattering". In: *Journal of Computational Physics* 380 (2019), pp. 400–407. ISSN: 0021-9991. DOI: https://doi.org/10.1016/j.jcp.2018.11.043. URL: https://www.sciencedirect.com/science/article/pii/S0021999118307885 (cit. on p. 67).

[CC75] L L Carter and E D Cashwell. *Particle-transport simulation with the Monte Carlo method*. Tech. rep. Jan. 1975. DOI: 10.2172/4167844. URL: https://www.osti.gov/biblio/4167844 (cit. on p. 119).

[Che+19] Y. Q. Cheng, L. L. Daemen, A. I. Kolesnikov, et al. "Simulation of Inelastic Neutron Scattering Spectra Using OCLIMAX". In: *Journal of Chemical Theory and Computation* 15.3 (2019). PMID: 30735379, pp. 1974–1982. DOI: 10.1021/acs.jctc.8b01250. eprint: https://doi.org/10.1021/acs.jctc.8b01250. URL: https://doi.org/10.1021/acs.jctc.8b01250 (cit. on pp. 67, 68).

[CR20] Y. Q. Cheng and A. J. Ramirez-Cuesta. "Calculation of the Thermal Neutron Scattering Cross-Section of Solids Using OCLIMAX". In: *Journal of Chemical Theory and Computation* 16.8 (2020). PMID: 32700910, pp. 5212–5217. DOI: 10.1021/acs.jctc.0c00569. eprint: https://doi.org/10.1021/acs.jctc.0c00569. URL: https://doi.org/10.1021/acs.jctc.0c00569 (cit. on pp. 67, 68).

[CBO56] R.R. Coveyou, R.R. Bate, and R.K. Osborn. "Effect of moderator temperature upon neutron flux in infinite, capturing medium". In: *Journal of Nuclear Energy (1954)* 2.3 (1956), pp. 153–167. ISSN: 0891-3919. DOI: https://doi.org/10.1016/0891-3919(55)90030-9. URL: https://www.

sciencedirect.com/science/article/pii/0891391955900309 (cit. on pp. 29, 30, 118, 189, 190).

[DB06] R Dagan and CHM Broeders. "On the effect of resonance dependent scattering-kernel on fuel cycle and inventory". In: *Proceedings of the PHYSOR-2006 meeting*. 2006 (cit. on pp. 30, 119, 190).

[DMG13] J. I. Marquez Damian, D. C. Malaspina, and J. R. Granada. "Vibrational spectra of light and heavy water with application to neutron cross section calculations". In: *The Journal of Chemical Physics* 139.2 (2013), p. 024504. DOI: 10.1063/1.4812828. eprint: https://doi.org/10.1063/1.4812828. URL: https://doi.org/10.1063/1.4812828 (cit. on p. 57).

[Dam] J.-I. Marquez Damian. *NCrystal : a library for thermal neutron transport in crystals*. https://github.com/marquezj/ncrystal. Accessed: 2019-08-22 (cit. on p. 68).

[DER04] Alberto De Santis, Alessandro Ercoli, and Dario Rocca. "Comment on "An interpretation of the low-frequency spectrum of liquid water" [J. Chem. Phys. 118, 452 (2003)]". In: *The Journal of Chemical Physics* 120.3 (2004), pp. 1657–1658. DOI: 10.1063/1.1634251. eprint: https://doi.org/10.1063/1.1634251. URL: https://doi.org/10.1063/1.1634251 (cit. on p. 58).

[Des+17] L. Desgranges, Y. Ma, Ph. Garcia, et al. "What Is the Actual Local Crystalline Structure of Uranium Dioxide, UO2? A New Perspective for the Most Used Nuclear Fuel". In: *Inorganic Chemistry* 56.1 (2017). PMID: 27977186, pp. 321–326. DOI: 10.1021/acs.inorgchem.6b02111. eprint: https://doi.org/10.1021/acs.inorgchem.6b02111. URL: https://doi.org/10.1021/acs.inorgchem.6b02111 (cit. on pp. 95, 97, 98, 105, 106, 109, 112, 115, 202).

[DCW65] G. Dolling, R. A. Cowley, and A. D. B. Woods. "THE CRYSTAL DYNAMICS OF URANIUM DIOXIDE". In: *Canadian Journal of Physics* 43.8 (1965), pp. 1397–1413. DOI: 10.1139/p65-135. eprint: https://doi.org/10.1139/p65-135. URL: https://doi.org/10.1139/p65-135 (cit. on pp. 48, 49).

[ES62] P. A. Egelstaff and P. Schofield. "On the Evaluation of the Thermal Neutron Scattering Law". In: *Nuclear Science and Engineering* 12.2 (1962), pp. 260–270. DOI: 10.13182/NSE62-A26066. eprint: https://doi.org/10.13182/NSE62-A26066. URL: https://doi.org/10.13182/NSE62-A26066 (cit. on pp. 53, 65).

[Ege62] P.A. Egelstaff. "Neutron scattering studies of liquid diffusion". In: *Advances in Physics* 11.43 (1962), pp. 203–232. DOI: 10.1080/00018736200101282. eprint: https://doi.org/10.1080/00018736200101282. URL: https://doi.org/10.1080/00018736200101282 (cit. on p. 62).

[FHG14] G. Ferran, W. Haeck, and M. Gonin. "Development Progress of the GAIA Nuclear Data Processing Software". In: *Nuclear Data Sheets* 118 (2014), pp. 491–493. ISSN: 0090-3752. DOI: https://doi.org/10.1016/j.nds.2014.04.115. URL: https://www.sciencedirect.com/science/article/pii/S0090375214001458 (cit. on p. 67).

[Fis+02] HE Fischer, GJ Cuello, P Palleau, et al. "D4c: A very high precision diffractometer for disordered materials". In: *Applied Physics A* 74.1 (2002), s160–s162. DOI: 10.1007/s003390101087. URL: https://doi.org/10.1007/s003390101087 (cit. on p. 95).

[GA11] Miguel A. González and José L. F. Abascal. "A flexible model for water based on TIP4P/2005". In: *The Journal of Chemical Physics* 135.22 (2011), p. 224516. DOI: 10.1063/1.3663219. eprint: https://doi.org/10.1063/1.3663219. URL: https://doi.org/10.1063/1.3663219 (cit. on pp. 57, 125, 203).

[Gon+08] Fátima González Sánchez, Fanni Jurányi, Thomas Gimmi, et al. "Translational diffusion of water and its dependence on temperature in charged and uncharged clays: A neutron scattering study". In: *The Journal of Chemical Physics* 129.17 (2008), p. 174706. DOI: 10.1063/1.3000638. eprint: https://doi.org/10.1063/1.3000638. URL: https://doi.org/10.1063/1.3000638 (cit. on p. 60).

[Goo+12] T. Goorley, M. James, T. Booth, et al. "Initial MCNP6 Release Overview". In: *Nuclear Technology* 180.3 (2012), pp. 298–315. DOI: 10.13182/NT11-135. eprint: https://doi.org/10.13182/NT11-135. URL: https://doi.org/10.13182/NT11-135 (cit. on p. 48).

[Gra+21] José Rolando Granada, José Ignacio Márquez Damián, Javier Dawidowski, et al. "Development of neutron scattering kernels for cold neutron reflector materials". In: (Mar. 2021). arXiv: 2103.09145 [physics.ins-det] (cit. on pp. 71, 194).

[GG16] B Granger and J Grout. "JupyterLab: Building Blocks for Interactive Computing". In: *Slides of presentation made at SciPy* (2016) (cit. on pp. 69, 192).

[HR81] Peter L. Hall and D.K. Ross. "Incoherent neutron scattering functions for random jump diffusion in bounded and infinite media". In: *Molecular Physics* 42.3 (1981), pp. 673–682. DOI: 10.1080/00268978100100521. eprint: https://doi.org/10.1080/00268978100100521. URL: https://doi.org/10.1080/00268978100100521 (cit. on p. 60).

[Hau65] H. Hausner. "Determination of the melting point of uranium dioxide". In: *Journal of Nuclear Materials* 15.3 (1965), pp. 179–183. ISSN: 0022-3115. DOI: https://doi.org/10.1016/0022-3115(65)90178-9. URL: https://www.sciencedirect.com/science/article/pii/0022311565901789 (cit. on pp. 94, 199).

[HU17] Jon Herman and Will Usher. "SALib: An open-source Python library for Sensitivity Analysis". In: *Journal of Open Source Software* 2.9 (2017), p. 97. DOI: 10.21105/joss.00097. URL: https://doi.org/10.21105/joss.00097 (cit. on p. 100).

[Jai18] Vaibhav Jaiswal. "Theoretical and Experimental Approach Towards Generation of Thermal Scattering Law for Light Water". PhD thesis. Université de Lille, 2018 (cit. on p. 67).

[Klu+16] Thomas Kluyver, Benjamin Ragan-Kelley, Fernando Pérez, et al. "Jupyter Notebooks—a publishing format for reproducible computational workflows". In: *Positioning and Power in Academic Publishing: Players, Agents and Agendas*. Ed. by Fernando Loizides and Birgit Scmidt. IOS Press, 2016, pp. 87–90. URL: https://eprints.soton.ac.uk/403913/ (cit. on pp. 69, 192).

[KF96a] G. Kresse and J. Furthmüller. "Efficiency of ab-initio total energy calculations for metals and semiconductors using a plane-wave basis set". In: *Computational Materials Science* 6.1 (1996), pp. 15–50. ISSN: 0927-0256. DOI: https://doi.org/10.1016/0927-0256(96)00008-0. URL: https://www.sciencedirect.com/science/article/pii/0927025696000080 (cit. on pp. 49, 68).

[KF96b] G. Kresse and J. Furthmüller. "Efficient iterative schemes for ab initio total-energy calculations using a plane-wave basis set". In: *Phys. Rev. B* 54 (16 Oct. 1996), pp. 11169–11186. DOI: 10.1103/PhysRevB.54.11169. URL: https://link.aps.org/doi/10.1103/PhysRevB.54.11169 (cit. on pp. 49, 68).

[LPS15] Siu Kwan Lam, Antoine Pitrou, and Stanley Seibert. "Numba: A llvm-based python jit compiler". In: *Proceedings of the Second Workshop on the LLVM Compiler Infrastructure in HPC*. 2015, pp. 1–6 (cit. on pp. 70, 192).

[Lam39] Willis E. Lamb. "Capture of Neutrons by Atoms in a Crystal". In: *Phys. Rev.* 55 (2 Jan. 1939), pp. 190–197. DOI: 10.1103/PhysRev.55.190. URL: https://link.aps.org/doi/10.1103/PhysRev.55.190 (cit. on pp. 31, 138, 191).

[LT58] A. M. Lane and R. G. Thomas. "R-Matrix Theory of Nuclear Reactions". In: *Rev. Mod. Phys.* 30 (2 Apr. 1958), pp. 257–353. DOI: 10.1103/RevModPhys.30.257. URL: https://link.aps.org/doi/10.1103/RevModPhys.30.257 (cit. on pp. 29, 189).

[Lau] Institut Laue-Langevin. *Instruments list*. https://www.ill.eu/users/instruments/instruments-list/. Accessed: 2021-04-01 (cit. on p. 95).

[LSR09] Deokjung Lee, Kord Smith, and Joel Rhodes. "The impact of ^{238}U resonance elastic scattering approximations on thermal reactor Doppler reactivity". In: *Annals of Nuclear Energy* 36.3 (2009). PHYSOR 2008, pp. 274–280. ISSN: 0306-4549. DOI: https://doi.org/10.1016/j.anucene.2008.11.026. URL: https://www.sciencedirect.com/science/article/pii/S0306454908003083 (cit. on pp. 30, 120, 190).

[Lep+15] Jaakko Leppänen, Maria Pusa, Tuomas Viitanen, et al. "The Serpent Monte Carlo code: Status, development and applications in 2013". In: *Annals of Nuclear Energy* 82 (2015). Joint International Conference on Supercomputing in Nuclear Applications and Monte Carlo 2013, SNA + MC 2013. Pluri- and Trans-disciplinarity, Towards New Modeling and Numerical Simulation Paradigms, pp. 142–150. ISSN: 0306-4549. DOI: https://doi.org/10.1016/j.anucene.2014.08.024. URL: https://www.sciencedirect.com/science/article/pii/S0306454914004095 (cit. on p. 48).

[Ler+13] Adrien Lerbret, Alain Hédoux, Burkhard Annighöfer, et al. "Influence of pressure on the low-frequency vibrational modes of lysozyme and water: A complementary inelastic neutron scattering and molecular dynamics simulation study". In: *Proteins: Structure, Function, and Bioinformatics* 81.2 (2013), pp. 326–340. DOI: https://doi.org/10.1002/prot.24189. eprint: https://onlinelibrary.wiley.com/doi/pdf/10.1002/prot.24189. URL: https://onlinelibrary.wiley.com/doi/abs/10.1002/prot.24189 (cit. on pp. 58, 59).

[Lux18] Iván Lux. *Monte Carlo Particle Transport Methods: Neutron and Photon Calculations*. May 2018. ISBN: 9781351074834. DOI: 10.1201/9781351074834 (cit. on pp. 30, 118, 190).

[Ma17] Yue Ma. "A study of point defects in UO 2+ x and their impact upon fuel properties". PhD thesis. Aix-Marseille Université, 2017 (cit. on pp. 94, 194).

[Mac94] R E MacFarlane. "New thermal neutron scattering files for ENDF/B-VI release 2". In: (Mar. 1994). DOI: 10.2172/10192168. URL: https://www.osti.gov/biblio/10192168 (cit. on p. 67).

[Mac+17] Robert Macfarlane, Douglas W Muir, RM Boicourt, et al. *The NJOY Nuclear Data Processing System, Version 2016*. Tech. rep. Los Alamos National Lab.(LANL), Los Alamos, NM (United States), 2017 (cit. on pp. 40, 47, 63, 67).

[Már+16] J.I. Márquez Damián, J.R. Granada, F. Cantargi, et al. "Generation of thermal scattering libraries for liquids beyond the Gaussian approximation using molecular dynamics and NJOY/LEAPR". In: *Annals of Nuclear Energy* 92 (2016), pp. 107–112. ISSN: 0306-4549. DOI: https://doi.org/10.1016/j.anucene.2016.01.036. URL: https://www.sciencedirect.com/science/article/pii/S0306454916300469 (cit. on pp. 53, 60).

[MGM14] J.I. Márquez Damián, J.R. Granada, and D.C. Malaspina. "CAB models for water: A new evaluation of the thermal neutron scattering laws for light and heavy water in ENDF-6 format". In: *Annals of Nuclear Energy* 65 (2014), pp. 280–289. ISSN: 0306-4549. DOI: https://doi.org/10.1016/j.anucene.2013.11.014. URL: https://www.sciencedirect.com/science/article/pii/S0306454913005987 (cit. on pp. 57–59, 138).

[McC+99] L. B. McCusker, R. B. Von Dreele, D. E. Cox, et al. "Rietveld refinement guidelines". In: *Journal of Applied Crystallography* 32.1 (Feb. 1999), pp. 36–50. DOI: 10.1107/S0021889898009856. URL: https://doi.org/10.1107/S0021889898009856 (cit. on p. 99).

[New+14] Matthew Newville, Till Stensitzki, Daniel B. Allen, et al. *LMFIT: Non-Linear Least-Square Minimization and Curve-Fitting for Python*. Version 0.8.0. Sept. 2014. DOI: 10.5281/zenodo.11813. URL: https://doi.org/10.5281/zenodo.11813 (cit. on pp. 100, 101).

[NR66] B.R.A. Nijboer and A. Rahman. "Time expansion of correlation functions and the theory of slow neutron scattering". In: *Physica* 32.2 (1966), pp. 415–432. ISSN: 0031-8914. DOI: https://doi.org/10.1016/0031-8914(66)90068-1. URL: https://www.sciencedirect.com/science/article/pii/0031891466900681 (cit. on p. 107).

[NMD18] G Noguere, Pablo Maldonado, and C De Saint Jean. "Doppler broadening of neutron-induced resonances using ab initio phonon spectrum". In: *The European Physical Journal Plus* 133.5 (2018), p. 177. DOI: 10.1140/epjp/i2018-12009-y. URL: https://doi.org/10.1140/epjp/i2018-12009-y (cit. on pp. 29, 49, 189).

[Nog+21] G. Noguere, J. P. Scotta, S. Xu, E. Farhi, et al. "Temperature-dependent dynamic structure factors for liquid water inferred from inelastic neutron scattering measurements". In: *The Journal of Chemical Physics* 155.2 (2021), p. 024502. DOI: 10.1063/5.0055779. eprint: https://doi.org/10.1063/5.0055779. URL: https://doi.org/10.1063/5.0055779 (cit. on p. 5).

[Nog+20a] G. Noguere, J. P. Scotta, S. Xu, A. Filhol, et al. "Combining density functional theory and Monte Carlo neutron transport calculations to study the phonon density of states of UO_2 up to 1675 K by inelastic neutron scattering". In: *Phys. Rev. B* 102 (13 Oct. 2020), p. 134312. DOI: 10.1103/PhysRevB.102.134312. URL: https://link.aps.org/doi/10.1103/PhysRevB.102.134312 (cit. on pp. 5, 95, 138).

[Nog+20b] Noguere, Gilles, Xu, Shuqi, Filhol, Alain, et al. "Measurement of the double-differential neutron cross section of UO2 from room temperature to hot full power conditions". In: *EPJ Web Conf.* 239 (2020), p. 14003. DOI: 10.1051/epjconf/202023914003. URL: https://doi.org/10.1051/epjconf/202023914003 (cit. on p. 5).

[OS99] Iwao Ohmine and Shinji Saito. “Water Dynamics: Fluctuation, Relaxation, and Chemical Reactions in Hydrogen Bond Network Rearrangement”. In: *Accounts of Chemical Research* 32.9 (1999), pp. 741–749. DOI: 10.1021/ar970161g. eprint: https://doi.org/10.1021/ar970161g. URL: https://doi.org/10.1021/ar970161g (cit. on p. 58).

[Ong+13] Shyue Ping Ong, William Davidson Richards, Anubhav Jain, et al. “Python Materials Genomics (pymatgen): A robust, open-source python library for materials analysis”. In: *Computational Materials Science* 68 (Feb. 2013), pp. 314–319. ISSN: 09270256. DOI: 10.1016/j.commatsci.2012.10.028. URL: http://linkinghub.elsevier.com/retrieve/pii/S0927025612006295 (cit. on pp. 37, 72).

[Ong+] Shyue Ping Ong, William Davidson Richards, Anubhav Jain, et al. *UO2 unit cell with $Fm\bar{3}m$ symmetry*. https://materialsproject.org/materials/mp-1597/. Asscessed: 2021-04-07 (cit. on p. 38).

[PM03] Joan Àngel Padró and Jordi Martí. “An interpretation of the low-frequency spectrum of liquid water”. In: *The Journal of Chemical Physics* 118.1 (2003), pp. 452–453. DOI: 10.1063/1.1524619. eprint: https://doi.org/10.1063/1.1524619. URL: https://doi.org/10.1063/1.1524619 (cit. on p. 58).

[PM04] Joań Àngel Padró and Jordi Martí. “Response to “Comment on ‘An interpretation of the low-frequency spectrum of liquid water’” [J. Chem. Phys. 118, 452 (2003)]”. In: *The Journal of Chemical Physics* 120.3 (2004), pp. 1659–1660. DOI: 10.1063/1.1634252. eprint: https://doi.org/10.1063/1.1634252. URL: https://doi.org/10.1063/1.1634252 (cit. on p. 58).

[Pal+19] Raul I. Palomares, Marshall T. McDonnell, Li Yang, et al. “Oxygen point defect accumulation in single-phase UO_{2+x}”. In: *Phys. Rev. Materials* 3 (5 May 2019), p. 053611. DOI: 10.1103/PhysRevMaterials.3.053611. URL: https://link.aps.org/doi/10.1103/PhysRevMaterials.3.053611 (cit. on pp. 108, 110, 201, 203).

[PLK97] K. Parlinski, Z. Q. Li, and Y. Kawazoe. “First-Principles Determination of the Soft Mode in Cubic ZrO_2”. In: *Phys. Rev. Lett.* 78 (21 May 1997), pp. 4063–4066. DOI: 10.1103/PhysRevLett.78.4063. URL: https://link.aps.org/doi/10.1103/PhysRevLett.78.4063 (cit. on p. 49).

[Par99] Krzysztof Parlinski. “Calculation of phonon dispersion curves by the direct method”. In: *AIP Conference Proceedings* 479.1 (1999), pp. 121–126. DOI: 10.1063/1.59457. eprint: https://aip.scitation.org/doi/pdf/10.1063/1.59457. URL: https://aip.scitation.org/doi/abs/10.1063/1.59457 (cit. on p. 49).

[PDP14] Václav Petříček, Michal Dušek, and Lukáš Palatinus. "Crystallographic Computing System JANA2006: General features". In: *Zeitschrift für Kristallographie - Crystalline Materials* 229.5 (2014), pp. 345–352. DOI: doi:10.1515/zkri-2014-1737. URL: https://doi.org/10.1515/zkri-2014-1737 (cit. on pp. 102, 103).

[Pla52] G. Placzek. "The Scattering of Neutrons by Systems of Heavy Nuclei". In: *Phys. Rev.* 86 (3 May 1952), pp. 377–388. DOI: 10.1103/PhysRev.86.377. URL: https://link.aps.org/doi/10.1103/PhysRev.86.377 (cit. on p. 108).

[Plo+20] AJM Plompen, O Cabellos, C De Saint Jean, et al. "The joint evaluated fission and fusion nuclear data library, JEFF-3.3". In: *The European Physical Journal A* 56.7 (2020), pp. 1–108. DOI: 10.1140/epja/s10050-020-00141-9. URL: https://doi.org/10.1140/epja/s10050-020-00141-9 (cit. on pp. 45, 46).

[Al-08] Iyad Ibrahim Al-Qasir. "Thermal neutron scattering in graphite". PhD thesis. North Carolina State University, 2008 (cit. on p. 70).

[QSH11] Johan Qvist, Helmut Schober, and Bertil Halle. "Structural dynamics of supercooled water from quasielastic neutron scattering and molecular simulations". In: *The Journal of Chemical Physics* 134.14 (2011), p. 144508. DOI: 10.1063/1.3578472. eprint: https://doi.org/10.1063/1.3578472. URL: https://doi.org/10.1063/1.3578472 (cit. on p. 60).

[RSS62] A. Rahman, K. S. Singwi, and A. Sjölander. "Theory of Slow Neutron Scattering by Liquids. I". In: *Phys. Rev.* 126 (3 May 1962), pp. 986–996. DOI: 10.1103/PhysRev.126.986. URL: https://link.aps.org/doi/10.1103/PhysRev.126.986 (cit. on p. 52).

[Ram+21] Kemal Ramic, Jose Ignacio Marquez Damian, Thomas Kittelmann, et al. *NJOY+NCrystal: an open-source tool for creating thermal neutron scattering libraries*. 2021. arXiv: 2108.11737 [physics.ins-det] (cit. on pp. 67, 193).

[Rie69] H. M. Rietveld. "A profile refinement method for nuclear and magnetic structures". In: *Journal of Applied Crystallography* 2.2 (June 1969), pp. 65–71. DOI: 10.1107/S0021889869006558. URL: https://doi.org/10.1107/S0021889869006558 (cit. on pp. 94, 199).

[Rot96] W. Rothenstein. "Neutron scattering kernels in pronounced resonances for stochastic Doppler effect calculations". In: *Annals of Nuclear Energy* 23.4 (1996). A Special Issue in Honour of M. M. R. Williams, pp. 441–458. ISSN: 0306-4549. DOI: https://doi.org/10.1016/0306-4549(95)00109-3. URL: https://www.sciencedirect.com/science/article/pii/0306454995001093 (cit. on pp. 119, 124).

[Rot04] W. Rothenstein. "Proof of the formula for the ideal gas scattering kernel for nuclides with strongly energy dependent scattering cross sections". In: *Annals of Nuclear Energy* 31.1 (2004), pp. 9–23. ISSN: 0306-4549. DOI: https://doi.org/10.1016/S0306-4549(03)00216-0. URL: https://www.sciencedirect.com/science/article/pii/S0306454903002160 (cit. on p. 120).

[RD95] W. Rothenstein and R. Dagan. "Two-body kinetics treatment for neutron scattering from a heavy Maxwellian gas". In: *Annals of Nuclear Energy* 22.11 (1995), pp. 723–730. ISSN: 0306-4549. DOI: https://doi.org/10.1016/0306-4549(95)00002-A. URL: https://www.sciencedirect.com/science/article/pii/030645499500002A (cit. on pp. 30, 119, 120, 190).

[RD98] W. Rothenstein and R. Dagan. "Ideal gas scattering kernel for energy dependent cross-sections". In: *Annals of Nuclear Energy* 25.4 (1998), pp. 209–222. ISSN: 0306-4549. DOI: https://doi.org/10.1016/S0306-4549(97)00063-7. URL: https://www.sciencedirect.com/science/article/pii/S0306454997000637 (cit. on pp. 119, 120).

[Rue+05] P. Ruello, L. Desgranges, G. Baldinozzi, et al. "Heat capacity anomaly in UO2 in the vicinity of 1300K: an improved description based on high resolution X-ray and neutron powder diffraction studies". In: *Journal of Physics and Chemistry of Solids* 66.5 (2005), pp. 823–831. ISSN: 0022-3697. DOI: https://doi.org/10.1016/j.jpcs.2004.10.009. URL: https://www.sciencedirect.com/science/article/pii/S0022369704003944 (cit. on pp. 94, 95, 100, 101, 194).

[Rue01] Pascal Ruello. "Étude du changement de comportement du dioxyde d'uranium au voisinage de 1300K: propriétés électriques, optiques et structurales". PhD thesis. École Centrale Paris, 2001 (cit. on pp. 97, 98, 100).

[Sch+20] Mycle Schneider, Antony Froggatt, Julie Hazemann, et al. *The World Nuclear Industry Status Report 2020*. Tech. rep. 2020. URL: https://www.worldnuclearreport.org/IMG/pdf/wnisr2020-v2_hr.pdf (cit. on pp. 29, 189).

[Sch14] Helmut Schober. "An introduction to the theory of nuclear neutron scattering in condensed matter". In: *Journal of Neutron Research* 17.3-4 (2014), pp. 109–357. DOI: 10.3233/JNR-140016. URL: https://content.iospress.com/download/journal-of-neutron-research/jnr016?id=journal-of-neutron-research%2Fjnr016 (cit. on pp. 30, 34–36, 107, 118, 190).

[Sch60] P. Schofield. "Space-Time Correlation Function Formalism for Slow Neutron Scattering". In: *Phys. Rev. Lett.* 4 (5 Mar. 1960), pp. 239–240. DOI: 10.1103/PhysRevLett.4.239. URL: https://link.aps.org/doi/10.1103/PhysRevLett.4.239 (cit. on p. 52).

[Sco17] Juan Scotta. “Improvement of the thermal and epithermal neutron scattering data for the interpretation of integral experiments”. PhD thesis. Aix-Marseille Université, 2017 (cit. on pp. 125, 127, 203, 204).

[Sco+16] Scotta, Juan Pablo, Noguere, Gilles, Bernard, David, et al. “Impact of the thermal scattering law of H in H2O on the isothermal temperature reactivity coefficients for UOX and MOX fuel lattices in cold operating conditions”. In: *EPJ Nuclear Sci. Technol.* 2 (2016), p. 28. DOI: 10.1051/epjn/2016020. URL: https://doi.org/10.1051/epjn/2016020 (cit. on p. 119).

[Sea66] V. F. Sears. “THEORY OF COLD NEUTRON SCATTERING BY HOMONUCLEAR DIATOMIC LIQUIDS: II. HINDERED ROTATION”. In: *Canadian Journal of Physics* 44.6 (1966), pp. 1299–1311. DOI: 10.1139/p66-109. eprint: https://doi.org/10.1139/p66-109. URL: https://doi.org/10.1139/p66-109 (cit. on p. 61).

[SS60] K. S. Singwi and Alf Sjölander. “Diffusive Motions in Water and Cold Neutron Scattering”. In: *Phys. Rev.* 119 (3 Aug. 1960), pp. 863–871. DOI: 10.1103/PhysRev.119.863. URL: https://link.aps.org/doi/10.1103/PhysRev.119.863 (cit. on p. 60).

[Sjo58] Alf Sjolander. “Multi-phonon processes in slow neutron scattering by crystals”. In: *Arkiv Fysik* 14 (1958) (cit. on pp. 41, 47, 54).

[Ski+14] L. B. Skinner, C. J. Benmore, J. K. R. Weber, et al. “Molten uranium dioxide structure and dynamics”. In: *Science* 346.6212 (2014), pp. 984–987. ISSN: 0036-8075. DOI: 10.1126/science.1259709. eprint: https://science.sciencemag.org/content/346/6212/984.full.pdf. URL: https://science.sciencemag.org/content/346/6212/984 (cit. on pp. 109, 202).

[Squ12] G. L. Squires. *Introduction to the Theory of Thermal Neutron Scattering*. 3rd ed. Cambridge University Press, 2012. DOI: 10.1017/CBO9781139107808 (cit. on pp. 30, 34–36, 51, 53, 68, 70, 118, 190).

[Ste99] Peter W. Stephens. “Phenomenological model of anisotropic peak broadening in powder diffraction”. In: *Journal of Applied Crystallography* 32.2 (Apr. 1999), pp. 281–289. DOI: 10.1107/S0021889898006001. URL: https://doi.org/10.1107/S0021889898006001 (cit. on p. 103).

[Tam+00] El Mostapha Tammar et al. “Contribution à l’étude du facteur de structure dynamique des liquides simples”. PhD thesis. Metz, 2000 (cit. on p. 61).

[Tea03] X-5 Monte Carlo Team. *MCNP — A General Monte Carlo N-Particle Transport Code, Version 5 Volume I: Overview and Theory*. Tech. rep. Los Alamos National Laboratory, 2003. URL: https://mcnp.lanl.gov/pdf_files/la-ur-03-1987.pdf (cit. on p. 118).

[Tei+85] J. Teixeira, M.-C. Bellissent-Funel, S. H. Chen, et al. "Experimental determination of the nature of diffusive motions of water molecules at low temperatures". In: *Phys. Rev. A* 31 (3 Mar. 1985), pp. 1913–1917. DOI: 10.1103/PhysRevA.31.1913. URL: https://link.aps.org/doi/10.1103/PhysRevA.31.1913 (cit. on p. 60).

[TT15] Atsushi Togo and Isao Tanaka. "First principles phonon calculations in materials science". In: *Scripta Materialia* 108 (2015), pp. 1–5. ISSN: 1359-6462. DOI: https://doi.org/10.1016/j.scriptamat.2015.07.021. URL: https://www.sciencedirect.com/science/article/pii/S1359646215003127 (cit. on pp. 49, 68).

[TB18] Andre Trkov and David A Brown. *ENDF-6 formats manual: Data formats and procedures for the evaluated nuclear data files*. Tech. rep. Brookhaven National Lab.(BNL), Upton, NY (United States), 2018 (cit. on pp. 30, 67, 98, 190, 199).

[TPK19] Masami Tsubota, Biswajit Paik, and Jiro Kitagawa. "Inter-comparison of lattice parameters and evaluation of peak-shift obtained by Rietveld refinements". In: *Results in Physics* 15 (2019), p. 102640. ISSN: 2211-3797. DOI: https://doi.org/10.1016/j.rinp.2019.102640. URL: https://www.sciencedirect.com/science/article/pii/S2211379719306448 (cit. on p. 103).

[Tur61] R.E. Turner. "The quasi-classical approximation for neutron scattering". In: *Physica* 27.2 (1961), pp. 260–264. ISSN: 0031-8914. DOI: https://doi.org/10.1016/0031-8914(61)90046-5. URL: https://www.sciencedirect.com/science/article/pii/0031891461900465 (cit. on p. 62).

[Van+05] David Van Der Spoel, Erik Lindahl, Berk Hess, et al. "GROMACS: Fast, flexible, and free". In: *Journal of Computational Chemistry* 26.16 (2005), pp. 1701–1718. DOI: https://doi.org/10.1002/jcc.20291. eprint: https://onlinelibrary.wiley.com/doi/pdf/10.1002/jcc.20291. URL: https://onlinelibrary.wiley.com/doi/abs/10.1002/jcc.20291 (cit. on p. 57).

[Van54] Léon Van Hove. "Correlations in Space and Time and Born Approximation Scattering in Systems of Interacting Particles". In: *Phys. Rev.* 95 (1 July 1954), pp. 249–262. DOI: 10.1103/PhysRev.95.249. URL: https://link.aps.org/doi/10.1103/PhysRev.95.249 (cit. on p. 50).

[Vin58] George H. Vineyard. "Scattering of Slow Neutrons by a Liquid". In: *Phys. Rev.* 110 (5 June 1958), pp. 999–1010. DOI: 10.1103/PhysRev.110.999. URL: https://link.aps.org/doi/10.1103/PhysRev.110.999 (cit. on pp. 51–53).

[Vir+20] Pauli Virtanen, Ralf Gommers, Travis E. Oliphant, et al. “SciPy 1.0: Fundamental Algorithms for Scientific Computing in Python”. In: *Nature Methods* 17 (2020), pp. 261–272. DOI: 10.1038/s41592-019-0686-2 (cit. on p. 126).

[WL20] Peter Kjær Willendrup and Kim Lefmann. “McStas (i): Introduction, use, and basic principles for ray-tracing simulations”. In: *Journal of Neutron Research* Preprint (2020), pp. 1–16. DOI: 10.3233/JNR-190108. URL: https://content.iospress.com/download/journal-of-neutron-research/jnr190108?id=journal-of-neutron-research%2Fjnr190108 (cit. on p. 67).

[Wil63a] B. T. M. Willis. “Neutron diffraction studies of the actinide oxides I. Uranium dioxide and thorium dioxide at room temperature”. In: *Proceedings of the Royal Society of London. Series A. Mathematical and Physical Sciences* 274.1356 (1963), pp. 122–133. DOI: 10.1098/rspa.1963.0117. eprint: https://royalsocietypublishing.org/doi/pdf/10.1098/rspa.1963.0117. URL: https://royalsocietypublishing.org/doi/abs/10.1098/rspa.1963.0117 (cit. on p. 94).

[Wil63b] B. T. M. Willis. “Neutron diffraction studies of the actinide oxides II. Thermal motions of the atoms in uranium dioxide and thorium dioxide between room temperature and 1100 °C”. In: *Proceedings of the Royal Society of London. Series A. Mathematical and Physical Sciences* 274.1356 (1963), pp. 134–144. DOI: 10.1098/rspa.1963.0118. eprint: https://royalsocietypublishing.org/doi/pdf/10.1098/rspa.1963.0118. URL: https://royalsocietypublishing.org/doi/abs/10.1098/rspa.1963.0118 (cit. on pp. 94, 109, 110, 202).

[WH80] B. T. M. Willis and R. G. Hazell. “Re-analysis of single-crystal neutron-diffraction data on UO_2 using third cumulants”. In: *Acta Crystallographica Section A* 36.4 (July 1980), pp. 582–584. DOI: 10.1107/S0567739480001246. URL: https://doi.org/10.1107/S0567739480001246 (cit. on pp. 109, 114, 202).

[Wil64] Willis, B.T.M. “Structures of UO2, UO2+x and U4O9 by neutron diffraction”. In: *J. Phys. France* 25.5 (1964), pp. 431–439. DOI: 10.1051/jphys:01964002505043100. URL: https://doi.org/10.1051/jphys:01964002505043100 (cit. on pp. 109, 202).

[Wor+21] J. L. Wormald, N. C. Fleming, A. I. Hawari, et al. “Generation of the Thermal Scattering Law of Uranium Dioxide with Ab Initio Lattice Dynamics to Capture Crystal Binding Effects on Neutron Interactions”. In: *Nuclear Science and Engineering* 195.3 (2021), pp. 227–238. DOI: 10.1080/00295639.2020.1820826. eprint: https://doi.org/10.1080/00295639.2020.1820826. URL: https://doi.org/10.1080/00295639.2020.1820826 (cit. on pp. 48, 50).

[WH16] Wormald, J. L. and Hawari, A. I. "Ab Initio Generation of Thermal Neutron Scattering Law for Uranium Dioxide". In: *American Nuclear Society* 115 (2016), p. 1156. URL: https://www.ans.org/pubs/transactions/article-39400/ (cit. on p. 49).

[Xu+21] S. Xu, G. Noguere, L. Desgranges, et al. "Atomic scale Monte-Carlo simulations of neutron diffraction experiments on stoichiometric uranium dioxide up to 1664 K". In: *Nuclear Instruments and Methods in Physics Research Section A: Accelerators, Spectrometers, Detectors and Associated Equipment* 1002 (2021), p. 165251. ISSN: 0168-9002. DOI: https://doi.org/10.1016/j.nima.2021.165251. URL: https://www.sciencedirect.com/science/article/pii/S0168900221002357 (cit. on p. 5).

[ZH18] Y Zhu and Ayman I Hawari. "Full law analysis scattering system hub (FLASSH)". In: *Proc. PHYSOR*. 2018, pp. 22–26 (cit. on pp. 67, 68).

[Zhu18] Yuwei Zhu. "Analysis of Neutron Thermalization in Liquid FLiBe". PhD thesis. North Carolina State University, 2018 (cit. on p. 52).

[Zoi+13] Andrea Zoia, Emeric Brun, Cédric Jouanne, et al. "Doppler broadening of neutron elastic scattering kernel in Tripoli-4®". In: *Annals of Nuclear Energy* 54 (2013), pp. 218–226. ISSN: 0306-4549. DOI: https://doi.org/10.1016/j.anucene.2012.11.023. URL: https://www.sciencedirect.com/science/article/pii/S0306454912004689 (cit. on pp. 29, 118, 189).

ANNEXES

A. Liquid Water

Temperature-dependent dynamic structure factors for liquid water inferred from inelastic neutron scattering measurements

G. Noguere, J.P. Scotta, S. Xu
CEA, DES, IRESNE, Cadarache, F-13108 Saint Paul Les Durance, France

E. Farhi, J. Ollivier, Y. Calzavarra, S. Rols, M. Koza
Institut Laue-Langevin, F-38042 Grenoble, France

J.I. Marquez Damian
Neutron Physics Departement and Instituto Balseiro, Centro Atomico Bariloche, CNEA, Argentina

Temperature-dependent dynamic structure factors $S(Q,\omega)$ for liquid water have been calculated using a composite model which is based on the decoupling approximation of the mean square displacement of the water molecules into a diffusion and a solid-like vibrational parts. The solid-like vibrational part $S_{\rm vib}(Q,\omega)$ is calculated with the phonon expansion method established in the framework of the incoherent Gaussian approximation. The diffusion part $S_{\rm diff}(Q,\omega)$ relies on the Egelstaff-Schofield translational diffusion model corrected for jump diffusions and rotational diffusions with the Singwi-Sjolander random model and Sears expansion, respectively. Systematics of the model parameters as a function of the temperature were deduced from quasi-elastic neutron scattering (QENS) data analysis reported in the literature and from molecular dynamics (MD) simulations relying on the TIP4P/2005f model. The resulting $S(Q,\omega)$ values are confronted by means of Monte-Carlo simulations to inelastic neutron scattering data measured with the IN4, IN5 and IN6 time-of-flight spectrometers of the Institut Laue-Langevin (Grenoble, France). A modest range of temperatures (283 K to 494 K) has been investigated with neutron wavelengths corresponding to incident neutron energies ranging from 0.57 to 67.6 meV. The neutron-weighted multiphonon spectra deduced from the ILL data indicate a slight overestimation by the MD simulations of the frequency shift and broadening of the librational band. The descriptive power of the composite model was suited for improving the comparison to experiments via a Bayesian updating of prior model parameters inferred from MD simulations. The reported posterior temperature-dependent densities of state of hydrogen in H_2O would represent valuable insights for studying the collective coupling interactions in the water molecule between the inter and intramolecular degrees of freedom.

PACS numbers:

I. INTRODUCTION

Building predictive molecular models for water is the subject of intense studies that evidence the needs of high computer resources for reaching an accurate description of the underlying molecular interactions from rigorous many-body expansion methods [1, 2]. On the other side, classical molecular dynamics (MD) simulations represent computationally efficient tools for developing phenomenological potential energy function which are useful to directly correlate experimental observables with theoretical water properties [3]. The encouraging results obtained by the two approaches on the description of the water hydrogen-bonding network are not yet adequate to precisely describe the neutron-induced dynamic structure factors provided by inelastic neutron scattering experiments. Improving the agreement between the experiment and the theory will lead to better understand the coupling between the intra- and intermolecular vibrations in liquid water.

Works of interest for our study are those which succeeded to accommodate molecular dynamics (MD) simulations into the low-energy neutron-induced cross section theory. As an example, the jump diffusion motions of the water molecules has been revisited in Ref. [4] by applying a Gaussian approximation-assisted quantum correction to the classical self-intermediate scattering function provided by the three-site SPC model [5]. In that work, results obtained from the direct analysis of MD trajectory data succeeded to reproduce the half width at half maximum of the quasi-elastic neutron scattering (QENS) peaks measured by Teixeira et al. [6]. More recently, the use of polarizable models to derive dynamic structure factors for water has been investigated in Ref. [7] through the Van Hove formalism [8]. The calculations rely on velocity autocorrelation functions obtained from a revised version of the TCPE rigid model [9]. The main results indicate that within the temperature range of 300 to 500 K the frequency shift of the water librational mode and its width are less pronounced with increasing temperature than with four-site MD models. A quantitative investigation of these temperature-dependent effects with a flexible potential is required to correctly account for the hydrogen bonds in the coupling between the collective vibrational modes of the water molecule. This study is in progress thanks to inelastic neutron scattering data measured with the SEQUOIA spectrometer of the SNS facility [10].

The present work only focuses on both the description

of the QENS peaks and of the librational mode of water as a function of the temperature. For that purpose, a modified version of the water model developed at the atomic center of Bariloche [11, 12] was used to analyze by Monte-Carlo a series of inelastic neutron scattering data measured at the IN4, IN5 and IN6 time-of-flight spectrometers of the Institut Laue-Langevin (ILL). The experimental observables of interest for this work are the self-diffusion coefficient D, the residence time τ_0 between successive jumps, the rotational relaxation time τ_R and the density of states of water $\rho(\varepsilon)$ as a function of the energy transfer $\varepsilon = \hbar\omega$. The resulting composite dynamic structure factor $S(Q,\omega)$ would serve as input for the subsequent analysis of the SNS data.

The governing equations involved in the composite dynamic structure factor used in this work are given in section II. The section III presents the diffusion model parameters and the density of states obtained from MD simulations. The experimental details of the data under investigations and the principles of the Monte-Carlo interpretation of these data are presented in section IV. The obtained results are discussed in section V.

II. GOVERNING EQUATIONS

A. Dynamic structure factor in the incoherent Gaussian approximation

In the case of liquid water, the dynamic structure factor $S(\vec{Q},\omega)$ was obtained in the framework of the incoherent scattering approximation that allows to neglect the interference terms among different nuclei. It is defined as a function of the momentum transfer $\hbar\vec{Q} = \hbar(\vec{k} - \vec{k}')$ and energy transfer $\hbar\omega = E - E'$, in which $\vec{k}$ and $\vec{k}'$ represent the wavenumber of the incident and outgoing neutrons with energies E and E', respectively. The difference between E and E' will be noted ε. In the Van Hove's space-time representation [8], $S(\vec{Q},\omega)$ is defined as a two-fold Fourier transform of the self part of the generalized pair distribution function $G(\vec{r},t)$:

$$S(\vec{Q},\,\omega) = \frac{1}{2\pi}\iint G(\vec{r},t)\mathrm{e}^{i(\vec{Q}\cdot\vec{r}-\omega t)}\mathrm{d}\vec{r}\mathrm{d}t. \qquad (1)$$

where $\vec{r}$ is the position vector of the nuclei in the system and t represents the time. To obtain an analytical form of $G(\vec{r},t)$, Vineyard [13] introduces the Gaussian approximation that assumes a weak time-dependent atomic position coupling:

$$G(\vec{r},t) = \frac{1}{(2\pi)^{3/2}w^3(t)}\mathrm{e}^{-\frac{3}{2}\frac{r^2}{3w^2(t)}}, \qquad (2)$$

where $3w^2(t)$ represents the mean square displacement of the nucleus after time t, in which $w(t)$ is called the width function. By applying Fourier transforms to the Gaussian-type function (2), the self part of the dynamic structure factor becomes:

$$S(\vec{Q},\omega) = \frac{1}{2\pi}\int_{-\infty}^{\infty}\mathrm{e}^{-\frac{1}{2}Q^2w^2(t)}\mathrm{e}^{-i\omega t}\mathrm{d}t. \qquad (3)$$

The Q^2 dependence of Eq. (3) indicates that $S(\vec{Q},\omega)$ is isotropic with respect to the momentum transfer, leading to:

$$S(\vec{Q},\omega) \equiv S(Q,\omega). \qquad (4)$$

The width function $w(t)$ plays a central role in the calculation of the dynamic structure factor. An analytical expression of $w(t)$ was proposed in the sixties [14] for liquid water. However, introducing such an expression in Eq. (3) leads to numerical issues at zero energy transfer. These mathematical problems can be solved by decoupling the mean square displacement into a diffusion part $w_{\mathrm{diff}}(t)$ and a solid-like vibrational part $w_{\mathrm{vib}}(t)$:

$$w^2(t) = w^2_{\mathrm{diff}}(t) + w^2_{\mathrm{vib}}(t). \qquad (5)$$

The corresponding diffusion $S_{\mathrm{diff}}(Q,\omega)$ and solid-like $S_{\mathrm{vib}}(Q,\omega)$ parts of the dynamic structure factor are calculated with Eq. (3) by introducing different models for $w_{\mathrm{diff}}(t)$ and $w_{\mathrm{vib}}(t)$. The validity of such a decoupling approximation was studied in the framework of the two-phase thermodynamic (2PT) model [15] in which $w_{\mathrm{diff}}(t)$ is treated as a hard-sphere gas and $w_{\mathrm{vib}}(t)$ is approximated by harmonic oscillators. The obtained results probe that the 2PT model is able to correctly describe the thermodynamic properties of water [16] and liquids in general [17] over a wide range of temperature and pressure conditions.

According to the convolution theorem for Fourier transforms, the composite dynamic structure factor is calculated as follows:

$$S(Q,\omega) = \int_{-\infty}^{\infty} S_{\mathrm{diff}}(Q,\omega')S_{\mathrm{vib}}(Q,\omega-\omega')\mathrm{d}\omega', \qquad (6)$$

whose values depend on the density of states $\rho(\omega)$ of liquid water, which is partitioned in two parts:

$$\rho(\omega) = w_d\rho_{\mathrm{diff}}(\omega) + w_v\rho_{\mathrm{vib}}(\omega). \qquad (7)$$

The diffusion w_d and solid-like vibrational w_v weights satisfy the condition:

$$w_d + w_v = 1 \qquad (8)$$

B. Roto-translational diffusion model with random jump diffusion correction for $S_{\mathrm{diff}}(Q,\omega)$

In view of using a descriptive analytical model, the diffusion term in Eq. (6) related to liquid water is approximated by a translational diffusion motion corrected for rotational diffusion contributions:

$$S_{\mathrm{diff}}(Q,\omega) = \int_{-\infty}^{\infty} S_{\mathrm{trans}}(Q,\omega') S_{\mathrm{rot}}(Q,\omega-\omega')\mathrm{d}\omega'. \quad (9)$$

From the theoretical point of view [18–20], such a decoupling approximation is known to be inadequate above room temperature and differences of up to 10% between the experiment and the theory were reported for large Q values [21, 22]. As no consensus emerges to account for a translation-rotation coupling in analytical models, we will show in section V A that this level of accuracy remains acceptable for analyzing the selected data measured with the IN4, IN5 and IN6 time-of-flight spectrometers of the Institut Laue-Langevin. Consequently, the contribution of the rotational diffusion is presented as a correction of the translational diffusion motion in order to point out that the values of the diffusion model parameters may encompass part of the model deficiencies.

The translational diffusion behavior of the water molecule was interpreted with the Egelstaff-Schofield diffusion model [23], in which the width function is given by:

$$w^2_{\mathrm{trans}}(t) = \frac{2\,c\,w_d\,\hbar^2}{Mk_BT}\left(\sqrt{\left(\frac{tk_BT}{\hbar}\right)^2 + c^2 + \frac{1}{4}} - c\right) \quad (10)$$

where k_B stands for the Boltzmann constant, M is the mass of the scattering atom and c is a dimensionless diffusion parameter. Its meaning has been revisited in Ref. [12] by introducing the Singwi-Sjolander residence time τ_0 [24] to account for the non-continuous motions of the water molecules:

$$c = \frac{M}{\hbar w_d}\mathcal{D}(Q), \quad (11)$$

with

$$\mathcal{D}(Q) = \frac{D}{1+DQ^2\tau_0}, \quad (12)$$

in which D represents the self-diffusion coefficient of the liquid water. The dynamic structure factor $S_{\mathrm{trans}}(Q,\omega)$ can be derived analytically by introducing Eq. (10) in Eq. (3). The resulting expression corrected for detailed balance is given by:

$$S_{\mathrm{trans}}(Q,\omega) = \frac{\mathcal{D}Q^2}{\pi k_BT}\mathrm{e}^{\left(\frac{M\mathcal{D}^2Q^2}{w_dk_BT}+\frac{\hbar\omega}{2k_BT}\right)}\frac{\sqrt{c^2+1/4}}{\sqrt{\omega^2+(\mathcal{D}Q^2)^2}}K_1(x), \quad (13)$$

in which $K_1(x)$ is the modified Bessel function of the second kind, with:

$$x = \frac{\hbar}{k_BT}\sqrt{c^2+\frac{1}{4}}\sqrt{\omega^2+(\mathcal{D}Q^2)^2}. \quad (14)$$

The rotational diffusion correction in Eq. (9) is approximated with the Sears expansion [25] expressed in terms of spherical Bessel functions $j_l(QR_{\mathrm{cm}})$ of order l:

$$\begin{aligned} S_{\mathrm{rot}}(Q,\omega) &= j_0^2(QR_{\mathrm{cm}})\delta(\omega) \\ &+ \frac{1}{\pi}\textstyle\sum_{l=1}^{\infty}(2l+1) \\ &\times j_l^2(QR_{\mathrm{cm}})\frac{l(l+1)(\hbar/6\tau_R)}{\omega^2+[l(l+1)(\hbar/6\tau_R)]^2}. \end{aligned} \quad (15)$$

This model assumes a continuous and isotropic molecular rotation around the center of mass of the molecule with a rotational relaxation time τ_R. The rotation of the water molecule is confined to a spherical surface of radius R_{cm}, whose value is often taken equal to the O-H intramolecular distance. For practical purposes, the infinite summation in Eq. (15) is truncated to $l = 10$.

C. Phonon expansion model for $S_{\mathrm{vib}}(Q,\omega)$

For the solid-like vibrational part, the width function is given by [26]:

$$w^2_{\mathrm{vib}}(t) = \frac{\hbar^2}{Mk_BT}\lambda_s(1-\eta(t)), \quad (16)$$

in which $\eta(t)$ is defined as follows:

$$\eta(t) = \frac{1}{\lambda_s}\int_{-\infty}^{\infty} P(\omega)\mathrm{e}^{i\omega t}\mathrm{d}\omega, \quad (17)$$

and λ_s represents the Debye-Waller coefficient:

$$\lambda_s = \int_{-\infty}^{\infty} P(\omega)\mathrm{d}\omega, \quad (18)$$

with

$$P(\omega) = \rho_{\mathrm{vib}}(\omega)\mathrm{e}^{\frac{\hbar\omega}{2k_BT}}\left(\frac{2\hbar\omega}{k_BT}\sinh\left(\frac{\hbar\omega}{2k_BT}\right)\right)^{-1}. \quad (19)$$

The convergence of the integrals in the expressions (17) and (18) is satisfied in the case of a solid-like density of states $\rho_{\mathrm{vib}}(\omega)$ which has the property of varying in ω^2 when ω goes to zero.

The corresponding dynamic structure factor $S_{\mathrm{vib}}(Q,\omega)$ can be calculated by introducing Eq. (16) in Eq. (3). A suitable analytical expression was obtained thanks to the

conventionally called phonon expansion method [27] that consists in replacing the exponential term of Eq. (3) by its Taylor series expansion, leading to:

$$S_{\rm vib}(Q,\omega) = {\rm e}^{-\frac{\hbar^2Q^2}{2Mk_BT}\lambda_s}\sum_{n=0}^{\infty}\frac{1}{n!}\left(\frac{\hbar^2Q^2}{2Mk_BT}\lambda_s\right)^n\mathcal{T}_n(\omega), \tag{20}$$

with

$$\mathcal{T}_n(\omega) = \frac{1}{2\pi}\int_{-\infty}^{\infty}\eta^n(t){\rm e}^{-i\omega t}{\rm d}t. \tag{21}$$

The zero-phonon term $\mathcal{T}_0(\omega) = \delta(\omega)$ corresponds to the elastic scattering contribution and the one-phonon term is given by:

$$\mathcal{T}_1(\omega) = \frac{1}{\lambda_s}P(\omega). \tag{22}$$

The higher-order terms ($n > 1$) of the phonon expansion are obtained by recurrence. The convolution theorem for Fourier transforms gives:

$$\mathcal{T}_n(\omega) = \int_{-\infty}^{\infty}\mathcal{T}_1(\omega')\mathcal{T}_{n-1}(\omega-\omega')d\omega'. \tag{23}$$

D. Converting $S(Q,\omega)$ into thermal scattering law

The dynamic structure factor for liquid water is routinely used to simulate the neutron slowing-down in light water reactors. The neutron transport formalism implemented in dedicated Monte-Carlo or deterministic code systems relies on the symmetric form of the thermal scattering laws $\mathcal{S}(\alpha,\beta)$ [28, 29], which is defined as a function of the dimensionless parameters α:

$$\alpha = \frac{\hbar^2Q^2}{2Mk_BT} = \frac{E'+E-2\mu\sqrt{E'E}}{Ak_BT}, \tag{24}$$

and β:

$$\beta = -\frac{\hbar\omega}{k_BT} = -\frac{E-E'}{k_BT}. \tag{25}$$

where $\mu = \cos(\theta)$ is the cosine of the scattering angle θ in the laboratory system and A is the ratio of the mass M of the scattering atom to the neutron mass. The change of sign in Eq. (25) is introduced to keep neutron energy gains positive in neutron transport calculations. The relationship between $\mathcal{S}(\alpha,\beta)$ and $S(Q,\omega)$ is given by the following expression:

$$\mathcal{S}(\alpha,\beta) = \frac{k_BT}{\hbar}{\rm e}^{\frac{\hbar\omega}{2k_BT}}S(Q,\omega), \tag{26}$$

that directly allows to describe the neutron slowing-down in light water in terms of double differential scattering cross sections [8]:

$$\frac{d^2\sigma_n}{dE'd\theta} = \frac{\sigma_n^0}{4\pi k_BT}\sqrt{\frac{E'}{E}}{\rm e}^{-\beta/2}\mathcal{S}(\alpha,\beta), \tag{27}$$

where σ_n^0 is the bound neutron elastic scattering cross section of hydrogen in H_2O.

III. MODEL PARAMETERS

A. Diffusion model parameters

The diffusion part of the dynamic structure factor (Eq. (9)) depends on five diffusion model parameters which are the self-diffusion coefficient D, the residence time τ_0, the rotational relaxation time τ_R, the radius $R_{\rm cm}$ between the hydrogen atoms and the center of mass of the water molecule and the diffusion weight w_d. We took advantage of the numerous QENS data analysis reported in the literature to guess the systematic dependence with the temperature of the three first parameters (D, τ_0 and τ_R). The empirical relationships between these parameters are examined starting from the Price's prescription established to reproduce the continuous increase of the self-diffusion coefficient D with the temperature [30].

Above 240 K, Price suggests to use a fractional power law (FPL) of the form

$$D_{\rm FPL} = D_0T^{1/2}\left(\frac{T}{T_s}-1\right)^{\gamma}, \tag{28}$$

to better describe self-diffusion coefficients D of water measured with a pulsed-gradient spin-echo NMR diffusion technique from 238 K to room temperature. If D_0 and γ are fitting constants, T_s can be related to a low-temperature range indicating anomalies in the supercooled water properties. In the present work, a reasonable agreement with the experimental values $D_{\rm exp}$ reported in Fig. 1a is achieved with $D_0 = 8.4(5)$ m^{2}s^{-1}, $\gamma = 1.60(1)$ and $T_s = 226.5(10)$ K. The ratios $D_{\rm FPL}/D_{\rm exp}$ shown in Fig. 1b seem to slightly favor our fitting results compared to those obtained with the Price's prescription ($D_0 = 7.66(24)$ m^{2}s^{-1}, $\gamma = 1.74(10)$, $T_s = 219.2(26)$ K). It is also interesting to note that the data included in our fitting procedure fortuitously lead to a low-temperature limit T_s in agreement with the thermodynamic singularity at 228 K suggested by Speedy and Angell [31].

The residence time τ_0 is related to the self-diffusion coefficient D through the mean-square jump length L^2 of the center of mass of the water molecule:

$$\tau_0 = \frac{L^2}{6D_{\rm FPL}}, \tag{29}$$

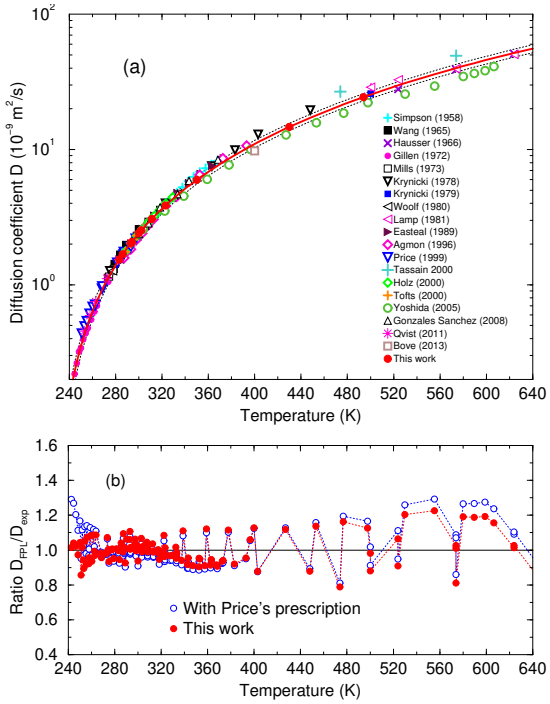

FIG. 1: (a) Self-diffusion coefficients D reported in the literature as a function of the temperature. The red solid line were obtained with the fractional power law (FPL) given by Eq (28). The values obtained in this work (red filled circles) are reported in Table I. (b) Ratio of the fitted D_{FPL} to experimental D_{exp} values. The reduced chi-squared obtained with our results is close to 1.3, while the one obtained with the Price's prescription [30] is close to 1.6.

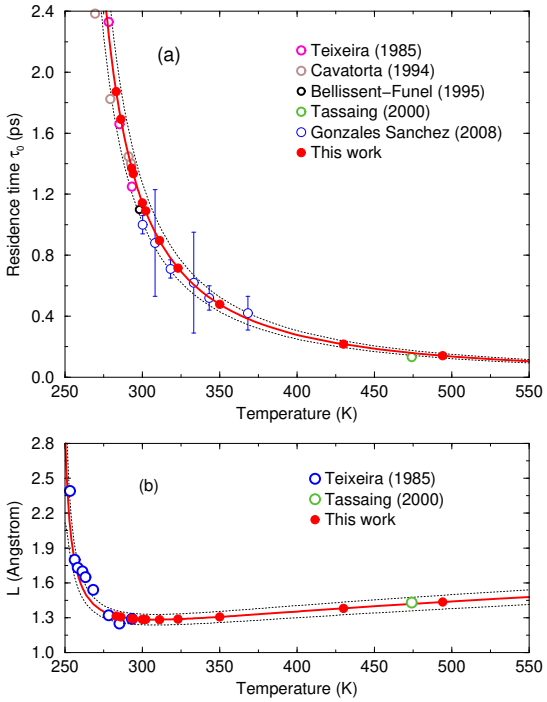

FIG. 2: Residence time τ_0 (a) and mean jump length L (b) reported in the literature as a function of the temperature. The red solid lines were obtained with Eqs (29) and (30), respectively. The values obtained in this work (red filled circles) are reported in Table I.

which is well described by the ratio of two fractional power laws:

$$L^2 = L_0^2 \frac{(T - T_s)^{\gamma}}{(T - T_0)^{\gamma_0}}, \tag{30}$$

where L_0^2, γ_0 and T_0 are free parameters whose values have been inferred from the simultaneous adjustment of τ_0 and L^2 reported in the literature. A few residence times for water can be found in the literature. However, the reported values depend on the distribution law hypothesized for describing the jump lengths, implying large differences between τ_0. Therefore, only τ_0 values reported in Refs. [6, 32–35] have been selected as the authors used a Singwi-Sjolander type model to analyze their QENS data. The trends for τ_0 and L^2 are reported in Figs. 2a and 2b respectively. The posterior values of the parameters involved in Eq. (30) are $L_0^2 = 0.20(5)$ Å^2, $\gamma_0 = 1.20(1)$ and $T_0 = 247(1)$ K. The value of T_0 is consistent with the experimental observations. Water filled capillaries begin to freeze at about 247 K in the case of the experiments of Speedy and Angell [31], and between 240 K and 250 K for the experiments lead by Qvist et al. [36]. The use of two fractional power laws in Eq. (30) illustrates the existence of competitive motions that dominates the diffusion of the water molecules from either side of room temperature. At 500 K, the low value of $\tau_0 \simeq 0.1$ ps indicates that the contribution of the non-continuous motions of the water molecules will be too fast to have a large contribution in the QENS peak.

The relaxation time τ_R associated to the rotational diffusion coefficient is $\tau_R = 1/6D_R$. According to the Stokes-Einstein relations, the ratio D/D_R would be a constant for temperatures well above the glass transition temperature of about 136 K. In the temperature range of interest for this work, the temperature dependence of τ_R can be deduced from Eq. (28) with the following simple relationship:

$$\tau_R \simeq \frac{\langle D/D_R \rangle}{6D_{\mathrm{FPL}}}, \tag{31}$$

in which $\langle D/D_R \rangle$ is a constant parameter that could ideally be assessed from results reported in the literature. Figure 3 shows ratios derived from a few rotational diffusion coefficients or integral rotational correlation times reported in the literature and compiled in Refs. [37, 38]. The temperature below which the constant approximation is no longer valid is close to the temperature $T_0 = 247(1)$ K coming from Eq. (30). Above this temperature, the large dispersion between the data sets

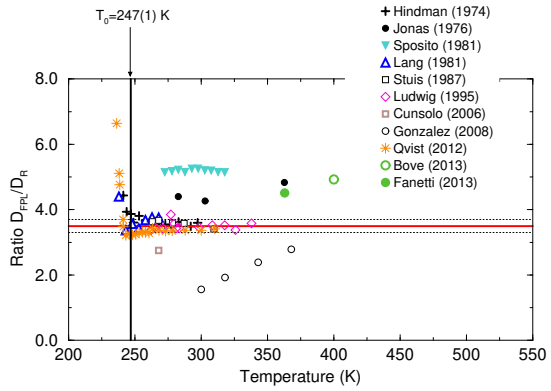

FIG. 3: Ratio of the fitted translational diffusion coefficient D_{FPL} to a few rotational diffusion coefficients D_R derived from values compiled in Refs. [37, 38] as a function of the temperature. The red solid line represents the constant ratio $\langle D/D_R\rangle = 3.5$ involved in Eq. (31). The black dotted lines represent its standard deviation close to 0.2. The low-temperature limit $T_0 = 247(1)$ K comes from Eq. (30).

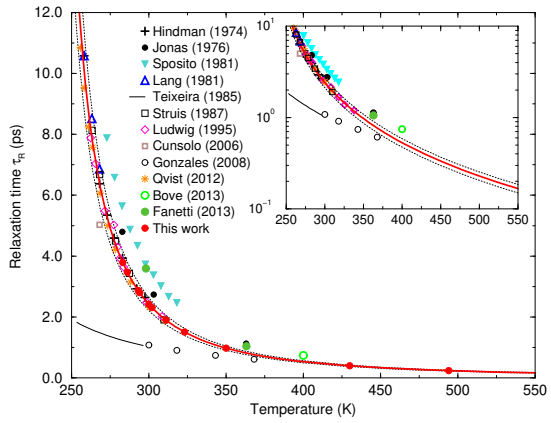

FIG. 4: Lin-lin and lin-log representations of the rotational relaxation time τ_R as a function of the temperature derived from a few rotational diffusion coefficients or integral rotational correlation times reported in the literature and compiled in Refs. [37, 38]. The red solid line was calculated with Eqs (31). The values obtained in this work (red filled circles) are reported in Table I.

makes it difficult to unambiguously determine an accurate $\langle D/D_R\rangle$ value over a broad temperature range. As indicated by Tassaing [34], the Lorentzian profile associated to the rotational diffusion contribution at high temperature would have a large width which is difficult to detect from QENS analysis. In the present work, we adopted the average ratio $\langle D/D_R\rangle = 3.5(2)$ deduced from the data sets which are in close agreement with the results of Qvist et al. [38]. The resulting trend of τ_R as a function of the temperature is shown in Fig. 4.

The rotational diffusion contribution given by Eq. (15) also depends on a second parameter which is the distance R_{cm} between the hydrogen atoms and the center of mass of the water molecule. Therefore, instead of using the O-H intramolecular distance (close to 0.96 Å), a slightly lower distance $R_{\mathrm{cm}} = 0.92(1)$ Å was considered in this work, assuming an average hydrogen bond angle of 105°.

For the diffusion weigth w_d (Eq. (7)), no direct experimental values as a function of the temperature are given in the literature. Its value strongly depends on the decoupling approximation of the mean square displacement of the water molecules into a diffusion and a solid-like vibrational parts. Weight values ranging from 0.009 ($T = 294$ K) to 0.019 ($T = 500$ K) were estimated by Marquez Damian [11] through diffusion masses reported by Novikov et al. [39]. For comparison, Mattes [28] proposed weight values ranging from 0.022 ($T = 294$ K) to 0.04 ($T = 474$ K) by interpolating experimental density of states measured at 294 and 624 K [40] and by using a free gas model to describe the diffusion part. These two studies converge on a weak temperature dependence and on a low value of w_d with a maximum of up to a few percent. Diffusion weights of similar amplitude were also found in this work with values ranging from 0.010(5) to 0.03(1). Owing to the large uncertainties emerging from the least-squares fitting procedure, we have adopted in the calculations an average value of $w_d = 0.02(1)$ over the full temperature range.

Values for the diffusion model parameters involved in the description of the diffusion part of the dynamic structure factor are summarized in Table I.

B. Density of states from molecular dynamics

The diffusion part $\rho_{\mathrm{diff}}(\omega)$ and the solid-like vibrational part $\rho_{\mathrm{vib}}(\omega)$ of the density of states of hydrogen in H_2O were deduced from Molecular Dynamic (MD) simulations performed with the GROMACS code [41]. The calculation route follows the prescriptions established by Marquez Damian [11], that relies on the four-site flexible model TIP4P/2005f [42]. MD results are accommodated in the mathematical framework presented in section II by computing the density of states as the cosine Fourier transform of the time-dependent velocity autocorrelation function (VACF):

$$\rho_{\mathrm{MD}}(\omega) = \frac{2M}{3\pi k_B T}\int_0^\infty \mathrm{VACF}(\tau)\cos(\omega\tau)\mathrm{d}\tau. \qquad (32)$$

The solid-like vibrational contribution is deduced from Eq. (7) as follows:

$$\rho_{\mathrm{vib}}(\omega) = \frac{\rho_{\mathrm{MD}}(\omega) - w_d\rho_{\mathrm{diff}}(\omega)}{1 - w_d}. \qquad (33)$$

The diffusion contribution is calculated in the framework of the Egelstaff-Schofield diffusion model (Eq. (13)):

TABLE I: Values for the translational diffusion weight w_d, self-diffusion coefficient D (in 10^{-9} m^2/s), residence time τ_0 (in ps), mean jump length L (in Å) and rotational relaxation time τ_R (in ps) as a function of the temperature (in K). The three last columns compare the self-diffusion coefficients obtained in this work (Fig. (1)) with those obtained from the Price's prescription [30] and GROMACS simulations (Eq. (37)).

T	w_d	L	τ_0	τ_R	D from Fig. 1	D from [30]	D_{MD} from Eq. (37)
283	0.02(1)	1.314(48)	1.87(23)	3.79(37)	1.5(2)	1.5	1.6
286	0.02(1)	1.305(47)	1.69(20)	3.48(33)	1.7(2)	1.6	1.8
293	0.02(1)	1.292(45)	1.37(16)	2.88(26)	2.0(2)	1.9	2.2
294	0.02(1)	1.291(45)	1.34(15)	2.80(25)	2.1(2)	2.0	2.2
300	0.02(1)	1.286(45)	1.14(13)	2.42(21)	2.4(2)	2.3	2.6
302	0.02(1)	1.285(45)	1.09(12)	2.31(20)	2.5(2)	2.4	2.7
311	0.02(1)	1.283(45)	0.90(10)	1.90(16)	3.1(2)	3.0	3.3
323	0.02(1)	1.287(45)	0.72(8)	1.51(12)	3.9(3)	3.7	4.2
350	0.02(1)	1.307(47)	0.48(5)	0.98(7)	6.0(4)	5.8	6.2
430	0.02(1)	1.380(54)	0.22(2)	0.40(3)	14.7(9)	14.8	13.9
494	0.02(1)	1.435(58)	0.14(2)	0.24(2)	24.4(15)	25.2	21.5

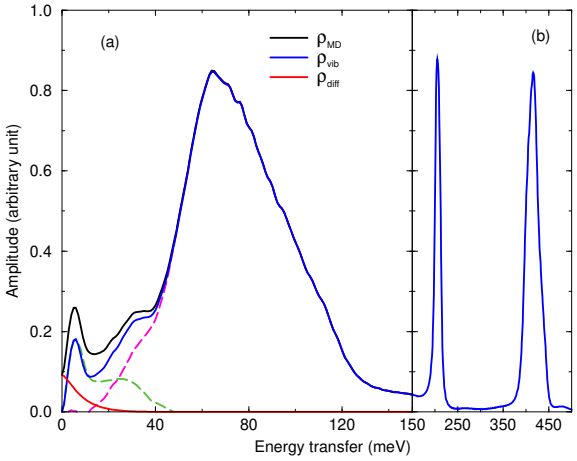

FIG. 5: Density of states ρ_{MD} of hydrogen in H_2O as a function of the energy transfer ε calculated at $T = 300$ K with the GROMACS code [41] using the TIP4P/2005f model for water [42]. The left and right hand panels focus on the intermolecular (a) and intramolecular (b) vibrations, respectively. The diffusion part ρ_{diff} is calculated with Eq. (34). The solid-like vibrational part ρ_{vib} is deduced from ρ_{MD} by subtracting the contribution of ρ_{diff} (Eq. (33)). Dotted lines separate the contribution of the broad librational band to the H-bond bending and streching modes [43].

$$\rho_{\mathrm{diff}}(\omega) = \frac{4\hbar c_0}{\pi k_B T}\sqrt{c_0^2+\frac{1}{4}}\,\sinh\left(\frac{\hbar\omega}{2k_BT}\right)K_1(y), \quad (34)$$

with

$$y = \frac{\hbar w}{k_B T}\sqrt{c_0^2+\frac{1}{4}}, \quad (35)$$

and

$$c_0 = \frac{MD}{\hbar w_d}. \quad (36)$$

The self-diffusion coefficient D can be estimated from MD simulations with Eq. (34) at zero energy transfer, where the solid-like vibrational contribution is zero:

$$D_{\mathrm{MD}} = \frac{\pi k_B T \rho_{\mathrm{MD}}(0)}{2M}. \quad (37)$$

Results obtained at 300 K are shown in Fig. 5 as a function of the energy transfer ε. The diffusion part plays a role in the low-energy transfer range. Its contribution is calculated with Eq. (34) by using $D_{\mathrm{MD}} = 2.6\times10^{-9}$ m^2/s and $w_d = 0.02$. The bands at around 200 and 430 meV come from intramolecular vibrations due to O-H bending and O-H stretching modes, respectively. Below 150 meV, the density of states is dominated by intermolecular vibrations. The peak at around 6 meV and the shoulder-like region from 20 to 40 meV are attributed to H-bond bending and stretching modes whose contribution (green dotted line) is well reproduced by the calculations of Lerbret et al. [43]. However, their microscopic origin is the subject of debates in the literature [44–46]. The large band spanning from 50 to 130 meV is related to the libration of the water molecules. The self-diffusion coefficients calculated with Eq. (37) at zero energy transfer are reported in the last column of Table I. The agreement between D_{MD} and the values established in this work or calculated with the Price's prescription remains within the limit of the quoted uncertainties up to 430 K.

The experimental validation of the density of states of water calculated with the TIP4P/2005f model was the subject of intense studies using a wide types of neutron measurements reported in the literature. An overall good agreement is achieved demonstrating its ability to predict the neutron total cross sections of H_2O as a function of

TABLE II: List of inelastic neutron scattering measurements performed on the IN4, IN5 and IN6 time-of-flight spectrometers of ILL with the experimental conditions of interest for the data analysis.

TOF	Author	Year	Ref.	H_2O sample	λ	E	Temperature	Pressure
IN4	Farhi et al.	2015	[50]	hollow cylinder	1.1 Å	67.6 meV	294, 311, 323 K	1 bar
	Farhi et al.	2015	[50]	hollow cylinder	2.2 Å	16.9 meV	294 K	1 bar
	Jaiswal et al.	2017	[51]	cylinder	2.4 Å	14.2 meV	300, 350, 430, 494 K	1, 42, 94, 115, 147, 176, 185 bar
IN5	Farhi et al.	2015	[50]	hollow cylinder	2.0 Å	20.5 meV	286, 293, 302 K	1 bar
	Farhi et al.	2015	[50]	hollow cylinder	5.0 Å	3.27 meV	291, 302, 311 K	1 bar
	Qvist et al.	2011	[36]	capillaries	5.0 Å	3.27 meV	283, 293 K	1 bar
	Qvist et al.	2011	[36]	capillaries	8.0 Å	1.28 meV	283, 293 K	1 bar
	Qvist et al.	2011	[36]	capillaries	12.0 Å	0.57 meV	283 K	1 bar
IN6	Jaiswal et al.	2017	[51]	cylinder	5.1 Å	3.15 meV	350, 494 K	1, 70, 470 bar

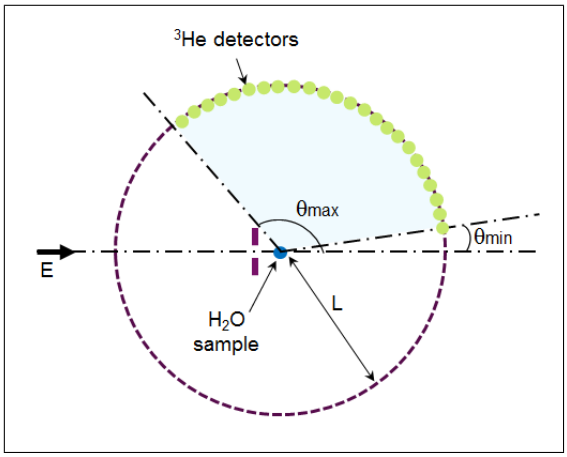

FIG. 6: Simplified top view of the IN4, IN5 and IN6 time-of-flight spectrometers of the Institut Laue-Langevin. The distance between the sample and the ^{3}He detector array is equal to $L = 2.00(1)$, $L = 4.00(1)$ and $L = 2.48(1)$ m, for IN4, IN5 and IN6 respectively.

the temperature [47, 48]. However, recent inelastic neutron scattering data measured at the ILL facility suggests that the shape of the water librational mode calculated by MD simulations needs further improvements [7, 49]. The data of interest for this work and their Monte-Carlo analysis are presented in the following sections.

IV. NEUTRON SCATTERING EXPERIMENTS ON LIGHT WATER

A. Time-of-flight experiments

Three experimental campaigns on liquid water reported by Qvist et al. [36], Farhi et al. [50] and Jaiswal et al. [51] were revisited by using the combined $S(Q,\omega)$ model presented in section II. The measurements were performed on the IN4, IN5 and IN6 time-of-flight spectrometers of ILL over a modest range of temperatures (283 to 494 K), pressures (1 to 470 bar) and incident neutron energies (0.57 to 67.6 meV). The experimental conditions are summarized in Table II.

The IN4, IN5 and IN6 spectrometers share the same basic design (Fig. 6). The neutron time-of-flight technique consists of measuring the time t traveled by the neutrons from their generation until their detection at a given scattering angle θ. If the energies are in eV, the length in m and the time in μs, the non-relativistic time-energy relation $E' = (72.298L/t)^2$ is used to obtain the experimental neutron scattering yield $Y_{exp}(\theta, E')$ as a function of the outgoing neutron energies E'. The distance between the sample and the detection setup is equal to $L = 2.00(1)$, $L = 4.00(1)$ and $L = 2.48(1)$ m, for IN4, IN5 and IN6 respectively. Each ^{3}He detector array covers scattering angles ranging from approximately 10° to 135°. In all cases, a rectangular monoenergetic neutron beam was focused to the sample, which was mounted in a cryostat or cryofurnace device placed at the center of the spectrometer. The experiments were performed with three different sample geometries. Qvist et al. used an ultrapur H_2O sample which was composed of 20 quartz capillaries of 0.3/0.4 mm inner/outer diameter distributed along the perimeter of a 20 mm diameter circle. The Farhi's data were obtained with high purity water in a 0.05 mm thick hollow aluminum cylinder. High temperature and pressure conditions were achieved by using a cylindrical CuBe cell of 6.0/8.0 mm inner/outer diameter filled with high purity water. Combining these three experimental campaigns in a simultaneous Monte-Carlo analysis provides unique experimental conditions to test the single and multiple neutron scattering corrections in thin and thick water samples.

Each experiment consisted in a sequence of H_2O and empty sample measurements, including a short irradiation of a vanadium sample at room temperature or at 273 K in the case of the measurements performed by Qvist et al. The data reduction steps were handled with the ILL in-house LAMP code [52]. The background is mainly due to neutrons scattered by the sample-holder and its environment. It was removed by subtracting the neutron scattering yield measured with the empty

sample times an empirically determined effective sample transmission factor. As indicated in Ref. [51], the shape of the experimental neutron scattering yields measured on IN4 and IN6 up to 470 bar weakly changes with increasing pressure. This result indicates that the pressure conditions investigated in this work were too low to observe any sizable modifications on the QENS peak and on the experimental density of states of liquid water. Therefore the pressure-dependent data sets measured at a given temperature were merged together within the LAMP code allowing to decrease the statistical uncertainties and to slightly smooth out the statistical fluctuations for experimental neutron scattering yield Y_{exp} obtained with a low data acquisition time. According to Eq. (27), the symmetric form of the thermal scattering law $\mathcal{S}_{exp}$ is then obtained as follow:

$$\mathcal{S}_{exp}(\alpha,\beta) = Y_{exp}(\alpha,\beta)\sqrt{\frac{E}{E'}}\mathrm{e}^{\beta/2}. \qquad (38)$$

The experimental neutron-weighted multiphonon spectra ρ_{exp} of H_2O were deduced from Y_{exp} outside the LAMP code through the incoherent one-phonon approximation. The one-phonon term (Eq. (22)) involved in the phonon expansion can be conveniently rewritten in terms of α and β:

$$\mathcal{T}_1(\beta) = \frac{\rho_{exp}(\beta)\mathrm{e}^{-\beta/2}}{2\lambda_s\beta\sinh(\beta/2)}. \qquad (39)$$

By introducing Eq. (39) in Eq. (20) for $n = 1$, we obtain:

$$\rho_{exp}(\beta) \simeq \lim_{\alpha\to 0}\mathcal{P}_{exp}(\alpha,\beta), \qquad (40)$$

with

$$\mathcal{P}_{exp}(\alpha,\beta) \simeq \frac{2\beta\sinh\beta/2}{\alpha}\mathcal{S}_{exp}(\alpha,\beta), \qquad (41)$$

In the present analysis, the main goal is to obtain an experimental quantity readily comparable to theoretical calculations (section IV B). No attempt was made to iterately correct the data from the multiphonon contribution and the multiple neutron scattering effects. Therefore, in view of obtaining $\mathcal{P}_{exp}(\alpha,\beta)$ at $\alpha = 0$, we have smoothed out fluctuations due to nuclei dynamics by using a lin-lin extrapolation to zero of the cumulative distribution functions of $\mathcal{P}_{exp}(\alpha,\beta)$:

$$Z(\alpha_0,\beta) = \int_{\alpha_0}^{\alpha_{\max}}\mathcal{P}_{exp}(\alpha,\beta)\mathrm{d}\alpha, \qquad (42)$$

and then assumed that $\rho_{exp} \propto Z(\alpha_0,\beta)/(\alpha_{\max}-\alpha_0)$. Examples of cumulative distribution functions as a function of the threshold α_0 are shown in Fig. 7a for five different values of energy transfer ε. The boundaries $\alpha_{\min}$ and $\alpha_{\max}$ delimit the α range measured for a given β value. The Figures 7b and 7c show that the corresponding neutron-weighted multiphonon spectrum slightly depends on the value of the threshold α_0. For $\alpha_0 = 0$, ρ_{exp} is close to the result provided by the MUPHOCOR option [53] of the LAMP code which relies on the phonon expansion method (section II C). In the case of $\alpha_0 = \alpha_{\min}$, our result agrees with the GDOS option of the LAMP code that relies on the incoherent one-phonon approximation. For simplicity, the experimental neutron-weighted multiphonon spectra will be compared to their theoretical analogues by using $\alpha_{\min}$.

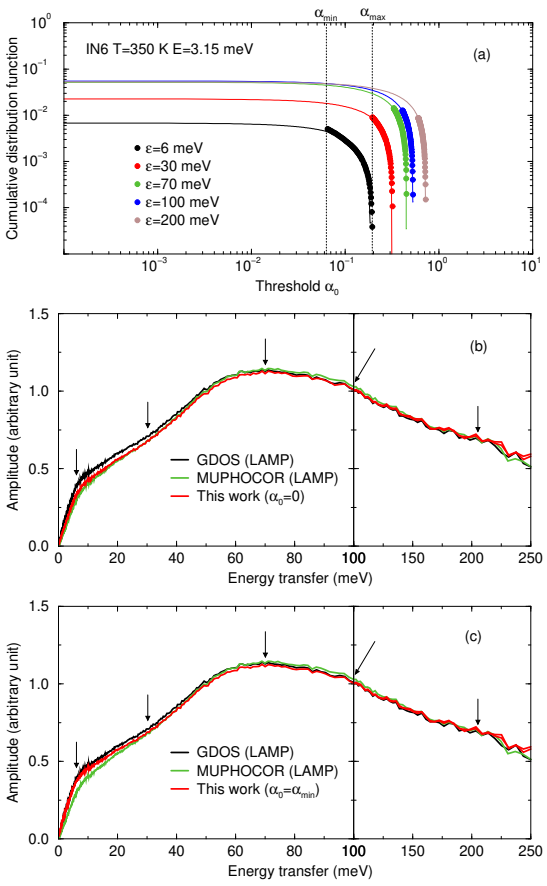

FIG. 7: The top plot (a) shows examples of cumulative distribution functions of $\mathcal{P}_{exp}$ (Eq. (42)) as a function of the threshold α_0 for IN6 data measured at 350 K [51]. The boundaries $\alpha_{\min}$ and $\alpha_{\max}$ delimit the α range measured for a given β value. The middle (b) and bottom (c) plots represent the corresponding neutron-weighted multiphonon spectra ρ_{exp} obtained at $\alpha_0 = 0$ and $\alpha_0 = \alpha_{\min}$. They are compared with those provided by the MUPHOCOR [53] and GDOS options of the LAMP code [52]. The arrows locate the five energies ε which are equal to 6, 30, 70, 100 and 200 meV.

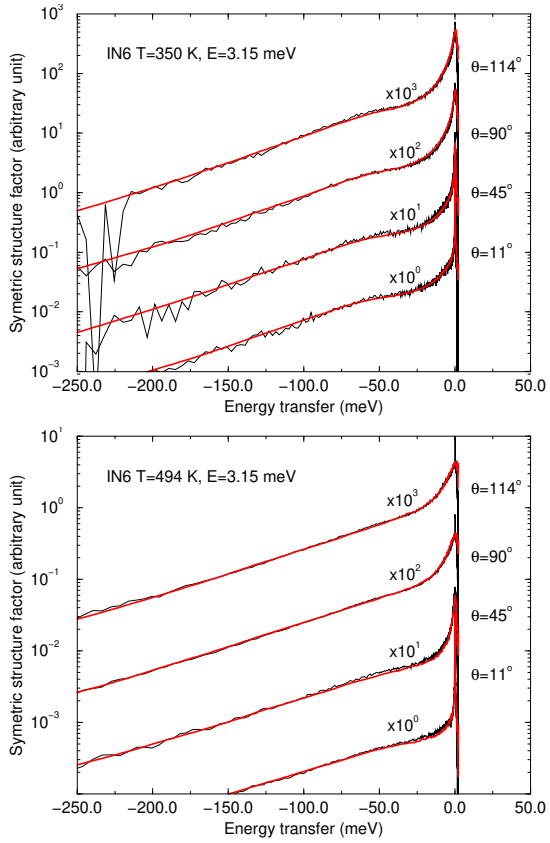

FIG. 8: Experimental symmetric dynamic structure factor $\mathcal{S}_{exp}$ measured with the IN6 spectrometer at 350 and 494 K [51]. The red solid lines correspond to the TRIPOLI4® simulations [54] based on the model parameters listed in Table I with densities of state of hydrogen in H_2O provided by the GROMACS code [41] using the TIP4P/2005f model for water [42].

B. Monte-Carlo neutron transport simulation

The experimental symmetric dynamic structure factors $\mathcal{S}_{exp}$ have been analyzed quantitatively by simulating the flight time t of each neutron with the neutron transport code TRIPOLI4® [54]. This code takes into account the multiphonon and multiple scattering contributions via thermal scattering laws stored in terms of $S(\alpha,\beta)$ tables as a function of the temperature (section II D). The time distribution of the initial neutron burst originating from the choppers is not included in the simulation. Therefore, the theoretical neutron yield Y_{th} is calculated from the neutron yields Y_{T4} provided by TRIPOLI4® as follows:

$$Y_{th}(\theta,E') = \int_0^{+\infty} R_{E'}(\theta,t) Y_{T4}(\theta,t)\mathrm{d}t. \qquad (43)$$

The probability density function $R_{E'}(\theta,t)$ stands for the time-dependent experimental response function of the spectrometer which is well approximated by a Gaussian. Its full width at half maximum was fitted to the neutron elastic scattering peak of vanadium. The obtained widths vary from 20 μs to 80 μs depending on the spectrometer and on the neutron wavelength.

Figure 8 shows the overall agreement achieved over a broad energy transfer range between the theoretical and experimental symmetric forms of the dynamic structure factors measured with the IN6 spectrometer at 350 and 494 K. The thermal scattering laws usable by the TRIPOLI4® code were calculated with the model parameters listed in Table I and densities of state of hydrogen in H_2O provided by the GROMACS code (section III B).

V. RESULTS AND DISCUSSIONS

A. QENS data analysis

The analysis of the QENS peaks provides an experimental validation of the model parameters that define the rotational and translational diffusions of the water molecules. As presented in section II B, the diffusion part of the dynamic structure factor is given by the Egelstaff-Schofield diffusion model corrected for random jump and rotational diffusions. The parameters involved in this model are listed in Table I. They were established thanks to the numerous studies reported in the literature in view of calibrating our model for (P,T) conditions where liquid water is thermodynamically stable.

Figure 9 shows examples of QENS peaks measured between 283 and 494 K with the IN5, IN6 and IN4 spectrometers. The obtained results probe that the TRIPOLI4® simulations are able to reproduce the experimental spectra over the entire scattering angles covered by each spectrometer. The QENS peaks measured on IN5 by Qvist et al. have a well-defined Lorentzian shape, because the data were obtained with ultrapur-H_2O filled capillaries, which reduce multiple neutron scattering effects. The Jaiswal's data were obtained with a thick cylindrical pressure CuBe cell leading to asymmetrical peaks with increasing scattering angles. In that case, agreement between the theory and the simulation strongly depends on the geometrical features introduced in the Monte-Carlo simulations. The simplified time-of-flight model shown in Fig. 6 would need further refinements for improving the simulations for $\varepsilon > 0$.

The trends of the experimental and theoretical half width at half maximum of the QENS peaks are reported in Fig. 10 as a function of the temperature. Each result is compared to the simulated curve obtained for a continuous diffusion that obeys Fick's law. In that case, around the QENS peak, the momentum and energy transfer tend to zero, so that the modified Bessel function of the second kind in Eq. (13) becomes $K_1(x) \simeq 1/x$ and the diffusion contribution can then be approximated by:

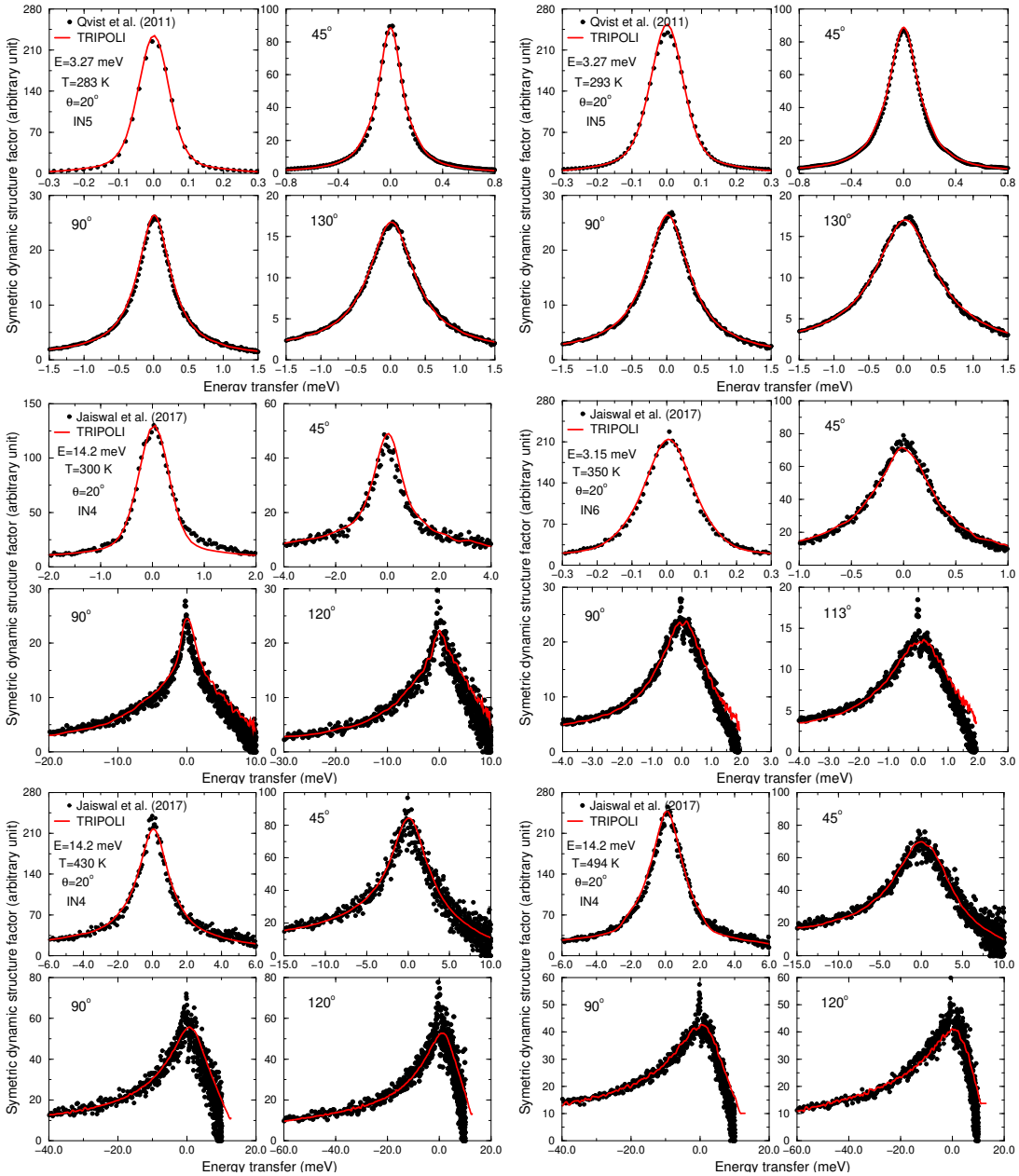

FIG. 9: Examples of experimental and theoretical QENS peaks for H_2O at 283, 293, 300, 350, 430 and 494 K. The experimental spectra were measured with the IN5, IN6 and IN4 spectrometers (Table II). The theoretical spectra were simulated with the TRIPOLI4® code by using the diffusion model parameters listed in Table I.

$$S_{\rm diff}^{\rm Fick}(Q,\omega) \simeq \frac{1}{\pi}\frac{\Gamma(Q)}{\omega^2+\Gamma(Q)^2}, \qquad (44)$$

where $\Gamma(Q) = DQ^2$ represents the half width at half maximum of the Lorentzian function. It depends on the self-diffusion coefficient D and has a linear dependence in Q^2.

At 293 K and 350 K, the TRIPOLI4® simulations performed with a residence time $\tau_0 = 0$ ps and a rotational relaxation time $\tau_R = 0$ ps probe the non-linearity of the experimental $\Gamma(Q)$ as a function of Q^2. The experimental results are adequately predicted by using τ_0 values ranging from 1.4 to 0.5 ps and τ_R values ranging from 2.9 to 1 ps. In this small temperature range, the rotational relaxation time is twice the residence time, indicating competitive contributions in favor of the rotational diffusion motions. For $T = 494$ K, the two sets of results obtained with the IN4 and IN6 spectrometers confirm that the non-continuous motions of the water molecules

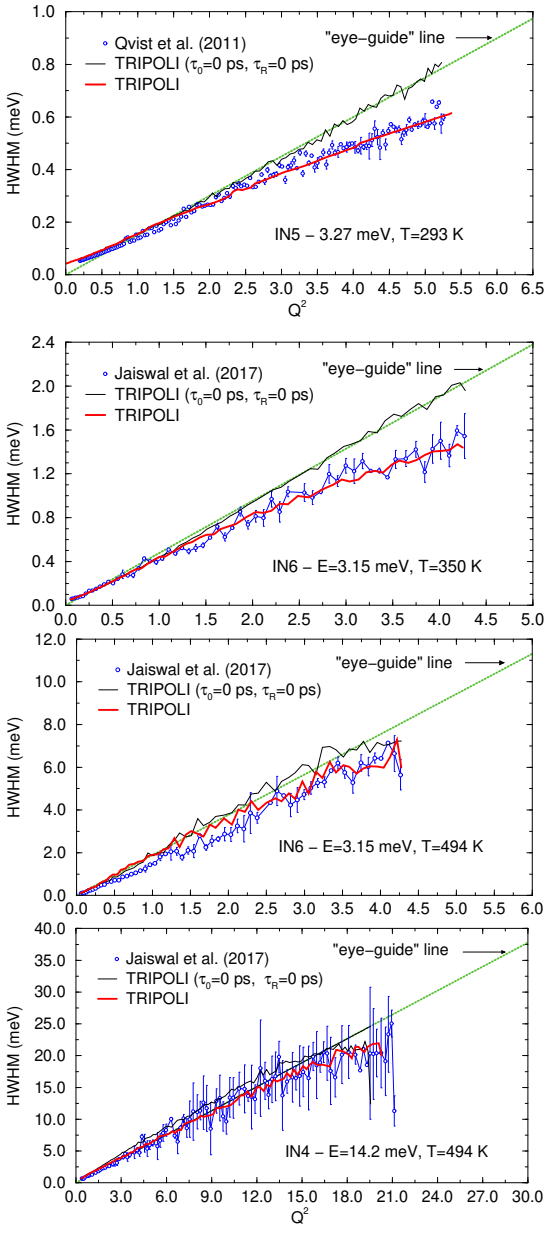

FIG. 10: Examples of experimental and theoretical half width at half maximum (HWHM) of the QENS peaks for water as a function of Q^2 (in Å^{-2}). The TRIPOLI4® simulations were performed with thermal scattering laws calculated with the diffusion model parameters listed in Table I. The green "eye-guide" lines follow the trends given by the TRIPOLI4® simulations performed within the Fick's law approximation.

are too fast to have a sizeable contribution to the QENS peak for temperatures approaching 500 K. If we assume that the observed differences between the experiments and the theoretical curves are attributed to the decoupling approximation (Eq. (9)), our results confirm that the level of accuracy of this approximation ranges from ±5% to ±10%.

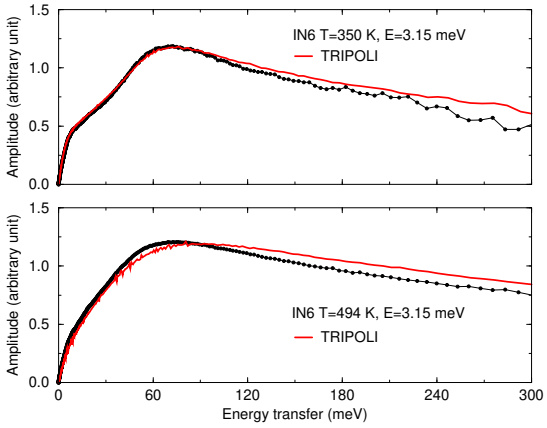

FIG. 11: Experimental and theoretical neutron-weighted multiphonon spectra of H_2O deduced respectively from the IN6 data [51] and from TRIPOLI4® simulations based on GROMACS calculations using the four-site flexible model TIP4P/2005f (red solid line).

B. Neutron-weighted multiphonon spectra

The comparison of the experimental and theoretical neutron-weighted multiphonon spectra obtained in the framework of the incoherent one-phonon approximation (Eqs. (40) to (38)) are shown in Fig. 11. Despite the observed differences, such results evidence that the model described in section II succeeds to reasonably accommodate MD simulations for water into the low-energy neutron-induced cross section formalism. The TRIPOLI4® results indicate that the energy position of the librational mode and its width seem to be slightly overestimated by MD simulations when the four-site flexible model TIP4P/2005f for water is used in the calculations.

In the present work, the phonon mode shift and the phonon broadening of the solid-like vibrational part $\rho_{\rm vib}(\omega)$ of the phonon density of states of hydrogen in H_2O were optimized on the IN4, IN5 and IN6 data with the iterative Bayesian least-squares fitting procedure implemented in the nuclear data code CONRAD [55]. Starting from the densities of states provided by the GROMACS code, our model gradually converged towards the posterior solutions shown in Figs. 12 and 13. These results indicate that the IN4 and IN6 spectrometers provide nearly similar information on the water librational mode observed at an energy transfer close to 70 meV, while the IN5 spectrometer focuses on the H-bond bending and stretching modes below 70 meV.

The comparison of the IN4 data reported in 2015 and 2017 confirms the weak temperature dependence of the librational mode between 286 and 350 K. A distortion of its shape and a slight frequency shift to the low energy transfer is observed with increasing temperature.

The shape of the neutron-weighted multiphonon spec-

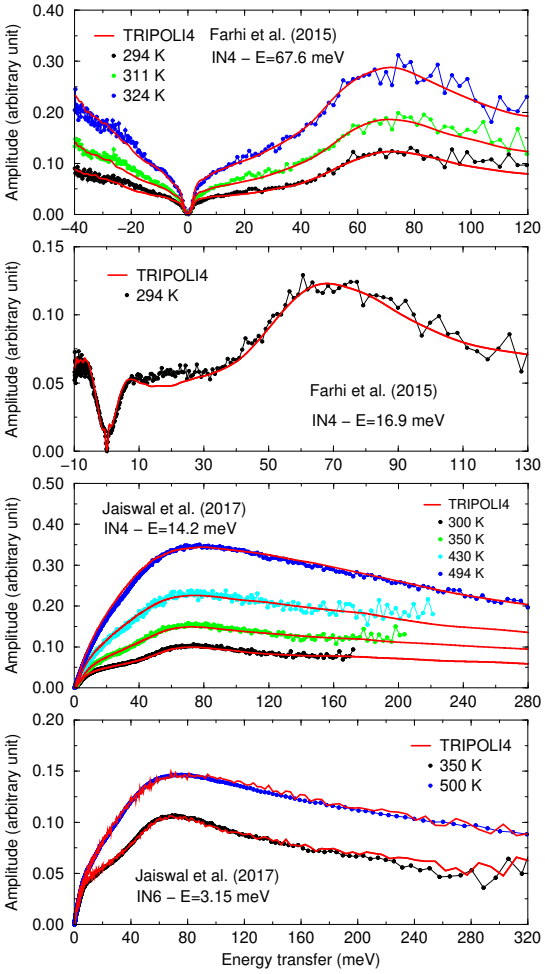

FIG. 12: Comparison of the experimental and theoretical neutron-weighted multiphonon spectra of H_2O. The experimental spectra were deduced from the neutron scattering yields measured with the IN4 and IN6 spectrometers. The theoretical curves were calculated from TRIPOLI4® simulations based on the solid-like vibrational density of states shown in Fig. 14.

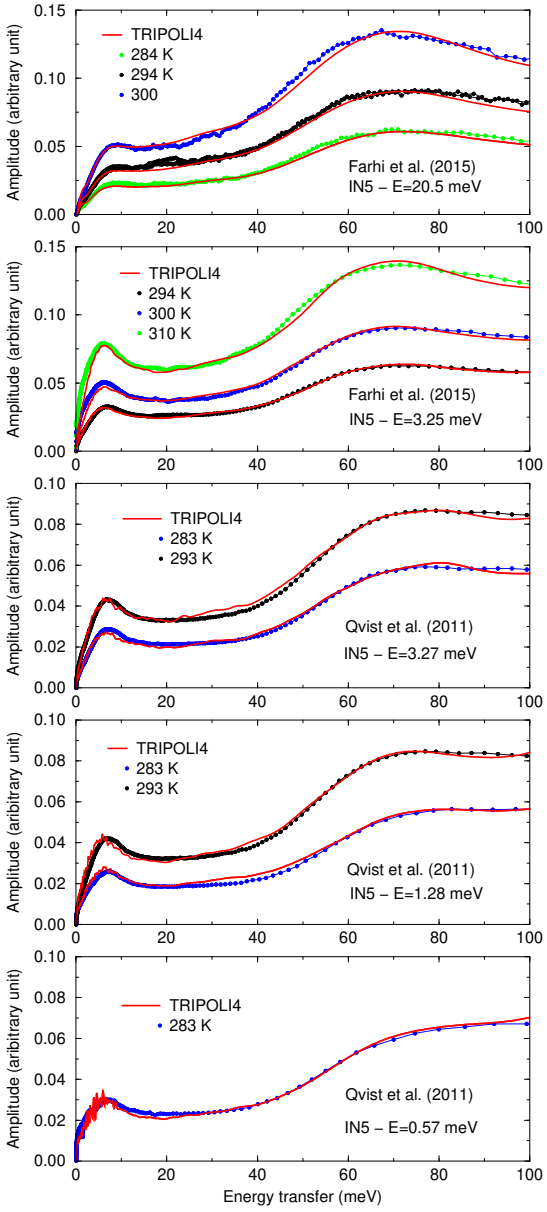

FIG. 13: Comparison of the experimental and theoretical neutron-weighted multiphonon spectra of H_2O deduced from the IN5 data and calculated from TRIPOLI4® simulations based on the solid-like vibrational density of states shown in Fig. 14.

tra measured with the IN5 spectrometer are very close whatever the sample geometry (capillaries and hollow cylinder). In both cases, the correction due to the multiple neutron scatterings is negligible, making these two experiments appropriate for probing the low-frequency spectrum of liquid water near the room temperature. Compared to the H-bond bending mode which is well resolved at around 6-7 meV, no H-bond stretching mode is observed between 20 and 40 meV. The too low amplitude of such a connectivity vibration is smoothed out by the time-response of the IN5 spectrometer and altered by the background subtraction. Neutron spectroscopy is a less favorable experimental technique than infrared spectroscopy in which H-bond has the appearance of substructures that gradually increase in intensity upon cooling. [56].

A satisfactory agreement is achieved between the experiments and the TRIPOLI4® curves. The differences observed around 20 meV are due to the empty-cell subtraction, confirming the difficulty to address H-bond dynamics through the selected inelastic neutron scattering data. The posterior vibrational part of the densities of states introduced in the calculations are shown in Fig. 14. The corresponding values are reported in appendix (Tables III). Figure 15 compares the mean value and the full width at half maximum (FWHM) of the librational mode

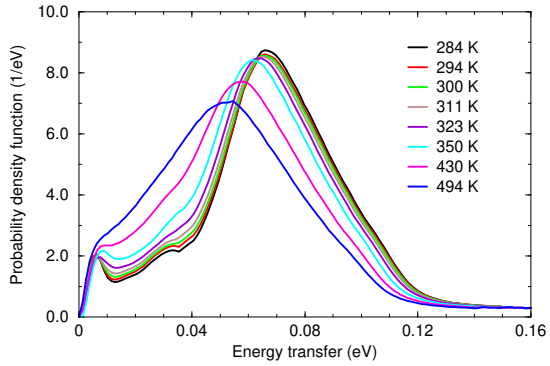

FIG. 14: Theoretical solid-like vibrational part of the density of states of hydrogen in H_2O deduced from the inelastic neutron scattering experiments listed in Table II. The corresponding values are reported in appendix (Table III).

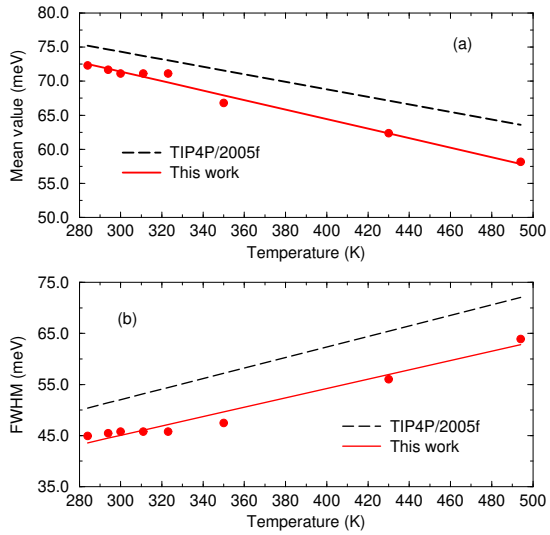

FIG. 15: Mean value (a) and full width at half maximum (b) of the librational mode obtained in this work and with the TIP4P/2005f model for water as a function of the temperature.

obtained in this work and with the TIP4P/2005f model for water. They were roughly calculated by removing the contribution of the H-bond bending and stretching modes as shown in Fig. 5 by using the trend reported by Lerbret et al [43]. No anomalies are observed in the monotonic behavior of the frequency shift and width over the full temperature range of interest for this work. Such a comparison mainly confirms the overestimation by the MD simulations of the two first moments of the librational mode whatever the temperature is.

The origin of a narrower water librational mode than predicted by MD simulations can be interpreted by missing coupling interactions between the inter and intramolecular degrees of freedom. In Fig. 16, the TIP4P/2005r model represents the rigid version of the TIP4P/2005f model in which we have removed the intramolecular parameters. The addition of flexibility changes the shape of the librational mode and decreases its width by a few meV. The remaining differences with our results confirm that adding a Morse potential with an angle harmonic function in a rigid model is not sufficient to account for effects of intramolecular vibrations. Such an issue is the subject of theoretical and experimental works deeply discussed in the literature [57, 58]. Past time-of-flight experiments carried out with the HRMECS spectrometers of the pulsed neutron source at the Argone National Laboratory [59, 60] highlight the complexity of the coupling interactions in the water molecule due to the presence of two broad structures of small amplitudes near 270 and 500 meV. These structures seem to correspond to O-H bending ($\simeq$ 200 meV) and stretching modes ($\simeq$ 430 meV) shifted by an amount roughlty equal to the average position of the librational mode ($\simeq$ 70 meV). Similar structures were recently observed with the SEQUOIA spectrometer of the SNS facility [10]. The association of the results presented in this work with the SNS data will provide valuable experimental insights for testing advanced theoretical studies on collective mode coupling mechanisms within the water molecule.

VI. CONCLUSIONS

The analysis of inelastic neutron scattering measurements performed with three time-of-flight spectrometers of ILL with different water sample geometries over a modest range of temperatures, pressure and neutron wavelengths was revisited with the Monte-Carlo neutron transport code TRIPOLI4®. The experiments were simulated by using a composite dynamic structure factors for water which is based on the decoupling approximation of the mean square displacement of the water molecules into a diffusion and a solid-like vibrational parts. Systematics of the temperature-dependent diffusion model parameters were established from QENS results reported in the literature. An iterative Bayesian least-squares fitting procedure was used to infer densities of states of hydrogen in H_2O from the selected inelastic neutron scattering data.

The diffusion part of the dynamic structure factor introduced in the Monte-Carlo simulations depends on the self-diffusion coefficient D, residence time τ_0 and relaxation time τ_R. A consistent description of these parameters was achieved in the temperature range where liquid water is thermodynamically stable by starting from the Price's prescription that suggests to use a fractional power law to reproduce the continuous increase of D with the temperature. As a result, the half width at half maximum of the QENS peaks of the ILL data was adequately reproduced over a broad range of Q^2 (< 21 Å^{-2}). The agreement between the experiment and the theory lies between $\pm 5\%$ and $\pm 10\%$. This level of accuracy is accept-

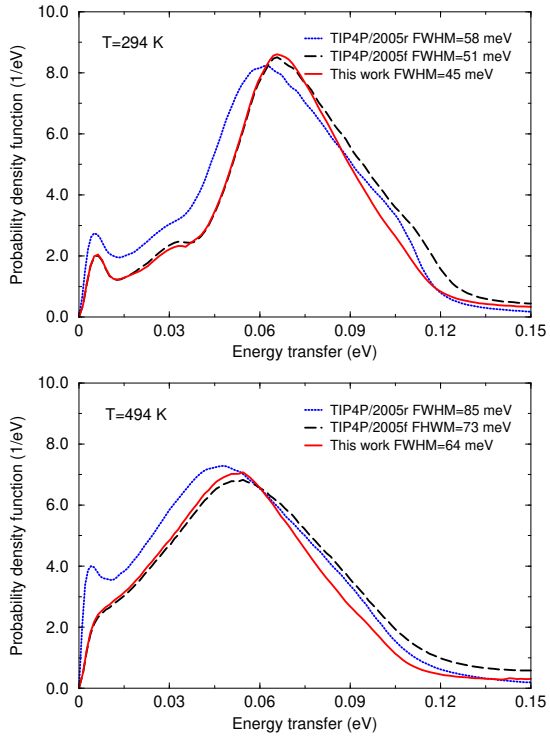

FIG. 16: Comparison of the solid-like vibrational part of the density of states of hydrogen in H_2O obtained in this work and calculated with GROMACS at 294 and 494 K with the flexible TIP4P/2005f model and its rigid version TIP4P/2005r.

able for the purpose of our study. It indicates the low contribution to the QENS peak of the non-continuous motions of the water molecules for temperature approaching 500 K. Our fitting results lead to a thermodynamic breakdown in the supercooled regime around $T_s = 226.5(10)$ K and a low-temperature limit close to $T_0 = 247(1)$ K for the Stokes-Einstein relations.

The analysis of the neutron-weighted multiphonon spectra derived from the ILL data mainly suggests a narrower water librational mode than predicted by the four-site flexible model TIP4P/2005f. This result can be attributed to missing coupling interactions between the inter and intramolecular degrees of freedom. The comparison with molecular dynamic simulations performed with rigid and flexible models confirms that adding a Morse potential with an angle harmonic function in a rigid model is not sufficient to account for the complexity of the collective mode coupling mechanisms within the water molecule. Since the posterior temperature-dependent densities of states of hydrogen in H_2O reported in this work are free from experimental corrections, they represent valuable insights for testing advanced theoretical hypothesis.

Despite the approximations introduced in this work, the descriptive power of the phenomenological water model, optimized thanks to results reported in the literature, allows to obtain a satisfactory agreement between the experiment and the theory. Future works will focus on reaching a similar agreement by developing a three-site polarizable model that could take into account coupling interactions between the inter and intramolecular degrees of freedom. The description of the non-continuous motions of the water molecules could be also improved by applying the Gaussian approximation-assisted quantum correction to the classical self-intermediate scattering function as proposed by the Japanese group of the Kyoto University leaded by Abe.

Acknowledgments

The authors wish to express their appreciations for the experimental work performed at ILL with the specific support of F. Marchal and his colleagues for the sample preparation. One of the authors also expresses his gratitude to J. Qvist, H. Schober and B. Halle for sharing their IN5 data which were used in the present study. This work also includes part of the experimental and theoretical results reported by V. Jaiswal, L. Leal and F. Real. A special thanks goes to J. Teixeira and M.-C. Bellissent-Funnel for their useful corrections and advices during the preparation of this paper.

Data Availability

The INS data used in the present study are available at ILL (https://data.ill.eu/) or from the authors upon request.

Appendix: Solid-like vibrational part of the density of states of hydrogen in H_2O

Table III reports the solid-like vibrational part $\rho_{\mathrm{vib}}(\varepsilon)$ of the density of states of hydrogen in H_2O shown in Fig. 14. They were established with the iterative Bayesian least-squares fitting procedure implemented in the nuclear data code CONRAD [55]. The inelastic neutron scattering data included in the procedure are listed in Table II. The model parameters involved in the description of the diffusion part are given in Table I.

TABLE III: Solid-like vibrational part of the density of states of hydrogen in H_2O (in 1/eV) as a function of the energy transfer (in meV) and temperature (in K).

ε	284	294	300	311	323	350	430	494
0.0	0.000	0.000	0.000	0.000	0.000	0.000	0.000	0.000
1.3	0.380	0.386	0.358	0.305	0.215	0.013	0.265	0.503
2.5	1.083	1.092	1.024	0.928	0.769	0.469	0.840	1.261
3.8	1.674	1.681	1.597	1.495	1.333	1.081	1.436	1.830
5.1	1.986	1.995	1.925	1.852	1.743	1.644	1.898	2.190
6.3	2.024	2.042	2.001	1.972	1.943	1.993	2.178	2.412

Solid-like vibrational part, continued ...

ε	284	294	300	311	323	350	430	494
7.6	1.839	1.872	1.871	1.894	1.953	2.148	2.311	2.549
8.9	1.530	1.583	1.638	1.714	1.856	2.164	2.348	2.662
10.1	1.286	1.353	1.444	1.555	1.743	2.077	2.342	2.740
11.4	1.178	1.255	1.345	1.463	1.656	1.973	2.343	2.853
12.6	1.143	1.226	1.312	1.427	1.611	1.911	2.376	2.949
13.9	1.160	1.248	1.327	1.436	1.611	1.898	2.424	3.044
15.2	1.210	1.300	1.369	1.471	1.636	1.910	2.481	3.159
16.4	1.259	1.352	1.417	1.514	1.671	1.933	2.556	3.272
17.7	1.307	1.404	1.467	1.560	1.713	1.977	2.640	3.402
19.0	1.355	1.457	1.518	1.611	1.765	2.037	2.733	3.542
20.2	1.404	1.509	1.577	1.672	1.829	2.102	2.836	3.669
21.5	1.475	1.584	1.651	1.746	1.904	2.173	2.941	3.828
22.8	1.556	1.669	1.740	1.835	1.993	2.256	3.057	3.999
24.0	1.663	1.778	1.842	1.936	2.089	2.344	3.188	4.132
25.3	1.772	1.888	1.947	2.037	2.184	2.437	3.325	4.294
26.6	1.869	1.988	2.045	2.132	2.280	2.553	3.462	4.431
27.8	1.958	2.080	2.138	2.227	2.383	2.685	3.609	4.597
29.1	2.041	2.166	2.224	2.319	2.485	2.817	3.750	4.750
30.4	2.110	2.238	2.299	2.400	2.581	2.964	3.891	4.885
31.6	2.158	2.293	2.356	2.466	2.667	3.103	4.023	5.070
32.9	2.183	2.323	2.391	2.512	2.737	3.220	4.146	5.199
34.2	2.174	2.323	2.402	2.541	2.809	3.339	4.273	5.390
35.4	2.145	2.303	2.434	2.601	2.906	3.445	4.405	5.549
36.7	2.235	2.396	2.517	2.700	3.006	3.524	4.573	5.724
38.0	2.324	2.490	2.612	2.794	3.094	3.640	4.753	5.898
39.2	2.415	2.583	2.704	2.891	3.207	3.803	4.957	6.048
40.5	2.504	2.676	2.818	3.023	3.370	3.981	5.185	6.219
41.7	2.661	2.833	2.983	3.204	3.569	4.200	5.429	6.379
43.0	2.865	3.033	3.193	3.426	3.807	4.457	5.687	6.487
44.3	3.123	3.285	3.449	3.688	4.078	4.748	5.957	6.638
45.5	3.418	3.573	3.736	3.978	4.376	5.082	6.227	6.769
46.8	3.736	3.879	4.045	4.292	4.705	5.427	6.486	6.841
48.1	4.073	4.205	4.377	4.634	5.060	5.787	6.739	6.920
49.3	4.443	4.560	4.738	5.001	5.433	6.177	6.993	6.968
50.6	4.841	4.942	5.123	5.387	5.822	6.540	7.204	7.026
51.9	5.261	5.343	5.522	5.786	6.215	6.879	7.371	7.024
53.1	5.689	5.751	5.929	6.187	6.597	7.241	7.509	7.026
54.4	6.117	6.161	6.336	6.586	6.981	7.566	7.618	7.072
55.7	6.558	6.578	6.747	6.988	7.350	7.815	7.684	6.987
56.9	7.006	7.001	7.152	7.368	7.661	8.030	7.712	6.891
58.2	7.426	7.396	7.514	7.683	7.911	8.203	7.706	6.767
59.5	7.765	7.712	7.804	7.937	8.128	8.326	7.680	6.631
60.7	8.036	7.964	8.045	8.159	8.314	8.404	7.591	6.482
62.0	8.283	8.192	8.264	8.360	8.440	8.412	7.466	6.320
63.2	8.516	8.407	8.449	8.500	8.474	8.365	7.317	6.166
64.5	8.684	8.560	8.545	8.525	8.471	8.301	7.152	6.005
65.8	8.740	8.605	8.557	8.520	8.425	8.187	6.972	5.824
67.0	8.718	8.575	8.536	8.473	8.342	8.019	6.790	5.641
68.3	8.670	8.522	8.472	8.390	8.210	7.843	6.608	5.482
69.6	8.593	8.441	8.370	8.258	8.044	7.642	6.407	5.322
70.8	8.461	8.307	8.220	8.089	7.857	7.426	6.198	5.142
72.1	8.287	8.133	8.042	7.901	7.651	7.231	6.009	4.964
73.4	8.099	7.946	7.845	7.694	7.445	7.009	5.822	4.791
74.6	7.888	7.736	7.635	7.484	7.233	6.753	5.619	4.613
75.9	7.672	7.522	7.425	7.271	6.998	6.543	5.416	4.432
77.2	7.463	7.314	7.202	7.037	6.766	6.342	5.214	4.258
78.4	7.222	7.077	6.965	6.803	6.551	6.103	5.009	4.089
79.7	6.971	6.830	6.736	6.583	6.328	5.867	4.804	3.923
81.0	6.757	6.619	6.518	6.361	6.095	5.646	4.605	3.763
82.2	6.537	6.401	6.290	6.129	5.863	5.408	4.412	3.607

Solid-like vibrational part, continued ...

ε	284	294	300	311	323	350	430	494
83.5	6.289	6.158	6.053	5.893	5.630	5.171	4.223	3.458
84.8	6.049	5.922	5.819	5.659	5.394	4.950	4.041	3.309
86.0	5.814	5.691	5.583	5.423	5.162	4.729	3.865	3.153
87.3	5.568	5.448	5.344	5.189	4.936	4.517	3.693	2.992
88.6	5.326	5.211	5.112	4.962	4.717	4.312	3.517	2.839
89.8	5.096	4.985	4.888	4.742	4.505	4.114	3.334	2.702
91.1	4.869	4.763	4.669	4.528	4.300	3.923	3.156	2.570
92.3	4.650	4.548	4.458	4.322	4.100	3.718	2.993	2.444
93.6	4.439	4.341	4.254	4.121	3.899	3.503	2.839	2.322
94.9	4.236	4.141	4.054	3.919	3.693	3.309	2.693	2.199
96.1	4.033	3.942	3.850	3.712	3.489	3.135	2.551	2.067
97.4	3.817	3.729	3.639	3.506	3.298	2.964	2.407	1.931
98.7	3.600	3.516	3.436	3.313	3.120	2.805	2.257	1.793
99.9	3.406	3.325	3.250	3.135	2.952	2.647	2.101	1.656
101.2	3.227	3.148	3.075	2.966	2.787	2.475	1.943	1.519
102.5	3.054	2.977	2.908	2.800	2.619	2.297	1.786	1.386
103.7	2.890	2.815	2.743	2.633	2.446	2.117	1.631	1.258
105.0	2.723	2.649	2.572	2.459	2.268	1.936	1.479	1.138
106.3	2.542	2.472	2.394	2.279	2.087	1.759	1.336	1.028
107.5	2.355	2.289	2.212	2.097	1.907	1.585	1.202	0.928
108.8	2.167	2.105	2.029	1.915	1.730	1.420	1.081	0.841
110.1	1.977	1.921	1.848	1.737	1.560	1.271	0.974	0.769
111.3	1.792	1.742	1.672	1.566	1.401	1.135	0.882	0.705
112.6	1.612	1.567	1.503	1.405	1.254	1.016	0.802	0.648
113.8	1.442	1.403	1.345	1.258	1.124	0.919	0.735	0.602
115.1	1.288	1.255	1.203	1.127	1.010	0.834	0.679	0.565
116.4	1.150	1.121	1.077	1.012	0.912	0.759	0.630	0.530
117.6	1.031	1.007	0.969	0.914	0.829	0.703	0.589	0.500
118.9	0.933	0.911	0.879	0.832	0.760	0.656	0.553	0.473
120.2	0.846	0.828	0.801	0.762	0.702	0.611	0.521	0.449
121.4	0.773	0.757	0.736	0.704	0.653	0.575	0.494	0.428
122.7	0.717	0.703	0.684	0.656	0.611	0.542	0.470	0.412
124.0	0.668	0.656	0.639	0.614	0.574	0.512	0.449	0.396
125.2	0.624	0.613	0.598	0.577	0.542	0.491	0.430	0.380
126.5	0.587	0.577	0.564	0.545	0.515	0.470	0.415	0.368
127.8	0.553	0.544	0.534	0.517	0.491	0.448	0.402	0.359
129.0	0.524	0.516	0.508	0.493	0.470	0.435	0.389	0.349
130.3	0.502	0.495	0.486	0.473	0.453	0.423	0.378	0.339
131.6	0.480	0.473	0.466	0.455	0.437	0.409	0.368	0.331
132.8	0.460	0.454	0.448	0.439	0.423	0.397	0.359	0.324
134.1	0.446	0.440	0.434	0.425	0.411	0.387	0.350	0.317
135.4	0.433	0.428	0.422	0.413	0.400	0.378	0.343	0.310
136.6	0.419	0.414	0.409	0.401	0.389	0.369	0.337	0.306
137.9	0.407	0.402	0.398	0.391	0.380	0.362	0.328	0.301
139.1	0.397	0.392	0.389	0.382	0.373	0.361	0.321	0.291
140.4	0.388	0.383	0.380	0.374	0.364	0.341	0.318	0.285
141.7	0.379	0.375	0.371	0.364	0.354	0.333	0.313	0.300
142.9	0.372	0.370	0.365	0.359	0.350	0.342	0.308	0.325
144.2	0.365	0.362	0.357	0.353	0.345	0.335	0.314	0.315
145.5	0.348	0.345	0.345	0.341	0.335	0.318	0.318	0.302
146.7	0.344	0.343	0.341	0.337	0.331	0.321	0.310	0.309
148.0	0.349	0.347	0.344	0.339	0.330	0.319	0.306	0.303
149.3	0.341	0.339	0.336	0.331	0.322	0.304	0.309	0.298
150.5	0.331	0.330	0.327	0.322	0.316	0.309	0.305	0.313

[1] T.T. Nguyen et al., J. Chem. Phys. **148**, 241725 (2018).
[2] M. Riera et al., Chem. Sci. **10**, 8211 (2019).
[3] M.A. Gonzalez, Collection SFN **12**, 169 (2011).
[4] Y. Abe and S.Tasaki, Ann. Nucl. Energ. **83**, 302 (2015).
[5] L.X. Dang and B.M. Pettitt, J. Phys. Chem. **91**, 3349 (1987).
[6] J. Teixeira et al., Phys. Rev. A **31**, 1913 (1985).
[7] V. Jaiswal, Theoretical and experimental approach towards generation of thermal scattering law for light water, PhD Thesis, University of Lille, France, 2018.
[8] L. Van Hove, Phys. Rev. **95**, 249 (1954).
[9] F. Real et al., J. Chem. Phys. **139**, 114502 (2013).
[10] V. Jaiswal et al., Analysis of the time-of-flight scattering cross section data for light water measured at the SEQUOIA spectrometer, in Proc. Int. Conf. on Nuclear Data for Science and Technology, Beijing, China, 2019.
[11] J.I. Marquez Damian et al., Ann. Nucl. Energ. **65**, 280 (2014).
[12] J.I. Marquez Damian et al., Ann. Nucl. Energ. **92**, 107 (2016).
[13] H.G. Vineyard, Phys. Rev. **110**, 999 (1958).
[14] A. Rahman et al., Phys. Rev. **126**, 986 (1962).
[15] S-T. Lin et al., J. Chem. Phys **119**, 11792 (2003).
[16] S-T. Lin et al., J. Chem. Phys **114**, 8191 (2010).
[17] T. Sun et al., J. Chem. Phys **147**, 194505 (2017).
[18] A. Faraone et al., J. Chem. Phys. **119**, 6302 (2003).
[19] N. Meyer et al., J. Mol. Liq. **275**, 895 (2019).
[20] A.S. Nair et al., J. Chem. Phys. **151**, 034301 (2019).
[21] S.-H. Chen et al., Phys. Rev. E **56**, 4231 (1997).
[22] L. Liu et al., Phys. Rev. E **65**, 041506 (2002).
[23] P.A. Egelstaff and P. Schofield, Nucl. Sci. Eng. **12**, 260 (1962).
[24] K.S. Singwi and A. Sjolander, Phys. Rev. **119**, 863 (1960).
[25] V.F. Sears, Can. J. Phys. **44**, 1299 (1966).
[26] A. Sjolander, Arkiv Fysik **14**, 315 (1958).
[27] G.L. Squires, Proc. Roy. Soc. A **212**, 192 (1952).
[28] M. Mattes and J. Keinert, Thermal neutron Scattering Data for the moderator materials H_2O, D_2O and ZrH_x in ENDF format and as ACE library for MCNP(X) Codes, International Nuclear Data Committee report INDC(NDS)-0470, 2005.
[29] R.E. MacFarlane, The NJOY nuclear data processing system, Version 2016, Los Alamos National Laboratory Report LA-UR-17-20093, 2019.
[30] W.S. Price et al., J. Phys. Chem. A **103**, 448 (1999).
[31] R.J. Speedy and C.A. Angell, J. Chem. Phys. **65**, 851 (1976).
[32] F. Cavatorta et al., J. Phys.: Condens. Matter **6**, A113 (1994).
[33] M.-C. Bellissent-Funel et al., Phys. Rev. E **51**, 4558 (1995).
[34] T. Tassaing and M.-C. Bellissent-Funel, J. Chem. Phys. **113**, 3332 (2000).
[35] F. Gonzalez Sanchez et al., J. Chem. Phys. **129**, 174706 (2008).
[36] J. Qvist et al., J. Chem. Phys. **134**, 144508 (2011).
[37] K. Amann-Winke et al., Chem. Rev. **116**, 7570 (2016).
[38] J. Qvist et al., J. Chem. Phys. **136**, 204505 (2012).
[39] A.G. Novikov et al., J. Struc. Chem. **31**, 77 (1990).
[40] D.I. Page and B.C. Haywood, The HARWELL scattering law programme: frequency distributions of moderators, Harwell Report AERE-R-5778,1968.
[41] D. Van Der Spoel et al., J. Comp. Chem. **26**, 1701 (2005).
[42] M.A. Gonzales and J.L.F. Abascal, J. Chem. Phys. **135**, 224516 (2011).
[43] A. Lerbret et al., Proteins **81**, 326 (2013).
[44] J.A Padro and J. Marti, J. Chem. Phys. **118**, 452 (2003).
[45] A. De Santis et al., J. Chem. Phys. **120**, 1657 (2004).
[46] J.A Padro and J. Marti, J. Chem. Phys. **120**, 1659 (2004).
[47] J.I. Marquez Damian et al., Experimental validation of the temperature behavior of the ENDF/B-VIII.0 thermal scattering kernel for light water, in Proc. Int. Conf. on Nuclear Data for Science and Technology, Beijing, China, 2019.
[48] J.P. Scotta et al., EPJ Nuclear Sci. Technol. **4**, 32 (2018).
[49] J.P. Scotta, Improvement of the thermal and epithermal neutrons cattering data for the interpretation of integral experiments, PhD Thesis, Aix-Marseille University, France, 2017.
[50] E. Farhi et al., J. Nucl. Sci. Technol. **52**, 844 (2015).
[51] V. Jaiswal et al., EPJ Web of Conf. **146**, 13006 (2017).
[52] D. Richard et al., Analysis and visualisation of neutron scattering data ,J. Neutron Res. **4**,33 (1996).
[53] W. Reichardt, MUPHOCOR, a Fortran program to determine the phonon density of states from neutron scattering experiments, Report No. 13.03.01P06L, Institut fr Nukleare Festkorper Physik, Kernforschung Szentrum, Karlsruhe, Germany, 1984.
[54] E. Brun et al., Ann. Nucl. Ener. **82**, 151 (2015).
[55] P. Archier et al., Nucl. Data Sheets **118**, 488 (2014).
[56] J.B. Brubach et al., J. Chem. Phys. **122**, 184509 (2005).
[57] K. Ramasesha et al., Nat. Chem. **5**, 935 (2013).
[58] M. Grechko et al., Nat. Commun. 9:885 (2018).
[59] S-H. Chen et al., Phys. Rev. Lett. **53**, 1360 (1984).
[60] K. Toukan et al., Phys. Rev. A**37**, 2580 (1988).

B. Uranium dioxide

Combining density functional theory and Monte Carlo neutron transport calculations to study the phonon density of states of UO_2 up to 1675 K by inelastic neutron scattering

G. Noguere, J. P. Scotta, and S. Xu
CEA, DES, IRESNE, DER, Cadarache, F-13108 Saint Paul Les Durance, France

A. Filhol, J. Ollivier, E. Farhi, Y. Calzavarra, S. Rols, and B. Fak
Institut Laue-Langevin, F-38042 Grenoble, France

J.-M. Zanotti
Laboratoire Léon Brillouin (CEA-CNRS), Université Paris-Saclay, CEA Saclay, 91191 Gif-sur-Yvette Cedex, France

Q. Berrod
CNRS-CEA-Université Grenoble Alpes, SyMMES, 38000 Grenoble, France

(Received 5 June 2020; revised 26 August 2020; accepted 29 September 2020; published 30 October 2020)

Significant advances in the use of atomistic simulation techniques, such as *ab initio* density functional theory and the molecular dynamics method, made it possible to predictively calculate properties of materials. In parallel, low-energy neutron scattering instruments and data analysis tools available in different institutes become mature for providing high-quality data for experimental validation purposes. Despite such experimental and theoretical improvements, the accurate modeling of experimental neutron-weighted multiphonon spectra for UO_2 over a broad temperature range still remains an issue. Combining prior phonon density of states (PDOS) from density functional theory and Monte Carlo inelastic neutron scattering calculations in a Bayesian fitting procedure is a valuable alternative approach to assess the partial PDOS of uranium and oxygen in UO_2 from 294 to 1675 K for improving the comparison to experiment and exploring the first-principles calculation hypothesis.

DOI: 10.1103/PhysRevB.102.134312

I. INTRODUCTION

The complex insulating nature of uranium dioxide (UO_2) has been the subject of many experimental and theoretical studies since the pioneer works reported in the 1960s. At that time, major results about the vibration modes of UO_2 were published in a series of symposia on neutron scattering and neutron thermalization organized by the International Atomic Energy Agency, between 1960 and 1977 [1,2]. Over the past 20 years, the first-principles density functional theory became an invaluable resource for supplying material properties to simulate the neutron slowing down in nuclear fuels.

The latest version of the United States evaluated nuclear data library, namely ENDF\B-VIII [3], benefited from the extensive efforts led by the Low Energy Interaction Physics group of the North Carolina State University to accommodate condense matter physics into the low-energy neutron-induced cross-section formalisms [4]. In the case of UO_2, the VASP code [5] has been used to generate phonon density of states (PDOS) [6] for the ENDF\B library, replacing those established from the work of Dolling [7]. The corresponding PDOS for $T = 0$ K is shown in Fig. 1. The five normal modes of vibration of UO_2 can be distinguished around 10 meV, 20 meV, 30 meV, 55 meV, and 70 meV. The two first peaks correspond to the translational and longitudinal acoustic phonon modes of the uranium atoms. The highest energy structures are dominated by the optical phonon modes of the oxygen atoms. For comparison, the PDOS calculated at Uppsala University for $T = 294$ K [8] is shown in the same figure. The principle of the calculations performed in the quasiharmonic approximation is reported in Refs. [9,10] together with validation results. It consists of applying the finite-displacement method to a UO_2 supercell through the PHONOPY code [11]. The interatomic forces are provided by the VASP code within the framework of the first-principles density functional theory. The comparison of the two *ab initio* PDOS highlights the phonon mode shift to lower energy transfer with increasing temperature. It also shows how the calculations performed at the Uppsala University are able to capture the splitting between the TO1 and LO1 optical phonon branches around 28 and 33 meV.

The results reported by Pang *et al.* [12,13] represent the latest theoretical and experimental achievements of interest for our work. If first-principles PDOS simulations successfully reproduce inelastic neutron scattering data of UO_2 measured at 294 K using the ARCS spectrometer of the Spallation Neutron Source (SNS), similar simulations still fail to reproduce high-temperature neutron-weighted phonon density of states ($T = 1200$ K) which are characterized by a stronger anharmonic linewidth broadening [14]. These theoretical limitations make questionable the simulation of the neutron transport in nuclear fuel loaded in power reactors operating at hot full power. Indeed, the slowing down of neutrons in UO_2 is affected by the vibrations of the uranium and oxygen atoms from which emerge neutron up-scattering effects that

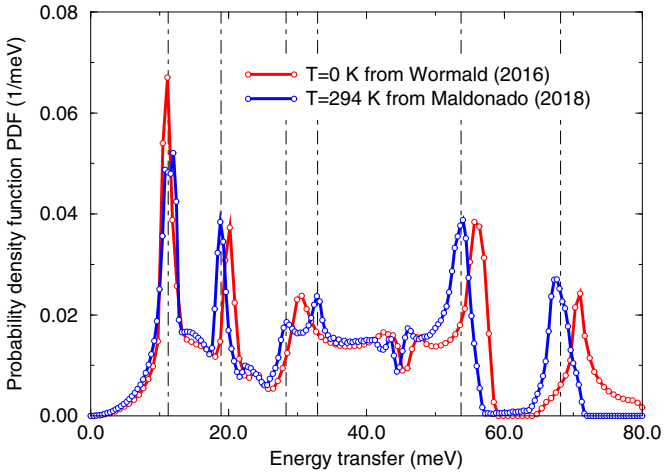

FIG. 1. *Ab initio* phonon density of states of UO_2 at $T = 0$ K [6] and $T = 294$ K [8]. The dot-dashed lines locate the main vibration modes of UO_2 calculated at $T = 294$ K. The two first peaks at 10 and 20 meV correspond to the translational (TA) and longitudinal (LA) acoustic phonon modes of the uranium atoms. The structures at around 30 meV, 55 meV, and 70 meV are dominated by the optical phonon modes (TO1, LO1, TO2, LO2) of the oxygen atoms.

modify the ^{238}U radiative capture reaction rate involving sizable changes on the neutron multiplication factor, Doppler reactivity coefficient, and ^{239}Pu inventory [15].

The present work aims to derive reliable temperature-dependent partial PDOS for oxygen and uranium in UO_2 from inelastic neutron scattering data measured at the IN4 and IN6 time-of-flight spectrometers of the Institute Laue-Langevin (ILL) between 294 and 1675 K. The originality of the work relies on the use of the Monte Carlo neutron transport code TRIPOLI4 [16] to simulate the experimental results by taking into account the multiple neutron scattering effects and the multiphonon contribution. The main prior input parameters are the partial phonon density of states for oxygen and uranium in UO_2 provided by *ab initio* calculations. The obtained results are expected to stimulate advanced theoretical studies for improving comparison to experiment over a broad temperature range of interest for nuclear applications.

The main expressions involved in the neutron scattering formalism are reported in Sec. II. Section III briefly describes the measurements performed at ILL. The experimental neutron-weighted multiphonon spectra of UO_2 as a function of the temperature are reported in Sec. IV. The interpretation of the data with the Monte Carlo neutron transport code TRIPOLI4 is presented in Sec. V. The obtained results are discussed in Sec. VI.

II. NEUTRON SCATTERING FORMALISM

In the low neutron energy range, typically below 5 eV, the slowing down of neutrons in UO_2 depends on the energy and angular distribution of the scattering process. The mathematical expression of the corresponding double-differential neutron scattering cross section is well described in the literature. The main equations are summarized in Ref. [17]. They were obtained in the framework of the incoherent scattering approximation that allows one to neglect the interference terms in the case of polycrystalline materials and to express the double-differential neutron scattering cross section of each atom X separately. If T is the temperature of the target and k_B is the Boltzmann constant, the temperature-dependent double-differential scattering cross section for X (^{238}U or ^{16}O) in UO_2 can be written as [18]

$$\frac{d^2\sigma_{n_X}^T}{dE'd\theta} = \frac{\sigma_{n_X}^0}{2k_BT}\sqrt{\frac{E'}{E}}e^{-\beta/2}S_X^T(\alpha,\beta), \tag{1}$$

where E is the neutron incident energy, E' stands for the energy of the scattered neutron, $\sigma_{n_X}^0$ is the bound neutron elastic scattering cross section at $T = 0$, and $S_X^T(\alpha,\beta)$ is the symmetric form of the dynamic structure factor [19] which is defined as a function of the dimensionless variables α and β. The latter variables are related to the momentum transfer q:

$$\alpha = \frac{q^2\hbar^2}{2M_Xk_BT} = \frac{E' + E - 2\mu\sqrt{E'E}}{A_Xk_BT}, \tag{2}$$

and energy transfer $\varepsilon = \hbar\omega$:

$$\beta = -\frac{\hbar\omega}{k_BT} = -\frac{E - E'}{k_BT}, \tag{3}$$

where $\mu = \cos(\theta)$ is the cosine of the scattering angle in the laboratory system and A_X is the ratio of the mass M_X of the scattering atom X to the neutron mass. An analytical form of $S_X^T(\alpha,\beta)$ was established for a cubic symmetry by using an isotropic harmonic potential which simplifies the complex averaging over all the possible orientations of the molecules. This model, known as the incoherent Gaussian approximation [20], led to the conventionally called phonon expansion:

$$S_X^T(\alpha,\beta) = e^{-\alpha\lambda_s}\sum_{n=1}^{\infty}\frac{1}{n!}(\alpha\lambda_s)^n\mathcal{T}_n(\beta), \tag{4}$$

where n represents the phonon expansion order, λ_s stands for the Debye-Waller coefficient, and $\mathcal{T}_n(\beta)$ has the generic form:

$$\mathcal{T}_n(\beta) = \int_{-\infty}^{\infty}\mathcal{T}_1(\beta')\mathcal{T}_{n-1}(\beta - \beta')d\beta'. \tag{5}$$

The one-phonon term $\mathcal{T}_1(\beta)$ is given by

$$\mathcal{T}_1(\beta) = \frac{\rho_X^T(\beta)e^{-\beta/2}}{2\lambda_s\beta\sinh(\beta/2)}. \tag{6}$$

This term explicitly depends on the partial phonon density of states $\rho_X^T(\beta)$. The aim of this study is to extract reliable values of $\rho_X^T(\beta)$ from the experimental quantity $\rho_{\rm exp}^T(\beta)$ which represents the neutron-weighted multiphonon spectrum of UO_2 measured at ILL as a function of the temperature. A suitable expression of $\rho_{\rm exp}^T(\beta)$ can be obtained in the framework of the incoherent elastic one-phonon approximation. By introducing Eq. (6) in Eq. (4) for $n = 1$ and by removing the contribution of the elastic peak, we obtain

$$\rho_{\rm exp}^T(\beta) \simeq \lim_{\alpha\to 0}P_{\rm exp}^T(\alpha,\beta), \tag{7}$$

with

$$P_{\rm exp}^T(\alpha,\beta) \simeq \frac{2\beta\sinh\beta/2}{\alpha}S_{\rm exp}^T(\alpha,\beta), \tag{8}$$

where $S_{\rm exp}^T$ represents the experimental symmetric form of the dynamic structure factor [Eq. (1)] without the contribution of

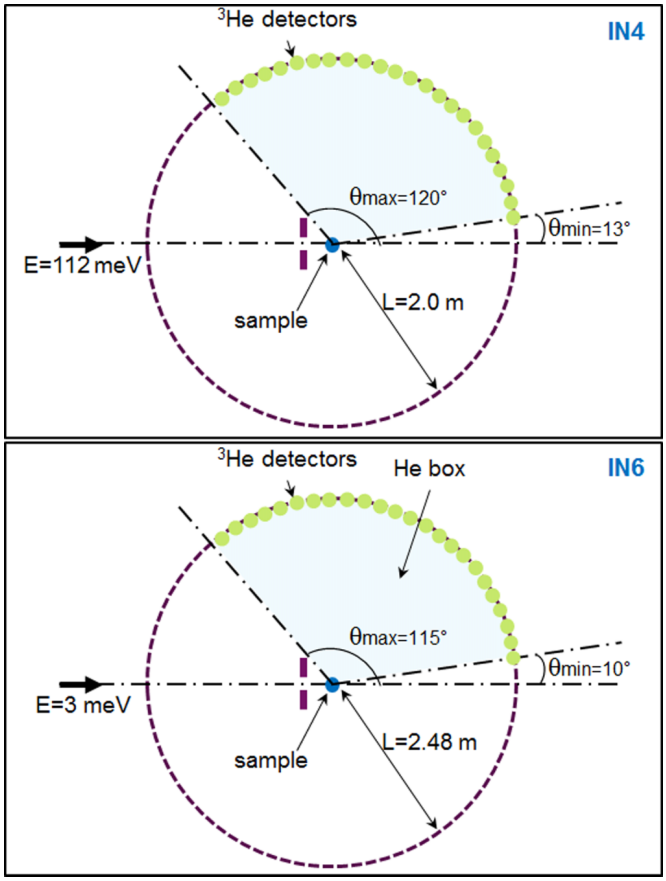

FIG. 2. Simplified top view of the IN4 and IN6 time-of-flight spectrometers of the Institute Laue-Langevin.

the quasielastic neutron scattering peak S_0^T. It is related to the experimental neutron yield $Y_{\rm exp}^T$ as follows:

$$S_{\rm exp}^T(\alpha,\beta) = Y_{\rm exp}^T(\alpha,\beta)\sqrt{\frac{E}{E'}}e^{\beta/2} - S_0^T(\alpha,\beta). \qquad (9)$$

III. INELASTIC NEUTRON SCATTERING EXPERIMENTS

Two experimental campaigns were undertaken in 2016 and 2019 to measure the experimental neutron yields $Y_{\rm exp}^T$ at 294, 300, 350, 420, 600, 900, 1200, and 1675 K on the IN6 and IN4 time-of-flight spectrometers of ILL for two incident neutron energies $E = 3$ meV ($\lambda = 5.1$ Å) and $E = 112$ meV ($\lambda = 0.85$ Å), respectively. Experimental details and preliminary results were reported in Refs. [21,22].

From the point of view of the neutron transport physics, both spectrometers share the same basic design (Fig. 2). The neutron time-of-flight technique consists of measuring the time t traveled by the neutrons from the sample until their detection at a given scattering angle θ. If the energies are in eV, the length in m, and the time in μs, the non-relativistic time-energy relation $E' = (72.298L/t)^2$ is used to obtain the experimental neutron yield $Y_{\rm exp}^T(\theta, E')$ as a function of the outgoing neutron energies E'. The flight distance between the sample and the detection setup is equal to $L = 2.00(1)$ m and $L = 2.48(1)$ m, for IN4 and IN6, respectively. Each ^{3}He detector array covers scattering angles ranging from approximately 10° to 120°. In both cases, a rectangular monoenergetic neutron beam was focused to the sample, which was mounted in a high-temperature furnace placed at the center of the spectrometer. The sample is a 4.09(1)-cm-long cylinder composed of a stack of four depleted UOX pellets of 8.26(1) mm diameter. The total weight of the sample is 23.642(1) g, with a mass-fraction composition in ^{238}U, ^{236}U, ^{235}U, ^{234}U, and ^{16}O of 87.598(1)%, 0.005(1)% 0.264(1)% 0.002(1)%, and 12.131(1)%, respectively. For the first experimental campaign, the UO_2 sample was sealed in a quartz tube under primary vacuum and encapsulated in a thin niobium sample-holder tube. For the second one, the UO_2 sample was simply encapsulated in a thick niobium sample-holder tube. Empty "dummy" samples were prepared to measure the background contribution.

The experiments consisted of a sequence of UO_2 and "dummy" sample measurements, including a short irradiation of a vanadium sample. As this material nearly behaves as a pure incoherent elastic scatterer, its elastic scattering peak is used as a reference for the purpose of calibration and detector efficiency correction. The data reduction steps were handled with the ILL in-house LAMP code, except for the background correction. Indeed, replacing depleted UOX pellets by void in the "dummy" sample cannot ensure an accurate background subtraction due to significant sample absorption and multiple neutron scatterings. The background was then defined as the sum of the "dummy" sample data times an effective transmission factor plus an additional contribution due to neutrons scattered by the sample-holder tube and furnace environment. The effective transmission factor and contributions of the sample environment have been estimated with the Monte Carlo neutron transport code TRIPOLI4 [16], using the models shown in Fig. 2 and the neutron scattering formalism described in Eqs. (1)–(6).

IV. EXPERIMENTAL NEUTRON-WEIGHTED MULTIPHONON SPECTRUM

The experimental neutron-weighted multiphonon spectra $\rho_{\rm exp}^T$ of UO_2 were deduced from the temperature-dependent neutron yields $Y_{\rm exp}^T$ measured on IN6 by using the expression (7). In view of obtaining $P_{\rm exp}^T(\alpha,\beta)$ at $\alpha = 0$, we have smoothed out fluctuations due to nuclei dynamics by using a log-log extrapolation to zero of the cumulative distribution functions of $P_{\rm exp}^T(\alpha,\beta)$ over α. The contribution of the quasielastic neutron scattering peak S_0^T was removed from the data using a pseudovoigt function. In the present analysis, no attempt was made to iteratively correct the data from the multiphonon contribution and the multiple neutron scattering effects, as usually proposed in the literature [23]. These two effects have different physical origins which will be included in the theoretical calculations. The multiphonon correction is mainly a temperature effect which is part of the dynamic structure factor. It is taken into account with the phonon expansion given by Eq. (4). The contribution of the scattered neutrons depends on several experimental factors such as the sample size and its environment. Such a correction is handled through Monte Carlo simulations whose principles are presented in Sec. V.

Figure 3 shows the neutron-weighted multiphonon spectrum of UO_2 and the background contributions measured on

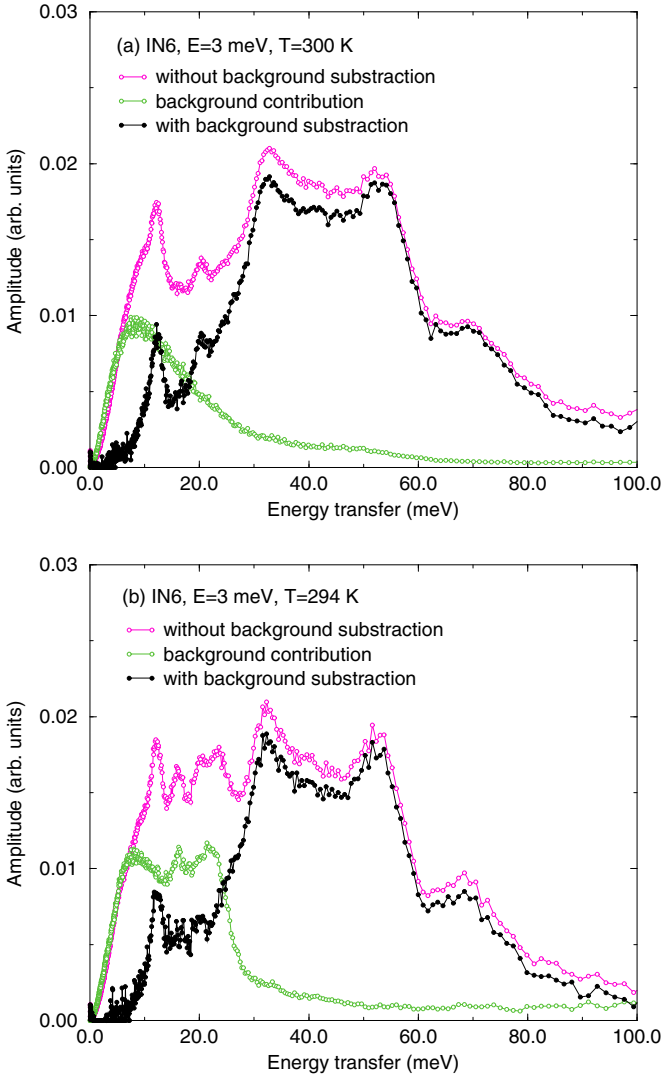

FIG. 3. Examples of background contributions at room temperature in the case of the neutron-weighted multiphonon spectrum of UO_2 deduced from the IN6 data measured with a quartz tube in a thin niobium sample-holder tube (a) and a thick niobium sample-holder tube (b).

IN6 at $T = 300$ K and $T = 294$ K. The non-negligible contribution of the vibration modes of niobium on the top of the phonon modes of the uranium atoms favors the use of a thin niobium sample-holder tube. Results obtained up to 1675 K are shown in Fig. 4. The vibration modes of UO_2 are observed at energy positions which are in excellent agreement with the theoretical predictions reported in Fig. 1 at room temperature. Our results show a low temperature dependence of the phonon mode shift. An overall decrease of about -2 meV from 300 to 1675 K can be estimated from both the acoustic and optical phonon mode positions. It has to be noted that the dip between the TO1 and LO1 phonon branches cannot be observed around 30 meV because of the too-broad response function of IN6. In addition, above 60 meV, the increasing broadening of the phonon linewidth due to the temperature makes it difficult to accurately determine the peak position corresponding to the highest longitudinal optical phonons.

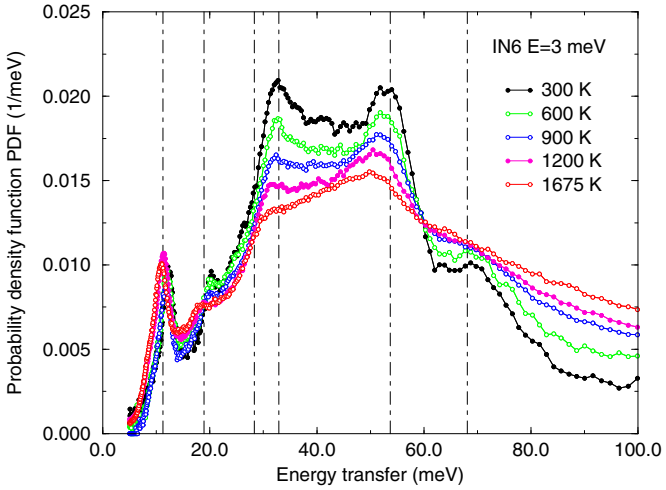

FIG. 4. Experimental neutron-weighted multiphonon spectrum $\rho^T_{\rm exp}$ of UO_2 deduced from the IN6 data. The dot-dashed lines show the energy positions of the vibration modes of UO_2 calculated at $T = 294$ K (Fig. 1).

V. MONTE CARLO NEUTRON TRANSPORT SIMULATIONS

Experimental neutron-weighted multiphonon spectrum $\rho^T_{\rm exp}$ of UO_2 can only be compared with their theoretical analogs $\rho^T_{\rm th}$ via Monte Carlo simulations that take into account the multiple neutron scattering effects and multiphonon contribution. In this work, the time of flight t of each neutron has been simulated with the neutron transport code TRIPOLI4 without taking into account the time distribution of the initial neutron burst originating from the Fermi chopper. Therefore, the theoretical neutron yield $Y^T_{\rm th}$ is calculated from the neutron yields Y^T_{T4} provided by TRIPOLI4 as follows:

$$Y^T_{\rm th}(\theta, E') = \int_0^{+\infty} R_{E'}(\theta, t) Y^T_{T4}(\theta, t) dt. \qquad (10)$$

The probability density function $R_{E'}(\theta, t)$ stands for the time-dependent experimental response function of the spectrometer which is well approximated by a Gaussian. Its full width at half maximum $\Delta t = 41(5)\,\mu$s (for IN6 at $E = 3$ meV) and $\Delta t = 22(5)\,\mu$s (for IN4 at $E = 112$ meV) was fitted to the neutron elastic scattering peak of vanadium.

Figure 5 compares the experimental and theoretical neutron-weighted multiphonon spectra obtained in the case of the IN6 spectrometer at $T = 294$ K when the *ab initio* phonon density of sates established at the Uppsala University (Fig. 1) are introduced in the TRIPOLI4 calculations. The top and middle plots illustrate the poor description of the experimental values when the single neutron scattering and one-phonon approximations are used. An overall agreement is achieved between the experimental and theoretical curves only if multiple scattering and multiphonon effects are taken into account in the simulation. The amplitude and the energy position of the vibration modes of the UO_2 molecule are well predicted confirming the validity of the main approximations involved in the *ab initio* calculations (quasiharmonic phonon-based model), neutron scattering formalism (inelastic and Gaussian approximations), Monte Carlo simulations (Gaussian response function), and data reduction procedure

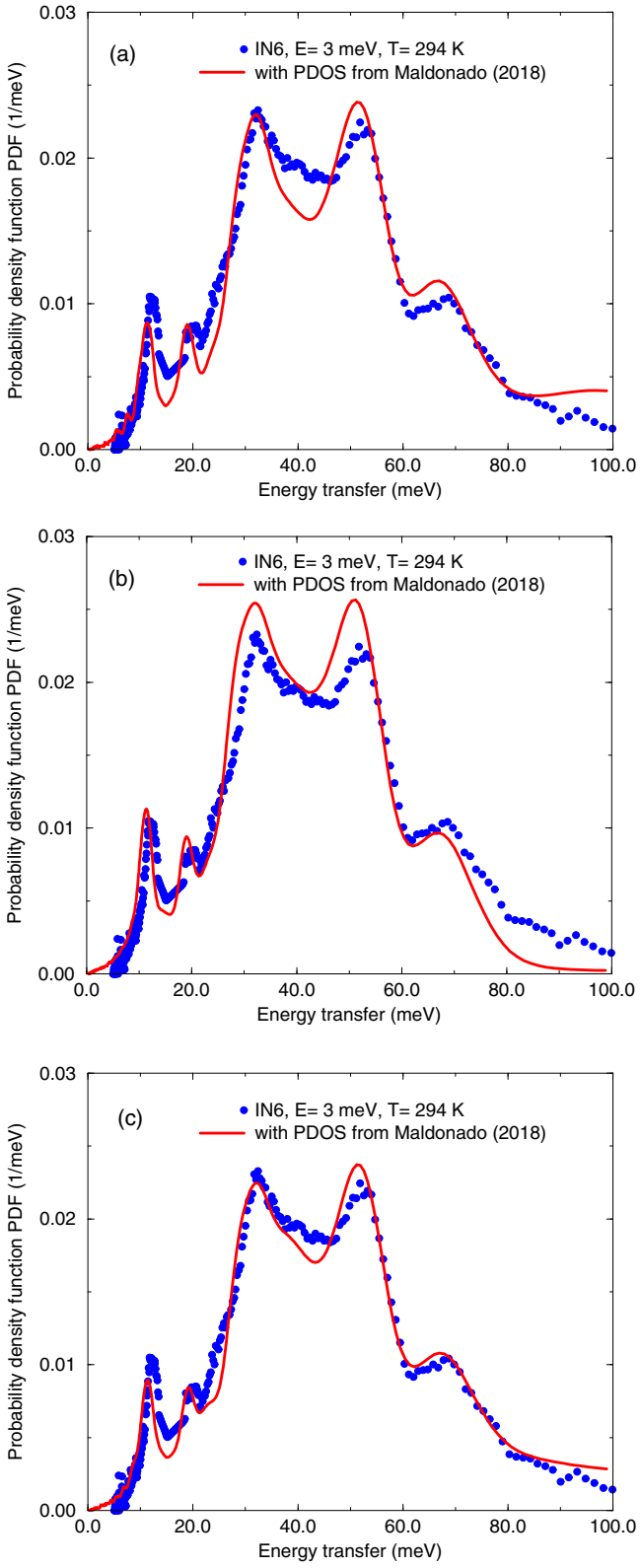

FIG. 5. Comparison of the neutron-weighted multiphonon spectrum ρ^T_{exp} and ρ^T_{th} deduced from the IN6 data and the TRIPOLI4 simulations, respectively. The calculations were performed at $T = 294$ K by using the PDOS shown in Fig. 1. The theoretical curves in plots (a) and (b) were obtained within the single neutron scattering and one-phonon approximations, respectively. The theoretical curve in the bottom plot (c) accounts for both the multiple neutron scattering effects and the multiphonon contribution.

(empty-cell subtraction strategy and extrapolation of the cumulative distribution function of $P^T_{\text{exp}}(\alpha, \beta)$ to $\alpha = 0$). Despite the achievement observed at room temperature, moving toward higher temperatures with *ab initio* simulations represents a theoretical challenge because anharmonicity may cause sizable interactions among phonons with increasing temperature. Even if anharmonic effects in neutron scattering by crystalline materials were the subject of numerical calculations from the early 1960s [24,25], they still remain an issue to study inelastic neutron scattering data.

VI. RESULTS AND DISCUSSIONS

To work around such theoretical limitations, combining *ab initio* PDOS and Monte Carlo inelastic neutron scattering calculations in a Bayesian learning framework can be an alternative approach to assess temperature-dependent PDOS for improving comparison to experiment and exploring first-principles calculation hypothesis. In the present work, the phonon density of states ρ^T_X of uranium and oxygen in UO_2 were optimized on the IN6 data with an iterative Bayesian least-squares fitting procedure. Best estimates of the phonon density of states were found thanks to the chi-square minimization capabilities implemented in the nuclear data code CONRAD [26]. Starting from the PDOS of Wormald *et al.* (Fig. 1), our model gradually converged towards the posterior solutions shown in Fig. 6 for 300, 350, 420, 600, 900, 1200, and 1675 K, leading to a good agreement between the posterior TRIPOLI4 simulations and the experimental symmetric form of the dynamic structure factor S^T_{exp}, in which the quasielastic neutron scattering peak has been removed [Eq. (9)]. An example of results is shown in Fig. 7 for $\theta = 90°$. Most of the differences between the prior calculations and the data have been reduced, especially around 30 meV. This energy range corresponds to the TO1/LO1 splitting which is softened by the response function of the IN6 spectrometer. This result agrees with the conclusions already reported by Pang *et al.* [12] about the contribution of the optical phonons to the thermal conductivity of UO_2 and the need for improving the theoretical description of the phonon broadening near 30 meV, where the contribution of the uranium atoms is still important.

The optimized partial phonon density of states ρ^T_X of uranium ($X = {}^{238}\text{U}$) and oxygen ($X = {}^{16}\text{O}$) in UO_2 are shown in Fig. 8 as a function of the temperature. The corresponding values are reported in the Appendix (Tables I and II). As expected from Fig. 4, the energy shift of the acoustic and optical phonon modes is close to -2 meV on average from 300 to 1675 K, corresponding to a phonon frequency shift $\omega_{1675\,\text{K}} - \omega_{300\,\text{K}} = -0.4$ THz. This order of magnitude is compatible with those obtained via models involving four-phonon scattering [27]. No meaningful anomaly is observed in the increasing broadening of the acoustic and optical phonon linewidths. The phonon linewidths corresponding to the TO2 ($\varepsilon \simeq 55$ meV) and LO2 ($\varepsilon \simeq 70$ meV) phonon branches increase by a factor of about 1.5 from 300 to 1675 K. As already observed by Hutchings [28], the broadening of the acoustic modes seems to be less important. Similarly, methods relying on interacting phonon theory, already applied over the last 10 years to investigate the anharmonicity-induced phonon broadening, should be able to explain part of the monotonic

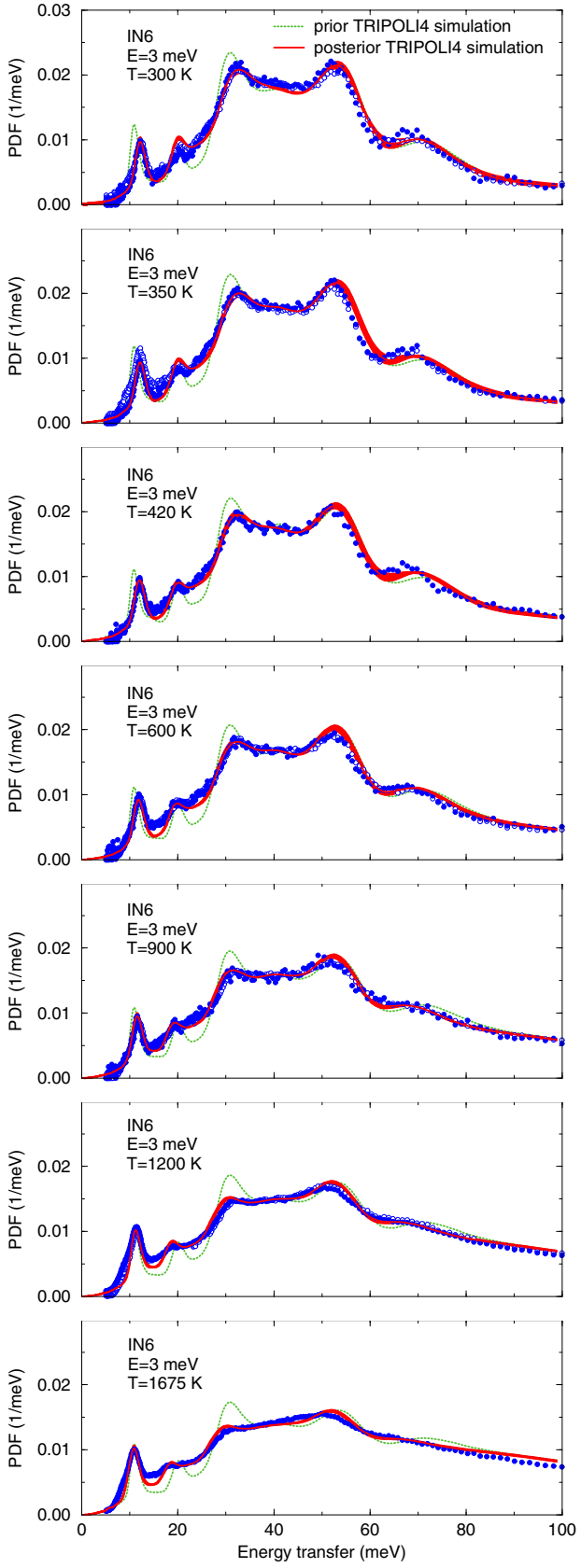

FIG. 6. Prior and posterior TRIPOLI4 simulations compared to the neutron-weighted multiphonon spectra deduced from the IN6 data.

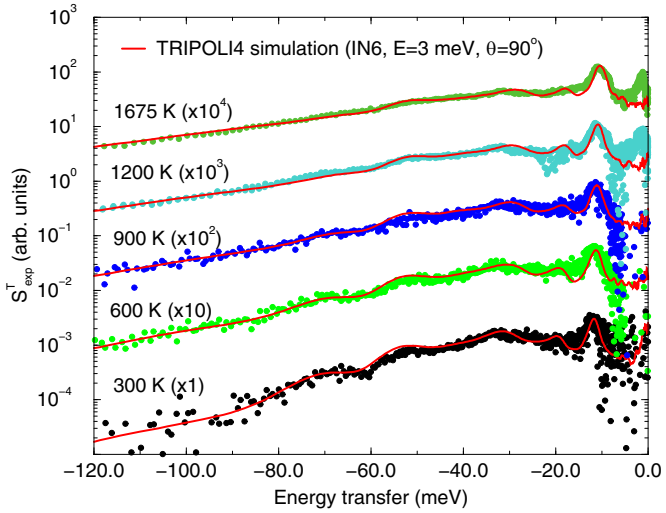

FIG. 7. Experimental symmetric form of the dynamic structure factor $S^T_{\rm exp}$ without the contribution of the quasielastic neutron scattering peak [Eq. (9)] measured at $\theta = 90^\circ$ with the IN6 spectrometer. The solid red lines correspond to the posterior TRIPOLI4 simulations obtained after the optimization of the partial phonon density of states ρ^T_X of uranium and oxygen in UO_2.

behavior of the phonon linewidth observed as a function of the temperature.

The higher incident neutron energy range was investigated with the IN4 spectrometer by using a monoenergetic neutron beam $E = 112$ meV. Although the poor response function of IN4 is not suited to study the fine phonon structures of UO_2, the spectrometer allows one to investigate the shape of the neutron-weighted multiphonon spectrum in the up- and down-scattering energy ranges. For that purpose, TRIPOLI4 simulations were repeated by using the IN4 model shown in Fig. 2 together with the partial PDOS deduced from the IN6 data (Fig. 8). Results obtained at 300, 600, and 900 K are

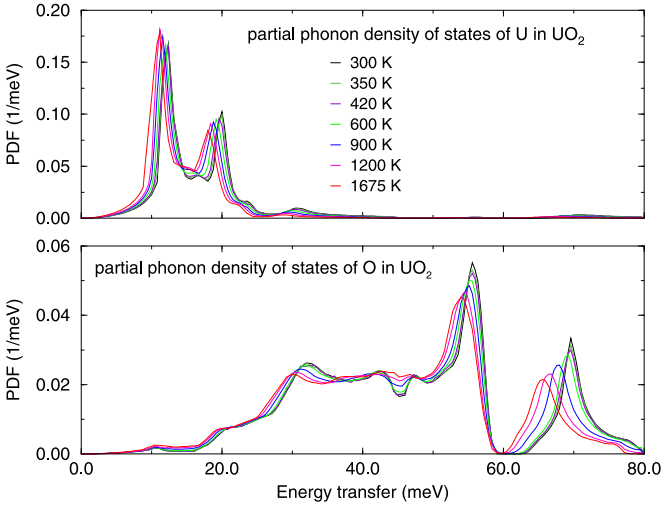

FIG. 8. Temperature-dependent partial phonon density of states ρ^T_X of uranium and oxygen in UO_2 deduced from the IN6 data. The corresponding values are reported in the Appendix (Tables I and II).

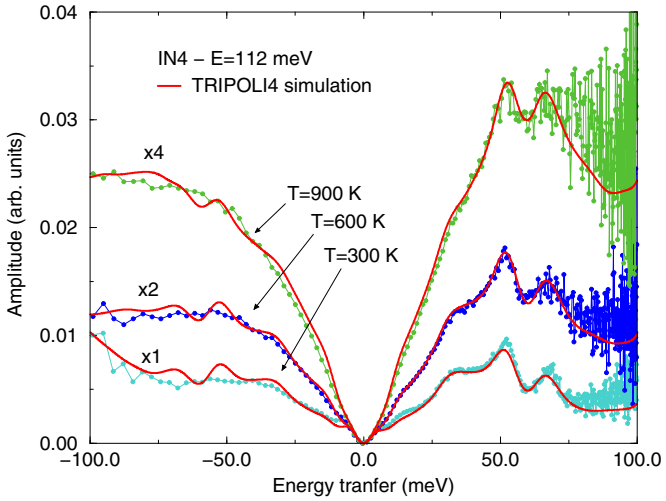

FIG. 9. Comparison of the neutron-weighted multiphonon spectra ρ^T_{exp} and ρ^T_{th} deduced from the IN4 data and the TRIPOLI4 simulations, respectively. The calculations were performed at 300, 600, and 900 K by using the partial PDOS obtained from the IN6 data (Fig. 8).

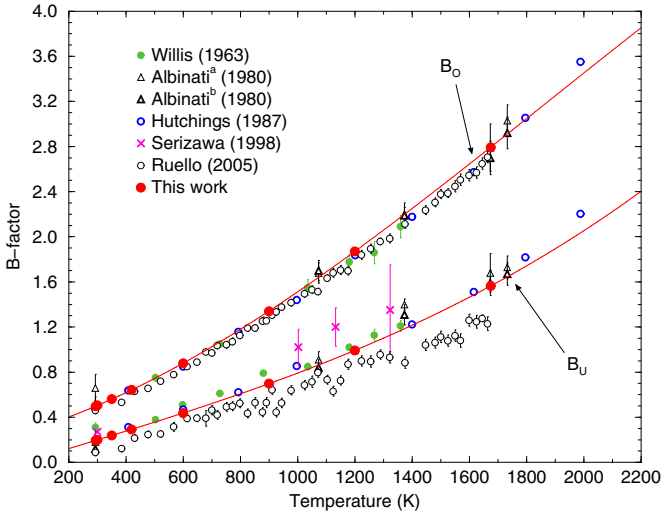

FIG. 10. The red filled circles (connected by the red "eye-guide" curves) represent the B factors (in Å^2) calculated with Eq. (11) by using the partial PDOS obtained from the IN6 data (Fig. 8). They are compared with experimental values reported in Refs. [28,33–37].

shown in Fig. 9 as a function of the energy transfer ranging from −100 to 100 meV. The overall agreement achieved between the IN4 data and the Monte Carlo results validates the Bayesian inference method, which is presented in this work as an alternative approach to assess temperature-dependent partial PDOS for uranium and oxygen in UO_2 starting from *ab initio* information.

The results inferred from the interpretation of the IN4 and IN6 data evidence the smooth deviation from the quasi-harmonic approximation of the PDOS characteristics as a function of the temperature. A part of this behavior can be illustrated via the underlying Debye-Waller coefficient λ_s involved in Eq. (4), a measure of which is given by the B factor. This parameter, also called the temperature parameter, is reported in the literature in units of Å^2. It gives a measure of the dynamical disorder of the material. At room temperature, a low B-factor value is expected since the amplitude of the atomic thermal motion being smaller than the dynamical disorder of atoms is reduced. The expression of the B factor $B_X(T)$ for the oxygen and uranium atoms is given by [29]

$$B_X(T) = 8\pi^2 \frac{\hbar^2}{2M_X} \int_0^{+\infty} \frac{\rho_X^T(\varepsilon)}{\varepsilon} \coth\left(\frac{\varepsilon}{2k_BT}\right) d\varepsilon. \quad (11)$$

Figure 10 shows the B factors obtained with the partial PDOS ρ_X^T deduced from the IN6 data. Our calculations adequately follow the trend of a few data sets retrieved from the literature. The B factor of the uranium atoms exhibits a nearly linear dependence with the temperature until 1200 K, which is in favor of an increasing anharmonic relaxation of the oxygen atom positions in a fluorite structure [30]. At 1675 K, the clear deviation from the linearity of B_U and B_O may confirm the existence of a more complex atomic disorder with the distortion of the oxygen and uranium sublattices [31,32].

VII. CONCLUSIONS

The IN4 and IN6 time-of-flight spectrometers of ILL were used to determine the main features of the partial phonon density of states of uranium and oxygen in UO_2 as a function of the temperature. At room temperature, the neutron-weighted multiphonon spectra of UO_2 derived from the inelastic neutron scattering data of IN6 is adequately reproduced by Monte Carlo neutron transport simulations relying on *ab initio* PDOS calculated at the Uppsala University. This result confirms the validity of the main approximations involved in the *ab initio* calculations, neutron scattering formalism, Monte-Carlo simulations, and data reduction procedure.

For mapping the full temperature range of interest for the nuclear applications, a consistent set of PDOS was calculated within a Bayesian fitting framework starting from *ab initio* information established by the Low Energy Interaction Physics group of the North Carolina State University. The posterior results confirm the need to improve the theoretical description of the TO1/LO1 splitting around 30 meV, where the contribution of the uranium atoms is still important. No anomalies with increasing temperatures were observed through the monotonic behavior of the phonon energy shift and of the phonon broadening. Our results also follow the behavior of the B-factor values, which smoothly increase with the temperature. The obtained PDOS can then be used to produce double-differential neutron scattering cross sections for simulating the neutron transport in UOX fuels from cold zero power to hot full power conditions.

In the temperature range between 294 and 1200 K, the IN4 and IN6 data favor an increasing anharmonic relaxation of the oxygen atom positions in a fluorite structure. The models involving four-phonon scattering should be able to explain part of the observed monotonic behavior of the PDOS features. Above 1675 K, the existence of a more complex atomic disorder with the distortion of the oxygen and uranium sublattices could be invoked to describe the experimental neutron-weighted multiphonon spectrum of UO_2 measured at the ILL facilities. It has to be noted that temperatures close to 1700 K represent an upper limit for applying a Bayesian analysis to UO_2 data measured on IN6 because the fine structures

of the PDOS, which are already broadened by the temperature effects, are also too softened by the response function of the spectrometer. Exploring higher temperatures, closer to an accident scenario in power reactors, would require facilities with a smaller incident neutron burst width.

ACKNOWLEDGMENTS

The authors wish to express their appreciation for the experimental work performed at ILL with the specific support of F. Marchal and P. Mouveau for the sample preparation. Special thanks goes to G. Carlot and L. Desgrange, working in the Fuel Studies Department of CEA/Cadarache, for their valuable help during the preparation of this work. The Monte Carlo simulations were performed thanks to the relevant advice of C. Jouanne from CEA/Saclay. One of the authors also expresses his gratitude to Judy W. L. Pang for sharing her data for intercomparison studies.

APPENDIX: PARTIAL PHONON DENSITY OF STATES OF URANIUM AND OXYGEN IN UO_2

Tables I and II report the temperature-dependent PDOS of uranium and oxygen in UO_2 which are shown in Fig. 8. They were inferred from the IN6 data with the iterative Bayesian least-squares fitting procedure implemented in the nuclear data code CONRAD [26].

TABLE I. Partial phonon density of states of uranium in UO_2 (in 1/eV) as a function of the energy transfer (in meV).

ε	300 K	350 K	420 K	600 K	900 K	1200 K	1675 K
0.0	0.00	0.00	0.00	0.00	0.00	0.00	0.00
0.4	0.04	0.04	0.05	0.05	0.05	0.06	0.07
0.8	0.09	0.10	0.11	0.12	0.14	0.14	0.17
1.2	0.21	0.22	0.23	0.25	0.27	0.29	0.35
1.6	0.34	0.36	0.38	0.41	0.45	0.48	0.60
2.0	0.54	0.56	0.58	0.62	0.68	0.73	0.92
2.4	0.76	0.79	0.81	0.88	0.95	1.03	1.32
2.8	1.04	1.06	1.09	1.18	1.27	1.37	1.76
3.2	1.34	1.38	1.42	1.53	1.67	1.82	2.34
3.6	1.72	1.76	1.80	1.95	2.14	2.32	2.98
4.0	2.13	2.19	2.25	2.44	2.68	2.91	3.75
4.4	2.63	2.69	2.76	2.99	3.28	3.57	4.61
4.8	3.16	3.24	3.32	3.60	3.96	4.31	5.54
5.2	3.76	3.85	3.94	4.28	4.70	5.12	6.62
5.6	4.41	4.52	4.63	5.03	5.52	6.02	7.77
6.0	5.13	5.26	5.40	5.87	6.47	7.08	9.20
6.4	5.96	6.11	6.27	6.84	7.55	8.28	10.77
6.8	6.88	7.07	7.26	7.94	8.79	9.67	12.60
7.2	7.95	8.15	8.38	9.20	10.23	11.32	14.85
7.6	9.13	9.41	9.69	10.67	11.94	13.26	17.38
8.0	10.59	10.89	11.23	12.42	13.95	15.57	20.66
8.4	12.22	12.62	13.02	14.48	16.33	18.31	24.28
8.8	14.24	14.66	15.17	16.92	19.25	21.77	29.31
9.2	16.44	17.04	17.72	19.98	23.00	26.41	57.94
9.6	19.42	20.07	20.99	23.88	28.17	32.87	86.58
10.0	22.67	23.84	25.49	30.13	38.80	54.27	115.21
10.4	28.32	30.00	33.61	43.52	70.60	106.01	143.85
10.8	34.53	43.29	54.88	82.52	119.74	155.99	168.72
11.2	79.97	88.46	99.39	128.41	151.31	181.70	178.35
11.6	131.02	133.48	136.45	151.63	174.24	168.26	133.20
12.0	150.29	151.72	159.85	166.04	149.31	128.01	97.96
12.4	167.45	166.22	165.31	135.43	116.40	96.11	75.51
12.8	131.03	125.79	118.44	104.97	89.31	74.83	62.55
13.2	95.81	96.22	92.21	82.33	69.63	62.03	53.72
13.6	78.82	76.86	73.23	65.42	57.51	53.72	51.88
14.0	62.46	61.53	58.48	53.64	50.51	51.21	50.51
14.4	50.56	49.55	47.96	46.54	47.83	50.38	49.71
14.8	40.53	41.82	42.21	43.85	47.16	49.45	48.78
15.2	38.60	39.35	40.28	43.13	46.83	48.84	47.69
15.6	37.53	38.85	40.24	43.52	46.43	47.86	46.25
16.0	39.06	40.00	40.96	43.53	45.55	46.33	44.71
16.4	40.59	40.91	41.65	43.11	44.03	45.35	50.79
16.8	40.97	40.81	40.87	41.72	43.06	50.06	57.68
17.2	39.49	39.43	39.37	40.70	46.93	58.79	66.81
17.6	37.67	37.70	38.34	43.12	56.02	70.11	75.69
18.0	35.67	37.55	40.31	50.10	69.41	80.44	84.35
18.4	39.19	42.44	47.10	66.72	81.03	90.77	78.03
18.8	47.29	55.58	65.27	81.00	92.65	83.47	67.41
19.2	73.76	76.20	81.20	95.01	85.50	69.78	52.75
19.6	92.72	91.08	95.80	87.84	69.81	54.07	39.30
20.0	102.41	98.94	89.02	70.25	53.03	39.91	28.56
20.4	86.46	77.78	68.92	52.86	38.71	29.17	21.38
20.8	60.24	56.30	49.97	38.22	28.19	22.17	16.92
21.2	42.03	38.82	34.96	28.13	21.64	17.92	15.13
21.6	27.10	26.61	25.40	21.83	17.77	15.94	13.97
22.0	21.75	21.36	20.34	18.12	15.95	14.93	13.64
22.4	18.21	18.11	17.37	16.44	14.94	13.49	12.60
22.8	16.41	16.49	16.10	15.13	13.47	12.85	10.21
23.2	16.24	16.04	15.24	13.79	11.54	10.44	7.51
23.6	16.43	14.40	13.65	12.42	10.38	7.70	4.61
24.0	14.50	13.67	12.67	10.29	7.58	5.28	3.03
24.4	12.01	11.19	10.08	7.61	5.33	3.68	1.79
24.8	8.28	7.98	7.30	5.72	4.06	2.85	1.51
25.2	6.28	6.18	5.71	4.59	3.32	2.29	1.36
25.6	5.55	5.26	4.83	3.84	2.91	1.98	1.38
26.0	4.82	4.57	4.22	3.50	2.62	2.03	1.46
26.4	4.10	4.20	3.93	3.20	2.60	2.13	1.56
26.8	4.00	3.95	3.70	3.21	2.73	2.29	1.79
27.2	3.99	3.90	3.71	3.35	2.94	2.59	2.08
27.6	4.12	4.03	3.88	3.61	3.34	3.00	2.53
28.0	4.35	4.28	4.17	4.04	3.91	3.63	2.92
28.4	4.69	4.69	4.66	4.67	4.70	4.20	3.23
28.8	5.35	5.37	5.38	5.62	5.41	4.54	3.25
29.2	6.14	6.30	6.40	6.54	5.69	4.59	3.14
29.6	7.48	7.52	7.51	7.09	5.92	4.53	2.81
30.0	8.72	8.54	8.28	7.32	5.75	4.14	2.48
30.4	9.50	8.91	8.41	7.19	5.33	3.66	2.16
30.8	9.76	9.03	8.36	6.71	4.75	3.20	1.91
31.2	9.43	8.75	7.89	6.06	4.18	2.84	1.74
31.6	8.66	8.00	7.13	5.35	3.71	2.57	1.60
32.0	7.72	7.11	6.31	4.75	3.36	2.36	1.47
32.4	6.78	6.25	5.59	4.29	3.08	2.18	1.38
32.8	5.94	5.57	5.04	3.92	2.85	2.03	1.29
33.2	5.43	5.08	4.61	3.62	2.65	1.90	1.21
33.6	4.98	4.67	4.25	3.37	2.48	1.79	1.14
34.0	4.61	4.34	3.95	3.15	2.33	1.68	1.07
34.4	4.31	4.05	3.70	2.96	2.20	1.59	1.02
34.8	4.02	3.79	3.47	2.78	2.07	1.50	0.96
35.2	3.79	3.57	3.27	2.63	1.96	1.43	0.92
35.6	3.57	3.37	3.09	2.49	1.86	1.36	0.88

TABLE I. (*Continued*.)

ε	300 K	350 K	420 K	600 K	900 K	1200 K	1675 K
36.0	3.38	3.19	2.92	2.36	1.78	1.30	0.84
36.4	3.20	3.02	2.77	2.25	1.70	1.24	0.81
36.8	3.03	2.87	2.64	2.15	1.62	1.19	0.77
37.2	2.89	2.74	2.52	2.06	1.56	1.14	0.75
37.6	2.76	2.62	2.41	1.97	1.49	1.10	0.72
38.0	2.65	2.51	2.31	1.89	1.44	1.07	0.69
38.4	2.54	2.41	2.22	1.82	1.39	1.03	0.67
38.8	2.44	2.31	2.13	1.76	1.34	0.99	0.64
39.2	2.34	2.23	2.06	1.70	1.30	0.95	0.61
39.6	2.26	2.15	1.99	1.64	1.25	0.91	0.58
40.0	2.19	2.08	1.93	1.58	1.20	0.87	0.54
40.4	2.12	2.01	1.86	1.52	1.15	0.82	0.50
40.8	2.05	1.94	1.79	1.47	1.09	0.76	0.47
41.2	1.97	1.87	1.73	1.40	1.02	0.71	0.42
41.6	1.90	1.80	1.66	1.33	0.95	0.65	0.34
42.0	1.83	1.73	1.58	1.24	0.89	0.56	0.27
42.4	1.75	1.64	1.48	1.16	0.80	0.45	0.19
42.8	1.63	1.53	1.38	1.07	0.68	0.33	0.15
43.2	1.52	1.43	1.30	0.95	0.52	0.25	0.13
43.6	1.44	1.33	1.18	0.79	0.38	0.20	0.11
44.0	1.32	1.19	1.02	0.60	0.30	0.18	0.10
44.4	1.15	1.00	0.81	0.45	0.25	0.16	0.09
44.8	0.91	0.76	0.58	0.35	0.22	0.14	0.07
45.2	0.63	0.56	0.46	0.30	0.19	0.12	0.07
45.6	0.50	0.44	0.37	0.27	0.17	0.10	0.06
46.0	0.40	0.37	0.33	0.24	0.15	0.09	0.06
46.4	0.37	0.34	0.29	0.21	0.13	0.09	0.07
46.8	0.33	0.30	0.26	0.18	0.12	0.09	0.07
47.2	0.29	0.26	0.23	0.16	0.12	0.10	0.08
47.6	0.25	0.23	0.20	0.15	0.12	0.10	0.09
48.0	0.22	0.20	0.18	0.14	0.13	0.11	0.10
48.4	0.20	0.18	0.17	0.15	0.14	0.13	0.11
48.8	0.18	0.18	0.17	0.16	0.15	0.14	0.12
49.2	0.18	0.18	0.17	0.17	0.17	0.16	0.14
49.6	0.19	0.19	0.19	0.18	0.19	0.18	0.15
50.0	0.20	0.20	0.20	0.20	0.21	0.20	0.17
50.4	0.22	0.22	0.22	0.23	0.23	0.22	0.19
50.8	0.24	0.24	0.25	0.26	0.26	0.25	0.21
51.2	0.27	0.27	0.27	0.29	0.29	0.27	0.23
51.6	0.30	0.30	0.31	0.32	0.32	0.30	0.26
52.0	0.33	0.34	0.34	0.35	0.35	0.34	0.29
52.4	0.37	0.37	0.38	0.39	0.38	0.38	0.31
52.8	0.41	0.41	0.42	0.43	0.43	0.43	0.31
53.2	0.45	0.46	0.46	0.47	0.49	0.45	0.26
53.6	0.49	0.50	0.50	0.53	0.55	0.44	0.21
54.0	0.54	0.55	0.56	0.59	0.58	0.39	0.12
54.4	0.60	0.61	0.62	0.67	0.58	0.30	0.06
54.8	0.66	0.68	0.71	0.71	0.52	0.20	0.02
55.2	0.75	0.78	0.78	0.72	0.42	0.10	0.00
55.6	0.86	0.85	0.83	0.67	0.28	0.04	0.00
56.0	0.92	0.90	0.83	0.55	0.15	0.01	0.00
56.4	0.96	0.88	0.76	0.39	0.06	0.00	0.00
56.8	0.89	0.78	0.62	0.23	0.02	0.00	0.00
57.2	0.76	0.61	0.43	0.09	0.00	0.00	0.00
57.6	0.53	0.40	0.24	0.03	0.00	0.00	0.00
58.0	0.31	0.19	0.10	0.01	0.00	0.00	0.00

TABLE I. (*Continued*.)

ε	300 K	350 K	420 K	600 K	900 K	1200 K	1675 K
58.4	0.09	0.07	0.03	0.00	0.00	0.00	0.00
58.8	0.03	0.02	0.01	0.00	0.00	0.00	0.00
59.2	0.00	0.00	0.00	0.00	0.00	0.00	0.00
59.6	0.00	0.00	0.00	0.00	0.00	0.00	0.00
60.0	0.00	0.00	0.00	0.00	0.00	0.00	0.01
60.4	0.00	0.00	0.00	0.00	0.00	0.00	0.02
60.8	0.00	0.00	0.00	0.00	0.00	0.01	0.04
61.2	0.00	0.00	0.00	0.00	0.00	0.02	0.07
61.6	0.00	0.00	0.00	0.00	0.00	0.04	0.12
62.0	0.00	0.00	0.00	0.00	0.01	0.09	0.18
62.4	0.00	0.00	0.00	0.00	0.04	0.15	0.26
62.8	0.00	0.00	0.00	0.01	0.08	0.22	0.36
63.2	0.00	0.00	0.00	0.03	0.15	0.32	0.48
63.6	0.00	0.00	0.01	0.07	0.23	0.44	0.59
64.0	0.00	0.01	0.03	0.13	0.34	0.60	0.70
64.4	0.01	0.03	0.07	0.23	0.47	0.77	0.78
64.8	0.04	0.08	0.14	0.34	0.65	0.94	0.86
65.2	0.11	0.17	0.25	0.47	0.85	1.08	0.94
65.6	0.22	0.28	0.37	0.66	1.07	1.18	1.01
66.0	0.34	0.42	0.52	0.89	1.27	1.29	1.06
66.4	0.49	0.57	0.72	1.15	1.43	1.41	1.05
66.8	0.66	0.80	0.98	1.42	1.57	1.47	1.03
67.2	0.94	1.08	1.28	1.64	1.70	1.50	1.01
67.6	1.25	1.42	1.59	1.83	1.82	1.52	0.99
68.0	1.63	1.75	1.86	1.99	1.90	1.50	0.95
68.4	1.94	2.02	2.08	2.15	1.94	1.47	0.89
68.8	2.21	2.24	2.25	2.30	1.95	1.43	0.82
69.2	2.40	2.42	2.45	2.37	1.92	1.37	0.76
69.6	2.58	2.63	2.65	2.43	1.88	1.30	0.70
70.0	2.84	2.84	2.73	2.42	1.82	1.23	0.66
70.4	3.05	2.93	2.81	2.37	1.75	1.16	0.62
70.8	3.15	3.01	2.81	2.31	1.67	1.10	0.59
71.2	3.14	2.98	2.75	2.25	1.59	1.04	0.57
71.6	3.06	2.91	2.69	2.17	1.51	0.98	0.54
72.0	3.00	2.85	2.63	2.07	1.42	0.93	0.53
72.4	2.95	2.78	2.53	1.96	1.33	0.89	0.52
72.8	2.85	2.67	2.41	1.83	1.26	0.86	0.52
73.2	2.71	2.52	2.26	1.71	1.20	0.84	0.51
73.6	2.51	2.34	2.10	1.61	1.16	0.82	0.49
74.0	2.32	2.16	1.95	1.53	1.12	0.79	0.43
74.4	2.14	2.01	1.83	1.46	1.07	0.72	0.35
74.8	2.02	1.90	1.74	1.40	1.01	0.64	0.24
75.2	1.91	1.81	1.66	1.33	0.93	0.54	0.13
75.6	1.82	1.72	1.58	1.25	0.84	0.44	0.06
76.0	1.73	1.64	1.50	1.16	0.75	0.37	0.01
76.4	1.66	1.56	1.43	1.10	0.70	0.34	0.00
76.8	1.60	1.51	1.37	1.05	0.67	0.33	0.00
77.2	1.55	1.47	1.34	1.03	0.66	0.32	0.00
77.6	1.54	1.45	1.32	1.02	0.66	0.32	0.00
78.0	1.53	1.44	1.32	1.02	0.66	0.32	0.00
78.4	1.54	1.44	1.31	1.01	0.64	0.32	0.00
78.8	1.49	1.39	1.27	0.98	0.62	0.30	0.00
79.2	1.39	1.34	1.23	0.94	0.61	0.30	0.00
79.6	1.16	1.34	1.23	0.94	0.61	0.30	0.00
80.0	0.00	0.00	0.00	0.00	0.00	0.00	0.00

TABLE II. Partial phonon density of states of oxygen in UO_2 (in 1/eV) as a function of the energy transfer (in meV).

ε	300 K	350 K	420 K	600 K	900 K	1200 K	1675 K
0.0	0.00	0.00	0.00	0.00	0.00	0.00	0.00
0.8	0.01	0.01	0.02	0.01	0.01	0.01	0.01
1.2	0.02	0.02	0.02	0.02	0.02	0.02	0.02
1.6	0.03	0.02	0.05	0.03	0.03	0.03	0.04
2.0	0.05	0.06	0.08	0.05	0.05	0.05	0.06
2.4	0.07	0.06	0.07	0.07	0.07	0.07	0.09
2.8	0.09	0.12	0.11	0.09	0.09	0.10	0.12
3.2	0.12	0.13	0.13	0.11	0.12	0.13	0.16
3.6	0.15	0.17	0.15	0.14	0.15	0.16	0.21
4.0	0.19	0.15	0.25	0.18	0.18	0.19	0.25
4.4	0.23	0.24	0.28	0.21	0.22	0.24	0.31
4.8	0.27	0.29	0.27	0.25	0.26	0.28	0.37
5.2	0.31	0.34	0.34	0.29	0.31	0.33	0.43
5.6	0.36	0.39	0.47	0.34	0.35	0.38	0.49
6.0	0.41	0.44	0.44	0.39	0.40	0.43	0.56
6.4	0.47	0.51	0.50	0.44	0.46	0.49	0.64
6.8	0.53	0.57	0.53	0.49	0.52	0.55	0.73
7.2	0.59	0.68	0.69	0.56	0.59	0.63	0.82
7.6	0.67	0.64	0.71	0.63	0.66	0.70	0.93
8.0	0.75	0.76	0.80	0.70	0.74	0.79	1.04
8.4	0.83	0.86	0.93	0.78	0.82	0.88	1.16
8.8	0.93	1.06	1.01	0.87	0.91	0.97	1.28
9.2	1.03	1.15	1.17	1.09	1.17	1.28	1.60
9.6	1.16	1.17	1.24	1.32	1.42	1.58	1.93
10.0	1.40	1.54	1.49	1.54	1.68	1.88	2.26
10.4	1.70	1.64	1.71	1.76	1.93	2.18	2.59
10.8	1.68	1.88	1.68	1.71	1.89	2.13	2.51
11.2	1.57	1.52	1.68	1.62	1.77	2.00	2.44
11.6	1.21	1.25	1.33	1.36	1.59	1.86	2.38
12.0	0.96	0.92	1.08	1.16	1.44	1.71	2.32
12.4	0.85	0.89	0.95	1.10	1.55	1.97	2.26
12.8	0.79	0.84	0.95	1.02	1.45	1.84	2.12
13.2	0.76	0.79	0.88	0.97	1.38	1.75	2.00
13.6	0.75	0.79	0.89	0.95	1.36	1.75	2.01
14.0	0.74	0.80	0.80	0.95	1.37	1.77	2.04
14.4	0.74	0.73	0.82	0.96	1.40	1.82	2.10
14.8	0.75	0.72	0.78	0.98	1.43	1.87	2.16
15.2	0.76	0.80	0.81	1.00	1.47	1.92	2.22
15.6	0.77	0.81	0.91	1.05	1.54	1.98	2.28
16.0	0.79	0.85	0.99	1.11	1.61	2.07	2.35
16.4	1.16	1.25	1.29	1.36	1.76	2.20	2.41
16.8	1.53	1.60	1.58	1.72	2.08	2.41	2.61
17.2	1.89	1.93	2.11	2.09	2.52	2.93	3.20
17.6	2.28	2.32	2.40	2.50	3.01	3.54	3.91
18.0	2.68	2.77	2.85	3.01	3.62	4.26	4.74
18.4	3.31	3.39	3.48	3.66	4.34	5.05	5.55
18.8	4.00	3.91	4.11	4.41	5.14	5.85	6.34
19.2	4.83	4.99	4.90	5.20	5.92	6.55	6.85
19.6	5.64	5.89	5.67	5.95	6.61	7.03	7.24
20.0	6.40	6.43	6.32	6.59	7.10	7.28	7.36
20.4	7.01	7.18	7.10	7.09	7.38	7.48	7.37
20.8	7.52	7.26	6.99	7.44	7.56	7.46	7.29
21.2	7.74	7.60	7.77	7.65	7.61	7.50	7.54
21.6	7.88	7.99	7.78	7.72	7.67	7.72	7.84
22.0	7.82	7.62	7.95	7.82	7.84	8.01	8.15
22.4	7.86	7.81	8.16	8.00	8.11	8.32	8.46
22.8	8.10	8.12	7.91	8.23	8.42	8.64	8.77
23.2	8.38	8.28	8.31	8.52	8.76	8.96	9.07
23.6	8.69	8.75	8.77	8.86	9.10	9.27	9.38
24.0	9.07	8.99	9.28	9.21	9.41	9.58	9.69
24.4	9.45	9.24	9.69	9.54	9.73	9.89	10.00
24.8	9.77	9.89	9.88	9.86	10.03	10.20	10.30
25.2	10.09	10.28	10.32	10.17	10.34	10.57	10.93
25.6	10.40	10.43	10.67	10.48	10.67	11.18	12.06
26.0	10.71	10.83	10.96	10.79	11.10	12.14	13.18
26.4	11.03	11.17	11.08	11.13	11.84	13.26	14.30
26.8	11.34	11.52	11.45	11.63	12.88	14.43	15.42
27.2	11.76	11.65	12.27	12.50	14.06	15.61	16.55
27.6	12.73	12.96	12.97	13.59	15.31	16.80	17.67
28.0	13.87	13.82	14.25	14.87	16.58	18.00	18.79
28.4	15.23	15.34	15.54	16.20	17.87	19.20	19.92
28.8	16.62	16.54	17.01	17.56	19.18	20.40	21.03
29.2	18.01	18.53	18.60	18.96	20.49	21.56	22.15
29.6	19.48	19.36	19.48	20.38	21.75	22.59	22.64
30.0	20.94	21.26	21.64	21.77	22.91	23.27	22.98
30.4	22.43	22.67	22.80	23.06	23.81	23.49	22.87
30.8	23.76	23.91	24.06	24.16	24.37	23.53	22.57
31.2	24.95	24.86	25.28	24.96	24.43	23.28	22.07
31.6	25.66	25.89	25.25	25.36	24.40	22.82	21.61
32.0	26.21	25.99	25.29	25.43	24.09	22.29	21.16
32.4	26.14	25.92	25.51	25.38	23.59	21.82	20.91
32.8	25.96	25.35	25.37	24.99	23.01	21.44	20.69
33.2	25.51	24.90	25.60	24.45	22.47	21.18	20.54
33.6	24.94	24.93	24.74	23.83	22.05	20.94	20.39
34.0	24.27	24.18	23.77	23.22	21.75	20.76	20.24
34.4	23.64	23.56	23.41	22.76	21.49	20.62	20.27
34.8	23.03	23.01	22.66	22.42	21.25	20.55	20.36
35.2	22.74	22.42	22.86	22.12	21.05	20.48	20.73
35.6	22.46	22.19	22.01	21.85	20.89	20.55	21.11
36.0	22.18	22.21	22.56	21.58	20.80	20.80	21.54
36.4	21.90	21.98	21.25	21.36	20.79	21.14	21.89
36.8	21.63	21.54	21.48	21.19	20.81	21.50	22.18
37.2	21.42	21.36	21.20	21.11	20.98	21.83	22.30
37.6	21.25	21.11	21.07	21.06	21.22	22.08	22.37
38.0	21.19	21.29	20.86	21.05	21.49	22.22	22.32
38.4	21.15	20.96	20.67	21.10	21.75	22.33	22.27
38.8	21.18	21.51	21.40	21.24	21.95	22.39	22.23
39.2	21.25	21.30	21.07	21.42	22.12	22.48	22.22
39.6	21.36	21.42	21.41	21.63	22.36	22.54	22.23
40.0	21.51	21.57	21.76	21.84	22.67	22.59	22.30
40.4	21.69	22.03	21.93	22.13	22.93	22.62	22.39
40.8	21.89	22.50	22.05	22.65	23.07	22.63	22.59
41.2	22.36	23.16	22.74	23.19	23.00	22.73	22.82
41.6	23.26	23.22	23.44	23.52	22.94	22.83	23.12
42.0	23.73	23.86	23.76	23.52	23.00	22.94	23.38
42.4	23.98	24.11	23.68	23.26	22.89	22.95	23.62
42.8	23.79	23.68	23.87	23.22	22.64	22.84	23.72
43.2	23.44	23.24	23.15	22.79	22.15	22.57	23.76
43.6	22.58	22.51	22.01	21.78	21.30	22.42	23.56
44.0	20.88	20.75	20.49	20.19	20.62	22.19	23.48
44.4	18.09	18.48	18.54	18.72	20.25	21.92	23.55
44.8	17.34	17.09	17.14	18.13	19.80	21.47	22.88
45.2	16.60	17.25	17.22	17.89	19.64	21.10	22.21
45.6	16.79	17.30	17.16	17.85	19.58	21.26	22.39
46.0	16.97	17.62	17.57	18.35	20.40	21.77	22.56
46.4	19.69	19.72	19.79	20.10	21.37	22.22	22.74

TABLE II. (*Continued.*)

ε	300 K	350 K	420 K	600 K	900 K	1200 K	1675 K
46.8	21.63	21.68	21.43	21.26	21.85	22.24	22.91
47.2	22.77	22.75	22.76	22.05	22.33	22.22	22.12
47.6	22.70	22.44	22.52	22.42	22.18	22.02	21.89
48.0	22.22	22.09	21.85	21.97	21.76	21.78	21.84
48.4	21.42	21.29	21.52	21.34	21.36	21.67	21.90
48.8	20.77	20.71	20.92	20.90	21.31	21.75	22.06
49.2	20.54	20.37	20.51	20.93	21.70	22.28	22.49
49.6	20.56	20.85	20.68	21.25	21.78	22.50	22.95
50.0	20.82	20.93	21.05	21.82	22.18	22.91	23.43
50.4	21.41	21.55	22.12	22.47	22.78	23.80	24.56
50.8	22.10	22.73	22.30	23.16	23.60	24.90	25.87
51.2	22.78	22.82	23.24	23.88	24.54	26.10	27.30
51.6	23.46	23.60	24.13	24.65	25.57	27.66	29.44
52.0	24.14	23.95	24.78	25.52	26.83	30.01	33.15
52.4	24.82	24.95	25.69	26.71	28.64	33.19	37.05
52.8	25.50	26.22	26.59	28.55	31.27	36.80	41.10
53.2	26.92	27.92	28.57	31.45	34.78	40.64	42.90
53.6	28.81	30.39	31.91	35.79	39.12	43.55	44.21
54.0	33.72	35.25	36.46	40.81	43.47	45.28	45.17
54.4	39.48	41.58	42.07	45.27	46.22	46.54	44.84
54.8	46.78	46.45	46.97	48.32	47.80	46.23	42.15
55.2	51.72	51.76	50.88	50.07	48.52	43.32	39.14
55.6	55.17	53.09	52.15	49.87	46.22	39.19	35.92
56.0	53.24	51.53	50.47	46.70	41.48	34.11	30.03
56.4	49.78	47.69	45.99	40.70	34.72	27.12	23.69
56.8	41.38	39.09	37.19	32.72	26.53	20.00	16.98
57.2	31.52	30.01	28.03	23.60	18.15	13.48	11.51
57.6	19.42	18.90	17.58	14.95	11.01	8.80	7.93
58.0	10.37	9.81	9.52	7.99	5.88	5.59	4.64
58.4	2.90	3.51	3.56	3.48	3.32	2.90	1.50
58.8	1.08	1.24	1.27	1.63	1.47	1.06	0.76
59.2	0.00	0.20	0.38	0.66	0.54	0.48	0.29
59.6	0.00	0.06	0.11	0.25	0.27	0.31	0.13
60.0	0.00	0.01	0.06	0.11	0.19	0.18	0.23
60.4	0.00	0.01	0.02	0.07	0.15	0.24	0.66
60.8	0.00	0.02	0.03	0.06	0.16	0.53	1.48
61.2	0.00	0.01	0.02	0.05	0.27	1.13	2.46
61.6	0.00	0.01	0.04	0.08	0.53	1.88	4.04
62.0	0.00	0.03	0.07	0.14	0.94	3.10	5.57
62.4	0.00	0.05	0.10	0.28	1.61	4.46	6.86
62.8	0.08	0.16	0.28	0.57	2.60	5.71	8.22
63.2	0.26	0.44	0.66	1.12	3.73	6.88	9.64

TABLE II. (*Continued.*)

ε	300 K	350 K	420 K	600 K	900 K	1200 K	1675 K
63.6	0.82	0.98	1.28	1.91	4.83	8.10	11.92
64.0	1.51	1.74	2.14	2.89	5.84	9.60	14.49
64.4	2.50	2.80	3.04	3.85	6.86	11.60	17.32
64.8	3.45	3.74	3.99	4.73	8.05	13.94	19.75
65.2	4.25	4.51	4.91	5.60	9.49	16.83	21.05
65.6	5.06	5.40	5.67	6.55	11.28	20.20	21.48
66.0	5.85	6.29	6.54	7.66	13.44	22.21	21.12
66.4	6.90	7.20	7.70	8.97	16.69	22.98	19.69
66.8	8.02	8.67	9.11	10.54	21.15	23.09	17.93
67.2	9.41	9.84	10.69	12.50	24.13	21.64	15.56
67.6	11.02	12.11	13.48	16.19	25.48	19.45	13.39
68.0	13.09	14.71	16.95	21.42	25.67	16.72	11.63
68.4	17.55	19.41	21.15	25.68	24.04	14.32	10.23
68.8	23.78	24.93	25.56	28.02	21.09	12.37	9.09
69.2	29.06	28.36	28.91	28.64	17.76	10.84	8.20
69.6	33.36	31.32	29.93	26.61	15.07	9.62	7.37
70.0	30.18	28.58	27.30	22.78	12.91	8.59	6.74
70.4	26.29	24.18	23.46	18.82	11.28	7.75	6.07
70.8	21.14	20.50	18.61	15.75	9.96	7.00	5.33
71.2	17.38	16.86	15.90	13.39	8.86	6.23	4.89
71.6	14.49	14.11	13.22	11.62	7.95	5.66	4.66
72.0	12.54	11.92	11.61	10.16	7.12	5.28	4.42
72.4	10.81	10.40	10.35	9.05	6.47	4.97	4.19
72.8	9.58	9.39	9.04	8.08	5.98	4.70	4.03
73.2	8.51	8.20	7.84	7.29	5.58	4.46	3.82
73.6	7.66	7.34	7.22	6.67	5.22	4.20	3.54
74.0	6.97	6.70	6.42	6.15	4.90	3.92	3.29
74.4	6.37	6.22	6.20	5.70	4.57	3.66	3.06
74.8	5.89	5.71	5.51	5.30	4.28	3.45	2.98
75.2	5.45	5.29	5.00	4.95	4.04	3.34	2.93
75.6	5.11	5.06	5.00	4.66	3.88	3.27	2.92
76.0	4.82	4.88	4.55	4.43	3.75	3.15	2.67
76.4	4.59	4.55	4.56	4.25	3.56	2.79	2.12
76.8	4.42	4.31	4.40	4.05	3.22	2.19	1.33
77.2	4.29	4.11	3.94	3.78	2.71	1.47	0.44
77.6	4.05	3.81	3.94	3.45	2.23	1.00	0.18
78.0	3.74	3.61	3.68	3.10	1.88	0.75	0.00
78.4	3.16	2.83	2.96	2.63	1.56	0.61	0.00
78.8	2.47	2.33	2.28	2.13	1.26	0.49	0.00
79.2	1.66	1.62	1.86	1.92	1.17	0.48	0.00
79.6	0.98	1.20	1.29	1.92	1.17	0.48	0.00
80.0	0.00	0.00	0.00	0.00	0.00	0.00	0.00

[1] I. M. Thorson and B. C. Haywood, Scattering law for UO_2, in *Proceedings of a Symposium on Inelastic Scattering of Neutrons in Solids and Liquids*, IAEA Rep. No. STI/PUB/62 (IAEA, Vienna, 1963), Vol. 2, p. 213.

[2] Purohit *et al.*, Inelastic neutron scattering in metal hydrides, UC and UO_2, and applications of the scattering law, in *Proceedings of a Symposium on Neutron Thermalization and Reactor Spectra*, IAEA Rep. No. STI/PUB/160 (IAEA, Vienna, 1967), Vol. 1, p. 407.

[3] D. Brown *et al.*, Nucl. Data Sheets **148**, 1 (2018).

[4] A. I. Hawari *et al.*, Nucl. Data Sheets **118**, 172 (2014).

[5] G. Kresse and J. Furthmuller, Comput. Matter. Sci. **6**, 15 (1996).

[6] J. L. Wormald and A. I. Hawari, Am. Nucl. Soc. **115**, 1156 (2016).

[7] G. Dolling, R. A. Cowley, and A. D. Woods, Can. J. Phys. **43**, 1397 (1965).

[8] G. Noguere, P. Maldonado, and C. de Saint Jean, Eur. Phys. J. Plus **133**, 177 (2018).

[9] Y. Yun, D. Legut, and P. M. Oppeneer, J. Nucl. Mater. **426**, 109 (2012).

[10] P. Maldonado, L. Paolasini, P. M. Oppeneer, T. R. Forrest, A. Prodi, N. Magnani, A. Bosak, G. H. Lander, and R. Caciuffo, Phys. Rev. B **93**, 144301 (2016).
[11] A. Togo, https://atztogo.github.io/phonopy/.
[12] J. W. L. Pang, W. J. L. Buyers, A. Chernatynskiy, M. D. Lumsden, B. C. Larson, and S. R. Phillpot, Phys. Rev. Lett. **110**, 157401 (2013).
[13] J. W. L. Pang, A. Chernatynskiy, B. C. Larson, W. J. L. Buyers, D. L. Abernathy, K. J. McClellan, and S. R. Phillpot, Phys. Rev. B **89**, 115132 (2014).
[14] M. S. Bryan, J. W. L. Pang, B. C. Larson, A. Chernatynskiy, D. L. Abernathy, K. Gofryk, and M. E. Manley, Phys. Rev. Mater. **3**, 065405 (2019).
[15] B. Becker *et al.*, Ann. Nucl. Ener. **36**, 281 (2009).
[16] E. Brun *et al.*, Ann. Nucl. Ener. **82**, 151 (2015).
[17] R. E. MacFarlane, The NJOY nuclear data processing system, Version 2016, Los Alamos National Laboratory Rep. No. LA-UR-17-20093 (Los Alamos National Laboratory, Los Alamos, 2019).
[18] L. Van Hove, Phys. Rev. **95**, 249 (1954).
[19] A. W. Solbrig, Am. J. Phys. **29**, 257 (1961).
[20] A. Sjolander, Arkiv Fysik **14**, 315 (1958).
[21] S. Xu *et al.*, Measurement of the double-differential neutron cross section of UO_2 from room temperature to hot full power conditions, in *Proceedings of the 11th International Conference on Nuclear Criticality Safety, Paris, France, 2019* (American Nuclear Society, La Grange Park, 2019).
[22] G. Noguere *et al.*, EPJ Web Conf. **239**, 14003 (2002).
[23] J. Dawidowski *et al.*, Nucl. Instrum. Meth. B **195**, 389 (2002).
[24] A. A. Maradudin and A. E. Fein, Phys. Rev. **128**, 2589 (1962).
[25] J. J. J. Kokkedee, Physica **28**, 374 (1962).
[26] P. Archier *et al.*, Nucl. Data Sheets **118**, 488 (2014).
[27] T. Feng, X. Yang, and X. Ruan, J. Appl. Phys. **124**, 145101 (2018).
[28] M. T. Hutchings, J. Chem. Soc., Faraday Trans. **83**, 1083 (1987).
[29] A. S. Poplavnoi and T. P. Fedorova, Moscow Univ. Phys. Bull. **65**, 397 (2010).
[30] B. T. M. Willis, J. Phys. France **25**, 431 (1964).
[31] L. Desgranges *et al.*, Inorg. Chem. **56**, 321 (2017).
[32] Y. Ma *et al.*, Inorg. Chem. **57**, 7064 (2017).
[33] H. Serizawa *et al.*, J. Alloys Compd. **271–273**, 386 (1998).
[34] P. Ruello *et al.*, J. Phys. Chem. Solids **66**, 823 (2005).
[35] B. T. M. Willis, Proc. R. Soc. London A **274**, 122 (1963).
[36] B. T. M. Willis, Proc. R. Soc. London A **274**, 134 (1963).
[37] A. Albinati, Acta Cryst. A **36**, 265 (1980).

C. Long résumé en français

C.1. Introduction

L'énergie nucléaire contribue à plus de 10% de la production mondiale d'électricité en 2019 (Schneider, Froggatt, Hazemann, et al. 2020), ce qui contribue à réduire considérablement les émissions de gaz à effet de serre. L'énergie est libérée principalement grâce à la fission de nucléides lourds (par exemple, l'uranium) induite par les neutrons. Par conséquent, les comportements des neutrons doivent être bien compris et contrôlés afin d'exploiter les réacteurs nucléaires de manière sûre et sécurisée. A cet effet, des codes de calcul neutroniques ont été développés au Commissariat à l'Énergie Atomique et aux Énergies Alternatives et aux Énergies Alternatives (CEA), comme le code Monte-Carlo de transport des neutrons TRIPOLI-4® (E. Brun, F. Damian, Diop, et al. 2015). Les simulations neutroniques réalisées à l'aide du code TRIPOLI-4® reposent sur la connaissance des sections efficaces des neutrons, qui permettent de quantifier les interactions neutron-noyau dans les réacteurs nucléaires.

Pour la plupart des réacteurs nucléaires, l'uranium a été utilisé comme combustible sous forme de dioxyde d'uranium (UO_2). Dans les simulations Monte-Carlo de transport de neutrons, la section efficace totale est une grandeur indispensable pour calculer la distance parcourue par le neutron entre deux interactions. Les sections efficaces neutroniques totales de l'uranium (U≡^{238}U) et de l'oxygène (O≡^{16}O) dans UO_2 en fonction de l'énergie des neutrons incidents E sont la somme des sections efficaces partielles des neutrons :

$$\sigma_{t_{\mathrm{U}}}(E) = \sigma_{\gamma_{\mathrm{U}}}(E) + \sigma_{f_{\mathrm{U}}}(E) + \sigma_{n_{\mathrm{U}}}(E), \tag{C.1}$$

$$\sigma_{t_{\mathrm{O}}}(E) = \sigma_{\gamma_{\mathrm{O}}}(E) + \sigma_{n_{\mathrm{O}}}(E), \tag{C.2}$$

où les indices γ, f et n sont respectivement liés aux réactions de capture radiative, de fission et de diffusion. Dans les simulations neutroniques des réacteurs nucléaires, les réactions de capture, de fission et de diffusion induites par les neutrons sur l'uranium et l'oxygène sont calculées dans le cadre de la théorie de la matrice R (Lane and Thomas 1958) et Doppler élargi à une température donnée T avec un modèle de gaz libre –ou *free gas model*–(FGM), dont la validité du formalisme est discutée dans Ref. (Noguere, Maldonado, and De Saint Jean 2018).

Dans ce travail, une attention particulière est accordée à la section efficace de diffusion $\sigma_n(E)$ en fonction de la température. Trois modèles distincts sont implémentés en routine dans le code Monte-Carlo de transport de neutrons TRIPOLI-4®, pour traiter la diffusion élastique neutron-noyau en fonction de l'énergie des neutrons incidents E (Coveyou, Bate, and Osborn 1956; Zoia, Emeric Brun, Jouanne, et al. 2013). Pour E inférieur à quelques eV, la section efficace de diffusion des neutrons doit être divisée en une partie élastique et une partie inélastique, avec des termes cohérents et incohérents. Dans le cas des réactions de diffusion induite par les neutrons sur UO_2, la section efficace élastique incohérente est négligeable et la section efficace de diffusion

des neutrons se réduit à :

$$\sigma_{n_j}(E) = \sigma_{\text{coh}}^{\text{el}}(E) + \sigma_j^{\text{inel}}(E), \tag{C.3}$$

où j représente les atomes d'uranium ou d'oxygène dans UO_2. Le premier terme de l'Eq. (C.3) est la section efficace de diffusion élastique cohérente qui est liée à la structure cristalline de UO_2. Le deuxième terme est la section efficace de diffusion inélastique qui peut être calculée en intégrant sa forme doublement différentielle sur l'énergie diffusée E_f et l'angle solide Ω :

$$\sigma_j^{\text{inel}}(E) = \iint \frac{\mathrm{d}^2\sigma_j^{\text{inel}}(E)}{\mathrm{d}\Omega \mathrm{d}E_f} \mathrm{d}E_f \mathrm{d}\Omega, \tag{C.4}$$

où $\frac{\mathrm{d}^2\sigma_j^{\text{inel}}(E)}{\mathrm{d}\Omega \mathrm{d}E_f}$ est la section efficace doublement différentielle –ou *double differential cross section*–(DDXS) inélastique de l'atome j dans UO_2, qui peut être obtenu par la fonction de diffusion ou le facteur de structure dynamique $S_j(\vec{Q}, \omega)$. $S_j(\vec{Q}, \omega)$, en fonction du transfert de quantité de mouvement $\hbar\vec{Q}$ et du transfert d'énergie $\hbar\omega$, rend compte des comportements vibratoires atomiques de l'atome j (Squires 2012; Schober 2014). La fonction de diffusion sans dimension ou facteur de structure dynamique $S(\alpha, \beta)$ est adoptée dans la bibliothèque de données de diffusion neutronique utilisée par le code TRIPOLI-4®, à la place de $S(\vec{Q}, \omega)$. $S(\alpha, \beta)$ est appelé lois de diffusion thermique –ou *thermal scattering laws*–(TSLs) avec α et β représentant respectivement la quantité de mouvement et les transferts d'énergie sans dimension. Les $\sigma_{\text{coh}}^{\text{el}}(E)$ et $S_j(\alpha, \beta)$ dépendant de la température de UO_2 peuvent être calculés à partir de les spectres de phonon –ou *phonon density of states*–(PDOS) qui caractérisent les mouvements atomiques et la dynamique structurale de UO_2. Les $\sigma_{\text{coh}}^{\text{el}}(E)$ et $S_j(\alpha, \beta)$ calculés sont stockés dans des fichiers ascii en suivant le format ENDF-6 conditions requises pour TSLs (Trkov and D. A. Brown 2018), pour préparer les bibliothèques de données de diffusion de neutrons utilisées par TRIPOLI-4®.

Pour E entre quelques eV et $400 k_B T$ (gamme d'énergie épithermale), où k_B est la constante de Boltzmann et T représente la température du matériau, l'algorithme *Sampling the Velocity of the Target nucleus* (SVT) est utilisé dans les simulations Monte-Carlo, qui échantillonnent les vitesses des nucléides cibles à partir d'une distribution Maxwell-Boltzmann (M-B) (Coveyou, Bate, and Osborn 1956; Lux 2018). Néanmoins, le traitement SVT pour les nucléides lourds avec de fortes résonances de diffusion (e.g., ^{238}U) serait inadéquat (Dagan and Broeders 2006; Becker, R. Dagan, and Lohnert 2009). Des méthodes de correction stochastique telles que *Doppler Broadening Rejection Correction* (DBRC) (Rothenstein and R. Dagan 1995) et *Weight Correction Method* (WCM) (Lee, Smith, and Rhodes 2009) ont été adoptées dans le code TRIPOLI-4® pour améliorer l'algorithme SVT.

Pour E au-dessus de $400 k_B T$, l'approximation *Asymptotic Kernel* (AK) est utilisée dans le code TRIPOLI-4®. Le traitement AK considère les nucléides cibles au repos, lorsque les vitesses des nucléides sont négligeables par rapport aux vitesses des neu-

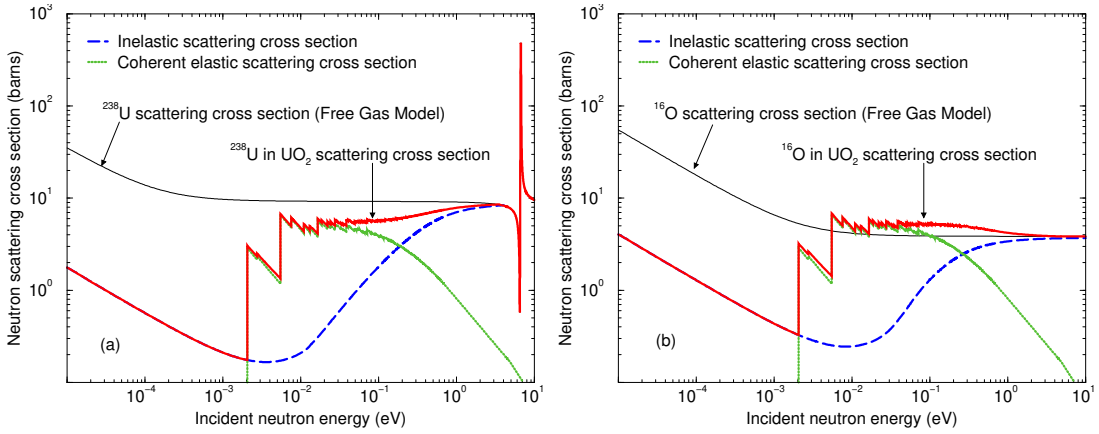

Figure C.1.: Sections efficaces de diffusion des neutrons de ^{238}U dans UO_2 (a) et ^{16}O dans UO_2 (b) en fonction de l'énergie neutronique incidente à $T = 300$ K. Les sections efficaces de diffusion cohérente élastique et inélastique ont été calculées avec le code CINEL. Les sections efficaces de neutrons calculées avec le modèle de gaz libre (FGM) sont tracées à des fins de comparaison. La structure observée à 6.6 eV correspond à la première résonance de l'onde s ^{238}U.

trons incidents.

Les composantes de la section efficace de diffusion des neutrons (Eq. (C.3)) sont représentées sur la Fig. C.1 en fonction de E pour $T = 300$ K. La comparaison avec les sections efficaces de diffusion élastique des neutrons calculées avec une approximation FGM (courbe noire) met en évidence les grandes différences entre le formalisme (courbe rouge), qui peuvent introduire des biais dans les calculs neutroniques. Par exemple, l'utilisation de l'approximation FGM, au lieu de $S(\alpha,\beta)$ en dessous de quelques eV, peut impliquer un biais d'environ 100 pcm (0,1%) sur le facteur de multiplication des neutrons k_{eff} calculé pour les benchmarks intégraux avec le combustible UOX. Un tel biais ne peut pas être considéré comme une source d'incertitude négligeable, étant donné que l'incertitude totale sur le k_{eff} calculé devrait être inférieure à 500 pcm (0,5%). Par conséquent, la validation des effets cristallins au niveau microscopique est toujours une nécessité pour motiver une mise à jour du traitement de diffusion des neutrons dans les schémas de simulation neutronique.

Les effets de liaison des atomes peuvent être pris en compte par la température effective T_{eff} (Lamb 1939). Dans le domaine de l'énergie épithermale où les lois de diffusion thermique ne sont pas disponibles, le rôle important de T_{eff} doit être étudié.

Le premier point clé de la présente étude est de préparer et valider les sections efficaces cohérentes de diffusion élastique des neutrons et les lois de diffusion thermique de UO_2 en fonction de la température au format ENDF-6 qui peuvent être utilisées dans le code Monte-Carlo de transport TRIPOLI-4®.

Le deuxième enjeu est d'étudier les traitements de diffusion des neutrons impliquant la température effective dans le domaine de l'énergie épithermale en utilisant

le code TRIPOLI-4®.

Premièrement, le développement de l'outil informatique CINEL est brièvement présenté. CINEL a été développé dans ce travail pour préparer les TSLs des matériaux au format ENDF-6. Les validations numériques de CINEL effectuées en utilisant divers types de matériaux cristallins sont également présentées.

Ensuite, le code Monte-Carlo de transport de neutrons TRIPOLI-4® est utilisé pour simuler des données de diffraction de poudres neutroniques sur le dioxyde d'uranium stoechiométrique (UO_2) mesurées jusqu'à 1664 K avec le D4 et le D20 des diffractomètres de l'Institut Laue-Langevin (ILL). Les TSLs de UO_2 nécessaires à la simulation sont calculés en utilisant le code CINEL. Les performances des calculs de Monte-Carlo avec les TSLs tabulés sont illustrées par la comparaison entre les diagrammes de diffraction expérimentaux et simulés et les fonctions de distribution de paires atomiques.

La partie suivante est consacré à l'étude de la diffusion des neutrons avec des nucléides légers ayant une section efficace de diffusion des neutrons non résonante inférieure à 10 eV. Les formalismes de AK et de SVT sont revus et validés. Les validations numériques de plusieurs traitements de diffusion de neutrons avec le code TRIPOLI-4® sont effectuées à température ambiante pour ^{1}H dans H_2O et ^{16}O dans UO_2. Une attention particulière sera portée au rôle important de la température effective T_{eff}. Enfin, des conclusions générales et des perspectives sont données en fin de document.

C.2. Code de calcul des lois de diffusion thermique : CINEL

Cette partie présente l'outil de traitement de données CINEL. CINEL a été développé pour calculer les sections efficaces de diffusion de neutrons élastiques cohérentes et incohérentes de matériaux cristallins solides dans l'approximation cubique. Le module mis en œuvre pour remplir cette tâche est appelé Cubic. Un deuxième module nommé INELastic a été implémenté pour calculer les lois de diffusion thermiques $S(\alpha, \beta)$ en prenant en compte les accélérations de *graphics processing unit* (GPU).

CINEL est développé à Python en utilisant JupyterLab (Granger and Grout 2016). JupyterLab est une nouvelle génération d'interface utilisateur (Kluyver, Ragan-Kelley, Pérez, et al. 2016) qui est un outil open-source permettant de mélanger le code en direct, les textes, les équations mathématiques et les graphiques interactifs. Un exemple d'interface JupyterLab est donné à la Fig. C.2 pour illustration. Cet environnement de développement interactif facilite la vérification et la visualisation des résultats.

Pour améliorer les performances de CINEL, un compilateur *Just-in-Time* (JIT) nommé Numba (Lam, Pitrou, and Seibert 2015) est utilisé. Numba permet de réduire directement le temps de calcul en ajoutant directement des syntaxes simples de Python aux fonctions initiales sans les réécrire dans des langages de bas niveau. En outre, Numba prend en charge la programmation GPU de *Compute Unified Device Architecture* (CUDA), qui permet à CINEL de bénéficier de la puissante capacité informatique de GPU.

La programmation GPU a été introduite au début des années 2000 et a été développée énormément au cours des deux dernières décennies. Dans notre travail, l'utilisation

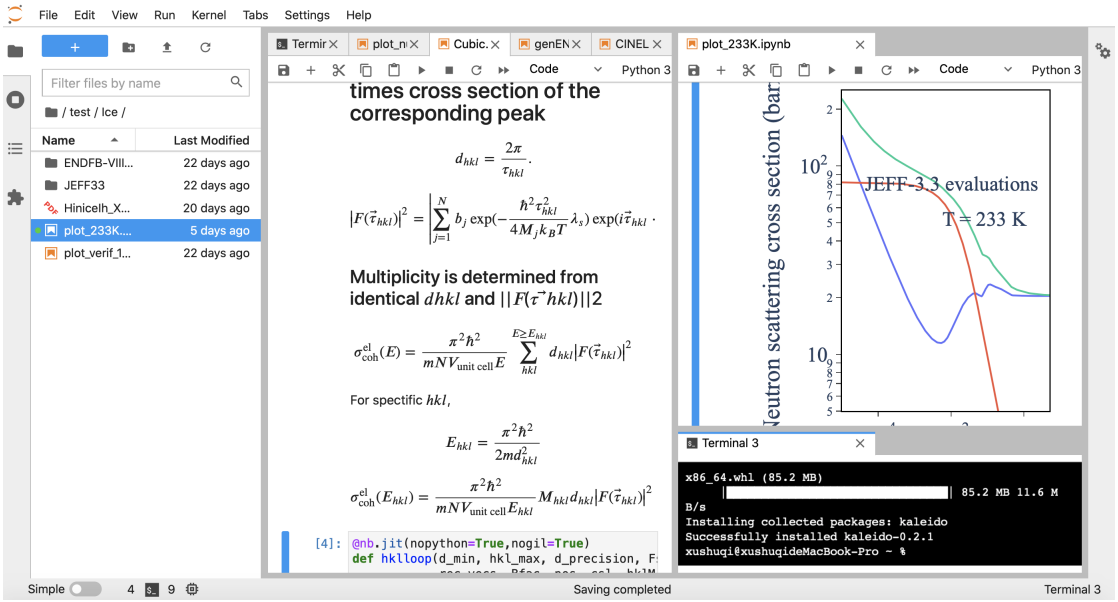

Figure C.2.: Interface de JupyterLab. Le code en direct, les textes, les équations mathématiques et les graphiques interactifs sont mélangés dans des Jupyter Notebooks qui sont intégrés à JupyterLab avec des blocs tels que le terminal et l'éditeur de texte.

de GPU permet d'accélérer le calcul de l'expansion de phonon. Pour tester l'accélération de GPU, les TSLs de l'hydrogène dans la molécule d'eau (^{1}H in H_2O) à la température ambiante a été calculée avec un ordre d'expansion de phonon $N_{\text{phonon}} = 2000$. Les comparaisons du temps de calcul sont présentées dans le Tableau C.1. Le GPU de haute performance permet de réduire considérablement le temps de calcul jusqu'à 2 minutes.

Table C.1.: Comparaison du temps de calcul des TSLs de ^{1}H in H_2O à la température ambiante avec un ordre d'expansion de phonon $N_{\text{phonon}} = 2000$.

	CPU	GPU K20	GPU K6000
GPU mémoire (gigabyte)	N/A	2	12
CUDA cores	N/A	384	2280
Temps de calcul	~ 3 h	~ 15 min	< 2 min

Les validations numériques de `CINEL` ont été effectuées en comparant les TSLs calculés de matériaux cristallins solides avec la base de données ENDF/B-VIII.0 (D. Brown, Chadwick, Capote, et al. 2018) et la librairie `NJOY-NCrystal` (Ramic, Jose Ignacio Marquez Damian, Thomas Kittelmann, et al. 2021). Quelques structures cristallines ont été étudiées: béryllium (^{9}Be) métal (hexagonal compact (HCP), groupe d'espace $P6_3/mmc$), fer (^{56}Fe) (cubique centré (BCC), groupe d'espace $Im\bar{3}m$), alu-

minium (^{27}Al) métal, dioxyde d'uranium (UO_2) et hydrure de lithium (LiH) (cubique à faces centrées (FCC), groupe d'espace $Fm\bar{3}m$), Hydrure de magnétisme (MgH_2) et deutéride de magnétisme (MgD_2) (structure tétragonale, groupe d'espace $P4_2/mnm$). La glace I_h est également étudié dans ce travail. Les entrées de `CINEL` ont été préparées à l'aide des quantités physiques disponibles dans la base de données ENDF/B-VIII.0 et de la librairie `NJOY-NCrystal`.

Le dioxyde d'uranium (UO_2) est le principal composant du combustible UOX. Dans la base de données ENDF/B-VIII.0, UO_2 est dans la structure fluorite idéale avec une symétrie $Fm\bar{3}m$. Le béryllium est un matériau important qui est largement utilisé comme modérateur et réflecteur de neutrons. L'hydrure de magnétisme (MgH_2) est un candidat potentiel pour les réflecteurs à neutrons froids (José Rolando Granada, Márquez Damián, Dawidowski, et al. 2021). Le deutéride de magnétisme (MgD_2) montre des améliorations sur le ralentissement des neutrons puisque la section efficace de capture des neutrons du deutérium est inférieure à celle de l'hydrogène. MgH_2 et MgD_2 partagent la même structure cristalline. En termes d'atomes dans la cellule unitaire, le béryllium métal dans la structure HCP a deux atomes, le fer dans la structure cristalline BCC a un seul atome, l'aluminium dans la structure cristalline FCC a un seul atome.

Les sections efficaces cohérentes et incohérentes de diffusion des neutrons élastiques et inélastiques ($\sigma^{\text{el}}_{\text{coh}}(E)$ et $\sigma^{\text{el}}_{\text{inc}}(E)$, et $\sigma^{\text{inel}}(E)$) d'une partie des matériaux étudiés calculés par `CINEL` sont comparés avec la base de données ENDF/B-VIII.0 et la librairie `NJOY-NCrystal` (C.3, C.4, C.5). Un excellent accord est obtenu pour $\sigma^{\text{el}}_{\text{coh}}(E)$, $\sigma^{\text{el}}_{\text{inc}}(E)$ et $\sigma^{\text{inel}}(E)$. $\sigma^{\text{el}}_{\text{coh}}(E)$ et $\sigma^{\text{el}}_{\text{inc}}(E)$ diminuent avec l'augmentation de la température T, tandis que $\sigma^{\text{inel}}(E)$ augmente avec T. Le premier pic de Bragg de UO_2 apparaît vers 2 meV, ce qui correspond à la diffraction des neutrons sur le plan (111).

C.3. Simulations Monte-Carlo d'expériences neutroniques pour UO_2 à l'ILL

L'objectif de cette partie est de montrer les performances des codes Monte-Carlo modernes de transport de neutrons pour revisiter l'analyse d'expériences de diffraction neutronique mesurées à des températures élevées, conçues à l'origine pour étudier les effets de la température sur l'agencement du réseau UO_2. En effet, si la structure de la fluorite (groupe d'espace $Fm\bar{3}m$) de UO_2 est bien établie à température ambiante, la compréhension de la relaxation inhabituelle avec l'augmentation de la température des atomes d'oxygène à partir de leurs positions régulières est encore en discussion. Parmi les quelques mesures de diffraction neutronique sur le dioxyde d'uranium stoechiométrique rapportées dans la littérature, nous avons sélectionné les travaux de Ruello (P. Ruello, Desgranges, Baldinozzi, et al. 2005) et Ma (Yue Ma 2017), dont les données sont toujours disponibles sur ILL de Grenoble (France). Les expériences ont été réalisées respectivement sur les diffractomètres D20 et D4. Ils ont consisté à mesurer le rendement de diffusion des neutrons dépendant de la température $Y^T_{\text{exp}}(\theta)$ en fonction de l'angle de diffusion θ. Les deux ensembles de données couvrent une

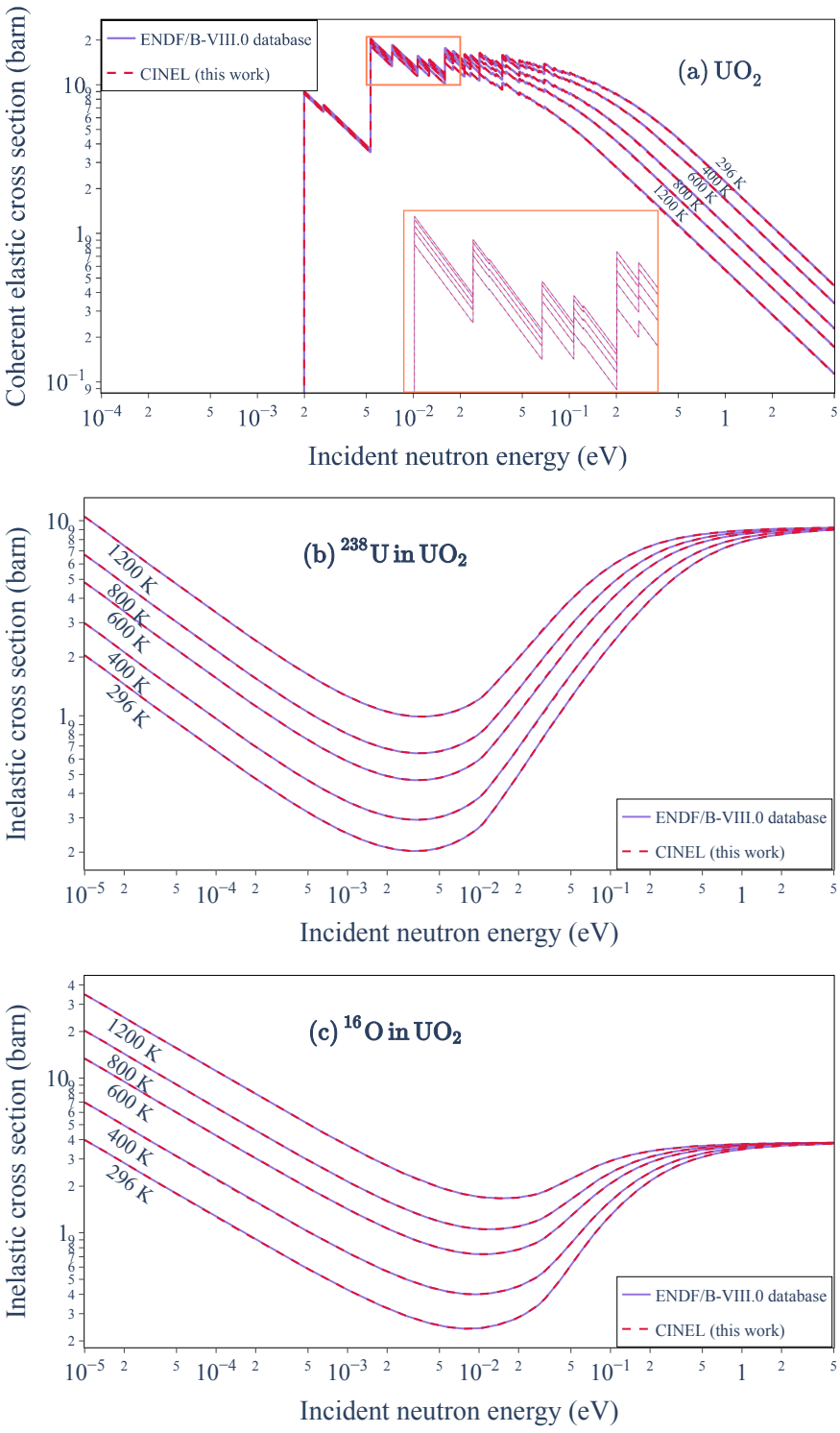

Figure C.3.: Comparaisons de la section efficace de diffusion cohérente élastique et inélastique calculée par `CINEL`de UO_2 (courbes en tirets) avec la base de données ENDF/B-VIII.0 (courbes pleines) de 296 à 1200 K. Les sections efficaces élastiques cohérentes les énergies sont zoomées entre 5 et 20 meV.

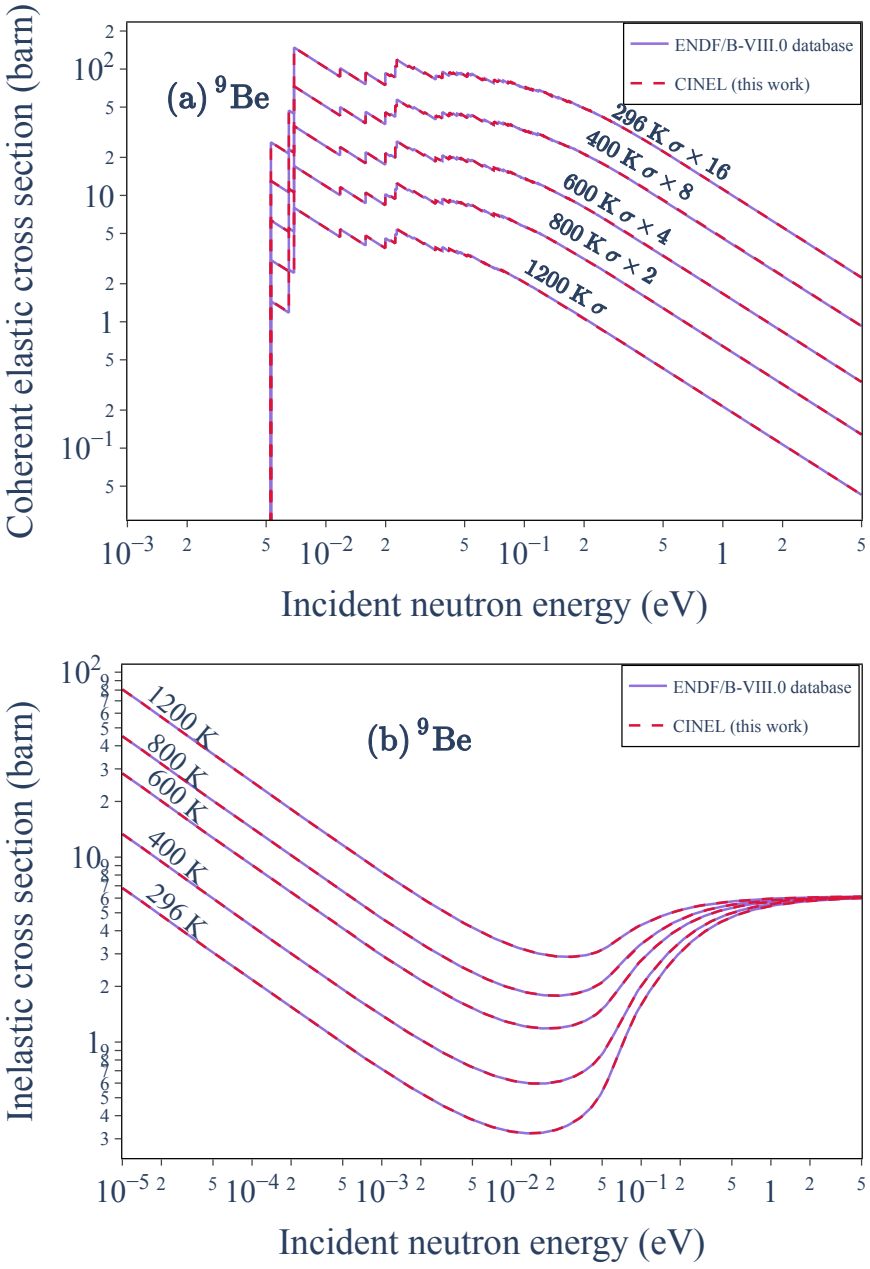

Figure C.4.: Comparaison des sections efficaces de diffusion élastique et inélastique cohérentes calculées par `CINEL`de ^{9}Be (courbes en tirets) avec la base de données ENDF/B-VIII.0 (courbes pleines) de 296 à 1200 K. Les sections efficaces élastiques cohérentes de la Fig. (a) sont multipliées par différents facteurs pour une meilleure visualisation.

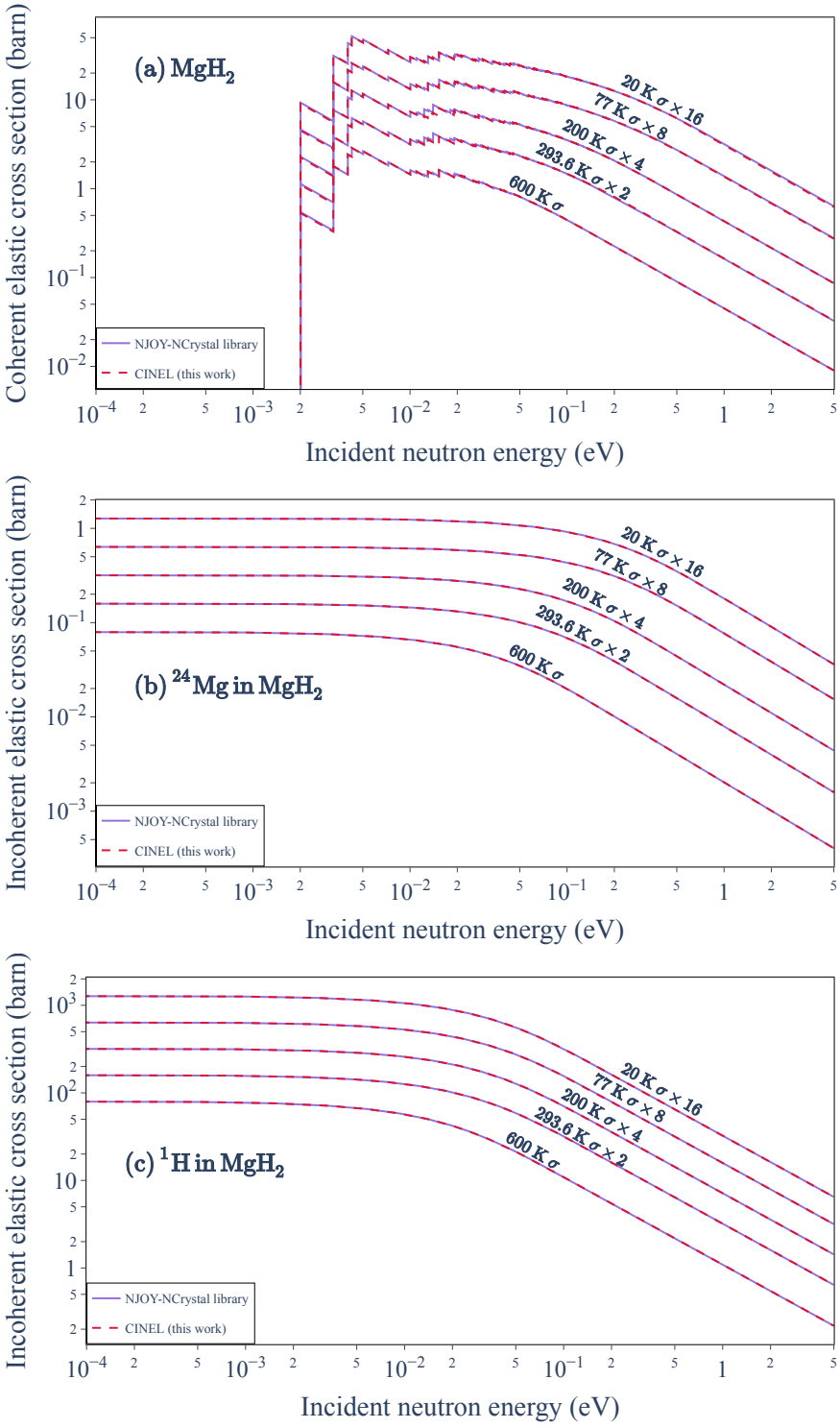

Figure C.5.: Comparaison des sections efficaces élastiques cohérentes calculées par `CINEL`de MgH_2, et des sections efficaces de diffusion élastique incohérentes de ^{24}Mg dans MgH_2 et ^{1}H dans MgH_2 (courbes en tirets) avec la librairie `NJOY-NCrystal` (courbes pleines) de 20 à 600 K.

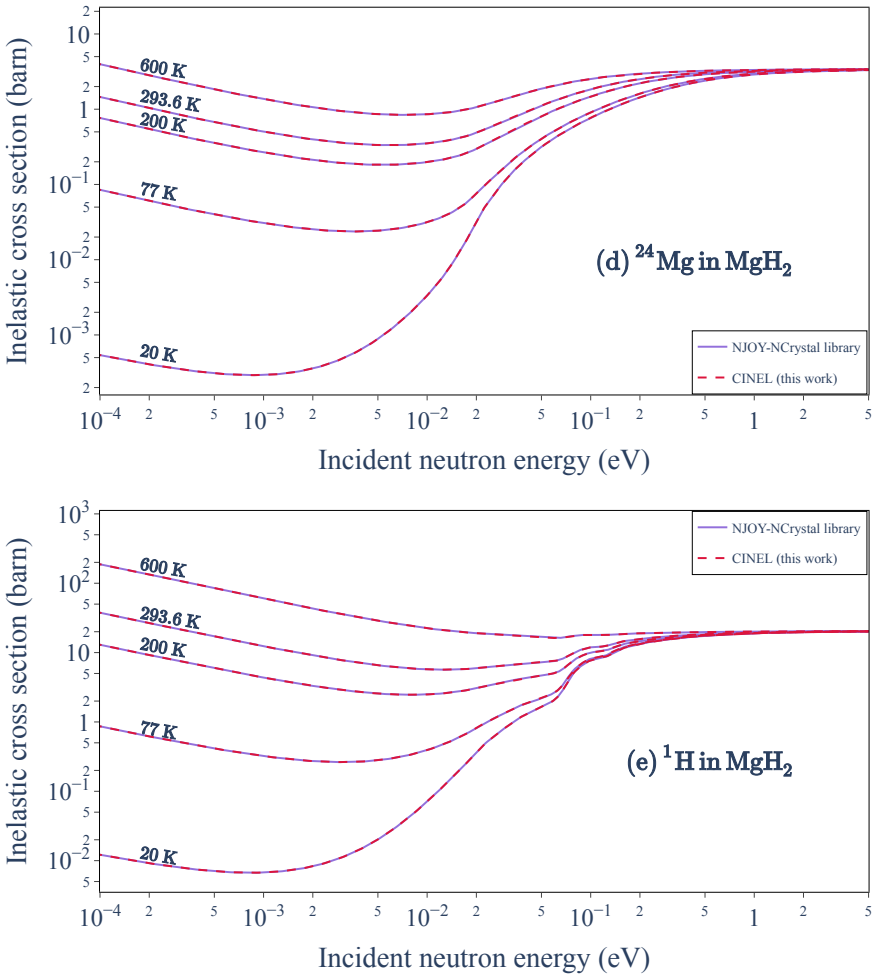

Figure C.5.: (suite) Comparaison des sections efficaces de diffusion inélastiques calculées par `CINEL`de ^{24}Mg dans MgH_2 et ^{1}H dans MgH_2 (courbes en tirets) avec la librairie `NJOY-NCrystal` (courbes pleines) de 20 à 600 K. Les sections efficaces élastiques cohérentes et incohérentes des Fig. (a), (b) et (c) sont multipliées par différents facteurs pour une meilleure visualisation.

large plage de températures allant de la température ambiante à 1664 K (le point de fusion de UO_2 est d'environ 3100 K (Hausner 1965)). L'originalité de notre travail repose sur l'utilisation du code Monte-Carlo TRIPOLI-4® (E. Brun, F. Damian, Diop, et al. 2015) pour simuler les diagrammes de diffraction expérimentaux en prenant en compte les effets de diffusion multiple des neutrons et la contribution des multiphonons. Les corrections expérimentales, qui ne sont pas introduites dans les simulations Monte-Carlo, sont la correction des bruits au fond, le décalage angulaire et la fonction de réponse angulaire du diffractomètre. Ils sont déduits des données en appliquant un raffinement de structure de type Rietveld (Rietveld 1969) sur les rendements de diffusion de neutrons simulés avec le code TRIPOLI-4®. Les résultats finaux dépendent principalement des sections efficaces de diffusion des neutrons de l'uranium et de l'oxygène dans UO_2 qui ont été introduites dans les simulations.

Le schéma de calcul utilisé dans ce travail est résumé dans la Fig. C.6. La première étape consiste à produire avec l'outil de traitement `CINEL` une bibliothèque d'applications qui contient des sections efficaces de diffusion des neutrons dépendantes de la température, qui sont stockées dans des fichiers ascii en suivant les exigences du format ENDF-6 pour les lois de diffusion thermique (Trkov and D. A. Brown 2018). La deuxième étape consiste à simuler les expériences de diffraction des neutrons avec le code Monte-Carlo TRIPOLI-4®. Les capacités de calcul haute performance permettent d'atteindre une incertitude statistique relative d'environ ±0.5% au sommet des pics de Bragg (et ±5.0% entre les deux) en quelques minutes pour une température donnée. La dernière étape est consacrée à la prise en compte des corrections expérimentales non introduites dans les simulations Monte-Carlo.

Les courbes finales calculées sont comparées aux résultats expérimentaux de la Fig. C.8 jusqu'à 1664 K. Aucune anomalie significative avec des températures croissantes n'a été observée à travers le comportement de ΔY qui représente la différence entre la théorie et l'expérience en fonction des angles de diffusion. Des variations ΔY presque équivalentes sont obtenues quelle que soit la température. La forme théorique des bords de Bragg aux angles de diffusion vers l'avant pourrait être améliorée en introduisant un modèle de raie de diffraction anisotrope, comme proposé dans les logiciels de raffinement de structure de Rietveld. Malgré une telle correction supplémentaire, qui n'est pas prise en compte dans le présent travail, la comparaison plus étroite des diagrammes de diffraction expérimentale et théorique, confirme que le code TRIPOLI-4® convient pour une analyse quantitative des données de diffraction en utilisant quelques nombres de paramètres libres. C'est également montré que la contribution croissante de la diffusion inélastique avec la température est assez bien reproduite par les calculs de Monte-Carlo. Cependant, cette composante de diffusion est assez faible dans le cas de l'expérience D20 qui a été réalisée avec des neutrons d'énergie $E = 48.05$ meV. Une telle question est abordée dans la section suivante grâce aux résultats obtenus avec l'instrument D4.

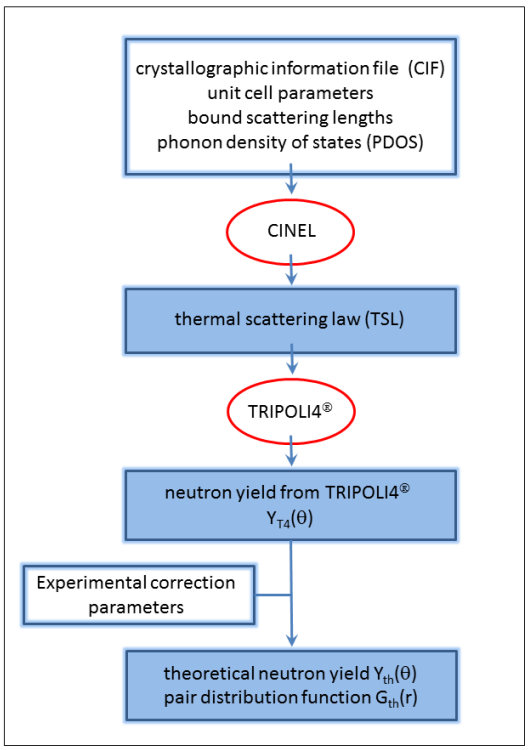

Figure C.6.: Organigramme présentant les étapes de traitement depuis le fichier d'informations cristallographiques jusqu'au rendement théorique de diffusion des neutrons et à la fonction de distribution de paires atomiques.

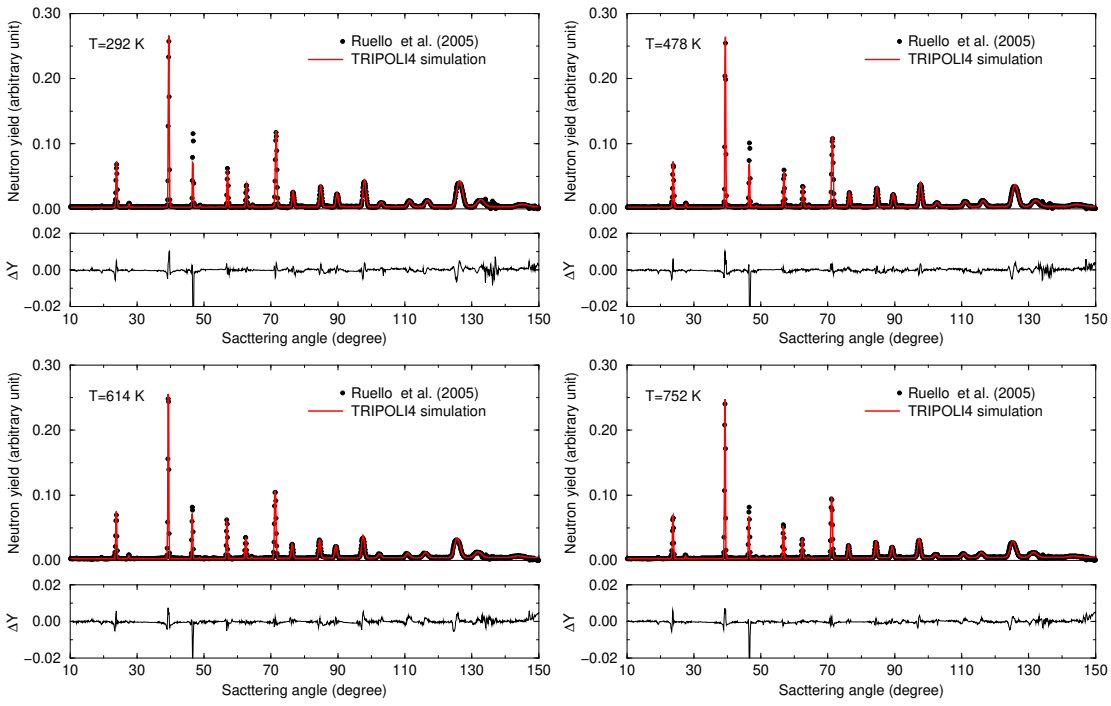

Figure C.7.: Diagrammes de diffraction UO_2 expérimentaux et théoriques pour D20 de 292 à 1664 K (E = 48.05 meV).

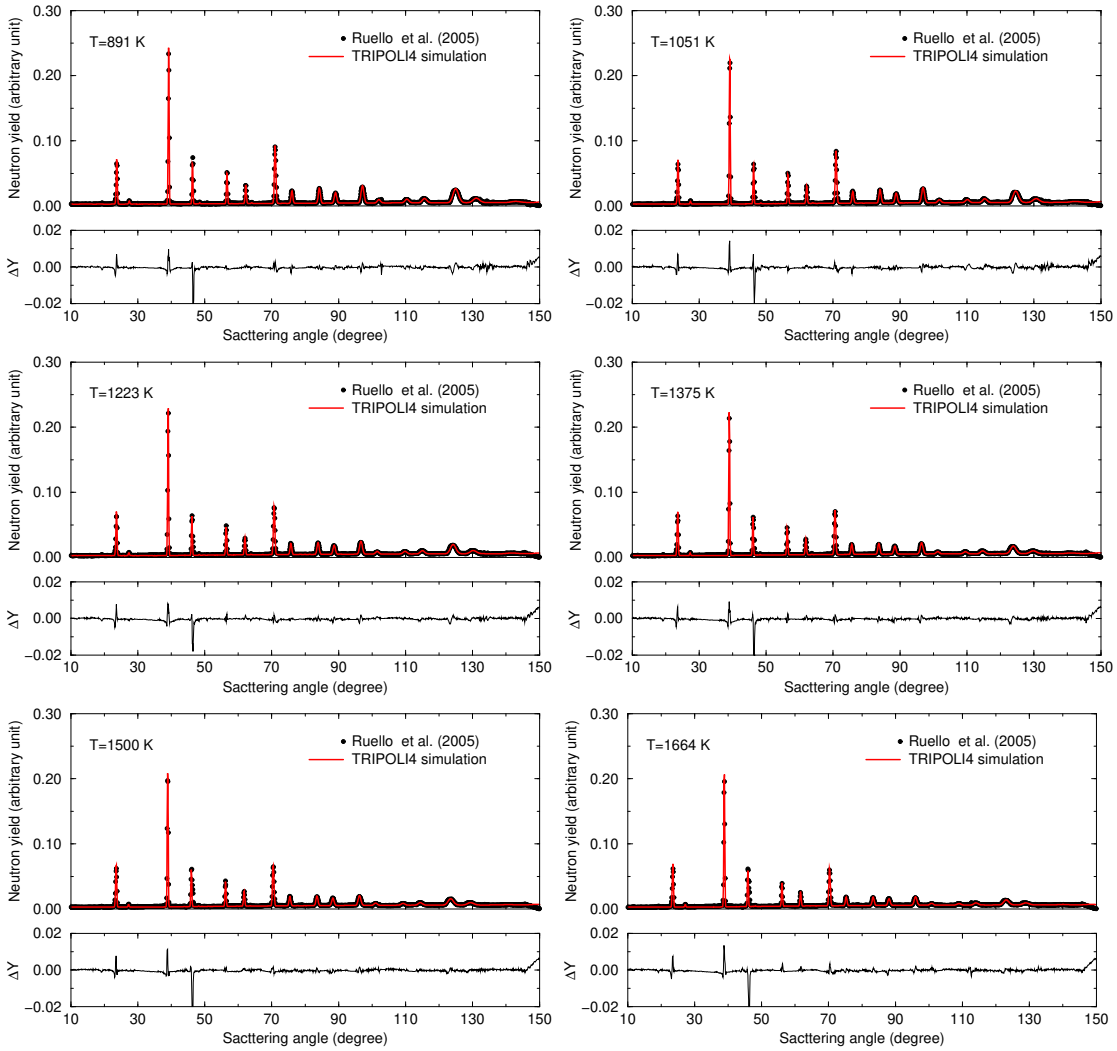

Figure C.8.: (suite) Diagrammes de diffraction UO_2 expérimentaux et théoriques pour D20 de 292 à 1664 K ($E = 48.05$ meV). ΔY représente la différence entre la théorie et l'expérience.

Fig. C.9 compare les diagrammes de diffraction neutronique expérimentale et théorique pour D4, dans laquelle la représentation lin-log met en évidence la contribution croissante de la diffusion inélastique avec l'angle de diffusion. Par souci de clarté, seuls quelques ensembles de température sont représentés.

Les fonctions expérimentales et théoriques de distribution de paires atomiques pour UO_2 sont comparées sur la Fig. C.10 de la température ambiante à 1273 K. Les simulations Monte-Carlo ont été réalisées en utilisant le group d'espace $Fm\bar{3}m$ avec des vibrations atomiques harmoniques. Les trois premiers pics correspondent principalement aux liaisons U-O, O-O et U-U (Palomares, McDonnell, Yang, et al. 2019). Un examen plus approfondi des résultats expérimentaux indique un décalage de pic négatif de -0.010(5) Åpour la liaison UO de 298 K à 1273 K, tandis que la position de pic de la liaison UU augmente de +0.020(5) Å. En revanche, les simulations de

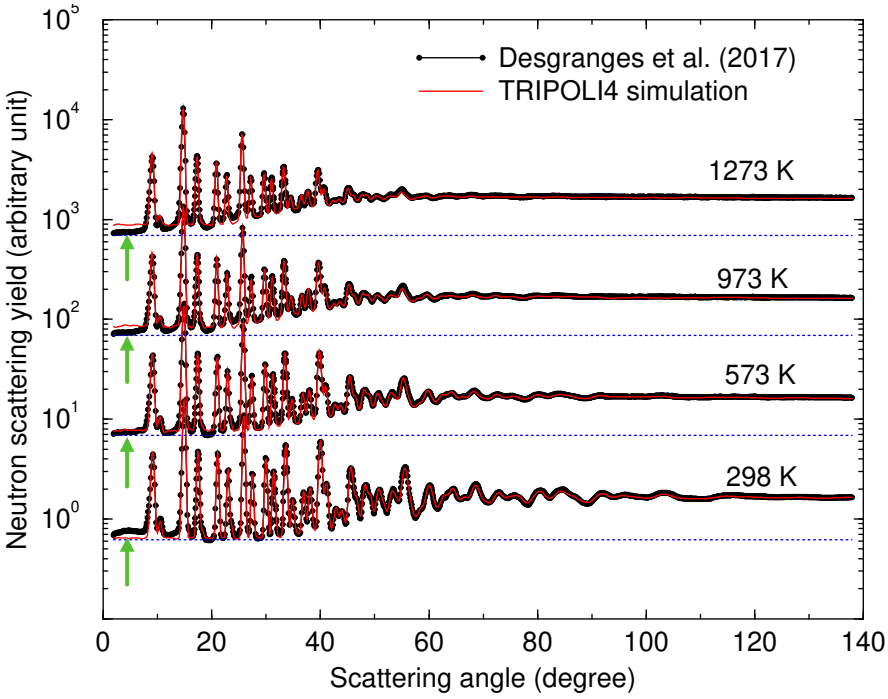

Figure C.9.: Diagrammes de diffraction UO_2 expérimentaux et théoriques pour D4 de 298 à 1273 K ($E = 331.18$ meV). Les flèches vertes mettent en évidence les différences observées entre l'expérience et la théorie aux angles de diffusion vers l'avant. Les lignes bleues en pointillés montrent la contribution croissante de la diffusion inélastique avec l'angle de diffusion.

Monte-Carlo fournissent des pics positifs qui sont proches de +0.040(5) Åpour les liaisons U-O et U-U.

Nos calculs sont en accord avec les travaux antérieurs rapportés dans la littérature. Ils concluent tous que l'arrangement des atomes d'uranium et d'oxygène ne peut pas être décrit en termes de structure fluorite idéale à température élevée. Les différences observées entre l'expérience et la théorie correspondent à un raccourcissement inattendu de la distance U-O avec l'augmentation de la température. Le mécanisme sous-jacent n'est pas bien compris. Elle fait l'objet de débats dans la littérature. Willis interprète les effets de la température sur la disposition du réseau en termes de vibrations atomiques anharmoniques (Willis 1963b; Willis, B.T.M. 1964; Willis and Hazell 1980). De même, Skinner et al. (Skinner, Benmore, Weber, et al. 2014) privilégient les mécanismes de désordre atomique dans l'espace des groupes $Fm\bar{3}m$ pour expliquer les longueurs de liaison U-O et U-U déduites des diagrammes de diffraction des rayons X mesurés jusqu'au point de fusion de l'UO_2. En revanche, l'existence d'une symétrie locale (telle que $Pa\bar{3}$) est suggérée par Desgranges et al. (Desgranges, Y. Ma, Garcia, et al. 2017) pour expliquer le raccourcissement de la distance U-O à 1273 K (Fig. 4.14).

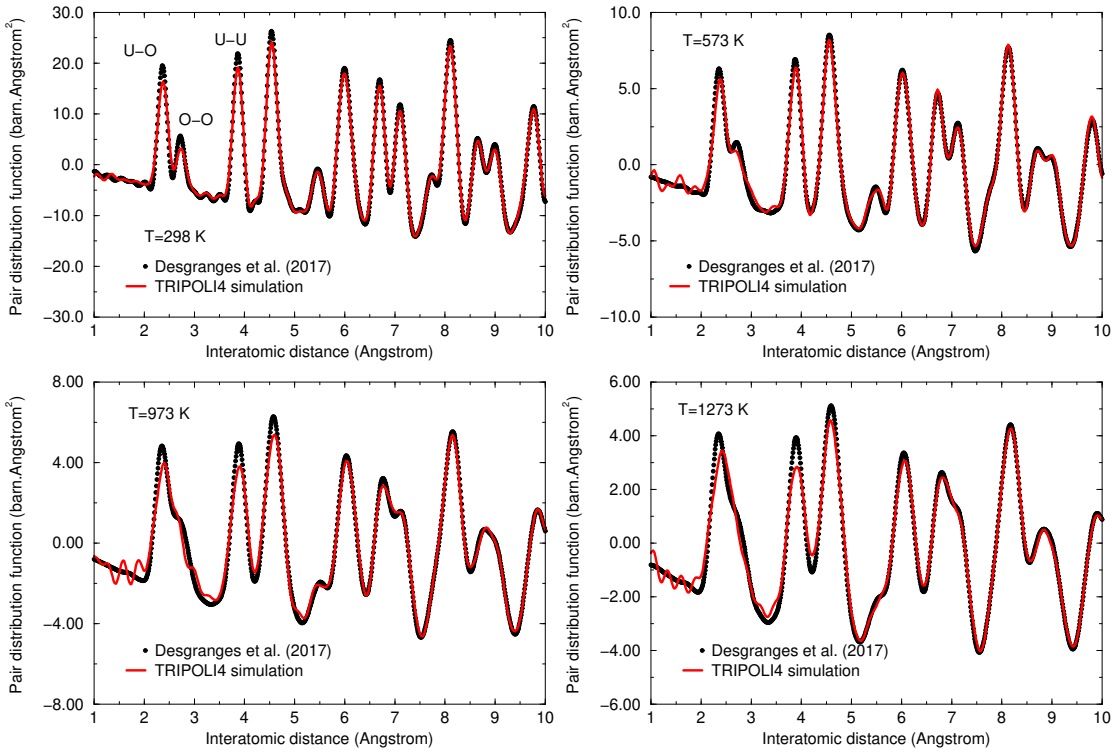

Figure C.10.: Fonctions expérimentales et théoriques de distribution de paires atomiques pour UO_2 (D4, $E = 331.18$ meV). La simulation TRIPOLI-4® a été réalisée en utilisant le groupe d'espace $Fm\bar{3}m$ avec des vibrations atomiques harmoniques. Les trois premiers pics correspondent principalement aux liaisons U-O, O-O et U-U (Palomares, McDonnell, Yang, et al. 2019).

C.4. Etude des traitements de diffusion des neutrons dans le domaine de l'énergie épithermale

La génération des fichiers de trajectoire pour l'eau en utilisant le code GROMACS de dynamique moléculaire (MD) est décrite dans la thèse de Scotta (J. Scotta 2017). Le modèle physique utilisé dans la simulation GROMACS consiste en un total de 512 molécules d'eau dans une boîte cubique avec une longueur de côté égale à 2.48 nm. Un potentiel en eau nommé TIP4P/2005f (González and Abascal 2011) est adopté pour quantifier les forces entre atomes. Le modèle TIP4P/2005f est un modèle de potentiel hydrique flexible qui permet de prendre en compte les interactions intermoléculaires et intramoléculaires. Grâce à ce potentiel, les positions et vitesses des atomes d'hydrogène et d'oxygène dans les molécules d'eau peuvent être obtenus pour un pas de temps donné et ils sont stockés dans des fichiers de trajectoire.

Les distributions de vitesse fournies par les fichiers de trajectoire de l'eau sont confirmées comme étant la distribution Maxwell-Boltzmann (M-B). Néanmoins, de fortes corrélations apparaissent entre les pas de temps, qui sont illustrées via le *velocity*

autocorrelation function (VACF) (J. Scotta 2017). Cependant, ces corrélations ne sont pas prises en compte dans l'algorithme SVT.

Pour valider l'algorithme SVT, les vitesses des noyaux cibles sont échantillonnées à partir de la distribution M-B à 294 K, et à partir des vitesses de H – 1 des fichiers de trajectoires GROMACS. Les rendements neutroniques obtenus (distributions des neutrons diffusés en fonction de l'énergie) à $\theta' = 10°, 45°, 90°$ pour les énergies neutroniques incidentes $E = 1, 5, 10$ eV sont respectivement présentés dans les Figs. C.11 et Fig. C.12. Ces résultats sont également comparés aux rendements neutroniques obtenus avec les TSLs $S(\alpha, \beta)_{\text{FGM}}$ calculés dans l'approximation du gaz libre.

Ces résultats montrent que les rendements neutroniques obtenus par l'algorithme SVT sont en excellent accord avec les résultats analytiques $S(\alpha, \beta)_{\text{FGM}}$ à la température $T = 294$ K pour l'énergie neutronique incidente supérieure à 5 eV. La dérivation de $S(\alpha, \beta)_{\text{FGM}}$ est basée sur l'hypothèse que les noyaux cibles sont des gaz libres avec des vitesses qui suivent une distribution M-B. Par conséquent, l'algorithme SVT doit être appliqué au-dessus du seuil proche de 5 eV pour l'hydrogène. Les rendements neutroniques obtenus avec les vitesses échantillonnées dans M-B et les fichiers de trajectoires GROMACS sont les mêmes car les corrélations entre vitesses présentées dans les fichiers de trajectoires ne sont pas incluses.

Les rendements neutroniques de ^{1}H dans $^{1}H_2O$ à $\theta' = 10°, 45°$ et $90°$ obtenus en utilisant le code TRIPOLI-4® pour les traitements de diffusion : SVT à T, SVT à T_{eff} et $S(\alpha, \beta)_{\text{SCT}}$ sont comparées aux résultats simulés par les $S(\alpha, \beta)$ tabulés à T. Les comparaisons des résultats sont montrées dans la Fig. C.13. Aux petits angles de diffusion ($\theta' = 10°$), les trois traitements étudiés ne parviennent pas à reproduire le pic quasi-élastique et les structures associées. Le traitement avec les tables $S(\alpha, \beta)_{\text{SCT}}$ reproduit mieux les rendements neutroniques liés à la diffusion ascendante, comparé au SVT à T_{eff}. À grande échelle θ', la diffusion ascendante des neutrons peut être négligée. Par conséquent, les traitements des tables $S(\alpha, \beta)_{\text{SCT}}$ et le SVT à T_{eff} sont équivalents. Ces deux traitements reproduisent mieux les rendements neutroniques, par rapport au SVT à T.

Les mêmes comparaisons sont effectuées dans le cas de ^{16}O dans UO_2. Les résultats obtenus sont présentés dans la Fig. C.14. À petit θ', les trois traitements de diffusion étudiés sont incapables de reproduire les structures liées aux mouvements atomiques des atomes d'oxygène liés dans UO_2. Ce résultat est en cohérence avec le cas de ^{1}H dans $^{1}H_2O$. La température effective de ^{16}O dans UO_2 ($T_{\text{eff}} = 381$ K) est proche de $T = 298$ K. Donc, en gros θ', les rendements neutroniques obtenus par l'algorithme SVT à T_{eff} ne montrent aucune différence significative avec les résultats obtenus par l'algorithme SVT à T. Il est recommandé d'ajouter une nouvelle option de diffusion dans le code TRIPOLI-4® qui permet de calculer en temps réel les tables $S(\alpha, \beta)$ avec le formalisme SCT en prenant en compte T et T_{eff} dans les calculs. Cette nouvelle option sera d'un grand intérêt pour tester l'impact de différents modèles de diffusion sur des benchmarks intégraux.

Ces résultats montrent l'importance d'utiliser la température effective pour prendre en compte les mouvements atomiques des atomes liés dans les molécules. Ils confirment également l'amélioration du traitement SCT pour les calculs de diffusion

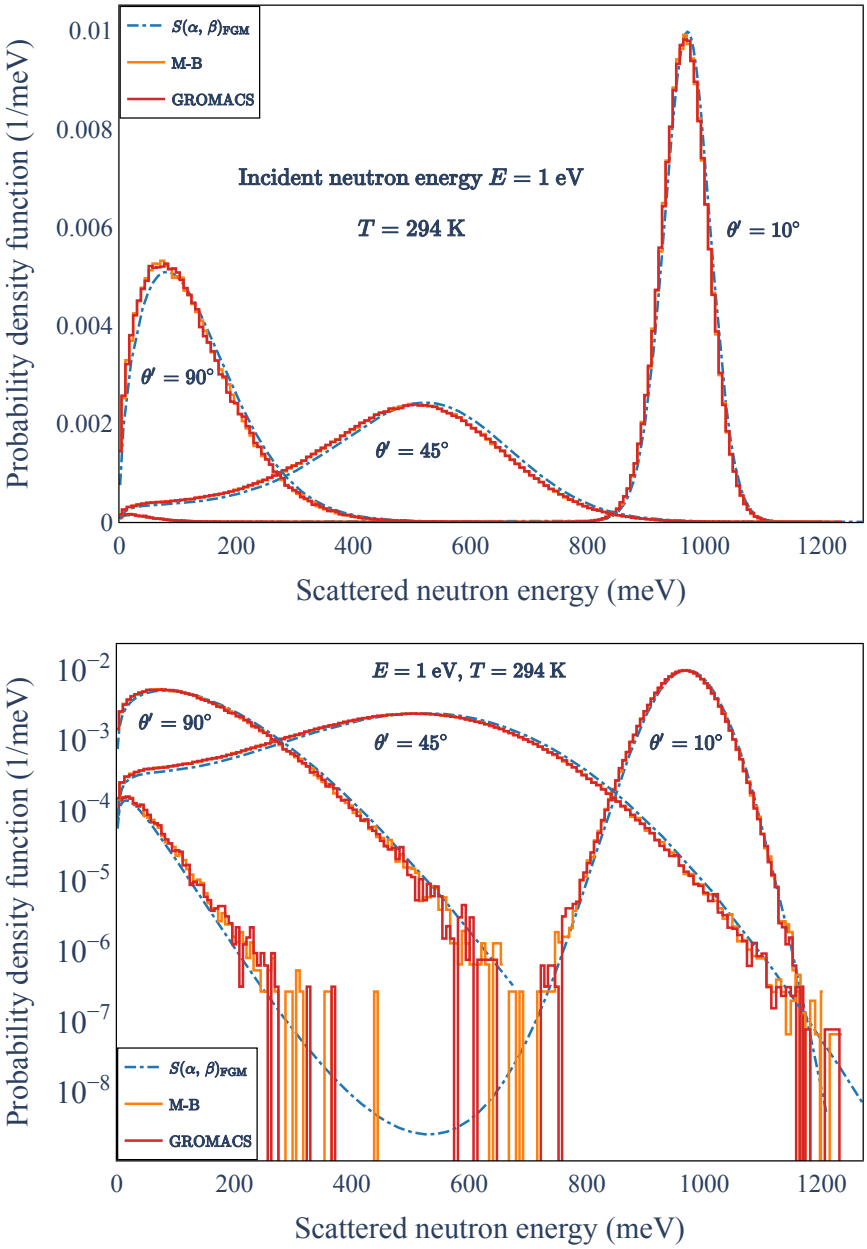

Figure C.11.: Distributions d'énergie des neutrons diffusés à $\theta' = 10°, 45°, 90°$ calculées par les lois de diffusion thermique pour le modèle de gaz libre $S(\alpha, \beta)_{\text{FGM}}$ et de *Sampling the Velocity of the Target nucleus* (SVT) à la température $T = 294$ K pour une énergie neutronique incidente égale à 1 eV. Le noyau cible est l'hydrogène. Les vitesses de l'hydrogène sont échantillonnées à partir de la distribution M-B à 294 K et des vitesses de l'atome H−1 dans les fichiers `GROMACS`. L'axe des y du graphique du bas est à l'échelle logarithmique pour une meilleure visualisation.

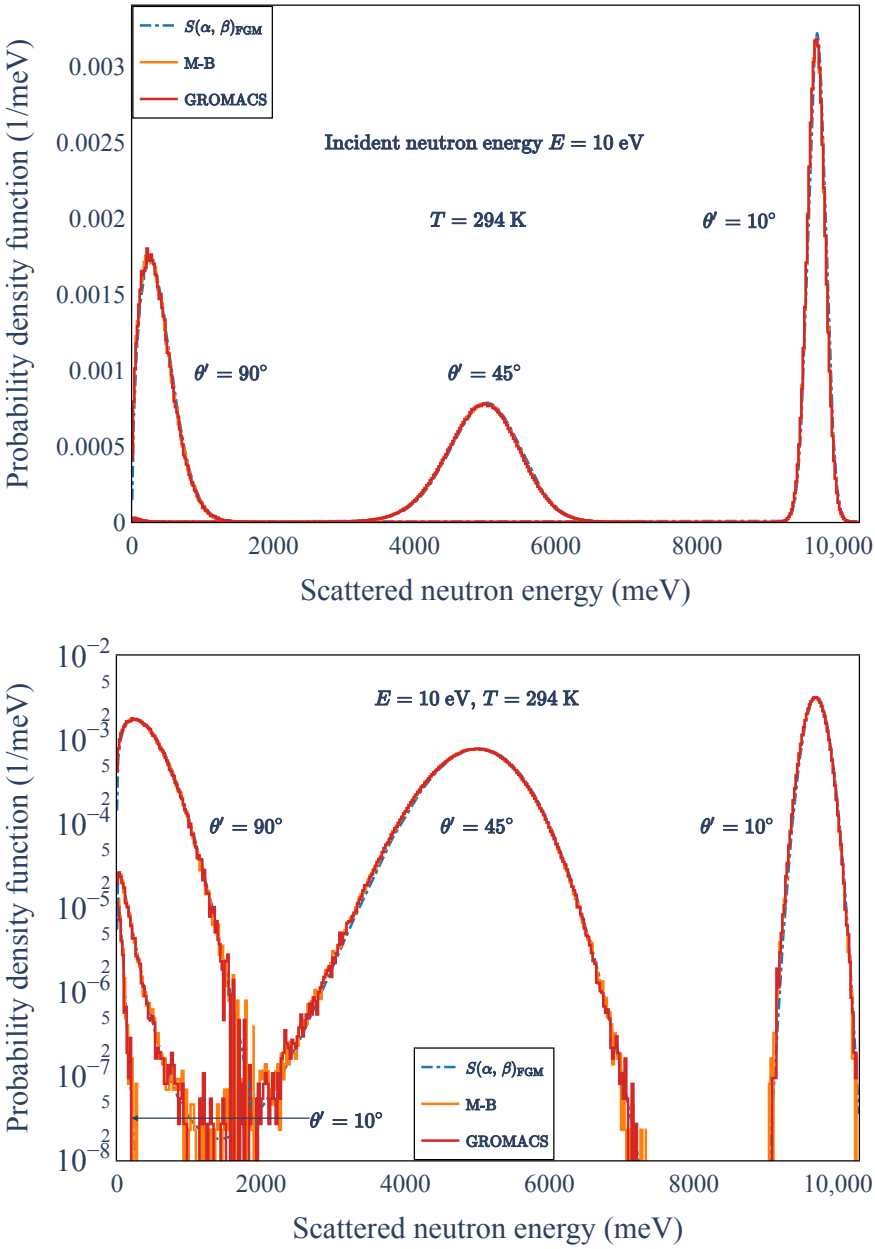

Figure C.12.: Distributions d'énergie des neutrons diffusés à $\theta' = 10°, 45°, 90°$ calculées par les lois de diffusion thermique pour le modèle de gaz libre $S(\alpha, \beta)_{\text{FGM}}$ et de *Sampling the Velocity of the Target nucleus* (SVT) à la température $T = 294$ K pour une énergie neutronique incidente égale à 10 eV. Le noyau cible est l'hydrogène. Les vitesses de l'hydrogène sont échantillonnées à partir de la distribution M-B à 294 K et des vitesses de l'atome H – 1 dans les fichiers `GROMACS`. L'axe des y du graphique du bas est à l'échelle logarithmique pour une meilleure visualisation.

ascendante, par rapport au SVT à T_{eff}.

Le présent travail se concentre sur le traitement des données et la validation des sections efficaces de diffusion élastique cohérente des neutrons $\sigma^{\text{el}}_{\text{coh}}(E)$ et des lois de diffusion thermique (TSLs) ou $S(\alpha, \beta)$ de UO_2 en fonction de la température.

Le formalisme de diffusion des neutrons à basse énergie a été présenté : des équations permettant de calculer les TSLs pour les matériaux solides cristallins, liquides et gazeux sont données. Sur la base de ces équations, l'outil informatique `CINEL` a été développé pour générer les TSL au format ENDF-6. `CINEL` est développé en Python en utilisant un environnement de développement interactif nommé JupyterLab. `CINEL` permet d'utiliser une unité de traitement graphique (GPU) pour accélérer le calcul des TSLs. Les validations numériques de `CINEL` sont effectuées en utilisant différents types de matériaux cristallins. Un excellent accord est obtenu par rapport à la base de données ENDF/B-VIII.0 et la librairie `NJOY-NCrystal`. Néanmoins, l'approximation incohérente adoptée dans le code `CINEL` serait inadéquate pour les matériaux cristallins fortement cohérents tels que le graphite pyrolytique. Par conséquent, la correction cohérente à un phonon sera implémentée dans la future version de `CINEL` pour améliorer l'approximation incohérente. L'approximation cubique utilisée dans la version actuelle de `CINEL` sera également supprimée.

Grâce à la PDOS de UO_2 mesurée aux spectromètres de temps de vol IN4 et IN6 de l'Institut Laue-Langevin (ILL) jusqu'à 1675 K, les TSL de UO_2 pour une large plage de température peut être calculé en utilisant le code `CINEL`. Une structure de fluorite idéale pour UO_2 sur toute la plage de température a été adoptée pour calculer $\sigma^{\text{el}}_{\text{coh}}(E)$. Les résultats fournis par `CINEL` sont stockés au format ENDF-6, qui peuvent être traités ultérieurement pour être utilisés comme bibliothèque de diffusion de neutrons dans le code de transport de neutrons de Monte-Carlo TRIPOLI-4®. Deux jeux de données d'expériences de diffraction des neutrons réalisées aux diffractomètres D4 et D20 de l'ILL jusqu'à 1664 K, ont été simulés en utilisant le code TRIPOLI-4®. Quelques paramètres expérimentaux ont été optimisés sur les données pour tenir compte du décalage angulaire, de la fonction de réponse du diffractomètre et d'une correction des bruits au fond. Le bon accord entre les diagrammes de diffraction neutronique expérimental et théorique valide notre schéma de calcul TRIPOLI-4® pour UO_2. Les résultats obtenus indiquent que TRIPOLI-4® est capable de reproduire ces diagrammes de diffraction des neutrons grâce au code `CINEL` développé. Cependant, quelques problèmes limités subsistent dans l'interprétation de la correction des bruits au fond. Les biais dus aux approximations théoriques devraient être étudiés.

Les performances de notre schéma de calcul ont également été étudiées en simulant des fonctions de distribution de paires atomiques pour sonder la structure de UO_2 à température élevée. Les différences observées à 1273 K entre l'expérience et la théorie confirment que les écarts locaux des atomes d'oxygène par rapport à la structure moyenne de UO_2 ne sont pas compatibles avec une structure fluorite idéale. Nous montrons que l'outil de traitement `CINEL` offre la possibilité de tester des configurations de désordre atomique, des modèles anharmoniques ou des groupes spatiaux qui sont suggérés dans la littérature pour explorer le raccourcissement inattendu de la distance U-O avec l'augmentation de la température.

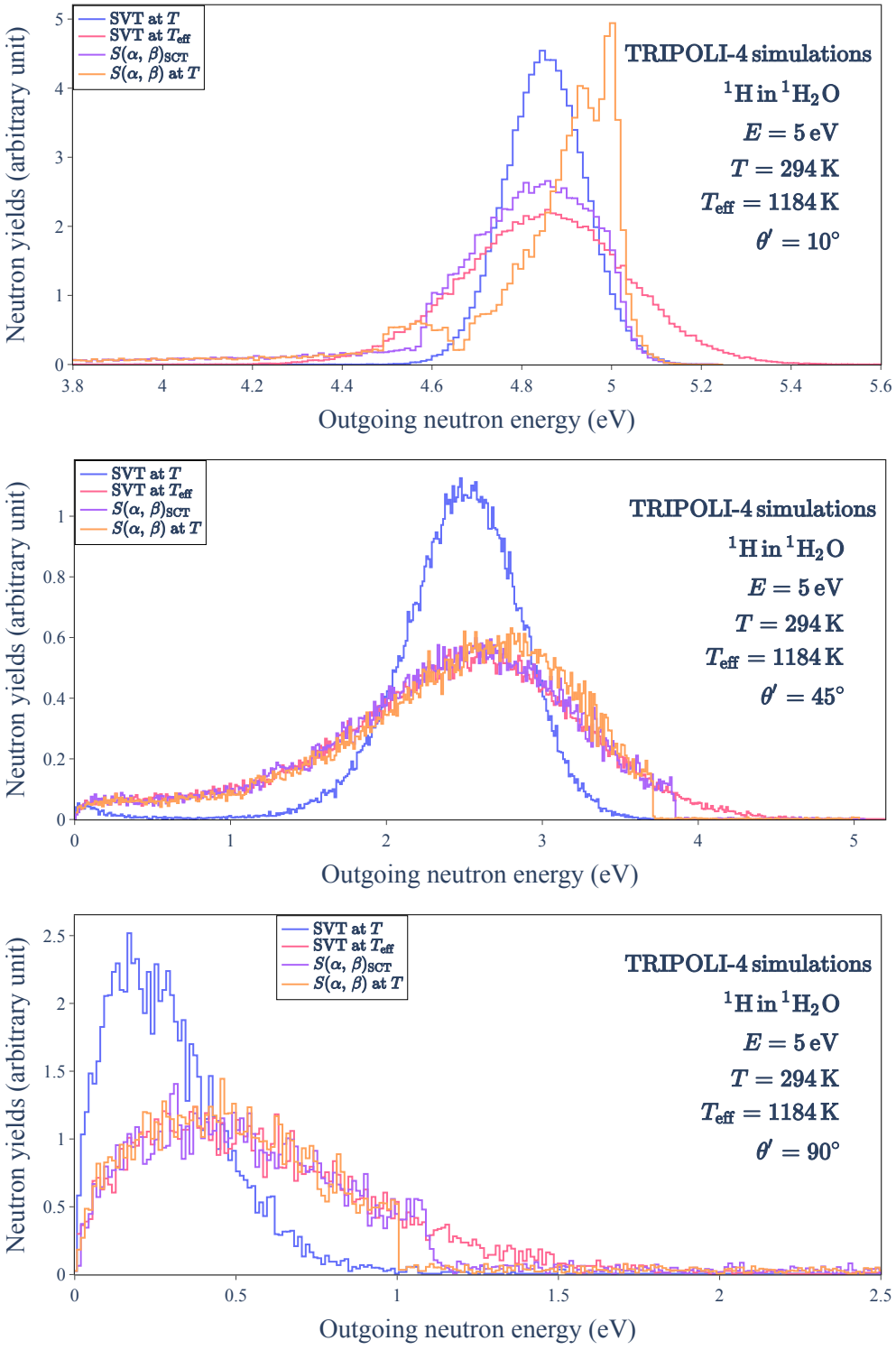

Figure C.13.: Rendements neutroniques de ^{1}H dans ^1H_2O à $\theta' = 10°$, 45° et 90° obtenus par en utilisant le code Monte-Carlo de transport de neutrons TRIPOLI-4® pour différents traitements de diffusion : SVT à $T = 294$ K (lignes bleues), SVT à $T_{\text{eff}} = 1184$ K (lignes roses), $S(\alpha, \beta)_{\text{SCT}}$ (lignes violettes), $S(\alpha, \beta)$ à T (lignes orange).

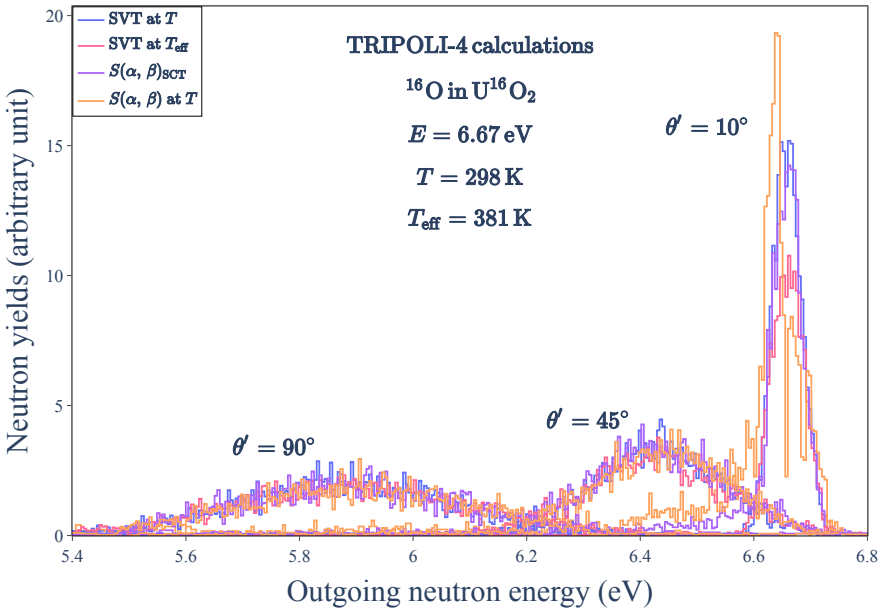

Figure C.14.: Rendements neutroniques de ^{16}O dans UO_2 à $\theta' = 10°$, 45° et 90° obtenus en utilisant le Monte-Code de transport de neutrons Carlo TRIPOLI-4® pour différents traitements de diffusion : SVT à $T = 298$ K (lignes bleues), SVT à $T_{\text{eff}} = 381$ K (lignes roses), $S(\alpha, \beta)_{\text{SCT}}$ tables (lignes violettes), $S(\alpha, \beta)$ à T (lignes orange).

Le schéma de calcul TRIPOLI-4® pour UO_2 a été validé pour une énergie neutronique incidente supérieure à quelques eV. Dans le domaine de l'énergie épithermale où les TSLs ne sont pas disponibles, la diffusion des neutrons avec des nucléides légers ayant une section efficace de diffusion des neutrons non résonante a été étudiée. Les traitements de diffusion neutronique étudiés sont : AK (pour *Asymptotic Kernel*), SVT (pour *Sampling the Velocity of the Target nucleus*) à température thermodynamique T et température effective T_{eff}, FGM (pour *Free Gas Model*), SCT (pour *Short Collision Time* approximation) et $S(\alpha, \beta)$ sous forme de tableau. L'algorithme SVT a été validé en échantillonnant les vitesses d'atomes d'hydrogène à partir d'une distribution de Maxwell-Boltzmann (M-B) et de fichiers de trajectoire obtenus à partir de calculs de dynamique moléculaire avec le code GROMACS. Les validations numériques des traitements de diffusion de neutrons ci-dessus avec le code TRIPOLI-4® sont effectuées à température ambiante pour ^{1}H dans $^{1}H_2O$ et ^{16}O dans UO_2. Les résultats obtenus indiquent que les tables $S(\alpha, \beta)$ sont correctement utilisées par le code TRIPOLI-4® pour simuler le transport de neutrons avec des énergies comprises entre quelques eV et $400 k_B T$. L'importance d'utiliser la température effective et l'amélioration du traitement SCT pour les calculs de diffusion ascendante sont confirmées. Les résultats obtenus pour les nucléides légers seront approfondis pour ^{238}U dans UO_2.